In-situ thermometry and spin transport in fermionic quantum wires

Clément de Daniloff

PSL UNIVERSITÉ PARIS

THÈSE DE DOCTORAT
DE L'UNIVERSITÉ PSL

Préparée à l'École Normale Supérieure

In-situ thermometry and spin transport in fermionic quantum wires

Soutenue par

Clément De Daniloff

Le 1er décembre 2021

École doctorale n° 564

Physique en Ile-de-France

Spécialité

Physique Quantique

Composition du jury :

Patrizia Vignolo	INPHYNI – Université Côte d'Azur	*Rapporteuse*
Isabelle Bouchoule	Laboratoire Charles Fabry – CNRS	*Rapporteuse*
Rudolf Grimm	IQOQI – Universität Innsbruck	*Examinateur*
Leonardo Fallani	LENS – Università degli Studi di Firenze	*Examinateur*
Thierry Giamarchi	DQMP – Université de Genève	*Président*
Frédéric Chevy	LKB – École Normale Supérieure	*Directeur de thèse*

PSL UNIVERSITÉ PARIS

1794 ENS ÉCOLE NORMALE SUPÉRIEURE

Abstract

The behaviour of low-dimensional interacting Fermi gases greatly differs from their three-dimensional counterparts. In absence of order in 3D, the majority of fermionic states of matter can be explained by the Landau-Fermi liquid theory. Within this framework the system is described as a gas of non- or weakly-interacting fermionic quasiparticles. By contrast, in one dimension, the low-energy excitation spectrum of the system is entirely made up of collective excitations obeying bosonic statistics.

This thesis reports on the experimental study of low-dimensional Fermi gases using ultracold ^{40}K atoms. The main results are threefold. First, we describe the conception of novel experimental techniques to load and individually image an array of tube-shaped micro traps in a large-spacing optical lattice. Second, using these atomic ensembles in a noninteracting setting, we perform a quantitative analysis of their *in-situ* density profiles to extract the degree of quantum degeneracy and effective dimensionality. In this context, we show evidence of the preparation of Fermi gases in the one-dimensional regime. Third, we present a technique to separate the spin components of the gas and apply it to study spin transport in low dimensions in the presence of strong interactions. We quantitatively model the spin dipole relaxation process in the diffusive regime as a function of the interaction strength tuned with an $s-$wave Feshbach resonance. We determine the spin drag and the diffusivity, the latter having a minimal measured value of $D_s = 8.9 \pm 0.6\,\hbar/m$. This is compatible with the quantum bound $\geq \hbar/m$ despite the absence of scale-invariance in the system, and supplements existing experimental studies in two- and three-dimensional Fermi gases.

Résumé

Le comportement des gaz de Fermi en basse dimension se distingue sensiblement de leurs équivalents tridimensionnels. En trois dimensions et en l'absence d'ordre, la majorité des états fermioniques de la matière sont décrits par la théorie du liquide de Landau-Fermi. Dans son cadre, le système est décrit comme un gaz de quasiparticules fermioniques en interaction faible, voire nulle. En revanche, dans le cas unidimensionnel, le spectre du système à basses énergies est entièrement déterminé par des excitations collectives de nature bosonique.

Cette thèse décrit l'étude expérimentale des gaz de Fermi en basse dimension en utilisant des atomes de ^{40}K . Nous présentons ici trois principaux résultats. Tout d'abord, nous mettons en évidence l'implémentation de techniques nouvelles pour charger et imager individuellement des échantillons d'atomes dans un réseau optique bidimensionnel à espacement large. Ensuite, en utilisant des gaz idéaux, nous conduisons une étude quantitative de profiles de densité *in-situ* obtenus dans un potentiel externe préalablement calibré pour quantifier le degré de dégénérescence et la dimensionnalité des échantillons préparés. Nous rapportons l'observation de gaz de Fermi dans le régime unidimensionnel. Finalement, nous développons une technique pour séparer et isoler les deux populations de spin d'un gaz de Fermi et l'appliquons pour étudier le transport de spin en présence d'interactions fortes. Nous analysons quantitativement la relaxation du mode dipolaire dans le régime diffusif en fonction de l'intensité des interactions en se plaçant au voisinage d'une résonance de Feshbach en onde s. Nous déterminons la force de traînée ainsi que le coefficient de diffusivité. La valeur minimale mesurée de ce dernier est $D_s = 8.9 \pm 0.6\hbar/m$, ce qui respecte la limite quantique $\geq \hbar/m$ malgré l'absence d'invariance d'échelle dans le système. Ce dernier résultat s'ajoute au corpus de connaissance existante issue de précédentes études expérimentales réalisées avec des gaz de Fermi en deux et trois dimensions.

Contents

Chapter 1

Introduction

Imagine living in a universe featuring three spatial dimensions[1] (3D), and you are wondering whether it is possible to create a system that behaves as if the laws of physics would stem from a one-dimensional universe (1D). Intuitively, it makes sense to think that this can be realized by simply restricting access to the undesired dimensions[2], which we will refer to as transverse degrees of freedom. This may be achieved by means of an external potential, which would strongly compress them. In this context, a question naturally arises: how much is enough compression? The answer heavily depends on what we mean by "laws of physics". Indeed, if we considered classical physics, this question would essentially be meaningless. As the amount of compression along the undesired directions is increased, the typical extent of trajectories in these directions merely decrease monotonously. Evidently, there is no obvious threshold signalling a change of dimensionality. However, if we looked at this problem from the perspective of quantum physics, moving objects would now be described by a combination of wavefunctions with well-defined discrete energy levels in each direction. Therefore, the quantum of energy that separates the lowest energy motional state to the first excited one in the transverse directions defines a natural threshold. If the kinetic energy of a moving object happened to be well below this threshold, its dynamics in the transverse directions would be completely frozen out. Nonetheless, the wavefunction still has a finite extent along the transverse direction, which is associated with a length scale that can influence the behaviour of the overall physical system. For that reason, we refer to such systems as quasi-1D[3].

There are numerous reasons why the 1D universe is worth investigating[4], especially in the context of many-body problems. The extreme level of kinematic constraints imply strong modifications of the underlying physics in comparison to the higher-dimensional case. As shown in figure, 1.1 any individual excitation eventually turns into a collective one. This simplified classical illustration is meant to illustrate a property that profoundly shapes the low-energy spectrum of interacting quantum systems [3, 4]. In 1D the complete collectivization of elementary excitations in gapless systems is captured by the paradig-

[1] Hopefully, most of the readers can relate.
[2] Just a normal Tuesday afternoon for a string theoretician [1].
[3] This terminology is sometimes used to refer to several 1D systems coupled together [2].
[4] Apart from the phobia of vectors.

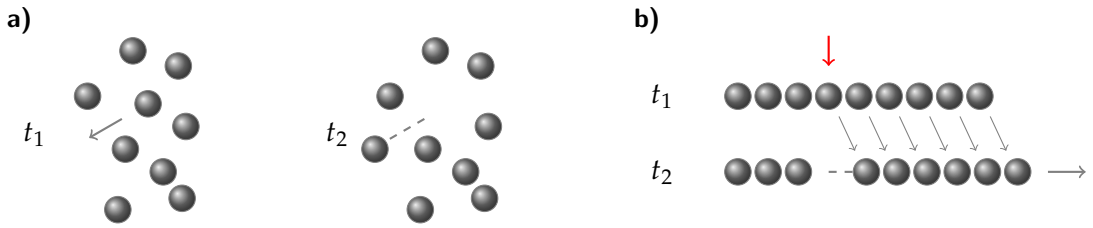

Figure 1.1: Dimensionality in a system of hard spheres. The system is assumed to be static until an excitation is applied at $t = t_1$. a) In two dimensions and above, there exist excitations that only involve a single particle. b) In one dimension, a single particle cannot move without pushing other ones. As a result, collective excitations are possible.

matic Tomonaga-Luttinger liquid (TLL) model [5–7]. Experimental evidence for TLL-type systems have been obtained in several classes of solid-state systems, including organic conductors [8, 9], carbon nanotubes [10, 11], semi-conductor wires [12–14], antiferromagnetic spin chains [15], metallic chains [16] and edge modes of integer and fractional quantum hall states [17]. The materials used to realize those systems are usually complex and do not permit to fine-tune the inter-dimensional couplings, which makes quantitative comparison with theories very challenging.

Quantum statistics

The most elementary constituents of our universe are, currently, best described by the standard model [18]. Among many properties, each fundamental building block possesses a "spin", which quantifies the internal angular momentum [19]. Remarkably, all particles that move in three dimensions have a spin that is either an integer or a half-integer multiple of the reduced Planck constant $\hbar$ [20, 21]. According to the spin-statistics theorem, the wave-function of a system of identical integer-spin (half-integer-spin) particles is symmetric (antisymmetric) when the positions of any pair of particles are exchanged, and the particles are called *bosons* (*fermions*) [22, 23]. Elementary bosons mediate the fundamental forces of nature, whereas matter is made up of fermions [24]. However, composite systems such as neutral atoms can be either bosons or fermions, which follows from the addition rules of the angular momentum. In a noninteracting many-body system made up of identical particles, the ground state properties depend critically on the spin-statistical nature of its constituents. In the bosonic case, all of the particles accumulate in the lowest energy state, resulting in a Bose-Einstein condensate (BEC) [25, 26], as shown in figure 1.2 a). However, for fermions the result is drastically different as the Pauli exclusion principle[5], prevents particles of equal spin from occupying identical single particle states [27]. In that case, the ground state of the system is the Fermi Sea, obtained by gradually

[5]Which is a trivial consequence of the antisymmetry of the wavefunction.

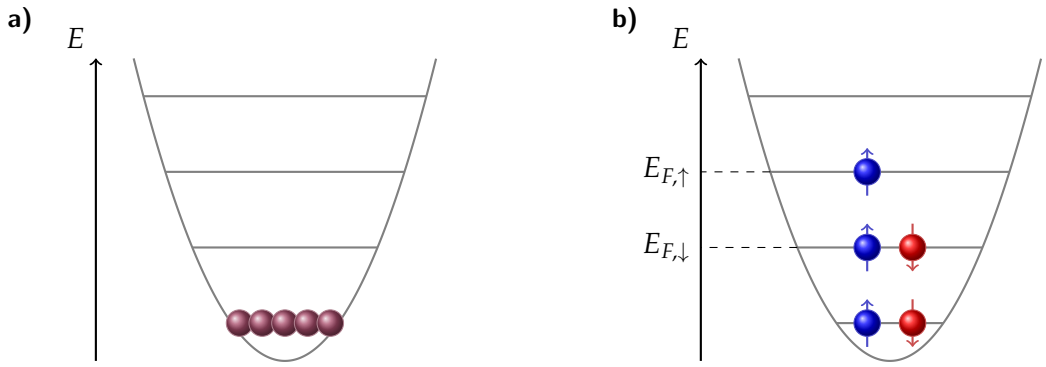

Figure 1.2: Bose-Einstein condensate versus degenerate Fermi Gas. Representation of bosonic and fermionic quantum gases in their ground states. a) Spinless bosons accumulate in the lowest-energy single particle state. b) Spin-1/2 fermions fill the energy levels from the bottom up to due to Pauli's exclusion principle. For each spin component, the highest occupied state defines the Fermi energies $E_{F,\uparrow}$ and $E_{F,\downarrow}$. For a spin-balanced system, these energies are equal and denoted by E_F.

filling up all of the available states, starting from the lowest energy ones. This situation is illustrated in figure 1.2 b). The exclusion principle is directly responsible for the stability of large scale systems, for instance solids, that would otherwise collapse upon electrostatic forces [28, 29].

At a finite temperature T, these effects arising from quantum statistics may or may not be relevant, depending on how dense the system is. We denote the density by[6] n_{3D}. At high temperature, the particles' thermal wavelength[7] $\lambda_T = \sqrt{2\pi\hbar^2/mk_BT}$ [30] is much smaller than their average inter-particle spacing $n_{3D}^{-1/3}$. In this case, they are correctly described by point-like particles that follow a Boltzmann distribution [31]. More precisely, this limit can be characterized by referring to the phase-space density, for which $\mathrm{PSD} = \lambda_T n_{3D}^3 \ll 1$, holds. In the opposite limit where $\mathrm{PSD} \gg 1$, the effects of quantum statistics dominate. In bosonic systems, a second order phase transition to a BEC occurs when the temperature drops below $T_c \approx 3.3125\,\hbar^2 n_{3D}^{2/3}/mk_B$, or equivalently, when $\mathrm{PSD} > 2.612$. In fermionic systems, there is no sharp transition between the classical and the degenerate regime, however, the temperature must ultimately be compared to the Fermi temperature $T_F = E_F/k_B$. The quantum limit then corresponds to $T/T_F \ll 1$.

[6] Assuming a homogeneous system.
[7] k_B is the Boltzmann constant and m is the mass of the constituents.

Interacting quantum gases

In addition to quantum statistics, interactions play a crucial role in defining the properties of many-body systems. In metals, where the delocalized electrons form an ensemble of fermions, their interactions can give rise to pairing and superconductivity provided the temperature is low enough. It was first understood by Cooper that this form of pairing is not occurring in a two-body system but rather in a many-body context due to constraints in phase space created by Pauli-exclusion [32]. This insight lead to the famous Bardeen-Cooper-Schrieffer (BCS) theory of superconductivity, which attributes pairing in metals at low temperature to phonon-mediated attractive interactions between electrons [33]. However, above the critical temperature associated with Cooper pair creation, the system is said to be in a normal state. In dimensions ≥ 2, it is correctly described by the Fermi liquid theory, which possesses certain similarities with respect to the free fermion gas and is effective beyond the perturbative regime [34–36]. In this model, the elementary constituents are not single particles anymore, but rather quasi-particles that can be seen as bare fermions dressed by density fluctuations, as illustrated in figure 1.3. Remarkably, despite their finite lifetime, which happens to be very large in the vicinity of the Fermi surface where the theory is applicable, they can be described using the same properties as bare particles: a well-defined momentum $\hbar\vec{k}$ and a renormalized mass $m^* \neq m$ incorporating the effect of interactions. Interactions between quasiparticles exist as well and are captured by the Landau parameters, which quantify the response of the system to an external probe [37]. Our previous discussion about 1D systems makes it clear why a description that treats excitations as individual quasiparticles is not appropriate in one dimension. It is superseded by the TLL theory, which pursues the same goal of describing the normal state beyond the perturbative regime, but features free bosonic collective excitations instead. In this context, the usual quadratic dispersion relation is replaced by a linear one around $k = k_F$, where $k_F = \sqrt{2mE_F/\hbar^2}$ is the Fermi wavevector. Therefore, the TTL model describes low-energy excitations. In an interacting spinless system, the net effect of interactions is fully captured by two Luttinger parameters u and K, which describe the velocity of collective modes and the algebraic decay of correlation functions, respectively[8]. When applied to a spin-1/2 Fermi gas, it predicts the complete separation of spin and charge sectors, a unique feature that has no equivalent in the Fermi liquid framework.

[8] In the non-interacting limit, $u \to v_F$ and $K \to 1$, where $v_F = \sqrt{2E_F/m}$ is the Fermi velocity.

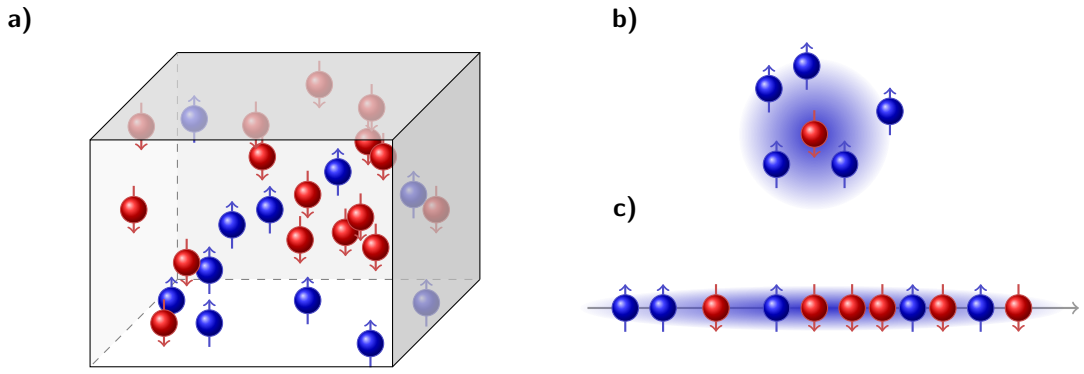

Figure 1.3: Interacting Fermi gases in 1D and 3D. a) Interacting Fermi gas in a 3D homogeneous box. b) Representation of a quasi-particle excitation. A spin down particle is dressed by the surrounding spin up atoms due to interactions. c) Illustration of an interacting two-components Fermi gas in 1D. Individual fermionic quasi-particle excitations are replaced by collective bosonic ones, where spin and density (charge) excitations propagate independently.

Ultracold atomic gases

By making use of the interactions of neutral atoms with electromagnetic fields, ultracold atoms have been used to create quantum simulators [38–40], in addition to ionic [41] or photonic systems [42]. The success of cold-atom based platforms for quantum simulation is the direct result of major breakthroughs regarding laser cooling and trapping techniques of neutral atoms suspended in vacuum [43]. After the first theoretical proposals for laser cooling in the 1970s [44, 45], cooling [46] and trapping [47–49] were achieved experimentally in the 1980s. Ultimately, this lead to the creation of the first BECs in 1995 [50, 51], followed by the first degenerate Fermi gas in 1999 [52]. The ensuing demonstration of superfluidity [53] and phase coherence of BECs [54, 55] quickly demonstrated the immense capacity of cold atoms as a mean to explore many-body physics. Since then, this field of research has undergone a tremendous expansion [56–59].

Controlling interactions

Physicists who try to understand the properties of materials from a microscopic perspective necessarily have to include interactions in their model, and control their relative relevance with a coupling strength. From the perspective of a theoretician this coupling strength is a variable, and the evolution of any observable derived from the model might depend on it. From this point of view, most materials in nature can be seen as a very specific realization of a model, which might actually have much more predictive power beyond the particular material that motived its development in the first place. This is fairly

frustrating since these models can sometimes predict new phases of matter or unique features in a parameter regime that is not accessible experimentally. On the one hand, it can be argued that predictions made by a model whose inputs do not correspond to any material known to exist in nature are by definition unscientific, in the strict sense that they cannot be compared to observations. On the other hand, the uncompromising curiosity and creativity of researchers across the world continuously expands the reach of experimental physics through the development of artificial systems, ultimately realizing situations initially deemed scientifically irrelevant. Especially in this respect, cold atoms truly stand out thanks to their flexibility in terms of tunable interaction strengths facilitated by magnetically tunable Fano-Feshbach resonances [60, 61].

In general, alkali atoms interact through a short-ranged[9] Van der Waals potential. Consequently, the effect of interactions at the many-body level is dominated by few-body collisions. Remarkably, at low energy, the spatial extent of the single-particle wavefunctions exceed the range of the potential by a large amount. By that reason, the outcome of the scattering events in the $s-$wave channel[10] is described by a single parameter, the scattering length a_{3D}, which incorporates all of the microscopic details of the interaction potential. The Feshbach resonances can then be used to tune a_{3D} by superimposing an external magnetic field at the resonant field strength [62]. Such scattering resonances are in general not universal and depend on the specific pair of atoms under consideration. A large number of them have already been catalogued [63].

The possibility to arbitrarily tune the scattering length has lead to a very important milestone in the research of interacting two-component Fermi gases: the realization of the BEC-BCS crossover [64], which has been thoroughly studied both theoretically and experimentally [65–67]. From the BCS to the BEC side, there is an increasing amount of attraction between individual atoms. The limit $1/k_F a_{3D} \gg -1$ corresponds to the former, where the many-body ground state consists of loosely bound Cooper pairs, analogously to electrons in superconducting metals. The opposite limit $1/k_F a_{3D} \gg 1$ corresponds to the BEC side, where atoms form deeply bound dimers which then condense as a consequence or their composite bosonic statistics. These dimers have a bound state energy of $E_b = -\hbar^2/m a_{3D}^2$ originating directly from the two-body scattering problem in a contact potential. This two-body bound state only exists only when $a_{3D} > 0$. A highly non-trivial regime is obtained when $1/k_F|a_{3D}| < 1$ and is characterized by strong correlations at the many-body level. A remarkable point of the crossover is $1/k_F a_{3D} = 0$, also known as unitary regime, and is easily reached by tuning the scattering length to diverging values. This way, the characteristic scale associated interactions is fixed a non-trivial regime for

[9] In comparison to the Coulomb interaction that would occur between charged particles.
[10] Scattering resonances also exist for higher partial wave collisions.

any values of k_F. The resulting physics is highly universal and scale-invariant, depending only on the density and temperature in a similar fashion as the noninteracting gas [68, 69].

Role of dimensionality

Ultracold atomic gases offer a very modular approach to realizing many-body systems in low dimensions [70–72]. In particular, their motional degrees of freedom can be tailored precisely via optical or magnetic potentials, and confinement induced resonances provide a means to tune the sign and strength of interactions in both 1D [73–75] and 2D [76]. Among the many ways available to shape the external potential landscape, optical lattices have played a particularly important role [77]. They allowed to observe exotic physics in a large variety of geometries, such as the superfluid to Mott insulator transition in 3D [78], the Berezinskii-Kosterlitz-Thouless crossover in 2D [79], or the Tonks-Girardeau gas in 1D. In particular, the spin-charge separation in two-component Luttinger liquids, as described earlier, have been observed as well [80–83]. However, only a handful of experiments have studied bulk Fermi gases in 1D [75, 84–87]. All of those experiments relied on two-dimensional lattices and suffered from having to average over stacked 1D systems of different densities and degrees of degeneracy. This constitutes a fundamental limitation for the observation of elusive states or spontaneous pattern formation, on top of severely complicating quantitative analysis. The principal goal of the present work is to develop a platform to prepare 1D bulk Fermi gases that can be probed individually, thereby opening the door to an entirely new class of experiments to study the effects of strong interactions in low dimensions.

Outline of this thesis

This manuscript presents the latest accomplishments and milestones realized on the Fermix experiment. There are three main achievements. First we realized the preparation and site-resolved imaging of tube-shaped quantum gases contained in a large-spacing optical lattice. Second, the associated realization of quasi-one-dimensional gases featuring a transverse ground state occupancy of nearly 100%. Finally, the study of longitudinal spin transport experiment in low dimensions, from which we extracted a minimal spin diffusivity coefficient of $D_s = 8.9 \pm 0.6\,\hbar/m$, consistent with the fundamental constraint in 3D predicted by quantum mechanics.

The main text follows the outline hereinbelow:

- Chapter 2 contains a brief description of the experimental apparatus and the key steps to prepare a degenerate Fermi gas in 3D.

- Chapter 3 details the working principle of the large spacing optical lattice as well as the method employed to achieve single-site imaging.
- Chapter 4 is focused on the calibration of the micro-trap potential and absorption imaging therein. Then, in Chapter 5, we present the equation of state of a noninteracting Fermi gas in one dimension, and generalize it to include transverse modes. We apply this model to perform *in-situ* thermometry in our system and characterize the dimensionality of our atomic samples. Finally, we report on the preparation of samples that are well within the one-dimensional regime.
- Making use of the thermometry techniques developed so far, chapters 6 and 7 are dedicated to the preparation of magnetization gradients and study of spin transport in low dimensions.
- Chapter 8 provides a brief summary of this work and presents perspectives for the future research making use of this novel platform.

Chapter 2

Production of 3D degenerate gases

This chapter briefly reviews the steps that are performed in our experimental setup in order to prepare a degenerate Fermi gas in a crossed optical dipole trap. This ultracold ensemble will be the starting point of all the experiments described in this manuscript, containing $N \sim 2 \times 10^4$ atoms per spin states and a reduced temperature of $T/T_F \sim 0.15$. An in-depth description of this preparation procedure can be found in [88, 89] since the steps and the setup remained nearly identical[1].

The FerMix experiment was launched in 2008 under the supervision of Frédéric Chevy and Christophe Salomon [88–96] , with the objective of studying the properties of the fermionic isotopes of the Potassium and Lithium alkalis ^{40}K and ^{6}Li , respectively. In particular, it was designed to explore the physics at the interplay of interactions, degeneracy, and superfluidity. The work presented in this manuscript relies exclusively on ^{40}K , and as a consequence we will omit the description of ^{6}Li gas preparation.

The natural abundance of ^{40}K amounts to only 0.012% [97] which is not sufficient to load a magneto-optical trap (MOT, or 3D-MOT) and thus a commercial ampule of enriched ^{40}K ($\gtrsim 1\%$) was bought[2]. A vacuum isolated environment is mandatory to increase the lifetime of trapped ultracold gases. The main limiting factor is given by collisions with residual particles present in the vacuum chamber, which are in thermal contact with the surrounding enclosure at room temperature. In order to allow lifetimes of several minutes in optically trapped gases, the pressure has thus to be kept below 10^{-10} mbar. By contrast, 10^{-7} mbar to 10^{-8} mbar are required to produce atomic jets to load the 3D-MOT, making it necessary to connect the various sections with differential pumping tubes.

[1] The most relevant change is the addition of new dipole trap arm to have a more symmetric trap at the end of the preparation.

[2] Alternatively, a technique to enrich ^{40}K specifically for MOT application was developed [98].

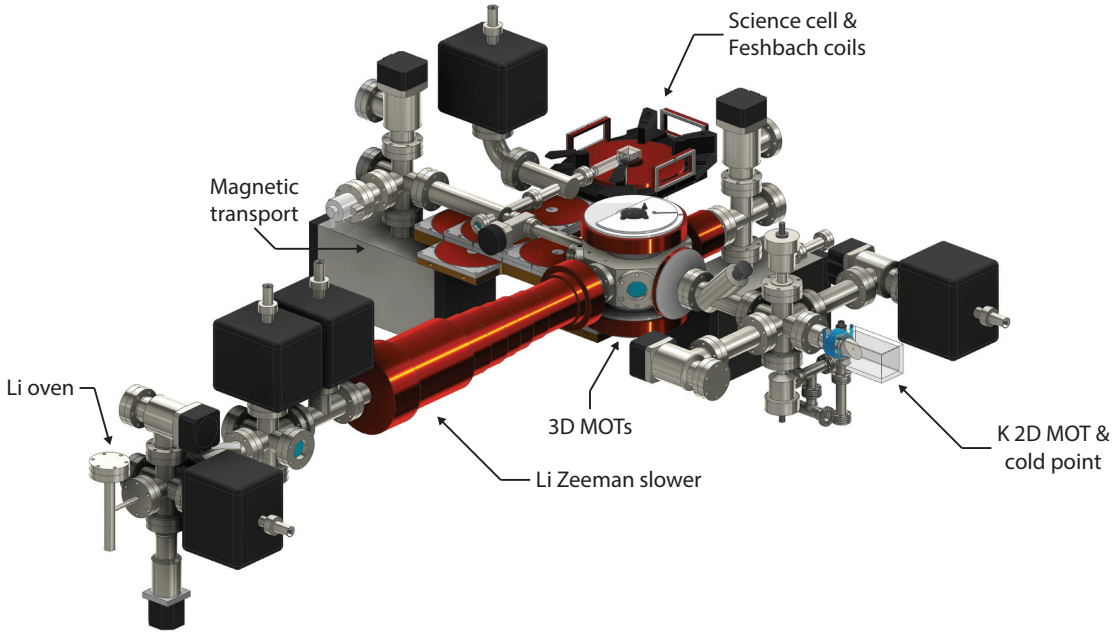

Figure 2.1: Overview of the vacuum system. Atomic beams of ^{40}K and ^{6}Li can be generated in the 2D-MOT and oven, respectively, and act as sources for the dual-species 3D MOT located at their intersection. Then, atoms can be loaded into a quadrupole magnetic trap and transported through an L-shaped tube to the science cell by using arrays of coils which move the magnetic center. Finally, sequences are performed in optical traps until quantum degeneracy is reached. The upper transport plate and the coils of the Potassium 2D MOT are not shown for clarity. Figure taken from [88].

The figure 2.1 shows an overview of vacuum system. The pre-cooled particle fluxes of ^{6}Li and ^{40}K are created by means of a Zeeman slower and a 2D-MOT, respectively. At the intersection of the two-atomic beams the 3D-MOT is loaded inside of an octagonal chamber. After being trapped and cooled in the 3D-MOT, atoms are loaded into a magnetic quadrupole trap. Subsequently, the clouds are transported magnetically through an L-shaped section to the science cell, where they are well protected from resonant stray light originating from the MOT chamber. The atomic sample ends up in the science cell where a better optical access is available. The glass cell[3] has outer dimensions of 23 mm $\times$ 23 mm$\times$ 10 mm and wall thickness of 4 mm.

2.1 Overview of the experimental cycle of ^{40}K

A typical experimental cycle of ^{40}K lasts 60 seconds and starts in the 2D MOT region. The flux of 1×10^{8} atoms$\cdot$s^{-1} is intercepted by the 3D-MOT, a standard technology implemented in all cold atoms experiment [99–101] that allows one to cool atoms close

[3]It is made of uncoated Vycor, a fused silica dioxide.

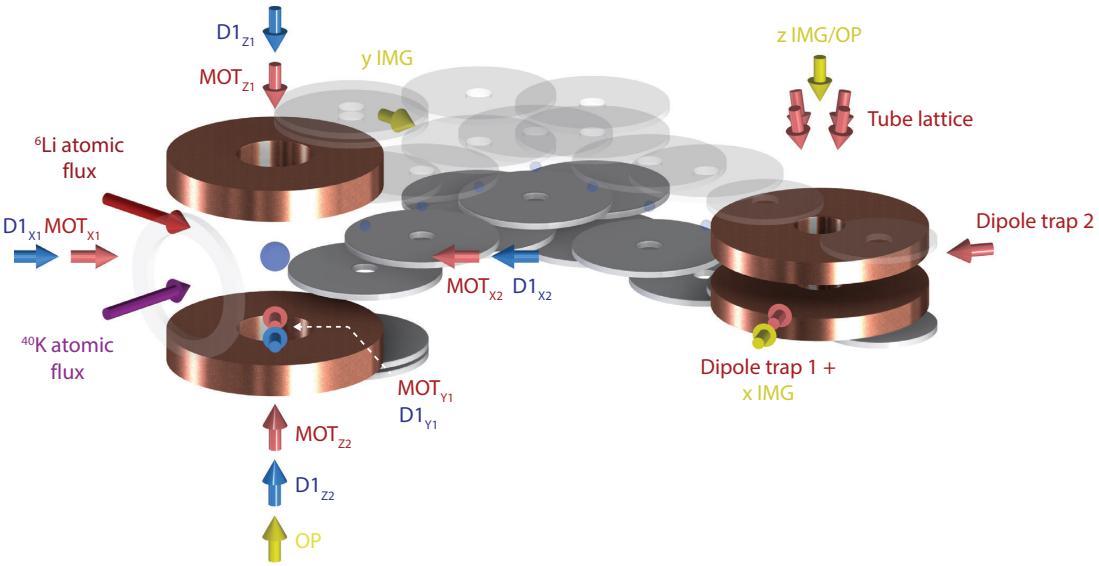

Figure 2.2: Overview of laser beams and magnetic coils in the experimental setup. The arrows represent the direction of propagation of the various beams. The opaque coils correspond to the main quadrupole/bias coils in the MOT chamber on the left, and in the science cell on the right. The transparent coils represent the transport coils. Figure taken from [88].

to the Doppler temperature [102]. After 30 seconds, the trapped sample contains up to 2×10^9 atoms and the 2D-MOT is switched off. After briefly compressing the 3D-MOT, all the magnetic fields are switched off[4], and a short phase of gray molasses is applied to increase greatly the phase-space density of the sample, achieving sub-Doppler temperatures [103]. This cooling technique relies on the D1 lines of potassium [104, 105], driven with laser light at a wavelength of 770 nm. Initially, this method was first conceptualized [106, 107] and experimentally realized [108, 109] on the more common D2 line at 767 nm [110]. The usage of the D1 transition was pioneered at FerMix and has, since then, been implemented in many other experiments due to the increased performance [111–116]. The now unpolarized sample is then optically pumped (OP) towards low-field seeking states over the course of few microseconds and immediately transferred into a purely magnetic trap [49]. Two arrays of commensurate coils, shown in figure 2.2, are used to smoothly move the magnetic potential through the L-shaped vacuum section[5]. The D1 cooling is essential to ensure high transport efficiency for this step.

Once atoms arrive in the science cell, a hybrid trap configuration is employed in which the magnetic trap slowly opens while an optical dipole trap placed just below progressively collects the spilling atoms [121]. During this gradual release and recapture, microwave

[4] Including the earth's magnetic field, which gets compensated by dedicated coils.

[5] Alternatively, magnetic transport can be achieved by moving the coil or magnet with a motorized translation stage [117, 118]. Optical transport can be realized using movable [119] or deformable [120] lenses.

evaporation is performed to increase the phase-space density of the cloud. As atom gets colder and the magnetic gradient weaker, it is necessary to introduce a bias field to ensure a well-defined quantization axis[6] and to limit the rate of Majorana losses [122, 123] and thus the associated heating [124–126]. Finally, several phases of evaporation are performed in the optical traps until degeneracy is reached.
In the ensuing section, we will present this final stage of the experimental cycle in greater detail.

2.2 Optical dipole traps

The use of optical dipole traps is widespread in the cold atom community and their working principle is very well understood [100, 127, 128]. It will be useful for the potential model detailed in section 4.2 to introduce the expression of the dipole potential $U_{\mathrm{dip}}(\vec{r})$ for alkalis. An atom in the $S_{1/2}$ ground state, which is subjected to a linearly polarized light field of intensity $I(\vec{r})$, experiences the following potential in the limit of large laser detuning[7]

$$U_{\mathrm{dip}}(\vec{r}) = \alpha_{\mathrm{pol}} I(\vec{r}), \qquad \alpha_{\mathrm{pol}} = \frac{\pi c^2 \Gamma_{\mathrm{nat,D1}}}{2\omega_{\mathrm{D1}}^3}\left(\frac{1}{\Delta_{\mathrm{D1}}} + \frac{2}{\Delta_{\mathrm{D2}}}\right), \tag{2.1}$$

where α_{pol} is the scalar polarizability originating from the virtual coupling to the D1 and D2 lines[8]. Here, $\Gamma_{\mathrm{nat,D1}} = 2\pi \times 5.956$ MHz is the natural linewidth of the D1-line, $\omega_{\mathrm{D1}} = 2\pi c/\lambda_{\mathrm{D1}}$ is its angular transition frequency, with c denoting the speed of light in vacuum and $\lambda_{\mathrm{D1}} \approx 770.11$ nm [129, 130]. For the D2-line, one has $\lambda_{\mathrm{D2}} \approx 766.7$ nm. The symbols $\Delta_{Di} = \omega - \omega_{\mathrm{D}i}$ represent the detunings from the angular frequency of the laser field $\omega = 2\pi c/\lambda$, with $i = 1, 2$.
The sign of the detuning dictates whether the potential is attractive or repulsive. The optical dipole traps of the experiment are created by lasers operating at $\lambda = 1064$ nm, which is red-detuned with respect to the the addressed transition and therefore correspond to attractive potentials. However, we will also make use of green laser beams at $\lambda = 532$ nm, which is blue-detuned, in order to produce repulsive potentials which play a crucial role in shaping the atomic cloud to our needs. For these wavelengths, operating at high intensities allows one to create substantial forces while maintaining a small scattering rate $\Gamma_{sc} \approx \Gamma_{\mathrm{nat,D1}} U_{\mathrm{dip}}/(\hbar\Delta_{\mathrm{D1}})$. When compared to the typical duration of experiments, it can be assumed that no photons are absorbed and, therefore, that the potential is conservative.

[6] At this stage, it is created by a pair of outer coils, not shown in figure 2.2, the axis of which is oriented in the vertical direction. Once the quadrupole trap is completely ramped down, the inner coils take over to create the bias magnetic field.
[7] Which means that the laser is far off resonance with respect to all of the energy levels contained in the $P_{1/2}$ manifold.
[8] Circular polarization introduces a dependence on the magnetic quantum number m_F, which is associated of the associated moment of the occupied Zeeman level.

There are three dipole trap beams in the experiment that all feature a gaussian TEM_{00} intensity distribution,

$$I(\vec{r}) = \frac{2P_{\mathrm{tot}}}{\pi w(z)^2} \exp\left(-\frac{2r^2}{w(z)^2}\right). \tag{2.2}$$

Here, $w(z) = w_0\sqrt{1+(z/z_R)^2}$ represents the radial beam size at distance z from the waist w_0. We also introduced the Rayleigh length of the beam $z_R = \pi w_0^2/\lambda$. At constant optical power P_{tot}, the maximum trap depth $U_0 = 2|\alpha_{\mathrm{pol}}|P_{\mathrm{tot}}/\pi w_0^2$ depends on the waist.
While a large waist is in principle convenient because it offers a large trap volume and therefore allows for the design more homogeneous traps, it also requires considerably more optical power for a given trap depth. We settled on a compromise in the experiment by implementing three dipole traps (ODTs): the first one (mODT) has a waist of $w_0 \approx 50\mu$m in order to create large trap depths and thus optimally capture the atoms during the microwave evaporation phase (also described in [88, 89]), and the two other traps (cODT1 and cODT2) both have waists of $w_0 \approx 140\mu$m to create a crossed dipole trap with a larger trap volume to contain the final ultracold cloud. The waists of the newly added beams have been measured prior to their installation, as shown in figure 2.3. The transfer into this optical dipole trap is necessary because its potential landscape is more suitable to load the optical lattice later on. The figure 2.4 depicts how the three ODTs come into play during the experimental cycle.
The next section will describe in detail how evaporative cooling and atomic state preparation is performed in these traps.

2.3 Evaporative cooling and state preparation

Evaporative cooling is an extremely effective tool to reduce the temperature beyond the capabilities of ordinary laser cooling for high density samples, and is oftentimes a crucial step to reach quantum degeneracy [131, 132].
After the microwave evaporation, the cloud contains up to 2.0×10^7 atoms in a mixture[9] of $|10\rangle \approx |F = 9/2, m_F = +9/2\rangle$, $|9\rangle \approx |F = 9/2, m_F = +7/2\rangle$ and a small amount of $|8\rangle \approx |F = 9/2, m_F = +5/2\rangle$ [88, 89]. This state composition originates from the optical pumping performed in the MOT chamber prior to magnetic transport, which requires positive m_F to ensure that the magnetic potential is trapping. Using these states, a first stage of evaporation is performed by ramping the power of mODT linearly from its loading value of 9 W to 1.5 W over the course of 1 second. Then, the bias field, initially set to $\sim$ 1G, is linearly increased to 29.87 G in 15 ms. A 20 ms radio-frequency (RF) sweep is

[9] The $|F, m_F\rangle$ are eigenstates only when the magnetic field B vanishes [130, 133] which is a good approximation after the microwave evaporation. Throughout this manuscript, we will denote the hyperfine eigenstates by $|1\rangle$,$|2\rangle$,...,$|9\rangle$,$|10\rangle$ in such a way that they coincide with $|9/2, -9/2\rangle$,$|9/2, -7/2\rangle$,...,$|9/2, +7/2\rangle$,$|9/2, +9/2\rangle$ when $B \to 0$.

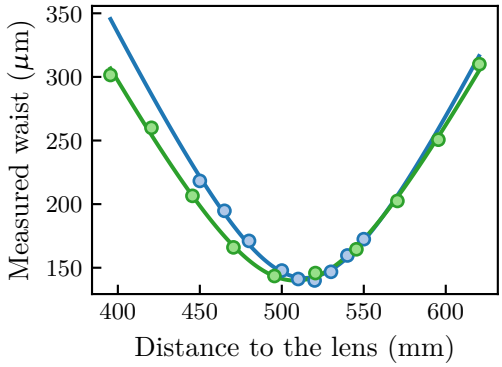

Figure 2.3: Crossed dipole traps waists. The waists were measured on the side with a beam profiler before building the optical setup around the science cell. This allowed us to figure out exactly where to exactly place the final focusing lens, and what is the expected value on the atoms. The fits give $w_{0,\mathrm{cODT1}} = 142.0 \pm 1.3\mu$m, $w_{0,\mathrm{cODT2}} = 139.9 \pm 2.2\mu$m.

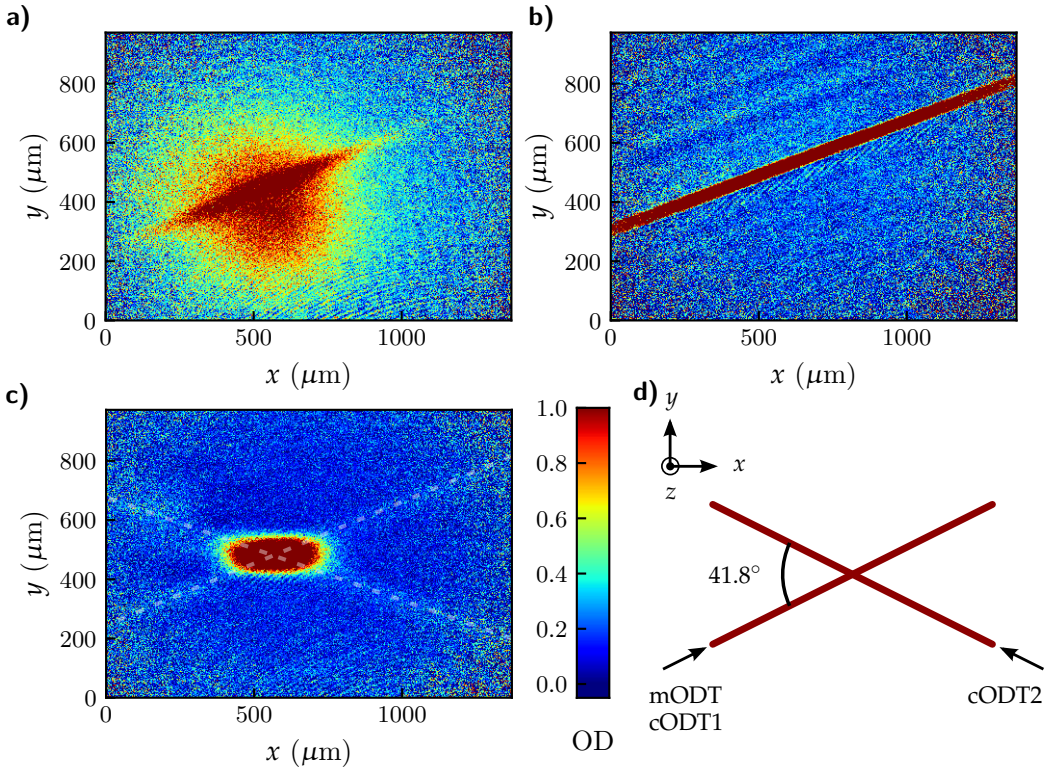

Figure 2.4: Dipole trap transfers. a) through c) shows absorption images of the atomic cloud along the vertical direction at various points of the experimental cycle. The color code represents optical density (OD). a) During the microwave evaporation, atoms escape the magnetic trap and get captured by the mODT beam. b) After evaporation the mODT beam is fully loaded. c) The cloud before final evaporation in a trap made up of the cODT1 and cODT2 traps. d) Direction of propagation of the 3 beams. The mODT1 and cODT1 beams are overlapped, and cODT2 intersects them at an angle of $(41.8 \pm 1)^\circ$.

applied to the atoms using an antenna adjacent to the science cell. The frequency is linearly decreased from 24.7 MHz to 12.7 MHz, inducing the transfers $|10\rangle \rightarrow |1\rangle$ and $|9\rangle \rightarrow |2\rangle$ through a succession of adiabatic transfers, also known as Landau-Zener transfers[10] (LZ-sweep). Once it is completed is completed, the bias field is raised to 237.83 G. At this point, a non-adiabatic linear RF sweep (50/50-sweep) from 50.4 MHz to 49.2 MHz is performed in 1 ms to equalize the populations of $|9\rangle$ and $|10\rangle$, which would otherwise contain around 30% and 70% of the atoms, respectively. Then, the larger crossed dipole traps cODT1 and cODT2 are ramped up to 6W each in 50 ms. Despite their power being larger than that of mODT, the latter is still deeper due to its smaller waist. The transfer is completed by decreasing mODT's power linearly until full extinction over 1.5 s, letting evaporation occur along the way.

As a consequence of the removal of mODT, the density of the gas is now smaller, and therefore entails a smaller collision rate reducing the efficiency of evaporation. This effect can be counterbalanced by increasing the scattering cross section, which depends on the scattering length a_{3D}. The scattering length can be tuned by applying external magnetic fields, which are resonant with s-wave Feshbach resonances[11] [63].

For ^{40}K , such a resonance exists between the states $|1\rangle$ and $|2\rangle$ for bias fields around 202.1G [137, 138], and is modelled by

$$a_{3D}(B) = a_{\text{bg}}\left(1 - \frac{\Delta}{B - B_0}\right), \tag{2.3}$$

where $a_{\text{bg}} = 169.7a_0$ is the background scattering length [139] with a_0 denoting the Bohr radius. The parameters Δ and B_0 describe the width and position of the resonance, which have been determined experimentally in prior studies [140–142]. In our case, when working around the resonance[12], we will use the values $B_0 = 202.14(1)$ G and Δ=6.70(3) from [142]. The scattering cross-section reaches its maximum value in the unitary limit, where $1/a_{3D} \rightarrow 0$ [67]. However, tuning the scattering length is also responsible for losses which in turn create heating, and are strongly enhanced on the BEC side (positive a_{3D} side of the resonance) [62, 144].

[10] For a two-level system the Landau-Zener formula [122, 134–136] gives the probability to effectuate a transfer between two states as

$$p = 1 - \exp\left(-\frac{\pi\Omega^2}{2\Delta'}\right),$$

where Ω is the Rabi frequency and Δ' the rate of change of the detuning with respect to the two-level transition. Full transfer is achieved when the RF power is large and the sweep rate small. The transfer described in the main text can be thought of as a succession of adiabatic two-level transfers. For the starting state $|8\rangle$, the avoided-crossings are too insignificant to allow transfer.

[11] The usage of an $s-$wave resonance over higher partial waves is required because collision in the latter channels are suppressed at low temperature.

[12] Another region of interest is the so-called zero-crossing, where $a_{3D}(B_{\text{zc}}) = 0$. Whenever we work close to the zero-crossing, we take advantage of the accurate parametrization of the scattering length around $B_{\text{zc}} = 209.094(8)$ G from [143].

In order to increase the efficiency of the evaporation without suffering from excessive losses, we ramp the magnetic field linearly to[13] 202.79 G in 20 ms, which allows us to reach a large scattering length of $-1580a_0$. This value is significantly larger compared to the background scattering length while staying on the BCS side. From there, evaporation is performed by ramping down the powers of cODT1 and cODT2 over the course of a 4 seconds long exponential ramp. The final power is varied depending on the atom number that one needs for the ensuing experiments in the lattice. Finally, the trap is recompressed to a value of 1.07 W in 300 ms. The figure 2.5 summarizes the evaporation steps described in this section so far.
The final temperature of this gas needs to be determined using models appropriate for highly degenerate ensembles. This will be the subject of the following section.

2.4 Thermometry of the degenerate Fermi gas

When it comes to performing thermometry, noninteracting gases are ideal as simple analytical fitting functions are available [57, 145] for both in-trap and ballistically expanded clouds. The column density of a noninteracting Fermi gas in thermal equilibrium released from a harmonic trap $V(x,y,z) = \frac{1}{2}m(\omega_x^2x^2 + \omega_y^2y^2 + \omega_z^2z^2)$ can be parametrized as[14]

$$n_{2D}(y,z) = n_{2D,0}\frac{\mathrm{Li}_2\left(-\exp\left[q - \left(\frac{y^2}{R_y^2} + \frac{z^2}{R_z^2}\right)\right]f(e^q)\right)}{\mathrm{Li}_2(-e^q)}, \quad f(x) = \frac{1+x}{x}\ln(1+x). \tag{2.4}$$

Here, the parameter q, which represents the logarithm of the fugacity, entirely determines the functional shape of the cloud as well as the normalized temperature through

$$\frac{T}{T_F} = \left[-6\mathrm{Li}_3(-e^q)\right]^{-1/3}. \tag{2.5}$$

This fraction quantifies the degree of degeneracy of the ensemble. It is worth noting that the knowledge of the angular trapping frequencies ω_i are not required to extract T/T_F. The parameters R_i are intentionally defined so that they reflect the cloud sizes along y and z in both the classical and degenerate limit

$$R_i^2 = \frac{2k_BT}{m\omega_i^2}f(e^{\beta\mu}) \to \begin{cases} \sigma_i, & T/T_F \gg 1, \\ R_{Fi}, & T/T_F \ll 1, \end{cases} \tag{2.6}$$

where $\sigma_i = \sqrt{2k_BT/m\omega_i^2}$ is the Gaussian radius of the classical limit and $R_{Fi} = \sqrt{2E_F/m\omega_i^2}$ is the Fermi radius toward which the cloud saturates to at $T = 0$.

[13] The field accuracy is $\sim 0.01G$, which was measured by radio-frequency spectroscopy.
[14] The function Li_s represents the polylogarithm of order s, and is defined in more details in sec. 5.1.5.

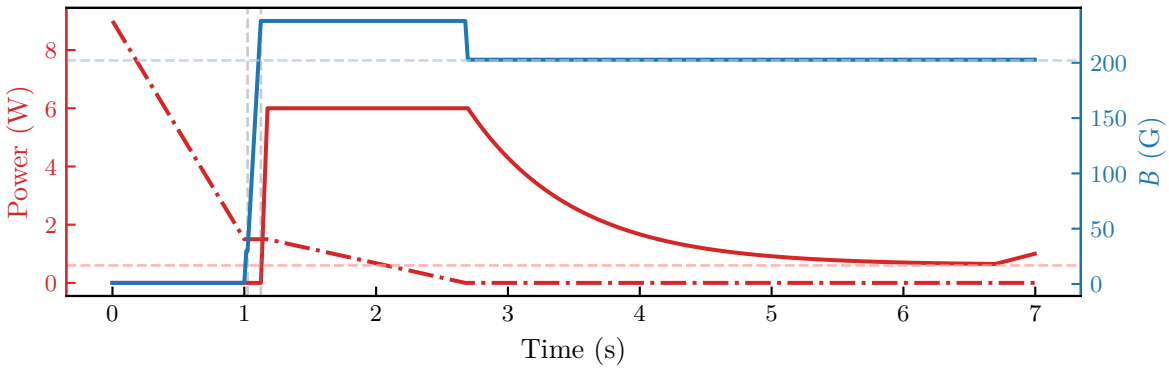

Figure 2.5: Evaporation ramps and state transfer. Illustration of the evaporation and transfer sequence described in the main text. The red lines represent the mODT (dash-dotted line) as well as CODT1 and cODT2 (solid line). The horizontal red dashed line corresponds to the spilling limit of the crossed dipole trap. The solid blue line represents the magnetic field, and the horizontal blue dashed line indicates the position of the s-wave Feshbach resonance between states $|1\rangle$ and $|2\rangle$. The vertical dashed lines mark the instants where the LZ-sweep (left) and 50/50-sweep (right) are performed.

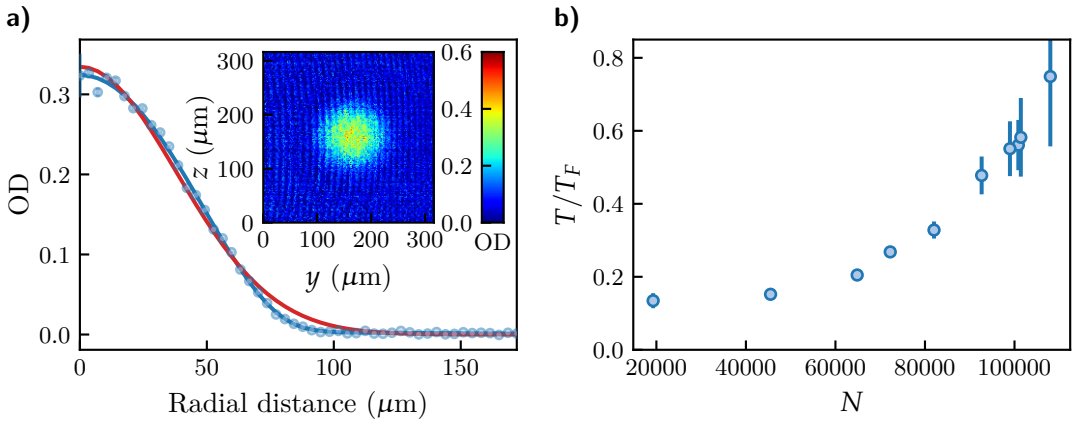

Figure 2.6: Thermometery in the crossed optical dipole trap. a) The blue data points represent the azimuthally-averaged optical density (OD) and the blue solid line is a fit using Eq. (2.4). After enough time of flight, the atomic distribution becomes radially symmetric and consequently we can set $R_y = R_z$ and only use the radial distance to the center of the cloud. The solid red line is a free Gaussian fit, which fails to capture the functional shape of the profile. The inset represents the corresponding absorption image. b) Typical evolution of the reduced temperature as a function of the atom number per spin state obtained by tuning the evaporation depth.

In order to determine T/T_F in our atomic samples after evaporation, we ramp the magnetic field close to the zero-crossing but leave a finite-scattering length $a_{3D} \sim -30a_0$ to ensure that the cloud stays well thermalized. Then, we abruptly switch off the optical traps and

image the cloud after a brief phase of ballistic expansion. The obtained atomic distributions are radially symmetric, and so we identify their respective centers of mass and calculate the azimuthally averaged profiles. Finally, we fit[15] the results using Eq. (2.4), obtaining the reduced temperature via the fitted q parameter. A typical example as well as the evolution of atom number and T/T_F are shown in figure 2.6. The smallest temperature corresponds to $T/T_F \sim 0.15$ with $N \sim 2.0 \times 10^4$ atoms per spin state. In 3D, this value signifies that the cloud is located well within the quantum regime. For example, a strongly interacting gas at a similar temperature would already be in the superfluid phase at unitarity [146]. As pointed out in [57], care has to be taken when determining the degeneracy parameter from the shape of the cloud alone. There are several mechanisms through which absorption imaging can lead to an overestimation (finite resolution, out of focus imaging, saturation, heating during imaging, ...) or an underestimation (detuning from resonance, opacity due to large density, ...) of the extracted T/T_F. Despite having gone to great lengths to avoid the aforementioned caveats in our temperature measurements, potential systematic errors caused by the non ideal nature of absorption imaging cannot be estimated. Consequently, the reported values of T/T_F should thus be taken as an estimate. By contrast, chapter 5 will present a quantitative thermometry technique to estimate the temperature of the quantum wires. This novel approach does not rely exclusively on the shape of distribution, but also on the precise knowledge of the potential landscape.
Having prepared an ultracold Fermi gas in 3D, the next chapter will present in detail how this ensemble is transformed into ultrathin quantum wires.

[15] This assumes that the trap from which the cloud was released is indeed harmonic. This assumption is justified by the observation of undampened sinusoidal oscillations in the trap (see e.g. fig. 4.6).

Chapter 3

Preparation and detection of highly anisotropic Fermi gases

In chapter 2 we detailed the first steps of the experimental cycle that leads to the production of a 3D degenerate Fermi gas in a crossed dipole trap, which is a crucial prerequisite for the preparation of quantum wires. The current chapter will focus on describing the second part of the experimental cycle, which consists of loading the gas in a large-spacing two-dimensional optical lattice.
After a brief introduction of the underlying the working principle, we will present a novel method used to load only a single layer of this lattice.

3.1 Large-spacing optical lattice

The significance of optical lattices in the field of ultracold gases cannot be overstated. The motion of neutral atoms in these types of traps is closely related to that of electrons in crystalline structures. Consequently, they are a wonderful tool to perform quantum simulation [58, 147, 148] of condensed matter systems and to explore exotic phases of matter and quantum phase transitions, such as the Mott insulators to superfluid transition [78, 149]. As explained in section 2.2, spatially inhomogeneous light sources generate a

dipole force that can be used to confine atoms. Optical lattices are typically generated using interfering laser beams, creating a spatially periodic potential. Many geometries and be achieved by tuning the direction and polarization of the beams, such as cubic [78], triangular [150, 151], honeycomb [152, 153], Kagomé [154] optical lattices, or even sub-lattices by superimposing several optical lattices [155]. When coupled to a cavity, optical lattices can mediate long-range interactions leading to self-organized systems [156, 157]. They can also be used to build quantum microscopes [158–160], which allow for quantitative measurements of spatial correlation functions. Control of the relative phase of interfering beams can be utilized to create periodically driven lattices [161], which have been shown to be well suited for the generation of well controlled artificial gauge fields [162]. The latter enabled, among other things, the study of topological systems [163].
Many of the avenues of research described above rely on tuning the tunnelling coefficient J between adjacent sites of the lattice. However, optical lattices can also be used to alter the dimensionality of bulk systems by suppressing any tunnelling, ultimately leading to two-dimensional [164] or one-dimensional gases [75, 83–87]. In the latter situation, past experiments typically suffered from addressing arrays of wires stacked along two spatial directions with varying atom number, thus yielding ensemble-averaged measurements. An illustration of this situation is shown in figure 3.2. While this drawback did not necessarily bias all previous studies, it certainly prevented progress towards the quantitative understanding of many-body problems in 1D. Indeed, as the thermodynamic state directly depends on the density, these ensemble-averages cover extended regions of the phase diagram, which severely complicates their interpretation and potentially obscures signatures of elusive states. On an even more fundamental level, ensemble-averages pose a problem for the observation of critical behaviour or states that are characterized by spontaneous pattern formation, e.g., magnetic domains.
As we will see in the rest of the chapter, this problem can be bypassed by only loading a single layer of lattice sites. As a result, the optical density collected from absorption images does contain mixed contributions from multiple sites anymore. Part of the requirements to implement this technique is the use of a large-spacing optical lattice [165]. Not only does it ease the technical constraints in the context of single-layer loading, but is also better suited for site-resolved imaging. This way, one can greatly enhance the quality of the absorption images and, thus, of the extracted data.

3.1.1 Working principle

We consider the total intensity of two coherent plane waves of equal intensity I_0 and of wavevectors $\vec{k}_1$ and $\vec{k}_3$ that describe the light field. We will work with the basis of orthogonal unit vectors $(\vec{e}_x, \vec{e}_y, \vec{e}_z)$. We denote α_{latt} the full-angle between $\vec{k}_1$ and $\vec{k}_3$ and assume that its corresponding bisector is aligned with the vertical direction $\vec{e}_z$, and that

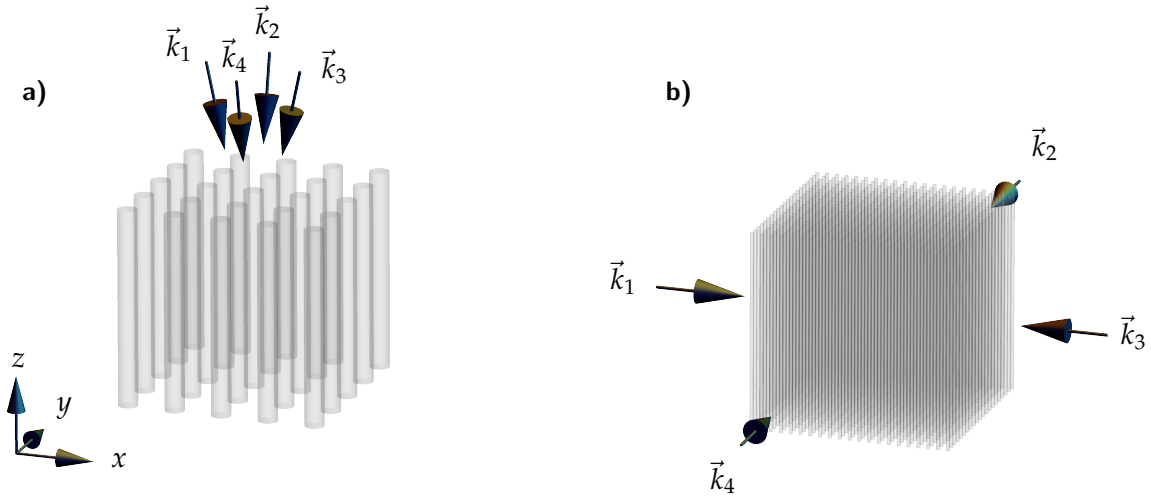

Figure 3.1: Two-dimensional large-spacing versus retro-reflected lattice. The interference pattern of a two-dimensional optical lattice results in highly elongated traps that we represent using grey tubes. a) Large-spacing configuration, where the four lattice beams are superimposed under a full angle of $\alpha_{\text{latt}} = 24.0°$. b) Retro-reflected lattice $\alpha_{\text{latt}} = 180°$, where $\vec{k}_1 = -\vec{k}_3$ and $\vec{k}_2 = -\vec{k}_4$.

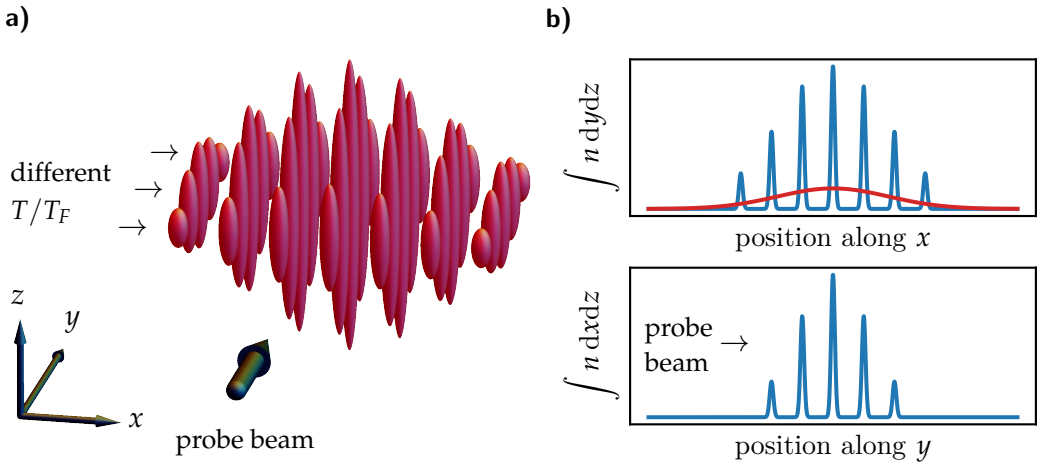

Figure 3.2: Plain loading of atoms in a two dimensional lattice. a) Illustration of atoms loaded in a two-dimensional optical lattice from a typical 3D geometry. The different lattice sites are independent. Due to differences in density during the loading, the degree of degeneracy is not constant accross the different tubes. b) Top: The integrated density along y and z as a function of x is represented in blue. The red line represents the same integrated density seen from an imaging system whose resolution is too large to resolve the lattice structure. Bottom: Integrated density along x and z as function of the position y, which corresponds to the imaging direction. This highlights that ensemble-averages are performed due to the presence of several layers of varying spatial density distribution.

both wavevectors belong to the (x, z) plane. The polarization of each plane wave has to be perpendicular to its respective wavevector, and as a consequence the condition for maximum interference requires that it must be collinear with $\vec{e}_y$. Therefore, the total intensity is readily calculated to be given by

$$I_{\alpha_{\text{latt},13}}(x, y, z) = I_0 \left| \left(e^{i\vec{k}_1 \cdot \vec{r}} + e^{i\vec{k}_3 \cdot \vec{r}} \right) \vec{e}_y \right|^2 = 2I_0 \left[1 + \cos\left(k_{\alpha_{\text{latt}}} x \right) \right], \tag{3.1}$$

where $k_{\alpha_{\text{latt}}} = |\vec{k}_1 - \vec{k}_3| = 2k \sin(\alpha_{\text{latt}}/2)$ and $k = 2\pi/\lambda = |\vec{k}_1| = |\vec{k}_3|$. A standard technique to produce optical lattices is to use one or several pairs of coherent counter-propagating beams, each of which are realized, for example, in retro-reflected configuration [77]. In such a configuration, $\alpha_{\text{latt}} = 180°$, so that the minima of the periodic potential will be separated by $d = \lambda/2$. For $0 < \alpha_{\text{latt}} < 180$, the spacing increases monotonously as

$$d_{\alpha_{\text{latt}}} = \frac{d}{\sin(\alpha_{\text{latt}}/2)}. \tag{3.2}$$

Similar to the optical dipole traps, we will use the red-detuned wavelength $\lambda = 1.064\mu$m for the lattice beams, which would correspond to a retro-reflected spacing of $d = 0.532\mu$m. This is smaller than the wavelength of the probe beam used during absorption imaging[1], which prevents one from optically resolving the sites[2]. To circumvent this problem, one can use a smaller angle of intersection. This eases the technical requirements for site resolved imaging, but, reduces the trapping frequency, as we shall see later.
A balanced two-dimensional lattice is obtained by adding a similar pair of coherent plane waves with wavevectors $\vec{k}_2, \vec{k}_4$ in the (y, z) plane. In order to maximize interferences, the polarization of this pair is along $\vec{e}_x$ and we can simply add incoherently the two pair contributions to obtain the total intensity. The potential created by such a configuration is thus given by

$$U_{\text{latt},2D}(x, y, z) = \alpha_{\text{pol}}(I_{\alpha_{\text{latt},13}} + I_{\alpha_{\text{latt},24}}) = U_0(4 + 2\cos(\alpha_{\text{latt}} x) + 2\cos(\alpha_{\text{latt}} y)). \tag{3.3}$$

A sketch of this geometry is shown in figure 3.1. In a real lattice, the plane wave description needs to be modified to take into account the Gaussian envelope of the beams[3].
Eq. (3.3) reveals that the lattice depth is independent of the angle α_{latt} and is determined by the peak intensity I_0. However, in the deep lattice limit, the parameter of interest that

[1] Alternatively, a larger wavelength could be used for the optical lattice. Using a CO_2 laser operating on the $\lambda = 10.6\mu$m line would give a spacing of 5.3μm in a retro-reflected configuration, which can be resolved easily as shown in [164]. However, this comes at a price as the additional technical constraints associated with working at this wavelength include less stable laser operation and very expensive optical components.

[2] Whereas other techniques that use a probe beam with smaller wavelength could work, for instance electron microscopy [166].

[3] A detailed model of the potential created by the four lattice beams, including the crossed dipole trap and gravity is presented in section 4.2.

governs the physics is rather the curvature around the minima. Clearly, this curvature depends on the spacing $d_{\alpha_{\text{latt}}}$. By Taylor expanding the lattice potential around a local minimum, one can define the angular transverse trapping frequency $\omega_\perp$ as

$$U_{\text{latt},2D}(x,y,z) \approx U_{\text{latt},2D}(0) + \frac{1}{2}m\omega_\perp^2(x^2+y^2), \qquad \omega_\perp = 2\pi\sqrt{\frac{2|U_0|}{m}}\frac{1}{d_{\alpha_{\text{latt}}}}, \tag{3.4}$$

where $U_0 = |\alpha_{\text{pol}}|I_0$ is the trap depth of a single beam ODT with intensity I_0. I_0 depends on both the available optical beam as well as the beam size. The former is limited by the laser source and the latter must not be too small otherwise the lattice sites will be highly inhomogeneous. This means that a compromise must be found in order to pick the angle α_{latt}. The spacing needs to be sufficiently large to be optically resolved, but it should not be larger than necessary as this would reduce $\omega_\perp$.

A related design parameter is the tunnelling rate. In order to study bulk physics in isolated micro-traps, the hopping rate must be extremely low. Using a large-spacing lattice is a major asset in that regard. The tunnelling matrix elements are related to the overlap of wavefunctions describing atoms on adjacent lattice sites, also known as Wannier wavefunctions. This overlap depends on both their individual size and their spatial separation, imposed by the lattice spacing. Both of these factors are modified when α_{latt} is decreased. On the one hand, the decrease of $\omega_\perp$ implies smaller sizes of the single-particle eigenstates, which contributes to increase the tunnelling coefficients. On the other hand, the increase of $d_{\alpha_{\text{latt}}}$ leads to their exponential suppression. Indeed, in the deep trap limit it can be shown [165] using the Mathieu equation, that the nearest-neighbour tunnelling element $J_{0,\alpha_{\text{latt}}}$ for an atom occupying the ground state band scales like

$$J_{0,\alpha_{\text{latt}}} \sim \frac{\exp(-Ad_{\alpha_{\text{latt}}})}{\sqrt{d_{\alpha_{\text{latt}}}}}. \tag{3.5}$$

Here, A is a constant that depends on the lattice depth only. A detailed numerical calculation which takes into account the band structure as derived from Bloch's theorem [167] is, for example, presented in [88, 89]. It consists in solving the following Hamiltonian[4]

$$\hat{\mathcal{H}}_{\text{bloch}}u_n(x,q) = E_{\alpha_{\text{latt}},n}(q)u_n(x,q), \qquad \hat{\mathcal{H}}_{\text{bloch}} = \frac{\hbar^2}{2m}\left(-i\frac{\mathrm{d}}{\mathrm{d}x}+q\right)^2 + U_{\alpha_{\text{latt},13}}(x), \tag{3.6}$$

from which eigenstates $\varphi_n(x,q) = e^{iqx}u_n(x,q)$ are derived. Here, the band index n is a positive integer and the quasi-momentum q is a continuous variable ranging from $-k_{\alpha_{\text{latt}}}/2$ to $k_{\alpha_{\text{latt}}}/2$. Provided the next-to-nearest neighbour hopping events can be neglected, which

[4] Since the free Hamiltonian does not couple the two directions, it is only necessary to solve it for one pair of lattice beams. Here, Eq. (3.5) was written for the direction that contains the pair with $\vec{k}_1$ and $\vec{k}_3$.

is certainly the case in deep large-spacing lattice, the band-dependent nearest-neighbour tunnelling coefficient $J_{n,\alpha_{\text{latt}}}$ can be expressed as[5]

$$J_{n,\alpha_{\text{latt}}} = \frac{1}{4}\left(\max\left[E_{\alpha_{\text{latt}},n}(q)\right] - \min\left[E_{\alpha_{\text{latt}},n}(q)\right]\right). \tag{3.7}$$

In the infinitely deep lattice limit bands become rigorously flat, meaning that the energy of a given band is a not a function of q anymore and the corresponding tunnelling element approaches 0. The band structure becomes irrelevant and it is more natural to describe the system with a set of transverse modes that depend exclusively on n, and whose wavefunctions converge to those of the harmonic oscillator. This is precisely the approach that we will adopt in section 5.2.1. As shown later in section 3.2.6, the spacing of the lattice that we implemented is $d_{\alpha_{\text{latt}}} \sim 2.55\mu$m, which corresponds to $\alpha_{\text{latt}} \sim 24.1°$. As shown in figure 3.3, for $\omega_\perp \geq 2\pi \times 10$ kHz, the tunnelling coefficient for $n \leq 10$ is at least 6 orders of magnitude below the physically relevant energy scale $\hbar\omega_\perp$. The higher lying bands will not be populated and thus do not partake in tunnelling processes. As a consequence, the tube traps can be safely considered to be isolated from each other. This creates an ideal environment to study the 1D-3D dimensional crossover in bulk Fermi gases. Studies so far have employed retro-reflected optical lattices containing either spin-imbalanced Fermi gases [168, 169] or weakly-interacting bosons [170]. However, in those cases, the change in dimensionality is automatically accompanied by the onset of nearest-neighbour hopping as the lattice power is decreased. This parasitic effect progressively couples the initially isolated 1D gases and admixes their - potentially unequal - thermodynamic states. In the large-spacing lattice presented here, it is possible to transition from one dimensional regime to another without compromising the isolated nature of the various micro traps. Therefore, one exclusively probes bulk physics of one single ensemble at a time.

3.1.2 Generation of the lattice beams

This section is dedicated to the description of the optical setup used in our experiment to generate a two-dimensional optical lattice as described previously. A more detailed description can be found in previous manuscripts [88, 89].

Four beams must be generated in order to create the two-dimensional lattice. They are all generated from one laser source to ensure high coherence, a 45 W ultra low noise fiber laser[6] operating at $\lambda = 1064$ nm with a bandwidth of less than 50 kHz. Shortly after the laser head output, the beam is split into two equal power components. Each of them is diffracted through an acousto-optic modulator (AOM), but with opposite diffraction order, such that a relative detuning of 220 MHz between the two beams averages out the

[5] Following the standard definition from [148].
[6] From the company ALS (AzurLight Systems).

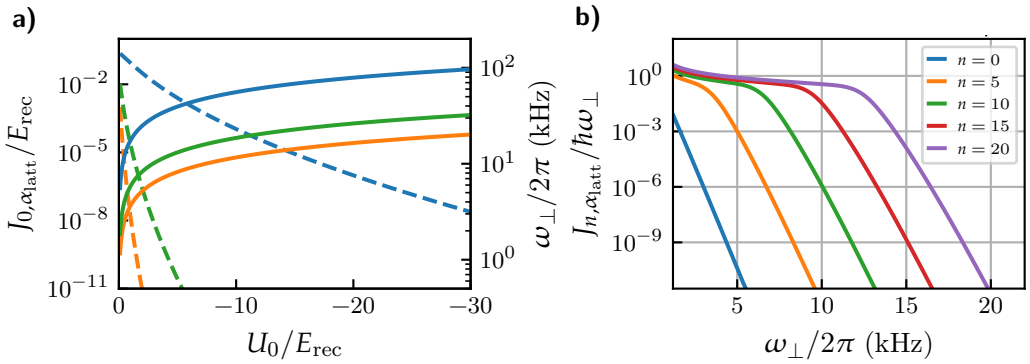

Figure 3.3: Tunnelling exponential suppression in large-spacing lattice. a) Evolution of the ground band tunnelling coefficient (dashed lines) and transverse angular frequency (solid lines) as a function of the trap depth producing a single plane wave. Three lattice spacing ratios $d_{\alpha_{\text{latt}}}/d$=1,3,4.8 are represented, corresponding to full angles $\alpha_{\text{latt}} = 180°, 38.9°, 24.1°$, in blue, green and orange respectively. Energies are normalized by the recoil energy $E_{\text{rec}} = \hbar^2k^2/2m$. b) Evolution of the band-dependent tunnelling coefficient as a function of the trapping frequency for $\alpha_{\text{latt}} = 24°$.

inter-pairs coherence to avoid undesired interferences. Finally, each diffracted beam is guided towards a large mode area polarization maintaining optical fiber. At the output of each fiber, a small fraction of the available power is sent towards a photodiode, which is connected to a feedback loop system. Its role is to actively adjust the radio-frequency power sent to the AOM to control and stabilize the final optical power that ultimately reaches the atoms[7].

After the optical fibers, the two beams are subdivided another time to create the X and Y lattice pairs. Then, each of the four Gaussian beams pass through a $f = 400$ mm lenses in order to produce a target waist of ~ 220 μm at the position of the atoms. This choice stems from a compromise between the need to produce large perpendicular angular trapping frequencies $\omega_\perp$ and have a homogeneous transverse potential at each central lattice sites. The breadboard onto which the setup is mounted has a cross-shaped opening centered above the science cell. The last two mirrors[8] of each beam path are inclined in order to have the beams propagating downwards through the opening to later intersect inside of the science cell under a relative full-angle of $\sim 25°$ for each pair. The X beams lie in the (x, z) plane and originate from opposite sides on the science cell, while the Y occupy the (y, z) plane. Polarizing beamsplitter cubes are placed in between these last two mirrors of each path to ensure that X and Y pairs are polarized along y and x, respectively. This ensures maximum interference contrast of nearly 100% within each pair. For each beam

[7] This power control setup is identical to the one that is used for the three optical dipole trap beams described in section 2.2. A similar scheme also regulates the power of the compression beam and the barrier beam described later in sections 3.2.5 and 6.5 respectively.

[8] Using two mirrors instead of one is not only convenient to use as little optical access as necessary, but also keeps the reflection angles below 45°.

path, one mirror is placed on a piezoelectric actuated mount, which allows to tune the pointing of the beams in order to perform routine alignment.

3.2 Loading and imaging a single layer of the lattice

We previously laid out in section 3.1 the fundamental benefits that arise from imaging a single layer of the two-dimensional optical lattice, and resolving each loaded site. Performing such an operation is challenging on a technical level, mostly because the separation between the sites remains small despite the use of a large-spacing optical lattice. The realization required developing several novel techniques in order to achieve robust single-layer loading and imaging. The corresponding steps and methods are the main subjects of this section.

3.2.1 Overview

In principle, there is no unique way to load and image atoms in a two-dimensional lattice without suffering from ensemble-average as described in figure 3.2 b). The first approach we considered consisted in using a configuration where atoms fill many layers in the imaging direction, as shown in 3.2 a), and shine in a masking beam to repump all the atoms into a transparent state[9], except those contained in the layer of interest [88, 89]. While this method fulfills the requirements on a fundamental level, we found that it is extremely challenging to execute due to limitations in terms of resolving power. The intensity profile of the mask would need to be extremely sharp so that no parasitic repumping occurs in the layer of interest. In practice, we could not find a satisfying compromise, having to either loose a large fraction of the signal of the central layer or deal with parasitic line-of-sight integration of atoms in other layers.

As a consequence, we opted for a different approach which consists in optically compressing the atoms in the cODTs prior to loading the optical lattice. If the cloud size along the imaging direction is made smaller than that of the lattice spacing, atoms can be loaded in a single layer. The level of compression is given by the curvature imposed upon the atoms, which, in turn, depends on optical power and beam size. This approach has the major advantage of being able to increase compression by means of optical power alone, while not requiring high degrees of optical resolution.

The figure 3.4 shows the loading procedure. The quantum degenerate gas initially loaded in the optical dipole trap (see sec. 2.4) is compressed along the y direction by exponentially ramping up a TEM_{01}-like repulsive green beam (see sec. 3.2.5). Once the spatial extent along the y direction is sufficiently small, both beam pairs of the 2D-lattice are ramped up exponentially until tunnelling is fully suppressed. Prior to increasing the lattice strength

[9] 'Transparent' means that they will not be resonant with the probe beam.

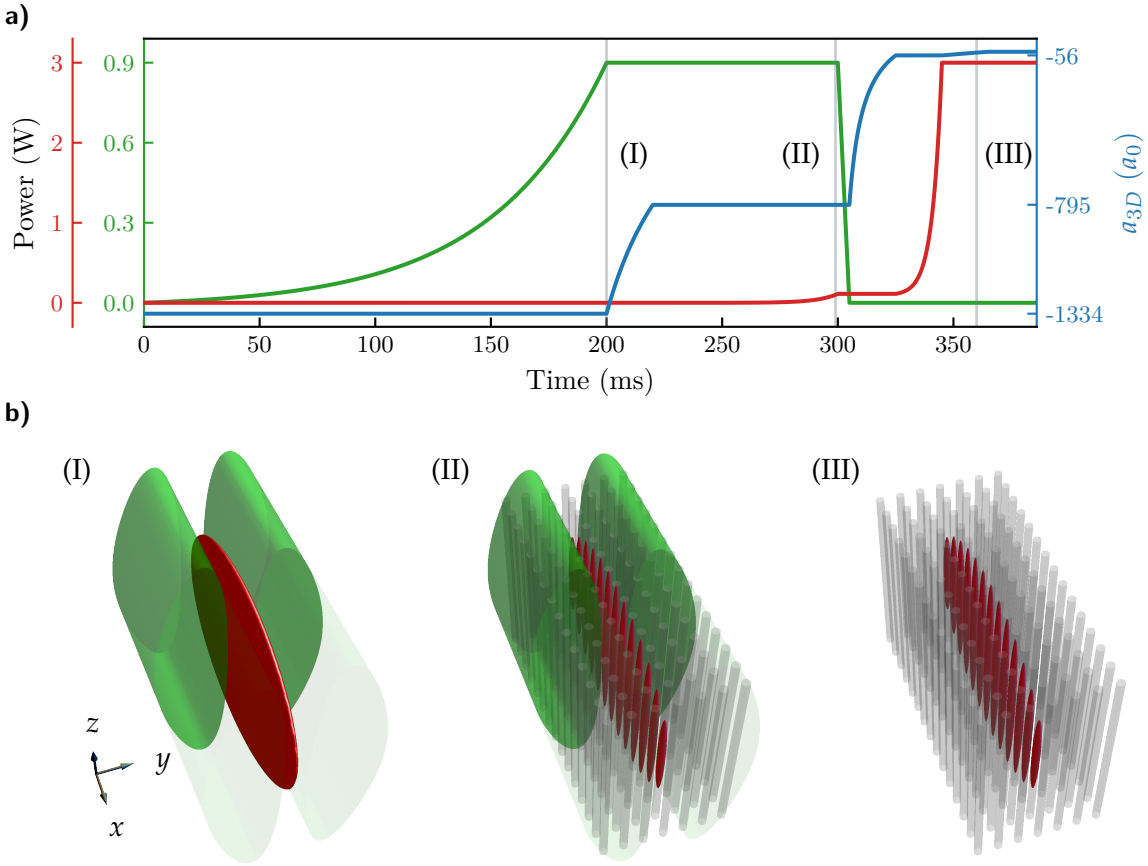

Figure 3.4: Preparation of a single layer of atomic wires. a) Ramp sequences for single beam power of the X and Y lattice pairs (red), power of the green compression beam (green) and 3D scattering length (blue). b) Representation of the system at different phases of the loading sequence. First, the compression beam, represented in green, flattens the atomic cloud into a pancake shape (I), then the two-dimensional optical lattice is ramped up, creating tube traps represented in gray (II). Finally, the compression beam is turned off. The atoms are loaded in a single layer of the lattice (III).

to full power, the compression beam is ramped down quickly. The lattice beams are exponentially ramped up to their final powers. During this whole process, the scattering length a_{3D} is progressively reduced to lower values by changing the magnetic field, reaching a final value of $-40a_0$. The increase in density makes it possible to maintain a decent collision rate, required to perform adiabatic loading, while avoiding three-body losses [144]. Finally, high resolution images are taken along the y direction, resolving the individual sites of the loaded lattice layer, as explained in section 3.2.6.

For the above procedure to be successful, the center of the compression beam must be appropriately placed with respect to the nodes of the lattice along y. The positions of the potential energy minima depend on the relative phase between the partaking beams, and

must be actively controlled. Section 3.2.4 will describe how it is done in our setup. For the sake of diagnostic purposes, it is possible to verify single-layer loading by simply imaging the cloud along the vertical z direction, see sec. 3.2.8.
Once loaded in the tube traps, the vertical spatial extent of the atomic clouds is dramatically increased due to the reduced levels of confinement. This poses a problem for high-resolution imaging along z and can be addressed by artificially reducing the vertical size of the sample with a masked repumping technique, as shown in sec. 3.2.7. For reference, the beam configuration around the science cell in the (x, y) plane is depicted in figure 3.5.

3.2.2 High-resolution objective

In order to realize highly resolved absorption imaging along the y direction, a custom object lens had to be designed and produced[10] in order to fulfil several unusual experimental requirements.
The lens assembly is made from fused silica and optimized for diffraction limited imaging. It has a numerical aperture of NA$=0.35$ and a depth of field of $\pm 3.1\mu$m, which is larger than the lattice spacing. Moreover, the objective has anti-reflective coatings to subdue internal reflections, which could cause interference effects and fringes on the absorption images[11]. The damage threshold of 1 MW/cm^2 is large enough to send the dipole trap and lattice beams through without any risk. The effective focal lengths are 20.00 mm, 20.55 mm, and 19.85 mm for $\lambda = 767$ nm, 1064 nm and 532 nm, respectively. Along the y direction, this corresponds to a working distance of 6 mm with respect to the science cell boundary. The design is optimized for a beam that travels through 6.5 mm of vacuum, 4 mm of planar fused silica, and 6 mm of air from the focal plane to the objective.
The cylindrical enclosure of the objective is 30 mm long (threads not included) and has a small diameter of 26 mm. Three custom extension tubes of lengths 30 mm, 90 mm and 140 mm were produced for a convenient usage of the objective along x, y and z respectively[12]. The RMS threaded objective is meant to be screwed in one dedicated side of an the extension tube while the other side has a male SM1 thread for compatibility with most standard 1 inch optics tubes. All extension tubes also have an external diameter of 26 mm everywhere expect at the end of the SM1 thread side. This allows the objective and the extension tubes to reach far inside the coil mounts that surround the science cell, so that the objective can be placed very close to it at the appropriate working distance.
Both the enclosure of the objective and the extension tubes are made of ultem plastic, which offers high levels of chemical resistance and rigidity. More importantly, it is a good insulator, and therefore does not couple inductively to the fast magnetic field ramps

[10] By the American company SpecialOptics.
[11] The coating guarantees $< 0.2\%$ of reflection per surfaces for incident angles of up to 20° at $\lambda =$767 nm, and 0.5% for 1064 nm and 532 nm.
[12] Even though we did not use it along x in this work.

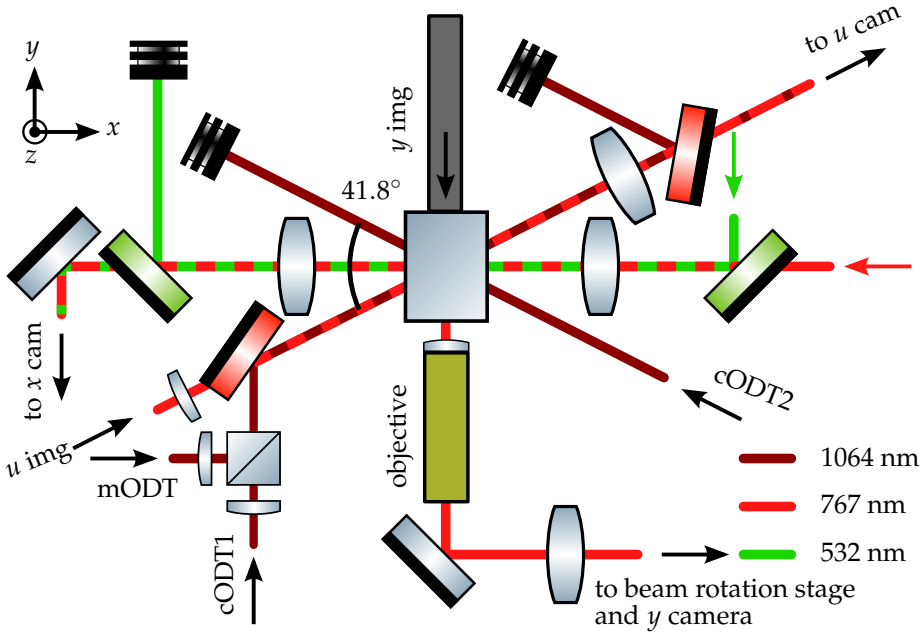

Figure 3.5: Beam configuration around the science cell. The central rectangle represents the science cell. The dipole trap beams (sec. 2.2), compression beam (see sec. 3.2.5), barrier beam (see sec. 6.5), mask repumper beam (see sec. 3.2.7), and several imaging beams are shown. There are four imaging directions x,u,y, and z with magnifications 8.34 ± 0.02, 1.68 ± 0.03, 37.87 ± 0.08 and 17.54 ± 0.2, respectively. The high-resolution objective, used along both z- (not represented) and y-axis, is described in sec. 3.2.2. The vertical imaging beam, collinear to the z direction, and the four lattice beams are not depicted.

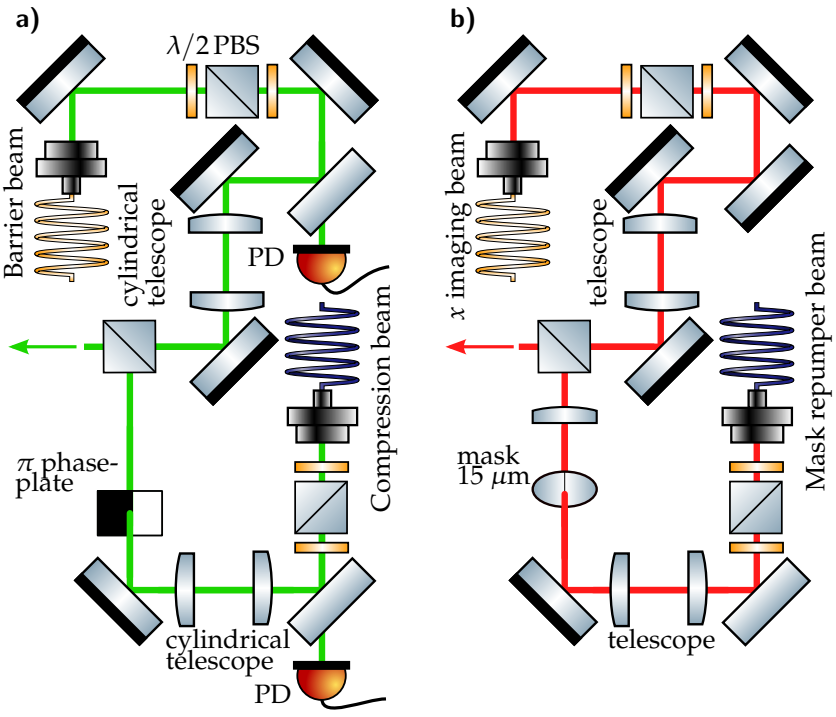

Figure 3.6: Beam preparation before the science cell. a) Generation of the compression and barrier beam, which are overlapped before reaching the science cell, following the green arrow. b) Preparation and combination of the mask repumper and x imaging beam, following the red arrow.

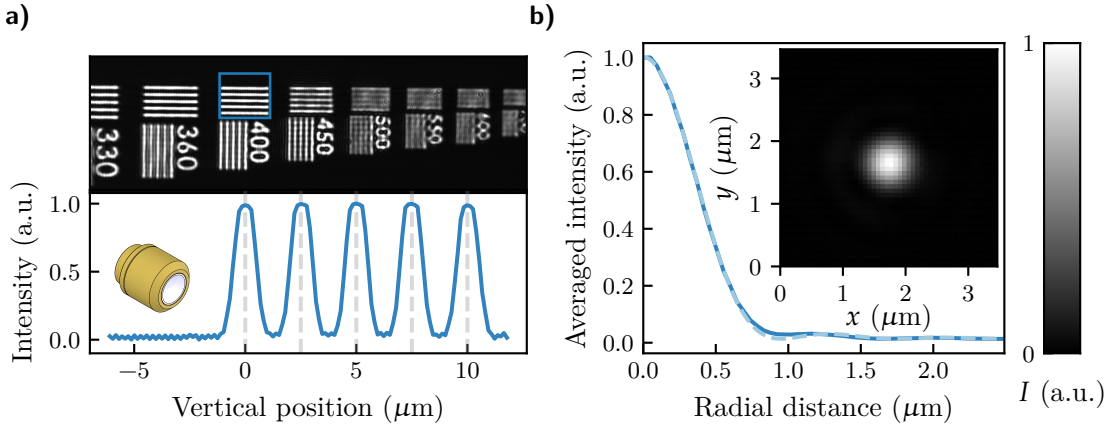

Figure 3.7: High resolution objective. a) Top: image of the resolution target. Numbers indicate the lines per mm. For the '400' group, this corresponds to a spacing of 2.5 μm. Bottom: Vertical integration of the '400' group over the region of interest indicated by the blue rectangle. The lines are fully resolved. b) Azimuthal average of the intensity distribution obtained after a 0.5μm pinhole shown in the inset (solid blue line). The dashed line corresponds to a fit to the Airy function $I(x) = I_0[2J_1(x/\sigma)/(x/\sigma)]^2$, where $J_1(x)$ is the Bessel function of the first kind of order 1 [171]. The resolution r according to the Rayleigh criterion corresponds to the first zero of J_1 located at $r = 3.831 \times \sigma = 0.92\mu$m [172].

occurring nearby during each experimental cycle. The suppression of these eddy currents prevents the formation of long-lived vibrations[13] resulting from the long lever of the object lens. The objective is used along both the y and z directions. For the former, it is combined with a plano-convex lens[14] of focal length $f = 757.9$ mm, leading to a theoretical magnification of 37.895 at $\lambda = 767$ nm, in good agreement with the measured magnification[15] of 37.87 ± 0.08. Prior to installing the objective, the optical performance was verified by imaging a resolution target as well as a 0.5 μm pinhole. The results, shown in 3.7, indicate that the system can easily resolves structures as small as 2.5 μm with a contrast of almost 100%. The image of the backlit pinhole light source allows a direct measurement of the Rayleigh resolution which gave 0.92μm. As we will see later on with absorption images of the loaded lattice, this last number is underestimates the actual resolution slightly.

In the z direction, the objective is used together with an achromatic doublet[16] of effective focal length $f = 350$ mm, leading to a theoretical magnification of 17.5 at $\lambda = 767$ nm.

[13] Vibrations are undesired because they induce a mismatch between the background signal of the absorption and the reference shot of an absorption image. This stems from the position change of the objective inbetween these two images and ultimately leads to unphysical fringes on the measured density.
[14] Thorlabs, LA1727-B.
[15] The magnification is measured by fitting a free-falling cloud in the gravity field g, with all magnetic fields switched off to avoid the occurrence of any magnetic force. It is also how the magnifications along x and u, stated in the caption of fig. 3.5, were determined.
[16] Edmund Optics, #49-395.

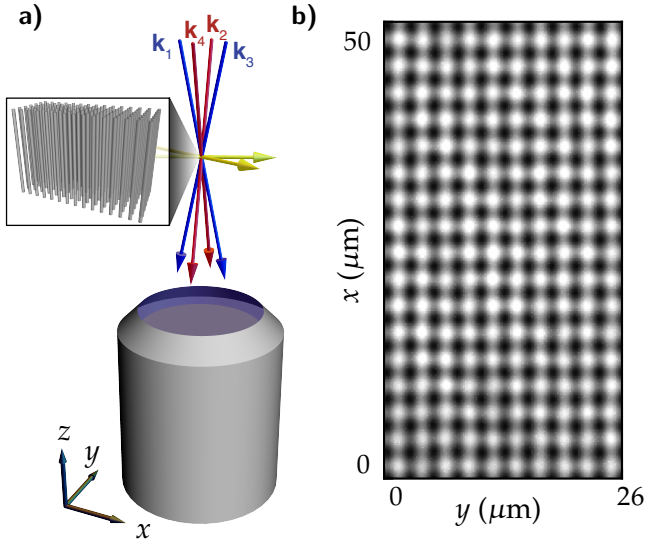

Figure 3.8: Lattice beam imaging. a) The four lattice beams are being collected by the high-resolution objective. b) Image of the interference pattern of the two-dimensional optical lattice obtained on a CCD camera. Using this image, we can measure the ratio between the lattice spacings along y and x, which amounts to $d_{\alpha_{\text{latt,y}}}/d_{\alpha_{\text{latt,x}}} = 0.962$.

This also agrees with the measurement[17] of 17.54 ± 0.2. As was mentioned earlier, the atomic clouds are elongated along the z direction, and therefore the short depth of field makes it impossible to resolve the lattice structure. In order to mitigate this issue, we placed an 11 mm aperture ring inside the tube mount as close as possible to the objective in order to artificially reduce the numerical aperture. This increases the depth of field to $\pm 5\mu$m while degrading the resolution. In combination with the repumping mask described in sec. 3.2.7, the z direction can be used to perform nearly site-resolved imaging at a diagnostic level.

3.2.3 Imaging the lattice beams

The working distance along z is small enough so that all of the four lattice beams can be collected by the objective, despite its small diameter. This allows both to safely manage the outgoing optical power and to image the interference pattern present at the position of the atoms. The corresponding optical setup is shown in figure 3.8 and 3.9.
The interference pattern plays a crucial role in the alignment procedure. In order to have a properly aligned two-dimensional lattice, the four beams need to satisfy the following constraints:

- Intersection in the science cell: there, the camera helped to track the position of each beam during each iteration of alignment.
- Horizontal counter-propagation within each pair: this was checked by looking at the reflections of the two beams for each pair on the two top surfaces of the science

[17] It is determined by moving the compression beam along y and measuring the corresponding position of loaded atoms along both x and z axis. Since the magnification along x is known, we can infer the one along z by comparison, assuming orthogonality between the axis.

cell, creating an array of spots that need be aligned in the horizontal plane.

- Orthogonality of the pairs: this can be monitored by looking at the interference pattern on the CCD camera. On top of that, they need to be collinear with the x and y direction, defined by the sides of the science cell.

The optimized interference pattern shown in 3.8 b) is the result obtained after iteratively optimizing these three points until convergence was reached.
For each experimental cycle the camera was used to record the interference pattern during the MOT loading phase, which allows to ensure that the contrast remains stable over time[18]. It was also used to ensure that the relative phase of the two lattice pairs was locked correctly, as will be described in the next section.

3.2.4 Phase control

In order to load a single layer of the two-dimensional lattice as shown in figure 3.4 b), it is crucial that the position of the compression beam (see sec. 3.2.5) is aligned with the exact position of lattice sites in the y direction (see sec. 3.2.8). This could only be guaranteed over many experimental cycles if the relative phase between the two beams composing the Y pair was sufficiently stable. Since the two beams use a different optical path after the 50:50 nonpolarizing beam splitter, they accumulate a different amount of phase delay along the way. This difference will determine the exact position of the (anti-)nodes in the interference pattern. This reasoning also applies to the X pair, whose relative phase also needs be controlled in order fix the position of the lattice sites in the x direction. In absence of such stabilization, absorption images taken along the y direction could not be safely averaged as the horizontal position of the loaded tube traps may not be static.
In the absence of any active feedback, the relative phase is not an ideal reference as it is very sensitive to the environment: air turbulence and temperature gradients that occur in the optical paths can easily give rise to longterm drift. This effect matters the most during propagation phase prior to reaching the science cell. Afterwards, the beams stay very close to each other and, consequently, experience marginal relative dephasing.
A feedback loop was implemented to suppress this drift, which requires to control and measure the relative phase of both beam pairs. An illustration of the setup is shown in 3.9 a).

Control The placement of a piezo-driven mirror in the optical path is shown in figure 3.9 a). Inspired by the tripod design from [173], we use three $2 \times 2 \times 2$ mm piezo plates[19],

[18] This means of monitoring is a straightforward way to catch subtle technical problems, that would otherwise go unnoticed. One example in this context are mode instabilities of the laser, which could be identified and fixed very conveniently.
[19] Thorlabs, PA4CEW. They feature $\sim$ 2.0 μm free stroke and $\sim$ 22 nF capacitance.

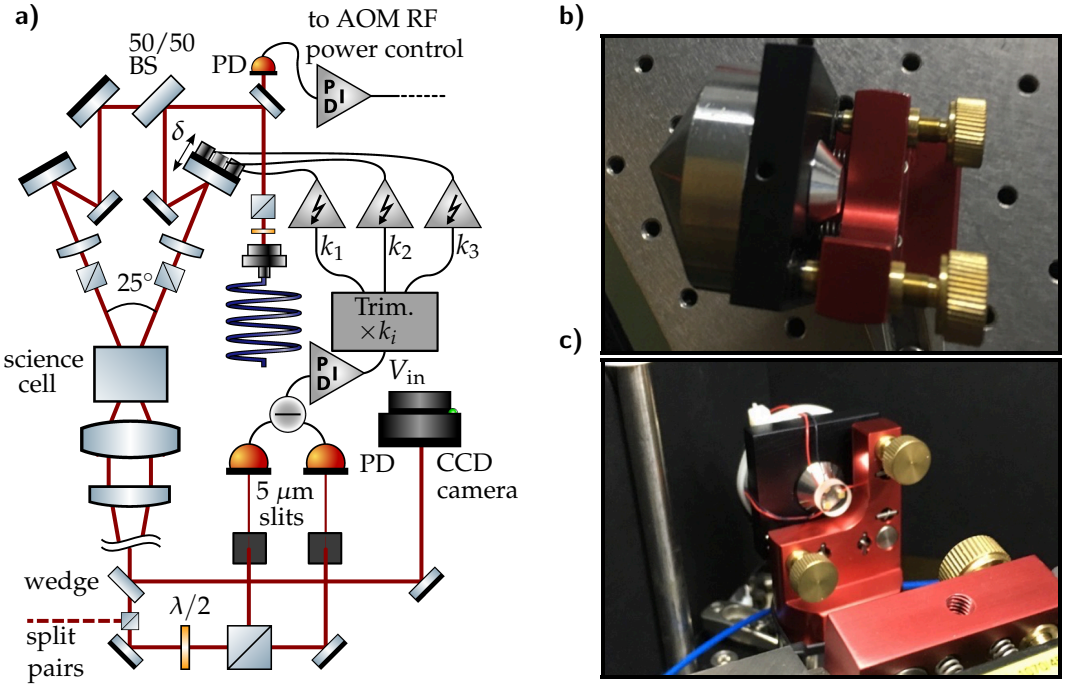

Figure 3.9: Phase control and custom piezo mirror assembly. a) Optical setup showing how a lattice beam pair is created and imaged onto a CCD camera after passing through the science cell (see sec. 3.2.4). A similar setup is used for the other lattice beam pair (not shown). Prior to the science cell, one of the two beam paths contains a piezo-driven mirror which allows the active control of the relative phase shift of each pair. b) Photo of the mount, showing the cylindrical-conical end on the opposite side of the mirror. c) Piezo mount with attached mirror. This design is based on the proposal in [173].

glued using epoxy resin in a equilateral triangle pattern to the tip of a custom heavy steel support mass, see figure 3.9 b) and c). The latter prevents undesired mechanical resonances from occurring at low frequencies. Each piezo plate can be controlled independently using an electronic circuit adapted from [173]. The input signal V_{in} is split into three output voltages $V_{\text{out}} = k_i V_{\text{in}}$, with k_i, $i = 1, 2, 3$, which later on seed high voltage amplifiers[20], whose outputs are connected to the three piezo plates. The applied voltages range from 0 V to $\sim 100\,V$. The values of $k_i \approx 1$ can be varied by a few percent using trimmers. This tuning allows to compensate for inhomogeneities of the piezo expansion and from the glueing process. The k_i's were adjusted in such a way that the beam pointing stays stable upon modulating the piezo voltage, which was optimized by looking at the beam position on a camera in real time. When the k_i's are properly adjusted, the relative phase between the beam can be varied by scanning V_{in} without changing the beam pointing significantly.

[20] Falco Systems, WMA-280.

Relative phase measurement The phase measurement starts by separating the X and Y beam pairs using a polarization beam splitter after their passage through the objective. Then, each pair is sent to a dedicated measurement setup. First, a $\lambda/2$ waveplate followed by another polarizing beam divider is used to duplicate the beam pair. Then, each copy is sent through a 5μm slit[21], whose width is small enough to let the light pass only if the copy interferes constructively at its position. The slits are aligned with the interference pattern of the pair, which happens to be horizontal (vertical) for the X pair (Y pair)[22], using a precision rotation mount[23]. The intensity passing through is recorded using a balanced amplified photodector[24]. It has an output that records the difference between the intensity signals s_1 and s_2 measured behind the two slits. They can be expressed in the following way,

$$s_i(\delta\varphi) = \frac{A_i}{2}[1 + \cos(\varphi_i + \delta\varphi)], \quad i = 1, 2, \tag{3.8}$$

where the amplitude A_i is proportional to the optical power before the slit, $\delta\varphi$ is a term that accounts for the dephasing accumulated prior to duplicating the beam pair, and φ_i originates from the fact that each copy follows a different path after the duplication. Both A_i and φ_i can be tuned by rotating the $\lambda/2$ waveplate and changing the path length after the duplication step, respectively. The phases φ_1 and φ_2 are not subject to drifts. Indeed, after collection and recollimation by the object lens, the lattice beams are largely overlapped and thus undergo comparable phase shifts as they propagate further. In the case of power matching $A_1 = A_2$ and phase matching $\varphi_2 = \varphi_1 + \pi \bmod 2\pi$, the signal subtraction yields

$$\Delta s(\delta\varphi) = s_1(\delta\varphi) - s_2(\delta\varphi) = A_1 \cos(\varphi_1 + \delta\varphi). \tag{3.9}$$

The quantity $\delta\varphi$ can be varied by tuning the piezo voltages as explained in the previous paragraph. As shown in figure 3.10 a), the change in phase can surpass 2π.

Feedback loop and integration into the experimental cycle The control and measurement setups described in the two previous paragraphs are linked together to form a feedback loop by using a PID controller[26]. Consequently, the relative phase $\delta\varphi$ defined above can be stabilized to a given value by having the piezo-driven mirrors compensate the slow phase drifts of each pair. We tune the PID controller to regulate the error signal from Eq. (3.9) to 0 V, because that is where it has the largest slope as a function of $\delta\varphi$ and

[21] Thorlabs, S5HK.
[22] This is due to the direction of the 45° mirror that we use to shoot the lattice beams back in the horizontal plane after their passage through the objective.
[23] Thorlabs, PRM1.
[24] Thorlabs, PDB210A.
[26] Standford Research System, SIM960.

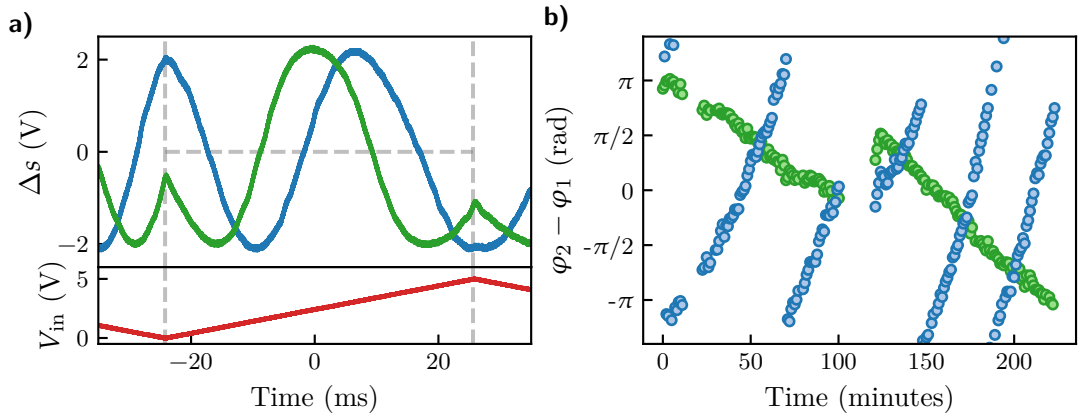

Figure 3.10: Phase lock error signal. a) Top: error signal obtained by scanning the voltages across the piezo plates for both X (green) and Y (blue). Bottom: corresponding sawtooth signal used as voltage input. The fact that the error signal is sine-like shows that the relation between relative phase and input voltage is roughly linear[25]. One can therefore approximately map the relative phase to the input voltage. b) Estimates of the phase inferred by the reported input voltage of the servo loop for successive experimental cycles of $\sim 60s$. Each data point corresponds to an experimental cycle.

its position does not depend on A_1. Obviously, this servo loop can only operate while the lattice beams are shooting through the science cell with enough power to measure the relative phase reliably. Given that the beams are not switched on all the time during an experimental cycle, it is necessary that the control computer communicates with the PID controller to enable and disable the regulation at the appropriate moments. The communication is realized via serial communication between the control computer and the mainframe hosting the PID module[27]. At the beginning of each experimental cycle, the four lattice beams are activated while atoms are still located in the MOT chamber, and the PID control is enabled during this time. The regulation and the lattice beams are switched off before the atoms reach the science cell, and the PID module retains in memory the last regulated value. This value is recorded and written to a logs file which allows us to not only follow the phase drift as shown in 3.10 b), but also to identify regulation failures. The regulation succeeds in more than 99% of the experimental runs, and the observed typical phase drift rate indicates that the lattice site is correctly stabilized with an accuracy of 2% of $d_{\alpha_{\text{latt}}}$ with respect to an arbitrary reference in the worst case[28]. It is sufficient to perform single-layer loading and average long series of absorption images. Since the absolute spatial location of the lattice nodes is fixed by the phase control procedure, the position of the single layer of sites that we would like to load is well-defined. In particular, we can align the compression potential in such a way that it coincides with this layer.

[27] Standford Research System, SIM900.

[28] We see that the drift is significantly faster for the Y pair. This originates from its longer beam path prior to shooting the atoms, from the 50:50 beam splitter to the science cell.

3.2.5 Green compression beam

In order to provide strong confinement along the y direction and realize the pancake configuration depicted in the first step of figure 3.4, we generate a repulsive optical potential with a green TEM_{01}-like mode [174, 175]. The corresponding optical setup is partially shown in figure 3.5 b). To begin with, we split off light from a 10W solid state laser source running 532 nm [29]. After some initial beamshaping, the output is split in two parts, one of which is being used for the barrier beam described later in section 6.5. Both beams are diffracted through AOMs and injected into high power single mode fibers. The intensity of both beams at the fibers' ouputs is regulated in a similar way as the lattice beams in sec. 3.1.2. The beam dedicated to the compression potential is sent through a cylindrical telescope creating a vertically stretched elliptical beam with a 1:10 aspect ratio. After the telescope, the collimated beam is sent through a π-phaseplate and focused down by an achromatic lens [30] of focal length $f = 120$ mm.
Assuming an infinitely sharp step of the phase plate and ideal alignment, the transmission through the phase plate transforms the incoming wave $\vec{E}_{\text{in}}$ into $\vec{E}_{\text{out}}(x, y) = e^{-i\phi_\pi(y,z)}\vec{E}_{\text{in}}$ with a spatially non-uniform wave front of the form

$$\phi_\pi(y, z) = \begin{cases} 0, & y < 0 \\ \pi, & y > 0. \end{cases} , \tag{3.10}$$

where y and z denote the distances with respect to the center of the elliptical Gaussian beam. In this ideal case, it can be shown [88, 174] that the intensity at the position of the atoms is described by

$$I_{\pi-\text{plate}}(y, z) = \frac{2P}{\pi w_y w_z} \text{erfi}^2\left(\frac{y}{w_y}\right) \exp\left(-\frac{2y^2}{w_y^2} - \frac{2z^2}{w_z^2}\right), \tag{3.11}$$

where w_y and w_z denote the waists along the y and z directions, respectively, P is the optical power, and $\text{erfi}(\cdots)$ represents the imaginary error function. The intensity vanishes around $y = 0$, creating a local minimum of potential energy. In order to make sure that the potential is shaped correctly, we image the compression beam on the x camera. After the science cell, the beam goes through a telescope[31] and is imaged with a magnification of 8.34 ± 0.02. The figure 3.11 shows the measured intensity distribution, which is in very good agreement with the expected profile. It also provides an estimate of the corresponding waists $w_y = 13.22 \pm 0.04$ μm and $w_z = 135.9 \pm 0.4$ μm. The waist along the vertical z direction is large enough to be able to assume that the horizontal compression will be

[29] Coherent, Verdi V12.
[30] Edmund Optics, #49-381.
[31] Made of another identical $f = 120$ mm achromatic lens and a plano-convex lens $f(\lambda = 532\text{nm}) = 992.1$ mm (Thorlabs, LA1779-B).

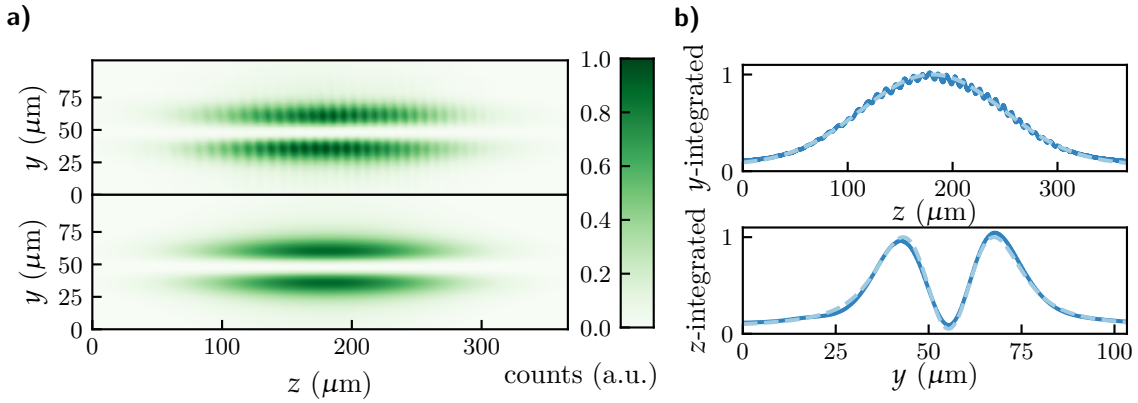

Figure 3.11: Compression beam intensity profile. a) Top: image of the compression beam. Bottom: fit of the profile using Eq. (3.11). b) Integrated counts along y and z for top and bottom, respectively. The solid line represents camera data and the dashed one denotes the fitted profile. The fit yields $w_y = 13.22 \pm 0.04$ μm and $w_z = 135.9 \pm 0.4$ μm, with error bars being dominated by uncertainty in the magnification. The visible fringes are imaging artefacts generated by a dichroic mirror placed after the science cell to dump the excess 532 nm optical power.

approximately homogeneous. Using theses values and Eq. (2.1), we can calculate the expected curvature created by this potential as a function of the optical power. Using $\mathrm{erfi}(y) = (2/\sqrt{\pi})y + \mathcal{O}(y^3)$, we can expand Eq. (3.11) around $y = 0$ at $z = 0$ and define the angular trapping frequency associated with the corresponding approximate harmonic oscillator as per

$$\frac{1}{2}m\omega_y^2 y^2 = \frac{8\alpha_{\mathrm{pol}}P}{\pi^2 w_y^3 w_z}y^2. \tag{3.12}$$

The maximum available power amounts to $P \sim 4$W, which corresponds to $\omega_y \approx 2\pi \times (2.54 \pm 0.11)$ kHz. As we will see empirically later, this is more than enough to achieve single-layer loading in the useful atom number and temperature regime of the experiment. Moreover, ω_y can be directly measured, as will be shown in 4.3.

3.2.6 Site-resolved imaging

In section 3.2.2 we already described the optical properties of the high resolution objective. In this section we will describe how it is used as part of the site resolved imaging system along the y direction. Moreover, the image analysis to extract the integrated one-dimensional density will be detailed.

Image acquisition We will see in chapter 5 that it is sometimes necessary to load less than 100 atoms per lattice site and per spin state in order to reach the one-dimensional regime. It is challenging to detect such a small number of atoms using absorption imaging, especially given that the signal is widely stretched out along the z direction due to the strong trap anisotropy. As a consequence, it is necessary to improve the signal to noise

ratio (SNR) of the acquired images as much as possible. We acquire the images using an Andor iKon-M 934 camera with a high quantum efficiency of 95% at 767 nm as well as very low levels of read-out noise. The image quality can also be degraded by the presence of non-stationary fringes or unstable light intensity. Both of these issues can be mitigated by reducing the time delay between the absorption and reference shot. We can reduce it by making use of the frame-transfer functionality of the camera[32]. A custom mask is placed right in front of CCD chip to cover half of its pixels. This way, by shifting over the charges accumulated in the illuminated area after the absorption light pulse, the reference light pulse can be recorded on the freed up pixels before the entire sensor is slowly read out to reduce noise. This way, we can decrease the time delay to 1 ms.

Rotation of the imaging beam The camera is mounted horizontally on the optical table. Ideally, the elongated direction of the tube traps should coincide perfectly with the orientation of the CCD pixel arrays, but in reality, a small deviation is unavoidable. In order to simplify the analysis of individual micro traps appearing on the image, it is important to control this relative orientation. Due to its large weight and size, it is not ideal to place the Andor camera on a rotation mount. The figure 3.12 a) shows a straightforward way to control the rotation of the imaging beam instead. The site resolved images could in principle be straightened by eye directly, but we used a more accurate method which consists in calculating the two-dimensional Fourier transform of the signal in the atomic region. By ensuring that the peaks appearing in the reciprocal space due to the lattice modulation intersect the horizontal axis one can precisely align the imaging beam as shown in figure 3.12 b) and c).

Selecting the tube traps Using these aligned images, it is straightforward to separate the tube traps and analyse them independently. We start by fitting the optical density (OD) averaged along the z direction with the following ansatz,

$$\langle OD \rangle_z(x) = \sum_{n=1}^{N_{\text{tubes}}} A_n \exp\left(-\frac{[x - (x_0 + n d_{\alpha_{\text{latt,x}}})]^2}{2\sigma_n^2} \right), \tag{3.13}$$

which is just a sum of Gaussians equally spaced by $d_{\alpha_{\text{latt,x}}}$, with individual amplitudes A_n and sizes σ_n. The integer N_{tubes} represents the number of peaks visible on the signal, and x_0 is an offset. Figure 3.12 c) shows a typical fit, which yields a lattice spacing of $d_{\alpha_{\text{latt,x}}} = 2.59 \pm 0.01$ μm in the x direction, which is associated with a full-angle of $\alpha_{\text{latt,x}} = 23.7 \pm 0.1^\circ$ between the X pairs. The various fitted σ_n are all very close to each other and thus indicate that the transverse size of the clouds inside the micro traps is smaller than the resolution limit. Therefore, it can be estimated and is be found to be

[32] Referred to as 'Fast Kinetics' by the manufacturer.

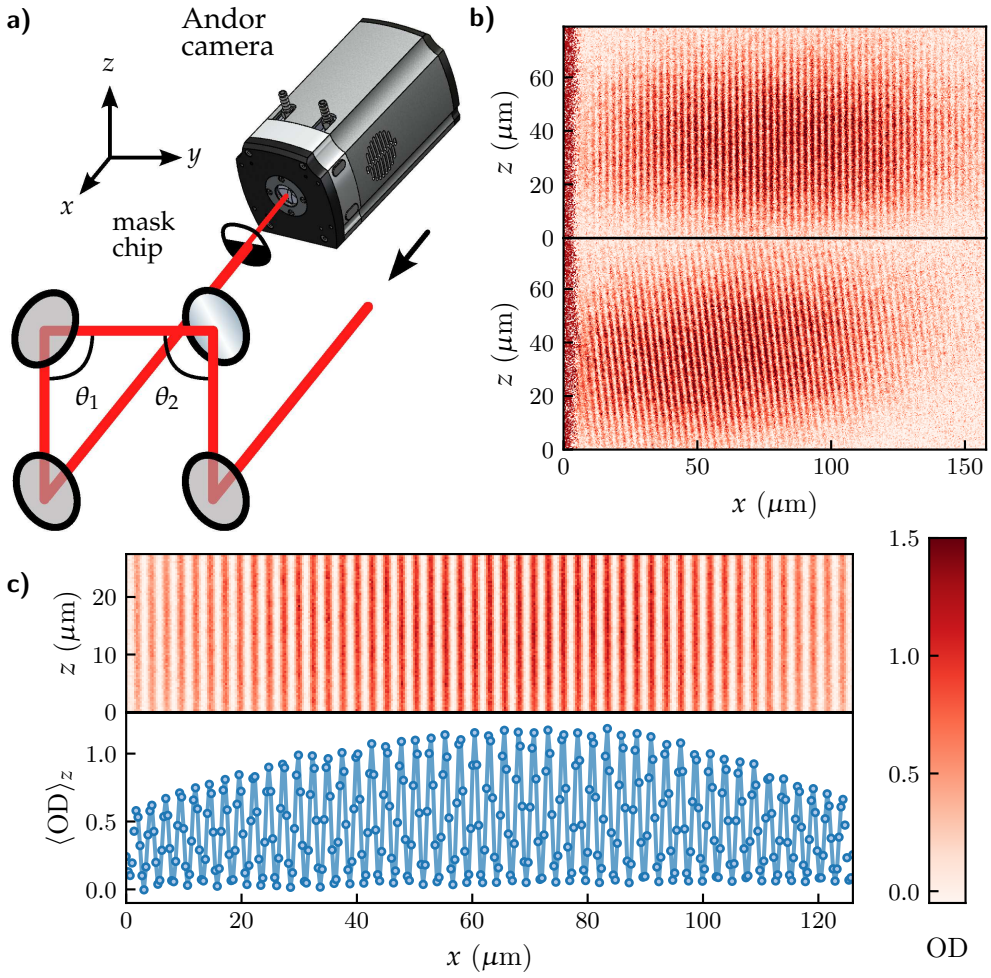

Figure 3.12: Site-resolved images along the y direction. a) Illustration of the beam rotation stage. The beam is temporarily moved out of the (x, y) plane, and its rotation is fine-tuned by changing the angles θ_1 and θ_2. b) Single absorption images corresponding to correct and incorrect beam alignment (top and bottom, respectively). The noisy region on left of the images is due to the chip mask intentionally covering the mid-section of the chip. This was done to prevent light from accidentally leaking from the reference to the absorption image. c) Close-up view of the optical density obtained from averaging 32 absorption images (top), and its vertically averaged line profile (bottom). The solid line represents the fit using Eq. 3.13, which yields a lattice spacing of $d_{\alpha_{\text{latt,x}}} = 2.59 \pm 0.01$ μm.

equal to 1.3 μm, according to Rayleigh criterion. This is higher than the value of 0.9 μm measured with the test target on the side, but consistent with the specification provided by the manufacturer of 1.24 μm (see sec. 3.2.2). It is small enough to provide very high contrast, close to 100%, despite averaging multiple images. This is a direct consequence of rigorously stabilizing the lattice phase in the x direction (see sec. 3.2.4). From the fitted values of x_0 and $d_{\alpha_{\text{latt,x}}}$, we can calculate the positions of the (anti-)nodes in terms of the

pixel size ℓ_{px}. Since the ratio $d_{\alpha_{\mathrm{latt,x}}}/\ell_{\mathrm{px}} \sim 7.53$ is not an integer, there will always be pixels located in-between two neighbouring lattice sites that share contributions from independent tube traps. To accommodate for this, we artificially split the corresponding pixels during data analysis. The separations are made at the exact inter-site positions by sharing the local optical density extracted from the full pixel between the two-sites in proportion to the area of the two sub-pixels. This way, we unambiguously separate the signal contributions of each loaded tube trap.

3.2.7 Repumping-induced vertical masking

The previous section described the acquisition of site-resolved images along the y direction. Given the depth-of-field of ~ 3.1 μm, which is larger than the lattice spacing in that direction, the observation of a very large contrast of $\sim 100\%$ is an indication that the atoms do not occupy many lattice sites along the line-of-sight. However, this is not sufficient to conclusively infer that only a single layer was loaded. This necessitates to image along the z direction, where an ideal site-resolved imaging setup would allow to observe the distribution of occupied lattice sites along x and y directions. However, as previously mentioned in sec. 3.2.2, the large size of the atomic clouds along z direction makes it challenging to implement.

We mitigate this issue by partially "clipping" the atomic cloud by repumping parts into states transparent to the imaging light [54, 176]. As previously mentioned in sec. 3.2.1, we initially intended to use this technique to realize single-layer imaging, and therefore detailed descriptions of the repumping scheme were already presented in [88, 89]. In a nutshell, atoms are sent into the upper hyperfine ground state manifold ($m_J = 1/2$), rendering them off-resonant to the probe beam.

The pumping beam illuminates an opaque slit on an optical window, which is then imaged onto the row of atomic wires from the side. The slit of 15μm is made of chromium as well as gold and is part of larger collection realized in a clean room, which contains several options of variable width [89]. The resulting beam, sent along the x direction, can later be imaged and detected in order to facilitate alignment and focusing, resulting in images shown in figure 3.13 a). An illustration of the corresponding optical setup is shown in b). After passing through the slit, the masking beam is imaged onto the atoms and demagnified by two lenses of focal lengths $f = 300$ mm and 120 mm. The second lens is an achromatic lens which is shared with with green compression beam as shown in figures 3.5 and 3.6. The theoretical demagnified slit size amounts to 6μm at the position of the atoms. It is slightly larger than the 5μm resolution of the imaging system. During an experimental cycle, the pumping beam is pulsed on for the duration of 1 μs, just before the absorption image is taken along the z direction. The effect on a compressed cloud loaded in the optical lattice is shown in 3.13 c) and d). The full width at half-maximum of the

addressed slices after pumping is $\sim 4\mu$m, which is smaller than depth of field of $\sim 5\mu$m along this direction. Therefore, the clipped atomic ensemble constitutes a much better target to perform site-resolved imaging along the z direction. However, this technique precludes the extraction of densities along the z direction.

3.2.8 Evidence of single-layer loading

So far, we have described how to create the best conditions to check whether one is only loading a single layer of the two-dimensional lattice along y, as illustrated in figure 3.4 b). In the following, we will detail how the auxiliary imaging axis z can be employed in this context.

We verified this by taking pairs of images of the compressed cloud, both with and without the two-dimensional optical lattice along z. In between pairs, we varied the horizontal position $y_{\text{compression}}$ of the green compression beam by tilting a mirror placed on a piezoelectric actuated mount. For each pair of images, we extracted the center of mass (CoM) of the cloud along y without lattice, denoted by $y_{\text{CoM-no latt}}$, and the same quantity with lattice $y_{\text{CoM-latt}}$. We observed that, while $y_{\text{CoM-no latt}}$ increased smoothly by moving the green beam, $y_{\text{CoM-latt}}$ would suddenly jump between evenly spaced positions. This discreteness is exactly what one would expect in an optical lattice where only one row is loaded. In order to empirically capture this effect, we fit the data using the following model,

$$y_{\text{CoM-latt}} = \sum_{n=1}^{N_{\text{steps}}} d_{\alpha_{\text{latt,y}}} \left[\frac{1}{\pi} \arctan\left(\frac{y_{\text{CoM-no latt}} - y_s - n d_{\alpha_{\text{latt,y}}}}{\ell_w} \right) + \frac{1}{2} \right] + y_0, \tag{3.14}$$

where N_{steps} corresponds to the number of observed steps, $d_{\alpha_{\text{latt,y}}}$ is the lattice spacing along the y direction, ℓ_w is a parameter that controls the step sharpness, y_s is a shift parameter to fix the absolute position of sites, and y_0 is an offset. The data shown in figure 3.14 agrees well with this model and provides a lattice spacing of $d_{\alpha_{\text{latt,y}}} = 2.48 \pm 0.03$ μm, which corresponds to a full-angle of $\alpha_{\text{latt,y}} = 24.8 \pm 0.3^\circ$ between the Y lattice beams. Here again the error bars are dominated by the magnification error. The fitted sharpness parameter $\ell_w \approx 0.22\mu$m is well below the lattice spacing, but has a finite value. This is due to the fact that inbetween two steps, when the compression beam is located in the middle of two lattices sites, the compressed cloud is loaded into both them. In the limit of infinitely small cloud size along y prior to loading, the step should become infinitely sharp. Despite the imperfect optical resolution which prevents us from directly observing the lattice modulation along the x direction, this effect can never be seen quite clearly as shown in figure 3.14 b). We also included an image that was taken when the compression beam's direction of propagation did not coincide with the lattice pattern along the y

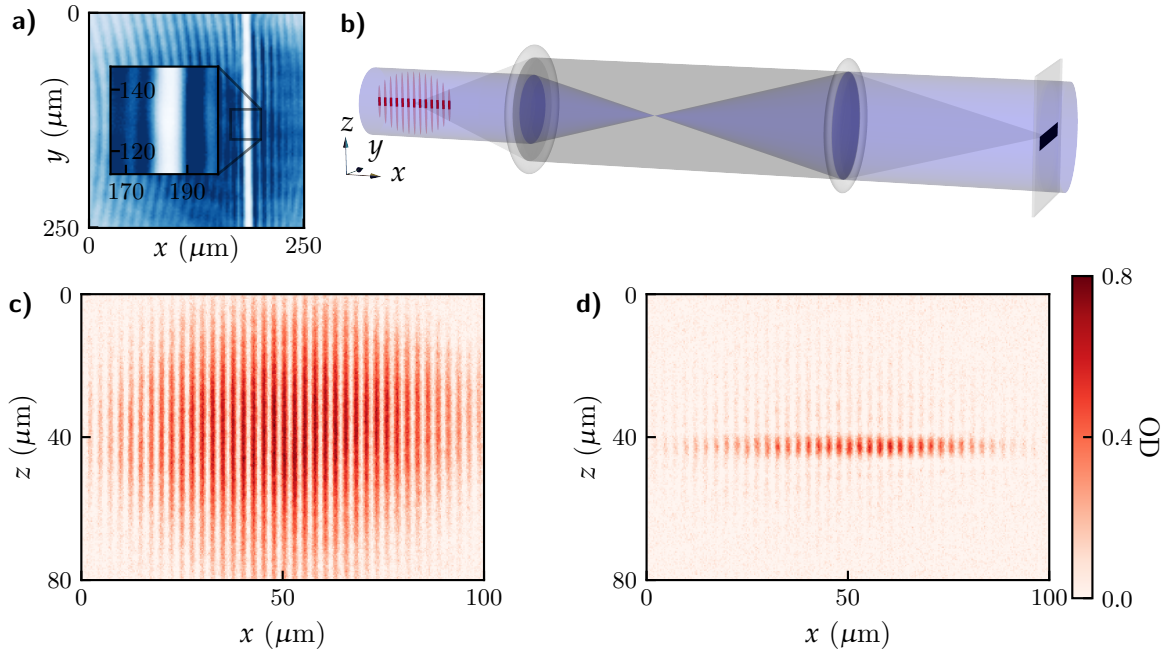

Figure 3.13: Atomic clipping along z facilitated by optical masking. a) Image of the masking beam focused on a camera, featuring a shadow region reflecting the opaque mask b) Optical setup to project the shadow image onto the atoms. c) Absorption image of the compressed cloud after being loaded in the two-dimensional lattice without masking. d) Similar image in the presence of masking, illustrating the drastic size reduction along z.

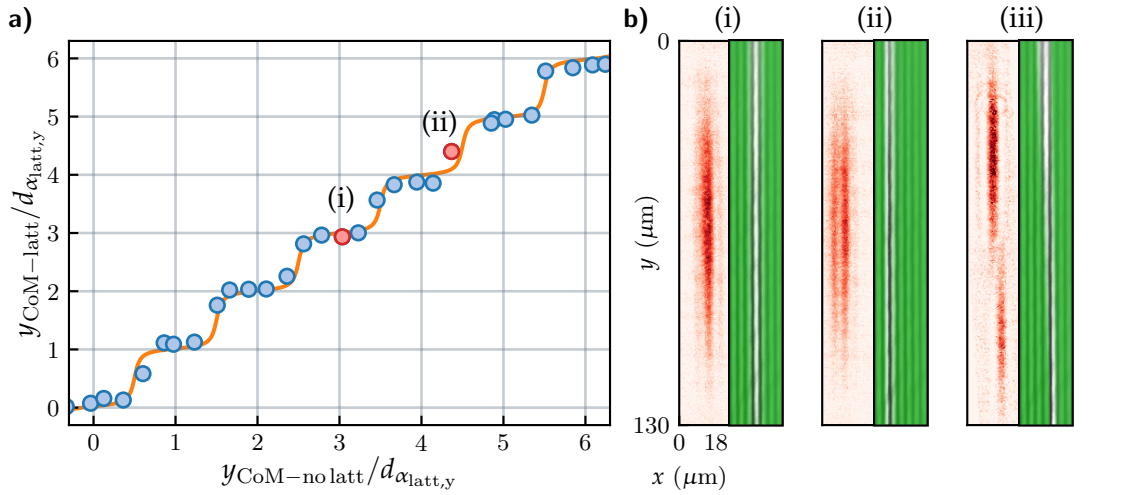

Figure 3.14: Direct evidence of single-layer loading. a) Position of the CoM of the compressed atoms after being loaded into the optical lattice as a function of the compression beam position. The latter is measured by the CoM of the compressed atoms without optical lattice. Whenever a plateau is reached, the position of the CoM does not depend on the compression beam's position until a new lattice site is approaching. The points highlighted in red correspond to images (i) and (ii) shown on the right. b) For each image, the left frame represents the OD acquired along z for compressed atoms loaded in the two-dimensional optical lattice, whereas the right frame shows an illustration featuring both the y interference pattern (in white for high intensities) and the compression potential (green). The optical resolution is insufficient to resolve the lattice spacing along x, however, we can distinguish single layer loading (i) from double layer loading (ii). The image (iii) represents the distribution when the compression beam is not correctly aligned with the lattice pattern along y.

direction, which would systematically lead to multi-layer loading. This underlines the extreme importance of precise alignment.
By combining the present measurement of $d_{\alpha_{\text{latt,y}}}$ and the one of $d_{\alpha_{\text{latt,x}}}$ made in sec. 3.2.6, we can extract the spacing ratio $d_{\alpha_{\text{latt,y}}}/d_{\alpha_{\text{latt,x}}} = 0.96 \pm 0.01$. This result depends on the calibration of the magnifications along y and z, which correspond to the axis where the spacings are extracted. Remarkably, this ratio can be obtained in an alternative and magnification-independent way using the interference pattern of the lattice beams collected on the z camera. Using the image shown in 3.8 b), it yields a ratio of 0.962. The fact that these two methods agree so well further highlights the overall reliability of the optical techniques developed here.
We have shown that we can load a single-layer of the two-dimensional optical lattice. This crucial milestone will allow us to perform quantitative analysis of the *in-situ* density profiles inside individual micro traps, in chapter 5. But before that, it is necessary to calibrate the external potential inside which atoms evolve. The next chapter is dedicated to that task, as well as the calibration of the density from absorption images.

Chapter 4

Reconstruction of the micro-trap potential

In chapter 3 we have presented a novel preparation procedure allowing us to load a single layer of a two-dimensional optical lattice. By employing site-resolved imaging, we are in a position to capture and individually analyse the quantum gases contained in different micro-traps. This technical achievement represents the crucial milestone required in order to quantitatively evaluate density profiles in the absence of ensemble averages. The remaining challenge in this context arises from the fact that the density profiles are not homogeneous in any direction of space.
This chapter will present how to calibrate the trapping potential of a given-micro trap and the density. First, we will empirically derive the proper model to convert optical density in atomic densities in the tube traps. Then, a model of the potential in the tube traps will be introduced to gauge the degree of similarity between the potentials of the loaded tubes. Finally, we will present a calibration method for both the perpendicular and the longitudinal curvature of the tube traps.

4.1 Absorption imaging and light intensity calibration

We perform standard absorption imaging to probe the density distribution of the atomic cloud. A resonant laser beam passes through the gas and is locally attenuated according to the density of the sample along the line-of-sight. This altered beam is magnified and imaged onto a CCD camera. Ultimately, the sample is destroyed due to the excessive energy transfer from the photons. Alternatively, non-destructive imaging techniques exist, such as phase-contrast imaging, which uses a slightly detuned probe beam to exploit the dispersive properties of the atomic sample to reconstruct the integrated density profile [177]. These dispersive effects are absent if the probe beam is perfectly resonant.

When the atomic sample is dense, using a low intensity to perform absorption imaging is problematic as very few photons make it through the entire sample, leading to a reduction of the signal-to-noise ratio. This issue can be mitigated by using higher light intensities which necessitates an additional calibration step, as will be described below.

In the low intensity limit, the transmitted beam profile is given by the Beer-Lambert law [178],

$$I_{\text{out}} = I_{\text{in}} e^{-\text{OD}(x,z)}, \qquad \text{OD}(x,y) = \sigma_{\text{eff}} \int n(x,y,z)\text{d}z, \tag{4.1}$$

where I_{in} and I_{out} are the incident and transmitted intensities, respectively, and OD denotes the optical density. The effective cross section is defined as $\sigma_{\text{eff}} = \gamma\sigma_0$, with $\sigma_0 = \frac{3\lambda^2}{2\pi}$ representing the resonant cross-section [179] and $\gamma \leq 1$ is a parameter that accounts for potential effects related to polarization-related effects. Finally, $n(x,y,z)$ is the three-dimensional atomic density distribution. As soon as the saturation of the optical transition becomes relevant, the Beer-Lambert law needs to be modified [180, 181]. The optical density then becomes

$$\text{OD}(x,y) = -\ln\left(\frac{I_{\text{out}}(x,y)}{I_{\text{in}}(x,y)}\right) + \frac{I_{\text{in}}(x,y) - I_{\text{out}}(x,y)}{I_{\text{sat}}^{\text{eff}}}, \tag{4.2}$$

where $I_{\text{sat}}^{\text{eff}} = I_{\text{sat}}/\gamma$, with the saturation intensity $I_{\text{sat}} = \pi hc\Gamma_{\text{nat,D2}}/3\lambda^3$ at $\lambda = 767$ nm, with a natural linewidth $\Gamma_{\text{nat,D2}} \approx 2\pi \times 6.035$ MHz. The first term originates from the Beer-Lambert law whereas the second one corresponds to saturation correction. For the remainder of this text and unless specified otherwise, we always image the atoms in the stretched state[1] $|1\rangle$ because it has a quasi-cycling transition, as described in [88, 89]. Along the y direction the light is linearly polarized, perpendicularly to the quantization axis. As a result, only half of the photons are actually resonant with the cycling transition and consequently we must take $\gamma \approx 0.5$.

Moreover, given that we use an imaging pulse of duration 12 μs, we used the method presented in [181] to ensure that no noticeable Doppler shift occurs in our imaging sequence.

Because they appear as ratios in Eq. (4.2), the intensities I_{in}, I_{out} and I_{sat} can be replaced with the their corresponding camera count rates, which we denote by C_{in}, C_{out} and C_{sat}, respectively [181]. Thus the equation becomes

$$\text{OD}(x,y) = -\ln\left(\frac{C_{\text{out}}(i,j)}{C_{\text{in}}(i,j)}\right) + \frac{C_{\text{in}}(i,j) - C_{\text{out}}(i,j)}{C_{\text{sat}}}, \tag{4.3}$$

where i and j are integers describing pixel rows and columns. In this description, all of the information required to incorporate the saturation effects is contained in C_{sat}, which

[1] Defined in section 2.3.

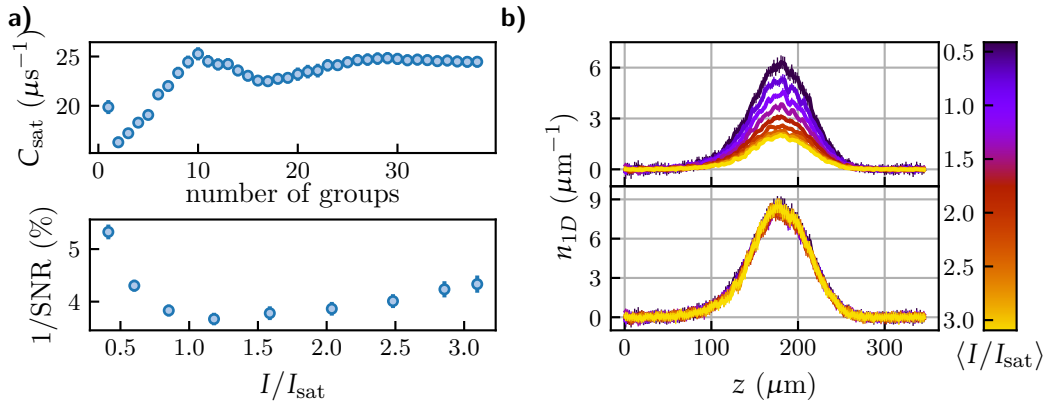

Figure 4.1: High-intensity absorption calibration. a) Calibration of the saturation count rate (top) and inverse SNR (bottom), showing a minimum around $\langle I/I_{sat}\rangle = 1.2$. b) Reconstructed density profiles obtained in the tube traps for different light intensities. Top: no saturation correction. Bottom: with correction for high probe intensity.

needs to be calibrated. This can be done by requiring that the reconstructed total atom number, obtained by integrating over the reconstructed column density, is independent of the probe beam intensity. To do so, we image the compressed cloud loaded in the two-dimensional lattice. We switch off the lattice beams just before the imaging pulse starts in order to avoid AC-Stark shits [182]. We calibrated the resonance frequency using the method from [181]. We take groups made of three shots at different light intensities. We repeat this operation until obtaining a large amount of groups. For each group i, we calculate the standard deviation σ_i of the atom number data, which depends on C_{sat} through Eq. (4.3). We find the value of C_{sat} that minimizes $\sum \sigma_i$, where the sum contains all the groups. Grouping the images by three minimizes the influence of external factors, which could potentially cause the atom number to drift. The top frame of figure 4.1 a) shows the convergence of C_{sat} as the number of groups increases, which ultimately leads to a statistical error of ± 4 %.

Once the value of C_{sat} is known, we can extract the mean saturation parameter $\langle I/I_{sat}\rangle$ by comparing the averaged count rate of the reference shots with the saturation count rate. We calculated the signal-to-noise ratio SNR $= \langle n_{max}\rangle / \langle \sigma_{pix}\rangle$, where $\langle \sigma_{pix}\rangle$ is calculated by averaging the typical standard deviation of the reconstructed densities at each individual pixel from a series of multiple shots taken at identical light intensity, and $\langle n_{max}\rangle$ is the maximum density reached at the center of the potential. As shown in the bottom half of 4.1 a), one can identify a clear optimum at $\langle I/I_{sat}\rangle \sim 1.2$. Consequently, we used this light intensity setting to acquire images for all quantitative measurements.

However, care has to be taken when deriving C_{sat} via atom number measurements. The presence of cooperative effects could strongly bias the signal as there are typically density dependent effects in dense samples [183–185]. For example, consider two atoms in close proximity to one another, initially in the ground singlet state, and therefore interacting via

a van der Waals potential $V(r) = -C_6/r^6$. If one atom absorbs a photon, it is pumped into a triplet state and suddenly interacts with the other ground state atom through the dipole-dipole potential $V(r) = -C_3/r^3$ instead. The range of this potential is much longer than in the case $1/r^6$ case. Any shift of the levels will then reduce the effective scattering cross section of the atom that remained in the ground state. This effect was employed in other works to induce light-assisted collisions, and requires large densities to be dominant [186]. We empirically rule out the significance of density-dependent effects in our experimental setup by looking carefully at the reconstructed density profiles, as shown in figure 4.1 b), and noting that they overlap very well for all values of the density.

Finally, a recent study presented a method to extract the density of ultracold gases that are smaller than the resolution limit [187]. In particular, they observed significant non-linear corrections to the local density compared to a standard analysis. In order to verify the relevance of this effect for us, we imaged the cloud after ~ 100 μs of free expansion. This duration was long enough to remove any visible modulation from the lattice, which is a guarantee no sub-resolution structures remained. We compared the corresponding total atom number from these images with their *in-situ* equivalents and observed no significant deviations, which empirically justified neglecting the effects observed in [187].

4.2 Modelling the trapping potential

In order to formulate a model of the external potential making up the micro traps, one needs to take into account all the factors contributing to the total optical intensity at the position of the atoms. There are two dipole traps (see sec. 2.2) and four lattice beams (see sec. 3.1.2) that we will label with an index j. All of the laser beams contributing to the potential are approximately Gaussian TEM_{00} modes. The electric field E_j of beam j is fully characterized by a direction of propagation $\vec{e}_j$, a polarization direction[2] $\vec{u}_j$, a waist $w_{0,j}$ and a power P_j. The Table 4.1 summarizes the possible values of j and the corresponding directions of propagation and polarization. Figure 4.2 contains a visual representation of the beam configuration. Then, $\vec{E}_j(\vec{r}) = e^{i\omega_j t} E_j(\vec{r})\vec{u}_j$, where ω_j is the angular frequency and

$$E_j(\vec{r}) = \sqrt{\frac{2P_j}{\pi w_j(z_j)^2}} \exp\left(-\frac{\rho_j^2}{w_j(z_j)^2}\right) \exp\left[-i\left(k_j z_j + k_j \frac{\rho_j^2}{2R_j(z_j)} - \psi_j(z_j)\right)\right], \quad (4.4)$$

is the expression of a TEM_{00} Gaussian mode [178, 188]. Here, $z_j = \vec{r}\cdot\vec{e}_j$ is the axial distance from the beam's waist and $\rho_j = ||\vec{r}\times\vec{e}_j||$ is the radial distance from the axis of propagation.

[2] All the laser beams used here are linearly polarized.

Also, the standard quantities were employed as well

$$w_j(z_j) = w_{0,j}\sqrt{1+\left(\frac{z_j}{z_{R,j}}\right)^2}, \quad z_{R,j} = \frac{\pi w_{0,j}^2}{\lambda_j}, \quad R_j(z_j) = \frac{z_j^2 + z_{R,j}^2}{z_j}, \quad \psi_j(z_j) = \arctan\left(\frac{z_j}{z_{R,j}}\right).$$

The Rayleigh range $z_{R,j}$ quantifies how quickly the radial beam size $w_j(z_j)$ diverges around its waist, $R_j(z_j)$ is the local radius of curvature of the wavefront and $\psi_j(z_j)$ is usually referred to as the Gouy phase. The quantities λ_j and $k_j = 2\pi/\lambda_j$ represent the wavelength and the wavevector of the beam, which are related to the angular frequency via the dispersion relation $\omega_j = ck_j$, where c is the speed of light in the vacuum. Note that we directly defined the electric fields such that they are homogeneous to $(\mathrm{W}\cdot\mathrm{m}^{-2})^{1/2}$. Consequently, the corresponding intensities can be obtained by simply squaring them. The true electric fields can obtained by dividing Eq. (4.4) with $c\epsilon_0/2$, where ϵ_0 is the vacuum permittivity.

For all of the beams, we can take $\lambda_j = \lambda_L = 1064$ nm. The two dipole traps are polarized in orthogonal directions, and are slightly detuned with respect to each other so that no interference effect can occur. Their corresponding intensity distribution is given by the incoherent sum

$$I_{\mathrm{cODT}} = |E_{\mathrm{cODT1}}|^2 + |E_{\mathrm{cODT2}}|^2. \tag{4.5}$$

The lattice beams have pairwise matching polarization and frequency to maximize interference inside pairs, and avoid them between pairs (see sec. 3.1.2). Their corresponding intensities are given by

$$I_{\mathrm{latt,X}} = |E_{\mathrm{latt,X1}} + E_{\mathrm{latt,X2}}|^2, \qquad I_{\mathrm{latt,Y}} = |E_{\mathrm{latt,Y1}} + E_{\mathrm{latt,Y2}}|^2. \tag{4.6}$$

The overall potential is obtained by using Eq. (2.1) and yields

$$U_{\mathrm{tot}}(x,y,z) = \alpha_{\mathrm{pol}} I_{\mathrm{tot}}(x,y,z) + mgz, \tag{4.7}$$

where $I_{\mathrm{tot}} = I_{\mathrm{cODT}} + I_{\mathrm{latt,X}} + I_{\mathrm{latt,Y}}$ is the total intensity. We also included the gravitational potential energy. Using this convention, all the beams intersect at $(0,0,0)$, which also coincides with the position of their waists.

It is straightforward to calculate U_{tot} numerically for any inputs of P_j and w_j. The waists of the two dipole traps are $w_{\mathrm{cODT1}} = 141\mu$m and $w_{\mathrm{cODT2}} = 138\mu$m (see fig. 2.3), and, in what follows, we will be using a power of 1.07 W in both arms, which corresponds to the recompressed final setting in the experiment (see fig. 2.5). We will take the lattice waists to be equal to[3] $w_{\mathrm{latt}} = 220\mu$m and set their power per beam to[4] 2.93 W.

[3] This corresponds to their design value and is close to their measured values using a beam profiler.
[4] To mimic the typical settings used in chapter 5.

Beam index j	Polarization direction $\vec{u}_j$	Propagation direction $\vec{e}_j$
cODT1	$(0,0,1)$	$(\cos\theta_{\frac{1}{2}}, \sin\theta_{\frac{1}{2}}, 0)$
cODT2	$(\sin\theta_{\frac{1}{2}}, \cos\theta_{\frac{1}{2}}, 0)$	$(\cos\theta_{\frac{1}{2}}, -\sin\theta_{\frac{1}{2}}, 0)$
latt, $X1$	$(0,1,0)$	$(\sin\alpha_{\frac{1}{2}}, 0, -\cos\alpha_{\frac{1}{2}})$
latt, $X2$	$(0,1,0)$	$(-\sin\alpha_{\frac{1}{2}}, 0, -\cos\alpha_{\frac{1}{2}})$
latt, $Y1$	$(1,0,0)$	$(0, \sin\alpha_{\frac{1}{2}}, -\cos\alpha_{\frac{1}{2}})$
latt, $Y2$	$(1,0,0)$	$(0, -\sin\alpha_{\frac{1}{2}}, -\cos\alpha_{\frac{1}{2}})$

Table 4.1: Beam parameters used to model the external potential. The half angle between the crossed dipole trap arms is $\theta_{\frac{1}{2}} = \theta_{\text{cODT}}/2 = 41.8°/2$, and the half angle between the lattice beams is $\alpha_{\frac{1}{2}} = \alpha_{\text{latt}}/2 = 23.6°/2$.

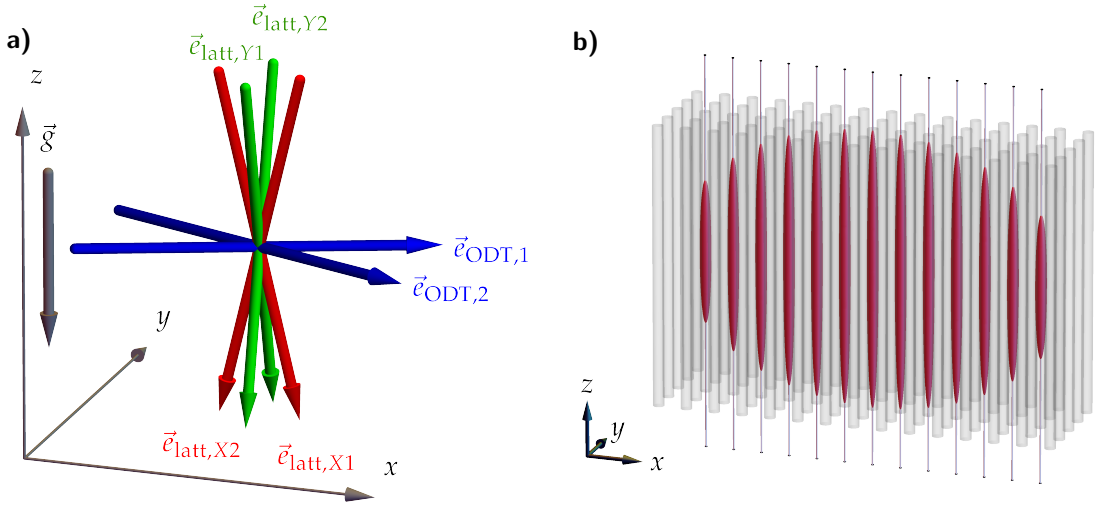

Figure 4.2: Geometrical configuration of the various optical traps. a) Representation of the six laser beams. The crossed dipole trap is made up of the two beams propagating in the horizontal plane, represented in blue. For the optical lattice, there are four beams propagating from top to bottom under an angle. The beams can interfere pairwise to generate two mutually independent optical lattices. The X and Y pairs are represented in red and green, respectively. We define the position where beams overlap as $x = y = z = 0$. b) Schematic representation of the atoms, in red, loaded in a single plane of tube traps represented by grey cylinders. The thin blue lines are centered on the loaded tubes located at $y = 0$. The vertical cuts described in the main text are taken along those lines. The x coordinate varies from one micro trap to another, but is always equal to multiples of $d_{\alpha_{\text{latt}}} \approx 2.59\mu$m where $U_{\text{tot}}(x,y,z)$ has a local minimum.

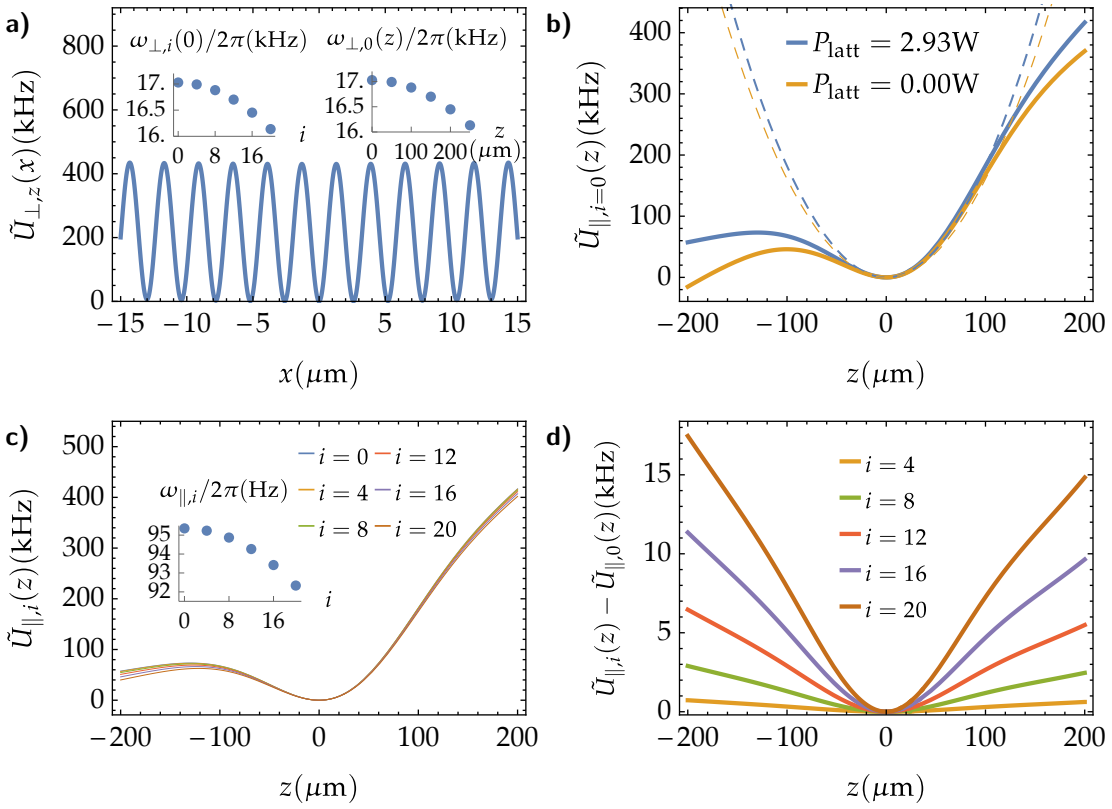

Figure 4.3: Simulation of the total potential. a) Cross section along the x direction with $y = z = 0$. The potential has local minima at positions $x_i = id_{\text{latt}}$, where i is an integer. The two insets show the variation of the local curvature, quantified by the position dependent angular trapping frequency $\omega_i(z)/2\pi$ at several lattice minima x_i (left), and as a function of z (right). b) Cut of the potential at $x = y = 0$, with and without lattice beams. The cross section with lattice beams correspond to a transverse trapping frequency of 17.03 kHz and 95.88 Hz longitudinally. Without lattice beams the longitudinal trapping frequency drops down to 90.20 Hz. The dashed lines represent the harmonic approximations of the potentials around their local minimum. c) Cut at different lattice minima x_i for $y = 0$. The inset represents the variation of the longitudinal trapping frequency as a function of the minimum position x_i. d) Absolute difference of the slice at $x = x_i$ and $y = 0$ with respect to the central one $x = y = 0$.

We first consider horizontal through the 3D potential for various z and at $y = 0$ by defining

$$\tilde{U}_{\perp,z}(x) = U_{\text{tot}}(x, 0, z) - U_{\text{tot}}(0, 0, z). \tag{4.8}$$

This potential is depicted in figure 4.3 a) for various settings and parameters. The minima are located at positions $x_i = id_{\alpha_{\text{latt}}}$, where i is an integer and $d_{\alpha_{\text{latt}}}$ is the spacing defined in Eq. (3.2). By expanding the potential around $x = x_i$ at constant $y = 0$ and z, we define the

local angular trapping frequency as $\omega_{\perp,i}(z)$ as

$$\tilde{U}_{\perp,z}(x) = \frac{1}{2} m\omega_{\perp,i}(z)^2 (x - x_i)^2 + \mathcal{O}((x - x_i)^3). \tag{4.9}$$

In the limit where the lattice waists are infinite, this coefficient would neither depend on z nor on the minimum position i anymore. However, due to the finite size of the beam it decreases with growing distance from center located at $i = 0$ and $z = 0$. The model allows us to gauge how significant this decrease is. It predicts a central value of $\omega_{\perp,i=0}(z = 0) = 2\pi \times 17.03$ kHz. If we move 9 tube traps away from the center in the horizontal direction, one has $\omega_{\perp,i=9}(z = 0) = 2\pi \times 16.84$ kHz, which corresponds a relative difference of only 1.1 % compared to the central value. Also, for a given tube trap, the local angular trapping frequency in the perpendicular direction is very homogeneous across the range populated by atoms. For instance, the model predicts that $\omega_{\perp,i=0}(z = 100\mu\text{m}) = 2\pi \times 16.88$ kHz, which corresponds to a relative difference of only 0.9% compared to the central value.

It also interesting to look at vertical cuts centered on tube traps. For that purpose, we define

$$\tilde{U}_{\parallel,i}(z) = U_{\text{tot}}(x_i, 0, z - z_{\text{min},i}) - U_{\text{tot}}(x_i, 0, z_{\text{min},i}), \tag{4.10}$$

where $z_{\text{min},i}$ is the gravity sag, corresponding to the local minimum along the vertical cut of $U_{\text{tot}}(x_i, 0, z)$. Its value at the center when the lattice beam powers are set to 2.93 W is $z_{\text{min},i} \approx -24\mu$m and varies by only 2% upon moving 9 tube traps away from the center. In analogy to the treatment of horizontal cross sections, we define the coefficient $\omega_{\parallel,i}(z)$ by Taylor expanding $\tilde{U}_{\parallel,i}(z)$ around its minimum,

$$\tilde{U}_{\parallel,i}(z) = 1/2 m\omega_{\parallel,i}^2 z^2 + \mathcal{O}(z^3). \tag{4.11}$$

Unlike in the previous situation, atoms can explore regions where the higher order terms $\mathcal{O}(z^3)$ contribute significantly. The longitudinal potential is influenced by the presence lattice beams as shown in 4.3 b). For a given power of the lattice beams, we can quantify how much $\tilde{U}_{\parallel,i}(z)$ depends on the positioning of the lattice site, as detailed in figure 4.3 c). We observe that the coefficient $\omega_{\parallel,i}$ slightly decreases from $2\pi \times 95.36$ Hz to $2\pi \times 94.74$ Hz as i increases from 0 to 9, which corresponds to a relative difference of 0.7 %. We can also compare the cuts beyond the harmonic approximation, as represented in 4.3 d). The relative differences with respect to the central cut are largest on the negative z side, which also correspond to side which also happens to be the area containing the majority of atoms due to the asymetry. However, for $z = 100\mu$m, which is very close to the spilling limit, the relative difference is below 3% between cuts at $i = 0$ and $i = 9$.

To summarize, we have derived the following conclusions:

- We can assume that for each tube trap at position i the potential is described by $V(x, y, z) = V_\perp(x, y) + V_\parallel(z)$, where $V_\perp(x, y)$ and $V_\parallel(z)$ are independent of i. This simplification is reasonable as long as we analyse tube traps that are not too far away from the center. By restricting ourselves to $|i| \leq 9$, the model indicates that errors arising from this assumption are on the order of $\sim 2\%$.

- At large lattice power, we can use the harmonic approximation $V_\perp(x, y) = \frac{1}{2}m\omega_\perp^2(x^2 + y^2)$ for the transverse direction. Indeed, the trap is limited by the longitudinal direction, which causes atom to spill before they have the opportunity to reach the transverse anharmonic region at equilibrium.

- Because of the typical trap frequency ratios that we will study, we expect the cloud to extend into regions where the non-harmonicity of $V_\parallel(z)$ contributes significantly. As a consequence, we need to find a way to reconstruct $V_\parallel(z)$ with a precision exceeding the harmonic approximation.

The exact validity of this model relies on several factors and assumptions. First, it depends on the assumption that beams are overlapped at a single point, and second, that each beam has its waist position located at this point as well. It also assumes that the propagation and polarization vectors are ideal, so that the lattice pairs interfere with a 100% contrast. Misalignment is easy to include mathematically, but very hard to control and quantify in the experimental context. For that reason we restricted ourselves to the analysis of this ideal configuration. However, this model was just meant to explore the expected geometry of trap and estimate the local variations of local curvatures in each given tube and inbetween tubes. It cannot be used an input to analyse future experiments. In the next sections, we calibrate those curvatures empirically.

4.3 Calibration of the perpendicular curvature of the potential

We argued previously that it is reasonable to consider the transverse potential to be purely harmonic. In other words, it can be fully described by a set of transverse angular trapping frequencies ω_x and ω_y that are approximately equal is each tube traps. We can vary them by changing the amount optical power contained in the lattice arms. In this section, we will briefly discuss how these frequencies can be measured by modulating the position and the curvature in a harmonic trap, and apply it to the transverse potential of the tube traps [189–191].

Curvature modulation We first consider the single-particle Hamiltonian

$$\widehat{H}_{\text{curv}} = \frac{\hat{p}^2}{2m} + \frac{1}{2}m\omega^2(1 + \epsilon(t))\hat{x}^2, \tag{4.12}$$

where $\epsilon(t)$ is a small time dependant perturbation. We denote by $|n\rangle$ the eigenstates of the one-dimensional harmonic oscillator[5], where n is a positive integer, and which correspond to the eigenstates of the unperturbed Hamiltonian when $\epsilon(t) = 0$. We assume a sinusoidal modulation $\epsilon(t) = \epsilon_0 \sin(\omega_{\text{mod}} t)$ with angular frequency ω_{mod} for arbitrary durations τ. We can use time-dependent perturbation theory to calculate the transition probability from an initial state n to a final state q via

$$p_{q,n} = \frac{m^2\epsilon_0^2}{4\hbar^2}|\langle q|\hat{x}^2|n\rangle|^2 f_{|q-n|}(\omega_{\text{mod}}, \tau), \quad f_u(\omega_{\text{mod}}, \tau) = \left|\int_0^\tau \mathrm{d}t \sin(\omega_{\text{mod}} t) e^{iu\omega t}\right|^2, u > 0. \tag{4.13}$$

We defined the function $f_u(\omega_{\text{mod}}, \tau)$, which has a peak at $\omega_{\text{mod}} = u \times \omega$ and a width (resp. amplitude) that decreases (resp. increases) as the modulation time τ increases. The matrix elements of $\hat{x}^2$ are non-zero only if $q = n \pm 2$ or $q = n$, but the latter case is not relevant as it does not correspond to a state transition. In the former case, it evaluates to

$$|\langle n \pm 2|\hat{x}^2|n\rangle|^2 = \frac{\hbar^2}{4m^2\omega^2}(n + 1 \pm 1)(n \pm 1). \tag{4.14}$$

It is worth noting that $\hat{x}^2$ cannot couple eigenstates with different parity due symmetry, which means that transitions $n \to n \pm j$, where j is an odd positive integer, are forbidden even beyond the perturbation regime whereas higher order even transitions are possible. The averaged energy increment $\Delta E_{n,\text{curv}}$ due to these two transitions is given by

$$\Delta E_{n,\text{curv}} = 2\hbar\omega(p_{n+2,n} - p_{n-2,n}) \propto \epsilon_0^2(n + \frac{1}{2}) f_2(\omega_{\text{mod}}) > 0. \tag{4.15}$$

Because this quantity is positive, it means that there is a macroscopic heating which can be calculated by weighting the energy increments $\Delta E_{n,\text{curv}}$ by the corresponding populations in states n [189, 191]. This straightforward calculation demonstrates that scanning the modulation frequency ω_{mod} gives rise to a resonance signal located at twice the underlying trapping frequency 2ω, and thus allows one to extract ω using spectroscopy.

Position modulation We redefine the single-particle hamiltonian to describe a perturbation of the position of the oscillator, instead of the curvature, as

$$\widehat{H}_{\text{pos}} = \frac{\hat{p}^2}{2m} + \frac{1}{2}m\omega^2(\hat{x} - \epsilon(t))^2. \tag{4.16}$$

[5] see Eq. (5.53).

By expanding the last term, we see that the perturbation couples to the position operator $\hat{x}$ rather than its square. As a consequence, the contributing matrix elements are

$$|\langle n \pm 1|\hat{x}|n\rangle|^2 = \frac{\hbar}{2m\omega}\left(n + \frac{1}{2} \pm \frac{1}{2}\right), \tag{4.17}$$

which leads to the energy increment

$$\Delta E_{n,\mathrm{pos}} \propto \epsilon_0^2 f_1(\omega_{\mathrm{mod}}) > 0. \tag{4.18}$$

In the previous case, we obtained Eq. (4.15) which was dependent on n, indicating that the more energy is present in the system, the higher the associated heating rate. This positive feedback loop leads to an exponential increase of the heating rate over time. In this case, we still have $\Delta E_{n,\mathrm{pos}} > 0$ but it is independent of n, producing a constant heating heating rate on the macroscopic level. Due to the symmetry of $\hat{x}$ it is proportional to $f_1(\omega_{\mathrm{mod}})$, implying a resonant response at $\omega_{\mathrm{mod}} = \omega$. Beyond the perturbative regime, only transitions between states with opposite parities can be excited.

Modulation spectroscopy of the optical lattice Both perturbations Eqs. (4.12) and (4.16) can be realized in the tube traps by modulating the intensity and the relative phase of the lattice beam pairs, respectively. This can be realized by ramping the set point of the corresponding regulation system, which works well as long the modulation frequency does not exceed the bandwidth of the feedback loop. For the intensity modulation we have a bandwidth of 100 kHz, whereas for the phase modulation we use the regulation setup described in section 3.2.4, which is limited to bandwidths of $\sim$ 20 kHz. A typical measurement using both techniques is shown in figure 4.4. An atomic cloud loaded in a single-layer of the two-dimensional lattice was subjected to intensity or phase modulation with varying frequencies. The in-trap cloud size σ_z along the vertical direction was measured using a Gaussian fit after applying the modulation, and compared to its value in absence of modulation $\sigma_{z,0}$. Since the energy is pumped into the transverse direction, $\sigma_{z,0}$ is a good metric only if the energy is redistributed in the longitudinal direction. In the case of intensity modulation, it is straightforward as energy is explicitly pumped in the degrees of freedom that describe the relative motions between particles, which explicitly couples to two-body interactions. For the phase modulation, only the center of mass degree of freedom is pumped, and it does not couple to anything, even in the presence of interactions due to Kohn's theorem [192] in a perfectly harmonic trap [193]. However, due to the finite trap depth in the transverse direction, anharmonicities will allow coupling to the longitudinal direction when the amplitude of the transverse motion gets large enough. Using the y imaging direction (see sec. 3.2.6), the various tube traps can be analysed individually. We observed no significant differences between them for neither ω_x nor ω_y,

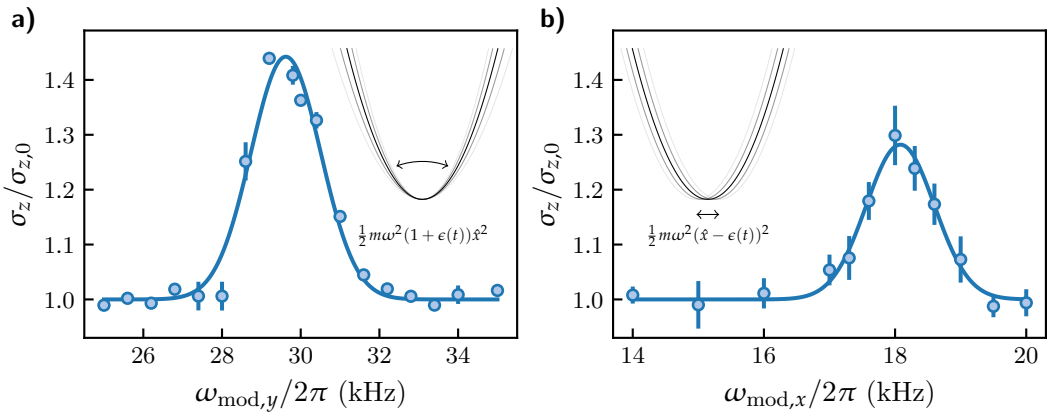

Figure 4.4: Driving heating in the optical lattice. a) Intensity modulation of the X lattice, using a mean power of 2.3 W per beam. The signal is empirically fitted by a Gaussian whose position and gives $\omega_x = 2\pi \times 14.8 \pm 0.1$ kHz. b) Phase modulation along y, using a mean power of 3.3 W per beam. The measurement yields $\omega_y = 2\pi \times 18.1 \pm 0.1$.

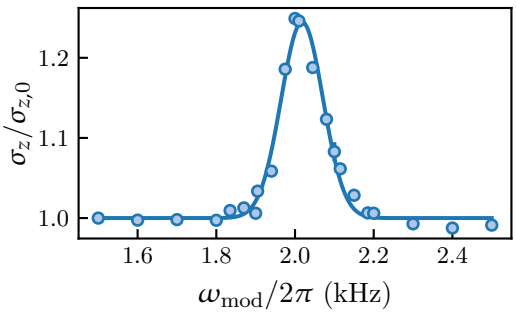

Figure 4.5: Curvature measurement of the compression beam. The angular trapping frequency is determined through parametric heating induced by intensity modulation. In this example the optical power is 0.83W, and the fit to the data yields $\omega_y = 2\pi \times 1.0 \pm 0.02$ kHz.

which is consistent with the model presented in section 4.2.

By measuring the X and Y trapping frequencies for different powers[6] of the four beams, it is possible to equalize them during experimental cycles by virtue of the resulting calibration curve[7]. For instance, setting $\omega_x = \omega_y = 2\pi \times 17.0$ kHz corresponds to the lattice beam powers $P_{\mathrm{latt},X1} = 3.28 \pm 0.02$ W, $P_{\mathrm{latt},X2} = 3.09 \pm 0.02$ W, $P_{\mathrm{latt},Y1} = 3.24 \pm 0.01$ W and $P_{\mathrm{latt},Y2} = 2.98 \pm 0.01$. These values need to be corrected to account for Fresnel reflection which creates ∼4% losses per surface of the uncoated glass cell. This results in an average power of 2.93W per beam, which was the value used for the model in figure 4.3 and underlines the consistency of the predictions it makes for $\omega_\perp$.

Modulation of the green compression beam Even though the compression beam does not contribute to the final potential, we make a brief digression here to mention that its curvature can also be estimated with parametric heating. While a modulation of the beam

[6] The powers are measured using a power sensor above the science cell.

[7] We use the model $\omega_i = K_i\sqrt{\overline{P}_i}$, with $i = x, y$, where $\overline{P}_i$ is the mean power in the optical beams pair i, and K_i is a fitted coefficient.

pointing cannot be realized due to technical limitations, the perturbation from Eq. (4.12) can be generated via intensity modulation. The lattice beams are not used during this measurement so that the green compression beam dominates the potential along y.
Using the waists measured in figure 3.11 and Eq. (2.1), we can calculate the expected curvature created by this potential as a function of the optical power. Using $\mathrm{erfi}(y) = (2/\sqrt{\pi})y + \mathcal{O}(y^3)$, we can expand Eq. (3.11) around $y = 0$ at $z = 0$ and define the angular trapping frequency associated with the corresponding approximate harmonic oscillator as

$$\frac{1}{2}m\omega_y^2 y^2 = \frac{8\alpha_{\mathrm{pol}}P}{\pi^2 w_y^3 w_z}y^2. \tag{4.19}$$

For $P = 0.83$W, this equation predicts $\omega_y \approx 2\pi \times (1.16 \pm 0.01)$ kHz. The measured value, shown in figure 4.5, is slightly lower[8].

4.4 Calibration of the longitudinal curvature

Besides trap modulation techniques shown in the previous section, another popular technique to calibrate the curvature of a harmonic potential consists in inducing center of mass oscillations and measuring their frequency, which usually yields a better accuracy provided the atomic motion can be resolved. It is a robust technique since, according to Kohn's theorem [192] applied to harmonic potentials [193], the dipole mode has the unique property that its frequency is equal to the trap frequency, irrespective of the interaction between the atoms. If the trapping potential is not perfectly harmonic, this can still work provided the size of the cloud and the amplitude of oscillations around the minimum are such that atoms do not explore the anharmonic parts. In experiments where the external confinement is provided by magnetic curvature, the harmonicity of the trap extends over a large range because the spacing between the coils is much larger than the scale of the atomic cloud. If the external confinement is generated by a laser beam, one has to compare the beam size with the spatial extent of the cloud. In our setup, we are able to induce harmonic oscillations along z when the atoms are loaded in the crossed dipole trap in a 3D geometry, as shown in figure 4.6. However, when the cloud is contained in the optical lattice, it is very elongated along the z direction and extends far into anharmonic region close to the spilling point of the trap. In order to avoid relying in the harmonicity of the potential, we developed a method to extract the longitudinal curvature from *in-situ* absorption images of atoms loaded in the tube traps. This is achieved by measuring the displacement of the minimum position of the potential in the presence of a well calibrated additional linear term. This approach also works when the atoms explores anharmonic

[8] A partial explanation to this discrepancy could be the underestimation of the magnification at $\lambda = 532$ nm of the imaging system used to image the green beam (see fig. 3.11), since it was determined by imaging free-falling atoms with $\lambda = 767$ nm light.

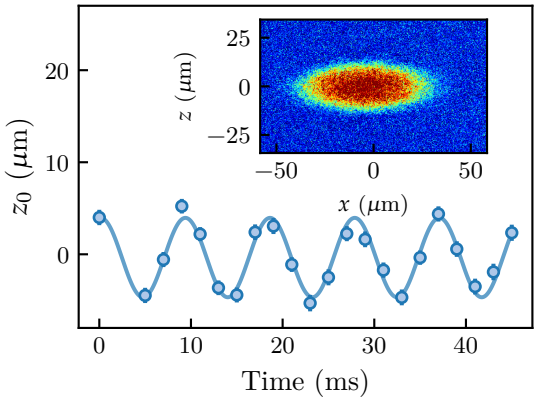

Figure 4.6: Oscillations in a harmonic potential. The cloud, initially shifted from its equilibrium position using a magnetic gradient, is suddenly released at $t = 0$. We observe clear harmonic oscillations in the dipole trap, from which the trapping frequency is readily extracted using a sinusoidal fit.

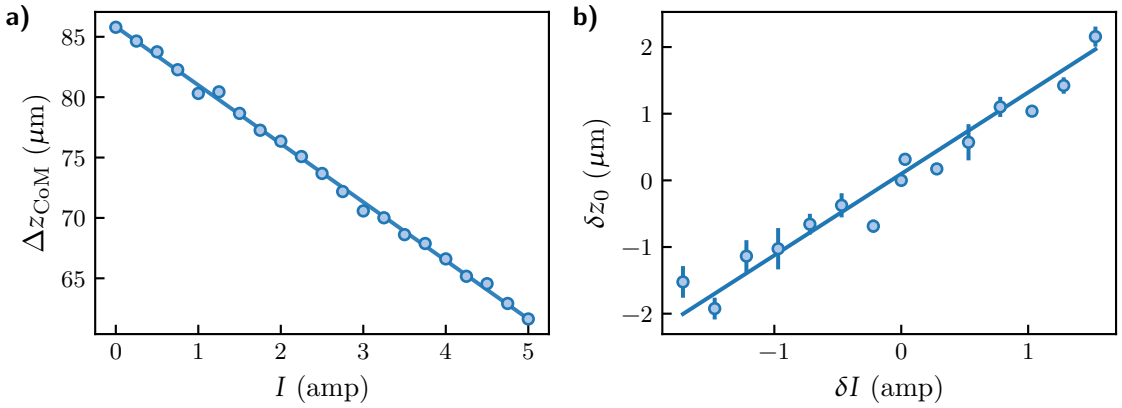

Figure 4.7: Calibration method of the axial curvature. a) Change of center of mass position after expansion as a function of the gradient current I. The slope of the linear fit allows us to infer $a_I = 0.605 \pm 0.002$ μm·ms^{-2}·amp^{-1} . b) Shift of the minimum position of $V_{\parallel,\mathrm{grad}}$ as a function of the gradient current offset δI. For this set, we measure $\omega_{\parallel} = 113.1 \pm 2.4$ Hz using Eq (4.26).

regions of the potential.

In order to generate such a linear term in the potential energy, we add a magnetic field gradient $\vec{B}_{\mathrm{grad}} = bz\vec{u}_z$ on top of the usual homogeneous bias field. The total potential is modified accordingly as

$$V_{\parallel,\mathrm{grad}}(z) = V_{\parallel}(z) - m_F g_F \mu_0 bz. \tag{4.20}$$

The new linear term corresponds to the local Zeeman shift, where we assumed a particle in the hyperfine state $|F, m_F\rangle$. The constant g_F represents the Landé factor and μ_B is the Bohr Magneton. The magnetic gradient is produced by running a current I through a nearby pair of coils in anti-Helmholtz configuration. Because the magnetic field is proportional to the current, it is much more convenient to write the energy as

$$V_{\parallel,\mathrm{grad}}(z) = V_{\parallel}(z) - ma_I \Delta I z, \tag{4.21}$$

where $\Delta I = I - I_{\text{comp}}$ is the current shift. I_{comp} is the value of current that compensates the unintentional gradient produced by the other coils that create the bias field[9] (see fig. 2.2). The coefficient of a_I is an acceleration per unit of current and can be calibrated empirically. Indeed, if we assume that all the laser beams are switched off at $t = 0$, the equation of motion for the center of mass of the atomic cloud takes on the simple form

$$\Delta z_{\text{CoM}}(t) = z_{\text{CoM}}(t) - z_{\text{CoM}}(t=0) = \frac{1}{2}(g - a_I \Delta I)t^2, \quad t \geq 0. \tag{4.22}$$

By measuring Δz_{CoM} after a constant time of flight t_{ToF} as a function of the current I, one can deduce a_I by fitting the slope $-a_I t_{\text{ToF}}^2/2$, as shown in figure 4.7 a). Once a_I is calibrated, one can return to the situation where the laser beams are turned on.

The minimum position $z = z_0$ of the potential $V_{\parallel,\text{grad}}(z)$ is found when its derivative with respect to z vanishes, which yields

$$\left.\frac{\mathrm{d}V_\parallel(z)}{\mathrm{d}z}\right|_{z=z_0} - m a_I \Delta I = 0. \tag{4.23}$$

Formally, this means that z_0 is a function of the current I. Eq (4.23) can be written in the form $F(I, z_0) = 0$. We can use implicit differentiation to get

$$\frac{\mathrm{d}z_0}{\mathrm{d}I} = -\frac{\partial F}{\partial I}\left(\frac{\partial F}{\partial z_0}\right)^{-1} = m a_I \left(\left.\frac{\mathrm{d}^2 V_\parallel(z)}{\mathrm{d}z^2}\right|_{z=z_0}\right)^{-1}. \tag{4.24}$$

If we measure the infinitesimal shift δz_0 of the minimum position of $V_{\parallel,\text{grad}}(z)$ due to an infinitesimal current change δI around the position $z = z_0$, then we can deduce curvature of $V_\parallel(z)$ at $z = z_0$. To make this clearer, we Taylor expand $V_\parallel(z)$ around $z = z_0$,

$$V_\parallel(z) = V_\parallel(z_0) + (z - z_0)\left.\frac{\mathrm{d}V_\parallel(z)}{\mathrm{d}z}\right|_{z=z_0} + \frac{(z-z_0)^2}{2}\left.\frac{\mathrm{d}^2 V_\parallel(z)}{\mathrm{d}z^2}\right|_{z=z_0} + \frac{(z-z_0)^3}{6}\left.\frac{\mathrm{d}^3 V_\parallel(z)}{\mathrm{d}z^3}\right|_{z=z_0} + \ldots$$

Taking $z_0 = z_{0,\text{comp}}$, where $z_{0,\text{comp}}$ is the minimum of the gradient-free potential $V_\parallel(z)$, the first two terms are zero, and we have

$$V_\parallel(z) = \frac{1}{2} m \omega_\parallel^2 (z - z_0)^2 + V_{\parallel,\text{anharmonic}}(z). \tag{4.25}$$

[9] The inner coils operate in Helmholtz configuration to create a bias field, which also inevitably creates a small curvature at the magnetic center. Further away from the center, this curvature turns into a local gradient. This unintentional gradient we have to compensate thus originates from a mismatch between the position of the atomic cloud and the position of the magnetic center.

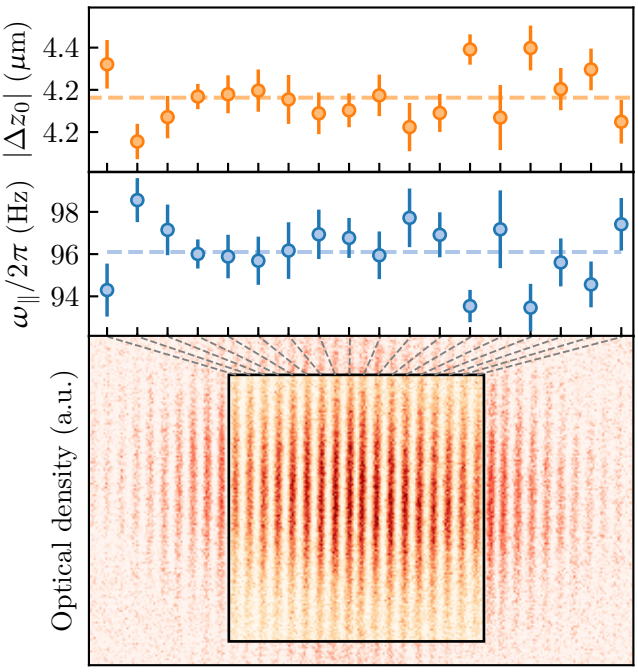

Figure 4.8: Tube resolved measurement of axial trapping frequencies. For each of the 18 selected tubes, we show the induced center-of-mass shift in orange, and the corresponding measured trapping frequency term in blue. This measurement results from averaging 71 pairs of images following the procedure described in the main text. We observe identical curvatures for the different tube traps up to the statistical noise of the measurement, which is larger than the variations predicted by the model in figure 4.2 for $i \leq 9$. For this configuration, the mean axial frequency is 96.10 Hz and the standard deviation across the tube traps is 1.4 Hz.

We can thus compute $\omega_\parallel$, provided δz_0 is small enough, as

$$\omega_\parallel \approx \sqrt{\frac{\delta I}{a_I \delta z_0}}. \tag{4.26}$$

The approximation symbol stems from the fact that $\delta z_0/\delta I$ is not rigorously equal to the derivative $\mathrm{d}z_0/\mathrm{d}I$. However, in the hypothetical case where $V_\parallel(z)$ is purely harmonic, the right-hand-side of Eq. (4.24) becomes independent of z_0 and the approximate relation (4.26) would be exact for any finite shift. As a consequence, this restricts the measurement to small shifts δz_0 such that $V_{\parallel,\mathrm{anharmonic}}(z_{0,\mathrm{comp}} + \delta z_0)$ is small. The main advantage of this method is that the produced shifts can be made much smaller than the cloud size to exclusively probe the harmonic region even if the former extends into the anharmonic one. Empirically we expect to see a linear relation in the harmonic region between δz_0 and δI, which coincides with our observation shown in figure 4.7 b).
We can therefore define the following protocol to measure the axial curvature around the minimum[10] of the gradient-free potential $V_\parallel$ of the tube traps:

- We take several absorption images of atoms loaded in the optical trap, alternating between shots with gradient current $I_+ = I_{\mathrm{comp}} + \Delta I$ and $I_- = I_{\mathrm{comp}} - \Delta I$.
- For each pair of images, we measure the position difference $\Delta z = (z_0(I_+) -$

[10] It is in principle also possible to measure the curvature away from the minimum by making small current shifts centered around a value I_{comp}.

$z_0(I_-))/2$, where Δz denotes the typical displacement from the minimum $z_{0,\mathrm{comp}}$ of the gradient-free calibrated potential $V_\parallel(z)$. For each absorption image, the minimum position corresponds to the maximum of atomic density, extracted from a Gaussian fit[11].

- We calculate $\omega_\parallel = \sqrt{\Delta I/(a_I \overline{\Delta z})}$ for each tube trap with a_I being the calibrated acceleration per unit of current and $\overline{\Delta z}$ is obtained by averaging over all of the displacements obtained from each pair of images. This way, the average displacement is robust against long term drift of the minimum of the trap due to beam pointing. The error on $\omega_\parallel$ is estimated using the standard deviation from of the Δz sets.

A realization of this measurement is shown in figure 4.8. Up to statistical noise, we observe no differences in $\omega_\parallel$ across the various tube traps. As a consequence, we will be using the mean value of $\omega_\parallel$ across 18 tube traps to describe the axial curvature of each tube trap. This measurement experimentally confirms the similarities between the micro-traps. In the following chapters we will always consider the external potential to be identical in the central micro-traps considered above, and exclusively analyse those in the following site-resolved experiments.

[11] Despite the obvious asymmetry in the measured density profiles which leads to a systematic error in the estimation of the absolute position of the maximum $z_0(I_\pm)$ from fitting density profiles with a Gaussian ansatz, this method was found to give a reliable result for measuring the shift $z_0(I_+) - z_0(I_-)$ by relying on systematic error compensation.

Chapter 5

In-situ thermometry of noninteracting Fermi gases in quantum wires

In chapter 3, we detailed the experimental techniques required to load the atomic ensemble in a single layer of a two-dimensional large-spacing lattice, and resolve its sites individually. Then, in chapter 4, we showed that it is a good approximation to assume identical external potentials along the central lattice sites. Building on that, we measured the curvature of this common potential in both the transverse and longitudinal directions, even though it is an incomplete description in the latter case. Moreover, by employing appropriate calibration methods we made sure that the density can be accurately determined from absorption imaging performed beyond the low saturation regime. The next step required to fully characterize the state of our system is to measure its temperature.

In this chapter, we will consider the thermodynamics of an ideal gas of fermions in one dimension (1D), and generalize the results to include higher transverse modes. The

obtained equation of state will allow us to perform *in-situ* thermometry and to reconstruct the longitudinal potential beyond the harmonic expression, which will be useful for the measurements described in chapter 7. Finally, relying on these methods and techniques, we will report on the observation of quantum degenerate one-dimensional Fermi gases.

5.1 Thermodynamics of the homogeneous ideal Fermi gas in one dimension

We perform a step by step derivation of the equation of state of a noninteracting Fermi gas in one dimension. But before that, we briefly introduce general thermodynamics relations in the grand canonical ensemble.

5.1.1 Grand canonical ensemble

The combination of the first and second laws of thermodynamics allow us to relate the change of internal energy of the gas to the changes of entropy S, atom number N and chain length L,

$$\mathrm{d}E = T\mathrm{d}S + \mu\mathrm{d}N - P\mathrm{d}L, \tag{5.1}$$

where T is the temperature, μ the chemical potential, and P the generalized pressure[1]. They can all be expressed as a partial derivative of the energy,

$$T = \left.\frac{\partial E}{\partial S}\right|_{N,L}, \qquad \mu = \left.\frac{\partial E}{\partial N}\right|_{S,L}, \qquad P = -\left.\frac{\partial E}{\partial L}\right|_{S,N}. \tag{5.2}$$

In this formulation, the variables on the right-hand side are entropy, atom number and chain length. Experimentally, it is more convenient to think of the temperature and chemical potential as the most relevant variables, and therefore we often introduce the grand canonical potential

$$\Omega(T, \mu, L) = E - TS - \mu N. \tag{5.3}$$

Using Eq. (5.1), we can express its total differential,

$$\mathrm{d}\Omega = -S\mathrm{d}T - N\mathrm{d}\mu - P\mathrm{d}L. \tag{5.4}$$

[1] In 3D, the conjugate variable of the volume is indeed homogeneous to a pressure, however it is homogeneous to a surface tension in 2D, and a force in 1D. Despite that, we will call it pressure as it is often done in the literature [194, 195].

This indicates that can we can express the entropy, atom number and pressure as partial derivatives of the grand potential

$$S = -\left.\frac{\partial\Omega}{\partial T}\right|_{\mu,L}, \qquad N = -\left.\frac{\partial\Omega}{\partial\mu}\right|_{T,L}, \qquad P = -\left.\frac{\partial\Omega}{\partial L}\right|_{T,\mu}. \tag{5.5}$$

The chain length L plays a special role since it is the only extensive variable Ω depends on. Since Ω is also extensive, the scaling relation $\Omega(T,\mu,cL) = c\Omega(T,\mu,L)$ must hold for any scaling factor c. Therefore

$$\frac{\Omega(T,\mu,L+\delta L)-\Omega(T,\mu,L)}{(L+\delta L)-L} = \frac{\delta L}{L}\frac{\Omega(T,\mu,L)}{\delta L} = \frac{\Omega(T,\mu,L)}{L}, \tag{5.6}$$

for any δL. If we consider the limit $\delta L \to 0$, we identify the starting expression of (5.6) as a partial derivative of Ω with respect to L at constant T and μ. In combination with (5.5), we obtain

$$P = -\left.\frac{\partial\Omega}{\partial L}\right|_{T,\mu} = -\frac{\Omega}{L}. \tag{5.7}$$

Inserting this new identity into the definition of the grand potential (5.3) yields

$$E = TS + \mu N - PL. \tag{5.8}$$

The total differential of this expression, together with the thermodynamic identity (5.1) gives the famous Gibbs-Duhem equation,

$$S\mathrm{d}T + N\mathrm{d}\mu - L\mathrm{d}P = 0, \tag{5.9}$$

which provides even more relations between the state variables. For instance,

$$\left.\frac{\partial\mu}{\partial P}\right|_{T,P} = -\frac{L}{N} = -\frac{1}{n_{1D}}. \tag{5.10}$$

5.1.2 Single particle states

To begin with, we consider a single particle on a line of length L with periodic boundary conditions. The Hamiltonian is simply given by the kinetic energy,

$$\hat{\mathcal{H}}_{\mathrm{sp,1D}} = \frac{\hat{p}_z^2}{2m}, \qquad \hat{p}_z = -i\hbar\frac{\partial}{\partial z}. \tag{5.11}$$

The Schrödinger equation leads to the following differential equation

$$-\frac{\hbar^2}{2m}\frac{\partial^2\psi}{\partial z^2} = E\psi. \tag{5.12}$$

Using $E = \hbar^2 k^2/2m$, we find the following normalized plane wave solutions $\psi(z) = e^{ikz}/\sqrt{L}$. The wavefunction $\psi(z)$ satisfies the boundary conditions $\psi(z = -L/2) = \psi(z = L/2)$ which restricts k to a discrete set of values

$$e^{ikL} = 1 \Leftrightarrow k_p = p\frac{2\pi}{L},\ p \in \mathbb{Z}. \tag{5.13}$$

We notice that the spacing between two k-states is constant and given by $\Delta k = k_{p+1} - k_p = \frac{2\pi}{L}, \forall p$. We write $|k_p\rangle$ the eigenstate associated with the quantum number p such that $\langle z\,|k_p\rangle = e^{ik_p z}/\sqrt{L}$.

5.1.3 Many-body Hamiltonian

We now extend the Hilbert space to include states that contain several particles. A state of system can be expressed in the Fock basis $\{|n_{z,0}, n_{z,1}, n_{z,-1}, ..., n_{z,p}, n_{z,-p}, ...\rangle\}$ where $n_{z,p}$ represents the number of particle in the single-particle state $|k_p\rangle$. Because we consider fermions, the Pauli exclusion principle applies and $n_{z,p}$ can only be equal to 0 or 1. We use the short notation $\{n_{z,p}\}$ to denote the set of possible values that the various $n_{z,p}$ can take. The Hamiltonian is given by

$$\hat{\mathcal{H}}_{\mathrm{mb,1D}} = \sum_{p=-\infty}^{+\infty} \frac{\hbar^2 k_p^2}{2m}\hat{n}_{z,p}, \tag{5.14}$$

where $\hat{n}_{z,p}$ is an operator that counts the number of particle occupying the single-particle state $|k_p\rangle$, such that $\hat{n}_{z,p}\,|..., n_{z,p}, ...\rangle = n_{z,p}\,|..., n_{z,p}, ...\rangle$. We also define the total atom number operator

$$\hat{\mathcal{N}}_{\mathrm{1D}} = \sum_{p=-\infty}^{+\infty} \hat{n}_{z,p}. \tag{5.15}$$

In the following, we will consider the thermodynamic limit, which has relevance when studying macroscopic systems made of a large number N of particles. It consists in letting $N, L \to +\infty$ at constant density $n_{1D} = N/L$. We will implement it by replacing sums over p by an integral according to the following rule

$$\sum_p ... \to \frac{L}{2\pi}\int \mathrm{d}k\, ... \tag{5.16}$$

5.1.4 The Fermi sea

Let us characterize the ground state of (5.14). If we consider a state that describes N particles, its energy is minimized by placing these particles into the single-particles states of lowest energy. Because of the Pauli exclusion principle, this is achieved by constructing

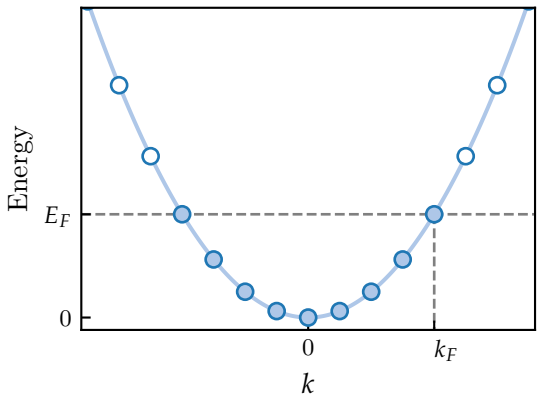

Figure 5.1: Fermi sea in a pure 1D system. Full and empty circles represent occupied and non-occupied states, respectively. By definition, the energy levels below the Fermi energy E_F are filled.

the following Fock state, also referred to as Fermi sea,

$$|\Psi_{GS}\rangle = |\underbrace{1,1,1,...,1,1}_{N},0,0,0,...\rangle\,. \tag{5.17}$$

The Fermi energy E_F corresponds to the highest occupied single-particle state energy, as shown in figure 5.1. It is associated to the Fermi wavevector k_F such that $E_F = \hbar^2 k_F^2/2m$ and the quantum number $p = p_F \geq 0$. It relates to the total atom number N by

$$N = \sum_{p=-\infty}^{+\infty} n_{z,p} = \sum_{p=-p_F}^{p_F} 1 = \frac{L}{2\pi}\int_{-k_F}^{k_F} \mathrm{d}k = \frac{Lk_F}{\pi}. \tag{5.18}$$

Introducing the density inside the homogeneous box as $n_{1D} = N/L$, we obtain the relations

$$k_F = \pi n_{1D} \qquad E_F = \frac{\hbar^2 k_F^2}{2m} = \frac{\hbar^2\pi^2}{2m}n_{1D}^2 = \frac{h^2 n_{1D}^2}{8m}. \tag{5.19}$$

The ground state energy is obtained by summing over the energies of each occupied single-particle state

$$E_{GS} = \langle\Psi_{GS}|\,\hat{\mathcal{H}}_{\mathrm{sp,1D}}\,|\Psi_{GS}\rangle = \sum_{p=-p_F}^{p_F}\frac{\hbar^2 k_p^2}{2m} = \frac{L}{2\pi}\int_{-k_F}^{k_F}\mathrm{d}k\frac{\hbar^2k^2}{2m} = \frac{Lk_F}{3\pi}E_F = \frac{1}{3}NE_F, \tag{5.20}$$

or equivalently, using (5.18),

$$E_{GS} = \frac{\pi^2\hbar^2}{6m}\frac{N^3}{L^2}. \tag{5.21}$$

5.1.5 Thermal states

The ground state described above is relevant to describe situations where the temperature T vanishes, and the system occupies the lowest energy state. However, as soon as the

temperature is increased, the relevant state to describe the system is a mixture of the ground state and excited states. Also, in the grand canonical ensemble, the number of atoms is a function of the chemical potential μ. The properties of thermal states are encapsulated in the grand canonical partition function Θ,

$$\Theta(T,\mu,L)_{1\mathrm{D}} = \mathrm{Tr}\left[\exp(-\beta(\hat{\mathcal{H}}_{\mathrm{mb,1D}} - \mu\hat{\mathcal{N}}_{1\mathrm{D}}))\right], \tag{5.22}$$

where we introduced $\beta = 1/k_B T$. $\mathrm{Tr}[...]$ denotes the trace operation. Since both $\hat{\mathcal{H}}_{\mathrm{mb,1D}}$ and $\hat{\mathcal{N}}_{1\mathrm{D}}$ are diagonal in the Fock state basis we can evaluate the trace as

$$\Theta_{1\mathrm{D}}(T,\mu,L) = \sum_{\{n_{z,p}\}} \left\langle \{n_{z,p}\} \left| \prod_{p'=-\infty}^{+\infty} \exp\left(-\beta \hat{n}_{z,p'}\left(\frac{\hbar^2 k_{p'}^2}{2m} - \mu\right)\right) \right| \{n_{z,p}\} \right\rangle \tag{5.23}$$

$$= \sum_{\{n_{z,p}\}} \prod_{p'=-\infty}^{+\infty} \exp\left(-\beta n_{z,p'}\left(\frac{\hbar^2 k_{p'}^2}{2m} - \mu\right)\right). \tag{5.24}$$

The sum on all sets of $n_{z,p}$ can be decomposed into several sums

$$\sum_{\{n_{z,p}\}} = \sum_{n_{z,0}=0,1} \sum_{n_{z,1}=0,1} \sum_{n_{z,-1}=0,1} \sum_{n_{z,2}=0,1} \sum_{n_{z,-2}=0,1} \dots, \tag{5.25}$$

and for each of the sums in the right-hand side, there is only one term of the product that depends on the sum index. This means that we can refactorize all the other terms after performing each sum, and we obtain

$$\Theta_{1\mathrm{D}}(T,\mu,L) = \prod_{p=-\infty}^{+\infty} \left[1 + Z\exp\left(-\beta\frac{\hbar^2 k_p^2}{2m}\right)\right], \tag{5.26}$$

where we introduced the fugacity $Z = \exp(\beta\mu)$. The grand potential Ω introduced in (5.3) can be calculated from the grand partition function using

$$\Omega(T,\mu,L) = -\frac{1}{\beta}\ln(\Theta_{1\mathrm{D}}(T,\mu,L)) \tag{5.27}$$

$$= -\frac{1}{\beta}\sum_{p=-\infty}^{+\infty} \ln\left[1 + Z\exp\left(-\beta\frac{\hbar^2 k_p^2}{2m}\right)\right] \tag{5.28}$$

$$= -\frac{1}{\beta}\frac{L}{\pi}\int_0^{+\infty} \mathrm{d}k \ln\left[1 + Z\exp\left(-\beta\frac{\hbar^2 k^2}{2m}\right)\right] \tag{5.29}$$

$$= \frac{L}{\beta\lambda_{\mathrm{th}}}\mathrm{Li}_{3/2}(-Z), \tag{5.30}$$

where, in order to obtain the last equality, we performed the change of variable $x = \sqrt{\beta/2m}\hbar k$, we introduced the thermal wavelength $\lambda_{\text{th}} = \sqrt{2\pi\beta\hbar^2/m}$, and we calculated the resulting integral[2]. The function $\text{Li}_n(Z) = \sum_{p=1}^{+\infty} \frac{Z^p}{p^n}$ is the polylogarithm of order n [196]. Since this series has a radius of convergence of 1, it is defined via analytical continuation when $Z \geq 1$. In fermionic systems, it is more natural to define the function $f_n(Z) = -\text{Li}_n(-Z)$ as it is more directly related to integrals of the Fermi-Dirac which appears in the expression of many observables. Indeed, it can be shown that

$$f_n(Z) = \frac{1}{\Gamma(n)} \int_0^{+\infty} \mathrm{d}t \frac{t^{n-1}}{e^t/Z + 1}, \tag{5.31}$$

where $\Gamma(n)$ is the gamma function. The following properties of the function $f_n(Z)$ will be useful in several derivations,

$$\frac{\mathrm{d}f_n(e^u)}{\mathrm{d}u} = f_{n-1}(e^u) \qquad \lim_{|Z|\to 0} \frac{f_n(Z)}{Z} = 1 \qquad \lim_{u\to+\infty} f_n(e^u) = \frac{u^n}{\Gamma(n+1)} \qquad u, Z, n \in \mathbb{R}, \tag{5.32}$$

the last property holds only if $n \neq -1, -2, -3, \ldots$. Using these definitions, the grand potential has the simple expression,

$$\Omega(T, \mu, L) = -\frac{L}{\beta\lambda_{\text{th}}} f_{3/2}(Z), \tag{5.33}$$

from which we can derive thermodynamics observables. By differentiating with respect to chemical potential, we obtain the mean atom number as

$$N = -\left.\frac{\partial\Omega}{\partial\mu}\right|_{T,L} = \frac{L}{\beta\lambda_{\text{th}}} \left.\frac{\partial f_{3/2}(e^{\beta\mu})}{\partial\mu}\right|_{T,L} = \frac{L}{\lambda_{\text{th}}} f_{1/2}(e^{\beta\mu}) = \frac{L}{\lambda_{\text{th}}} f_{1/2}(Z), \tag{5.34}$$

[2]Some elements on the derivation of the integral, ignoring details on convergence properties:

$$\begin{aligned}
I &= \frac{2}{\sqrt{\pi}} \int_0^{+\infty} \mathrm{d}x \ln\left(1 + Z\exp(-x^2)\right) \\
&= -\frac{2}{\sqrt{\pi}} \sum_{n=1}^{+\infty} \int_0^{+\infty} \mathrm{d}x \frac{(-Z)^n \exp(-sx^2)}{n} && \left(\ln(1+Z) = -\sum_{n=1}^{+\infty} \frac{(-Z)^n}{n}, Z \in \mathbb{R}, \text{ and exchanging sum and integral}\right) \\
&= -\sum_{n=1}^{+\infty} \frac{(-Z)^n}{n^{3/2}} && \left(\int_0^{+\infty} \mathrm{d}x \exp(-sx^2) = \frac{\sqrt{\pi}}{2\sqrt{s}},\ s > 0\right) \\
&= -\text{Li}_{3/2}(-Z)
\end{aligned}$$

and the corresponding density,

$$n_{1D} = \frac{N}{L} = \frac{1}{\lambda_{\text{th}}} f_{1/2}(Z). \tag{5.35}$$

To quantify the degeneracy we often define the phase-space density PSD $= n_{1D}\lambda_{\text{th}} = f_{1/2}(Z)$. The degenerate regime corresponds to $PSD \gg 1$. Alternatively, one can use the Fermi temperature $T_F = E_F/k_B$, with E_F defined by Eq (5.19). From Eq (5.35), we get an expression for normalized temperature,

$$\frac{T}{T_F} = \frac{1}{\beta E_F} = \frac{8m}{\beta h^2 n_{1D}^2} = \frac{8m\lambda_{\text{th}}^2}{\beta h^2 f_{1/2}(Z)^2} = \frac{4}{\pi}(f_{1/2}(Z))^{-2}, \tag{5.36}$$

from which we deduce immediately the normalized chemical potential,

$$\frac{\mu}{E_F} = \beta\mu\frac{T}{T_F} = \frac{4}{\pi}\ln(Z)(f_{1/2}(Z))^{-2}. \tag{5.37}$$

Using Eq (5.32), one sees that $\lim_{Z\to+\infty} \mu/E_F = \frac{4}{\pi}\Gamma(3/2)^2 = 1$, showing that the chemical potential is equal to the Fermi energy $\mu = E_F$ when $T = 0$. This is expected since the Fermi energy is by definition the highest filled level in the ground state and therefore coincides with the energy cost of adding another particle in the ground state. Next, we can calculate the entropy S by differentiating the grand potential with respect to temperature at constant chain length L and chemical potential,

$$\begin{aligned} S = -\left.\frac{\partial\Omega}{\partial T}\right|_{L,\mu} &= \frac{3}{2}\frac{Lk_B}{\lambda_{\text{th}}} f_{3/2}(Z) + \frac{L}{\beta\lambda_{\text{th}}}\frac{\partial}{\partial Z}(f_{3/2}(Z))\left.\frac{\partial Z}{\partial T}\right|_{L,\mu} \\ &= \frac{Lk_B}{\lambda_{\text{th}}}\left(\frac{3}{2}f_{3/2}(Z) - \ln(Z)f_{1/2}(Z)\right), \end{aligned}$$

where we used $\beta\mu = \ln(Z)$ in the last equality. From (5.34) we obtain the normalized entropy per particle as

$$\frac{S}{Nk_B} = \frac{3}{2}\frac{f_{3/2}(Z)}{f_{1/2}(Z)} - \ln(Z). \tag{5.38}$$

It is straightforward to obtain the pressure from the grand potential using Eq (5.7),

$$P = \frac{1}{\beta\lambda_{\text{th}}} f_{3/2}(Z). \tag{5.39}$$

The energy-pressure relation can be established from the pressure identity in (5.2). In order to calculate the right hand side, we notice that dimensionless ratio E/E_{GS} has to be a constant at fixed N and S, which can be inferred by dimensional analysis. Therefore, we

get

$$P = -\left.\frac{\partial\left(\frac{E}{E_{GS}}E_{GS}\right)}{\partial L}\right|_{N,S} = -\frac{E}{E_{GS}}\left.\frac{\partial E_{GS}}{\partial L}\right|_{N,S} = 2\frac{E}{L}, \tag{5.40}$$

where we used (5.21) to evaluate $\left.\frac{\partial E_{GS}}{\partial L}\right|_{N,S} = -2E_{GS}/L$. We can use this relation to compute the pressure of the ground state

$$P_0 = P(T=0,\mu) = 2\frac{E(T=0,\mu)}{L} = 2\frac{E_{GS}}{L} = \frac{h^2}{12m}n_{1D}^3, \tag{5.41}$$

and combine equations (5.35), (5.39) and (5.41) to obtain the normalized pressure

$$\frac{P}{P_0} = \frac{12m\lambda_{\text{th}}^2}{\beta h^2}\frac{f_{3/2}(Z)}{(f_{1/2}(Z))^3} = \frac{6}{\pi}\frac{f_{3/2}(Z)}{(f_{1/2}(Z))^3}. \tag{5.42}$$

Finally, we calculate the isothermal compressibility κ from the standard definition

$$\kappa = -\frac{1}{L}\left.\frac{\partial L}{\partial P}\right|_{T,N} = \frac{1}{n_{1D}}\left.\frac{\partial n_{1D}}{\partial P}\right|_{T,N} = \frac{1}{n_{1D}}\left(\frac{\partial n_{1D}}{\partial \mu}\frac{\partial \mu}{\partial P}\right)_{T,N} = \frac{1}{n_{1D}^2}\left.\frac{\partial n_{1D}}{\partial \mu}\right|_{T,N}, \tag{5.43}$$

where we used $L = N/n_{1D}$ for the second equality, (5.10) for the fourth equality. Using (5.35) and (5.32), we get

$$\kappa = \frac{1}{n_{1D}^2}\frac{\beta}{\lambda_{\text{th}}}f_{-1/2}(Z) = \beta\lambda_{\text{th}}\frac{f_{-1/2}(Z)}{(f_{1/2}(Z))^2}. \tag{5.44}$$

We can normalize this quantity by the zero-temperature compressibility κ_0 at similar density, like we did for the pressure. We must compute

$$\kappa_0 = \kappa(T=0) = \frac{1}{n_{1D}^2}\left.\frac{\partial n_{1D}}{\partial \mu}\right|_{T=0,N} = \frac{1}{n_{1D}^2}\frac{\partial n_{1D}}{\partial E_F} = \frac{1}{n_{1D}^3}\frac{4m}{h^2}, \tag{5.45}$$

where we used (5.19) to calculate the derivative. Combining (5.35) and (5.44), we get the normalized compressibility,

$$\frac{\kappa}{\kappa_0} = \frac{\beta h^2}{4m}\frac{1}{\lambda_{\text{th}}^2}f_{-1/2}(Z)f_{1/2}(Z) = \frac{\pi}{2}f_{-1/2}(Z)f_{1/2}(Z) \tag{5.46}$$

We could keep on calculating others thermodynamics quantities, but the ones presented here are sufficient for the scope of this work.

5.1.6 Comparison with 2D and 3D

In the previous sections, we focused on one-dimensional ideal gases. However, these quantities are easily calculated in 2D and 3D[3]. We dress a comparison between the observables considered in the previous section in 1D, 2D[4] and 3D in Table 5.1, and plot the normalized chemical potential, entropy per particle, pressure and compressibility in figure 5.2. Remarkably, the effect of dimensionality already matters on the noninteracting level. The one-dimensional gas is noticeably different compared to its higher-dimensional counterparts, for instance a local maximum exists in the universal curves μ/E_F and κ/κ_0 as a function of T/T_F only in 1D. Nonetheless, the role of dimensionality at the noninteracting level might be better illustrated in Bose gases, where a thermal phase transition toward a BEC occurs at finite temperature only if the dimension is strictly larger than two [198].

5.2 Extension of the model to quasi-1D systems

So far we focused on describing noninteracting fermions in a pure 1D situation. However, in the world we live in, the closest we can get to a 1D situation is by applying a potential to create a strong compression along two transverse directions. The quasi-1D regime is reached when the quantized degree of freedom along these directions can no longer be excited. In practice, there are several ways one can introduce the corresponding transverse modes. For instance, one can treat the transverse direction as infinite squares wells with a very small spatial extension. Another simple way is to use a tight transverse harmonic potential. As discussed in section 3.1.1, this later option is the relevant one given our experimental context.

5.2.1 Many-body ground state

We now consider 3D particles. We keep on considering that the z-direction is homogeneous and possesses a finite length L, and we keep on using periodic boundary conditions on this direction. From now on, we assume the existence of an isotropic potential in the (x, y) plane[5]. such that

$$V_\perp(x, y) = \frac{1}{2} m\omega_\perp^2 (x^2 + y^2) \tag{5.47}$$

[3]For noninteracting gases, they can be calculated in arbitrary dimension, and for arbitrary statistics [197].

[4]In 2D, the polylogarithms that appear in the expressions happen to have integer order. For integer orders smaller or equal to 1, the polylogarithms can be expressed in terms of elementary functions. In particular, the two functions below appear in the table and have simple expressions

$$f_1(Z) = -\mathrm{Li}_1(-Z) = \log(1+Z), \qquad f_0(Z) = -\mathrm{Li}_0(-Z) = \frac{Z}{1+Z}.$$

[5]It is also convenient sometimes to use polar coordinates (ρ, θ) and exploit that the fact $V_\perp(\rho, \theta, z) = \frac{1}{2} m\omega_\perp^2 \rho^2$, since the problem is invariant under rotation of angle θ around the z-axis [199], see for instance sec. 7.1.1.

Observable	1D	2D	3D
E_F	$\frac{\hbar^2\pi^2 n_{1D}^2}{2m}$	$\frac{2\pi\hbar^2 n_{2D}}{m}$	$\frac{\hbar^2(6\pi^2 n_{3D})^{\frac{2}{3}}}{2m}$
PSD	$f_{1/2}(Z)$	$f_1(Z)$	$f_{3/2}(Z)$
$\frac{T}{T_F}$	$\frac{4}{\pi}\frac{1}{(f_{1/2}(Z))^2}$	$\frac{1}{f_1(Z)}$	$\frac{4\pi}{(6\pi^2 f_{3/2}(Z))^{\frac{2}{3}}}$
$\frac{\mu}{E_F}$	$\frac{4}{\pi}\frac{\ln(Z)}{(f_{1/2}(Z))^2}$	$\frac{\ln(Z)}{f_1(Z)}$	$\frac{4\pi\ln(Z)}{(6\pi^2 f_{3/2}(Z))^{\frac{2}{3}}}$
$\frac{S}{Nk_B}$	$\frac{3}{2}\frac{f_{3/2}(Z)}{f_{1/2}(Z)} - \ln(Z)$	$2\frac{f_2(Z)}{f_1(Z)} - \ln(Z)$	$\frac{5}{2}\frac{f_{5/2}(Z)}{f_{3/2}(Z)} - \ln(Z)$
$\frac{P}{P_0}$	$\frac{6}{\pi}\frac{f_{3/2}(Z)}{(f_{1/2}(Z))^3}$	$\frac{2f_2(Z)}{(f_1(Z))^2}$	$\frac{60\pi^3}{(6\pi^2)^{5/3}}\frac{f_{5/2}(Z)}{(f_{3/2}(Z))^{\frac{5}{3}}}$
$\frac{\kappa}{\kappa_0}$	$\frac{\pi}{2}f_{-1/2}(Z)f_{1/2}(Z)$	$f_0(Z)$	$\frac{(6\pi^2)^{2/3}}{6\pi}\frac{f_{1/2}(Z)}{(f_{3/2}(Z))^{\frac{1}{3}}}$

Table 5.1: Noninteracting thermodynamics in 1D, 2D and 3D. Expression of various thermodynamics quantities of homogeneous ideal gases in 1D, 2D and 3D. The PSD is defined as $n_{1D}\lambda_{\text{th}}$, $n_{2D}\lambda_{\text{th}}^2$ and $n_{3D}\lambda_{\text{th}}^3$ in 1D, 2D and 3D respectively, and densities correspond to a single state densities.

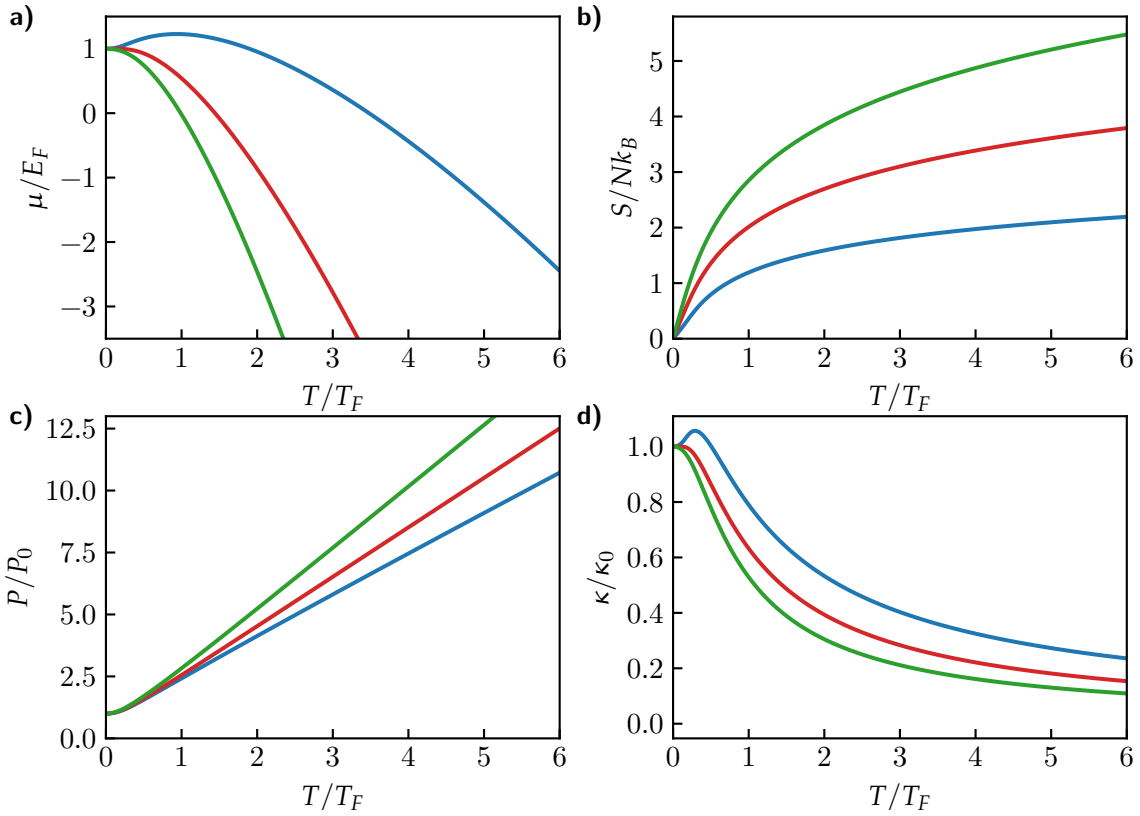

Figure 5.2: Homogeneous ideal gases in 1D, 2D and 3D. a) Evolution of the chemical potential normalized by the Fermi energy. As expected, we see that $\mu(T=0) = E_F$. b) Normalized entropy per particle, vanishing in the degenerate limit. c) Normalized pressure, reaching a finite value at $T = 0$, in contrast to the classical result which would vanish. d) Blue, red and green lines represent 1D, 2D and 3D homogeneous ideal gases respectively.

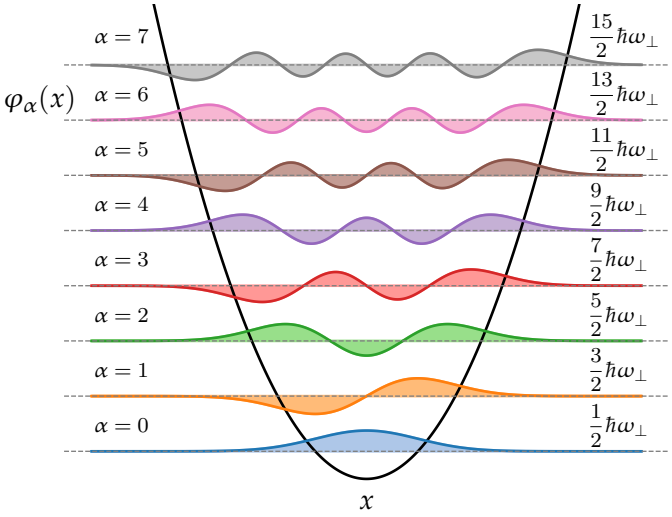

Figure 5.3: Wavefunctions of the harmonic oscillator. Representation of the wavefunctions of the harmonic oscillator from equation (5.53), together with their associated energy $\hbar\omega_\perp(1/2+\alpha)$. The black line represents the harmonic potential.

The single particle Hamiltonian from the previous section (5.11) is updated to take the transverse potential into account as well as the kinetic energies in the x and y directions

$$\hat{\mathcal{H}}_{\text{sp}} = \frac{\hat{p}_z^2}{2m} + \frac{\hat{p}_x^2}{2m} + \frac{\hat{p}_y^2}{2m} + V_\perp(x,y) \qquad \hat{p}_x = -i\hbar\frac{\partial}{\partial x}, \quad \hat{p}_y = -i\hbar\frac{\partial}{\partial y}. \tag{5.48}$$

Since there are no terms that couple the different dimensions, we shall seek separable solutions of the form

$$\Psi(x,y,z) = \varphi(x)\phi(y)\psi(z) \qquad \text{solving} \qquad \hat{\mathcal{H}}_{\text{sp}}\Psi = E\Psi, \tag{5.49}$$

such that the wavefunctions $\varphi(x), \phi(y)$ and $\psi(z)$ each satisfy the Schrödinger equation of their own subspace

$$E_x\varphi(x) = -\frac{\hbar^2}{2m}\frac{\partial^2\varphi(x)}{\partial x^2} + \frac{1}{2}m\omega_\perp^2 x^2, \tag{5.50}$$

$$E_y\phi(y) = -\frac{\hbar^2}{2m}\frac{\partial^2\phi(y)}{\partial y^2} + \frac{1}{2}m\omega_\perp^2 y^2, \tag{5.51}$$

$$E_z\psi(z) = -\frac{\hbar^2}{2m}\frac{\partial^2\psi(z)}{\partial z^2}. \tag{5.52}$$

The energy E of the whole Hilbert space is obtained by summing the energies of all the subspaces $E = E_x + E_y + E_z$. The problem (5.52) was encountered and solved in subsection 5.1.2. The equations (5.50) and (5.51) correspond to a single particle in a one-dimensional quantum harmonic oscillator. The solutions are all well known [200], we have

$$\varphi_\alpha(x) = \frac{1}{\sqrt{2^\alpha \alpha!}}\left(\frac{m\omega_\perp}{\pi\hbar}\right)^{1/4} e^{-\frac{m\omega_\perp x^2}{2\hbar}} H_\alpha\left(\sqrt{\frac{m\omega_\perp}{\hbar}}x\right), \qquad \alpha = 0,1,2,... \tag{5.53}$$

and a similar wavefunction $\phi_\gamma(y)$ obtained by replacing $x \to y$ and $\alpha \to \gamma$. The functions H_n are the Hermite polynomials [196]

$$H_n(u) = (-1)^n e^{u^2}\frac{\mathrm{d}^n}{\mathrm{d}u^n}\left(e^{-u^2}\right). \tag{5.54}$$

These eigenfunctions $\varphi_\alpha(x)$ and $\phi_\gamma(y)$ are associated with energies $E_x = \hbar\omega_\perp(\alpha + 1/2)$ and $E_y = \hbar\omega_\perp(\gamma + 1/2)$ respectively. They are represented in figure 5.3. We will denote $|\varphi_\alpha\rangle$ and $|\phi_\gamma\rangle$ the state vectors associated with these wavefunctions.

Now that we described the single particle solutions in the presence of transverse harmonic confinement, we shall update the Hamiltonian from (5.14) to include transverse modes as

such

$$\hat{\mathcal{H}}_{\text{mb}} = \sum_{p=-\infty}^{+\infty} \sum_{\alpha,\gamma=0}^{+\infty} \hat{n}_{p,\alpha,\gamma} \left(\frac{\hbar^2 k_p^2}{2m} + \hbar\omega_\perp(\alpha+\gamma+1) \right). \tag{5.55}$$

This new formula captures the correct energy spectrum since we added the transverse harmonic quanta. The operator $\hat{n}_{p,\alpha,\gamma}$ counts number of particle occupying the state associated with quantum numbers p, α and γ, which we construct using the tensor product $|\varphi_\alpha, \phi_\gamma, k_p\rangle = |\varphi_\alpha\rangle \otimes |\phi_\gamma\rangle \otimes |k_p\rangle$. The operator also has a tensor structure $\hat{n}_{\alpha,\gamma,p} = \hat{n}_{x,\alpha} \otimes \hat{n}_{y,\gamma} \otimes \hat{n}_{z,p}$. The operator $\hat{n}_{z,p}$ was introduced in subsection 5.1.3, together with Fock space onto which it acts. The operators $\hat{n}_{x,\alpha}$ and $\hat{n}_{y,\gamma}$ are also defined in their respective Fock spaces by their action on basis vectors,

$$\hat{n}_{x,\alpha} |n_{x,0}, n_{x,1}, ..., n_{x,\alpha}, ...\rangle = n_{x,\alpha} |n_{x,0}, n_{x,1}, ..., n_{x,\alpha}, ...\rangle , \tag{5.56}$$

$$\hat{n}_{y,\gamma} |n_{y,0}, n_{y,1}, ..., n_{y,\gamma}, ...\rangle = n_{y,\gamma} |n_{y,0}, n_{y,1}, ..., n_{y,\gamma}, ...\rangle , \tag{5.57}$$

where $|n_{x,0}, n_{x,1}, ..., n_{x,\alpha}, ...\rangle$ is a Fock state such that $n_{x,\alpha}$ are equal to 0 or 1 and represent the occupation of state $|\varphi_\alpha\rangle$. The Fock states $|n_{x,0}, n_{x,1}, ..., n_{x,\alpha}, ...\rangle$ are defined similarly, with the $n_{y,\gamma}$ describing the occupations of $|\phi_\gamma\rangle$ states. We denote $\{n_{x,\alpha}\}$ and $\{n_{y,\gamma}\}$ the set of all possible values that the $n_{x,\alpha}$ and $n_{y,\gamma}$ can take for $\alpha, \gamma = 0, 1, 2...$, respectively. The set $\{|\{n_{x,\alpha}\}\rangle \otimes |\{n_{y,\gamma}\}\rangle \otimes |\{n_{z,p}\}\rangle\}$ constitutes a basis which diagonalizes $\hat{\mathcal{H}}_{\text{mb}}$. We can again define a total atom number operator as

$$\hat{\mathcal{N}} = \sum_{p=-\infty}^{+\infty} \sum_{\alpha,\gamma=0}^{+\infty} \hat{n}_{p,\alpha,\gamma}. \tag{5.58}$$

In order to compute the ground state of $\hat{\mathcal{H}}_{\text{mb}}$, it is important to notice that the transverse modes are degenerate due to the isotropy of the potential in the transverse plane. We introduce the positive integer $s = \alpha + \gamma$, that fully characterizes the total transverse energy since $E_x + E_y = (s+1)\hbar\omega_\perp$. For a given value of s, there are $(s+1)$ possible combinations of positive integers (α, γ)[6]. Therefore, we build the ground state by filling single particle states in increasing value of energy until we reach E_F, as shown in figure 5.4. By convention, we define the Fermi energy E_F such that its minimal achievable value is 0. We thus subtract the total ground state energy $\hbar\omega_\perp$ in the transverse directions from the Hamiltonian (5.55).

[6] If $s = \alpha + \gamma$ and α and γ are positive integers, then we can label the corresponding degenerate modes by the possibles value of the integer $\ell = \alpha - \gamma$. If $\gamma = 0$, then $\ell = \alpha = s$. If $\alpha = 0$, then $\ell = -\gamma = -s$. This means that $\gamma \in [-s, s]$. Starting from the $\gamma = -s$ configuration, one can increase γ by steps by adding 1 to α while removing 1 to γ to conserve the value of $\alpha + \gamma = s$. This shows that γ can only change by steps of 2, and we conclude that there are $(s+1)$ possible values of ℓ. By linearity of the equations, there is a one-to-one mapping between (s, ℓ) and (α, γ), which means that the total transverse energies $(s+1)\hbar\omega$ are degenerate $s+1$ times.

For each transverse energy index s, we denote $p_{F,s} \geq 0$ the quantum number associated with the highest energy occupied state in the longitudinal direction, and we also define $k_{F,s} = 2\pi p_{F,s}/L$ its corresponding Fermi wavevector. In the thermodynamic limit, we can no longer label the longitudinal states with p because there is a continuum of states instead of a discrete set. However, it is still possible to define $k_{F,s}$ for each s, as shown in figure 5.5, via the equation

$$\frac{\hbar^2 k_{F,s}^2}{2m} + s\hbar\omega_\perp = E_F = \frac{\hbar^2 k_F^2}{2m} \Rightarrow k_{F,s} = \begin{cases} k_F\sqrt{1 - s\frac{\hbar\omega_\perp}{E_F}} & \text{if} \quad s \leq \frac{E_F}{\hbar\omega_\perp}, \\ 0 & \text{else.} \end{cases} \tag{5.59}$$

Using this result, we can express the density n_{1D} integrated in the transverse plane xy in the thermodynamic limit

$$n_{1D} = \frac{N}{L} = \frac{1}{L}\sum_{s=0}^{+\infty}(s+1)\sum_{p=-p_{F,s}}^{p_{F,s}} 1 = \frac{1}{2\pi}\sum_{s=0}^{+\infty}(s+1)\int_{k=-k_{Fs}}^{k_{F,s}} \mathrm{d}k. \tag{5.60}$$

Inserting Eq. (5.59) and defining the floor function $\lfloor ... \rfloor$ we obtain

$$n_{1D} = \frac{k_F}{\pi}\sum_{s=0}^{\left\lfloor \frac{E_F}{\hbar\omega_\perp} \right\rfloor}(s+1)\sqrt{1 - s\frac{\hbar\omega_\perp}{E_F}}, \tag{5.61}$$

and therefore we can relate the density to the Fermi energy as shown in figure 5.5. The density is monotonously increasing when E_F is increasing, but whenever $E_F/\hbar\omega_\perp$ crosses an integer value, the slope encounters a discontinuity because a new energy class of transverse modes suddenly starts filling. The first discontinuity happens when E_F becomes larger than $\hbar\omega_\perp$, which is associated with filling the $s = 1$ modes. This motivates the definition of a limit density $n_{1D,\mathrm{lim}}$ above which excited transverse states are populated in the many-body ground state

$$\frac{E_F}{\hbar\omega_\perp} = 1 \text{ when } n_{1D} = n_{1D,\mathrm{lim}} \Rightarrow n_{1D,\mathrm{lim}} = \sqrt{\frac{2m\omega_\perp}{\hbar\pi^2}}. \tag{5.62}$$

Using Eq. (5.61) and (5.62), we see that the q-th discontinuity such that $E_F/\hbar\omega_\perp = q$, with $q \in \mathbb{N}$, happens when

$$\frac{n_{1D}}{n_{1D,\mathrm{lim}}} = \sqrt{q}\sum_{s=0}^{q}(s+1)\sqrt{1 - \frac{s}{q}}. \tag{5.63}$$

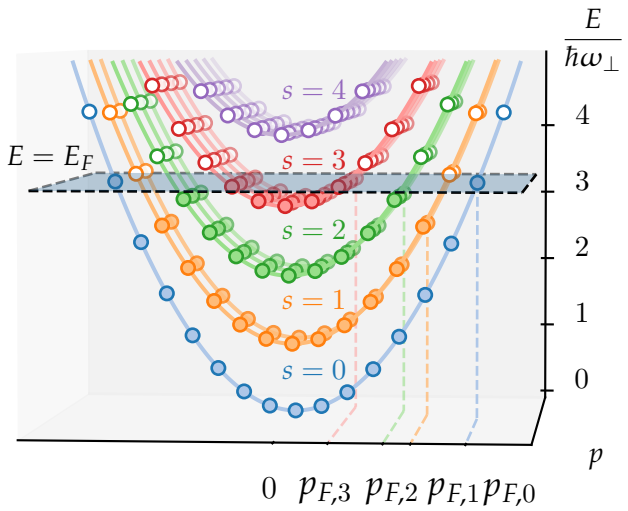

Figure 5.4: Fermi sea with transverse modes. Full and empty circles represent occupied and non-occupied states, respectively. The plane represents E_F, below which all the levels are filled. The transverse modes have the same quadratic dispersion relation as a function of the quantum number p, up to an offset $s\hbar\omega_\perp$, with $s = \alpha + \gamma$. For a given value of s, there are $s + 1$ combinations of α and γ that lead to the same transverse energy. For each s, there is a maximum $p = p_{F,s}$, and a corresponding Fermi wave-vector $k_{F,s} = 2\pi p_{F,s}/L$.

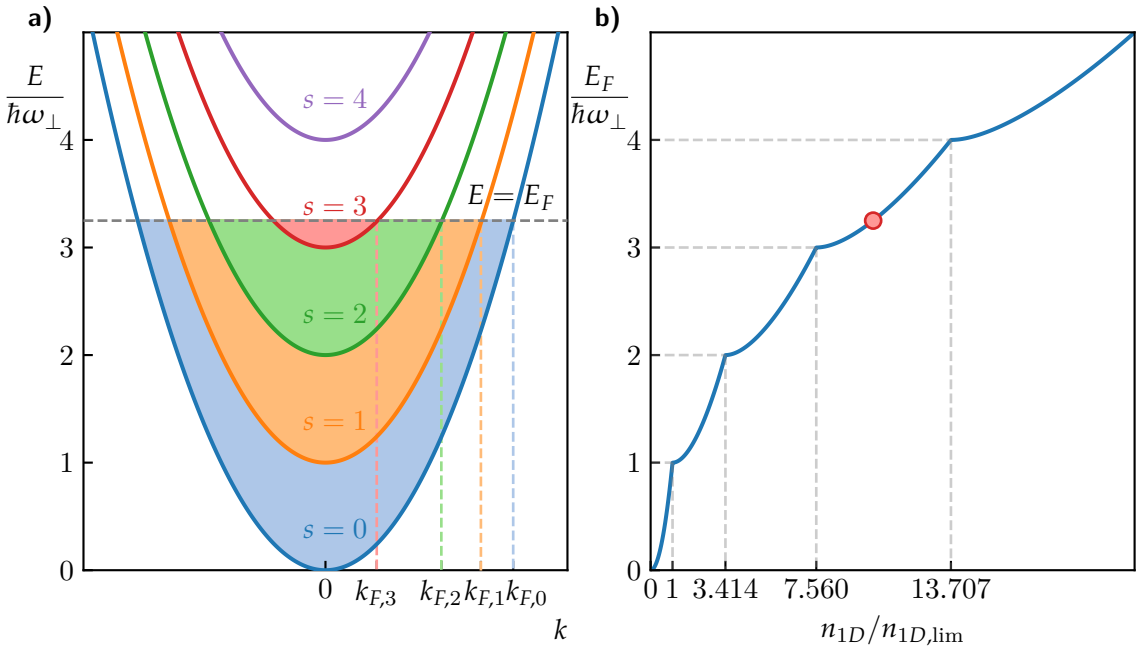

Figure 5.5: Thermodynamic limit of the Fermi sea with transverse modes. a) Thermodynamic limit of the Fermi sea with transverse modes. The vertical axis represents energy. For each band, the discrete energy levels turned into a continuum of levels that are occupied below the Fermi energy, as represented by the filled areas. The mode dependent Fermi wavevectors $k_{F,s}$ are still well defined. b) Fermi energy normalized by the transverse quantum of energy as a function of the density integrated in the transverse plane, normalized by $n_{1D,\mathrm{lim}}$ defined in the main text. The numbers appearing in the x axis were calculated using Eq. (5.63). The point correspond to the value of E_F used in the left graph.

5.2.2 Ensembles at non-zero temperature

In order to characterize the thermodynamics in the presence of transverse modes, we modify Eq. (5.1). Since the energy is now a function of $\omega_\perp$, we can write

$$\mathrm{d}E = T\mathrm{d}S + \mu\mathrm{d}N - P\mathrm{d}L + \hbar\Upsilon\mathrm{d}\omega_\perp. \tag{5.64}$$

We defined the quantity Υ as the conjugate quantity of $\hbar\omega_\perp$ and we will identify its meaning later. The grand potential is still defined as

$$\Omega(T,\mu,L,\omega_\perp) = E - TS - \mu N, \tag{5.65}$$

which means that is also depends on $\omega_\perp$. The important point of this modification is that all the partial derivative identities from Eqs (5.2), (5.5) and (5.10) are still valid provided $\omega_\perp$ is kept constant. Also, since $\omega_\perp$ is an intensive variable, the grand potential-pressure relation Eq. (5.7) holds too. Using equations (5.55) and (5.58), we can define a grand canonical partition function that includes the transverse modes as

$$\Theta(T,\mu,L,\omega_\perp) = \mathrm{Tr}\left[\exp\left(-\beta(\hat{\mathcal{H}}_{\mathrm{mb}} - \mu\hat{\mathcal{N}})\right)\right] \tag{5.66}$$

and we evaluate the trace in basis $\{|\{n_{x,\alpha}\}\rangle \otimes |\{n_{y,\gamma}\}\rangle \otimes |\{n_{z,p}\}\rangle\}$ where $\hat{\mathcal{H}}_{\mathrm{mb}}$ and $\hat{\mathcal{N}}$ are diagonal. We obtain

$$\Theta(T,\mu,L,\omega_\perp) = \prod_{p=-\infty}^{+\infty}\prod_{\alpha,\gamma=0}^{+\infty}\left[1+\exp\left(-\beta\left(\frac{\hbar^2k^2p}{2m}+\hbar\omega_\perp(\alpha+\gamma+1)-\mu\right)\right)\right].$$

We fix the origin of the new chemical potential by using $\tilde{\mu} = \mu - \hbar\omega_\perp$. We make use of the $(s+1)$ degeneracy of the transverse energies $(s+1)\hbar\omega_\perp$ to obtain

$$\Theta(T,\mu,L,\omega_\perp) = \prod_{p=-\infty}^{+\infty}\prod_{s=0}^{+\infty}\left[-\beta\left(\frac{\hbar^2k_p^2}{2m}-\tilde{\mu}+s\hbar\omega_\perp\right)\right]^{s+1}. \tag{5.67}$$

From here, we proceed similarly to what we did previously from Eq. (5.27) to Eq. (5.30). We can express the grand potential as

$$\Omega(T,\mu,L,\omega_\perp) = -\frac{L}{\beta\lambda_{\mathrm{th}}}\sum_{s=0}^{\infty}(s+1)f_{3/2}(Z_s), \tag{5.68}$$

where we introduced the fugacity of the transverse mode s as $Z_s = e^{\beta\mu_s}$, associated with the chemical potential of the band $\mu_s = \tilde{\mu} - s\hbar\omega_\perp$. From the grand potential, we can

calculate the density, the normalized temperature, the normalized entropy per particle, the pressure, the isothermal compressibility exactly the way we did it in subsection 5.1.5 without transverse modes. By doing so we obtain the following results for the density,

$$n_{1D} = \frac{1}{\lambda_{\text{th}}} \sum_{s=0}^{+\infty} (s+1) f_{1/2}(Z_s), \tag{5.69}$$

the normalized temperature,

$$\frac{T}{T_F} = \frac{4}{\pi} \left(\frac{\sum_{s=0}^{\left\lfloor \frac{E_F}{\hbar\omega_\perp} \right\rfloor} (s+1) \sqrt{1 - s\frac{\hbar\omega_\perp}{E_F}}}{\sum_{s=0}^{+\infty} (s+1) f_{1/2}(Z_s)} \right)^2, \tag{5.70}$$

the normalized entropy,

$$\frac{S}{Nk_B} = \frac{\sum_{s=0}^{+\infty} (s+1) \left(\frac{3}{2} f_{3/2}(Z_s) - \ln(Z_s) f_{1/2}(Z_s) \right)}{\sum_{s=0}^{+\infty} (s+1) f_{1/2}(Z_s)}, \tag{5.71}$$

the pressure,

$$P = \frac{1}{\beta \lambda_{\text{th}}} \sum_{s=0}^{+\infty} (s+1) f_{3/2}(Z_s), \tag{5.72}$$

and the compressibility,

$$\kappa = \beta \lambda_{\text{th}} \frac{\sum_{s=0}^{+\infty} (s+1) f_{-1/2}(Z_s)}{\left(\sum_{s=0}^{+\infty} (s+1) f_{1/2}(Z_s) \right)^2}. \tag{5.73}$$

All these expressions agree with with Eqs. (5.35), (5.36), (5.38), (5.39) and (5.44) respectively when $\omega_\perp \to +\infty$, which is equivalent to keeping only the first terms in all the sums over s. In order to understand the meaning of Υ, we express it as a partial derive derivative of the grand potential,

$$\Upsilon = \left. \frac{\partial \Omega}{\partial \omega_\perp} \right|_{T,\mu,L} = \frac{L}{\lambda_{\text{th}}} \sum_{s=0}^{+\infty} (s+1)^2 f_{1/2}(Z_s) = \sum_{s=0}^{\infty} (s+1) N_s, \qquad N_s = \frac{L}{\lambda_{\text{th}}} (s+1) f_{1/2}(Z_s). \tag{5.74}$$

We defined N_s as the number of atoms in the transverse states of energy $(s+1)\hbar\omega_\perp$. Therefore, Υ is equal to the number of transverse energy quanta $E_{\text{tot},\perp}/\hbar\omega_\perp$ where $E_{\text{tot},\perp}$ denotes the total transverse energy[7]. Finally, we can define the ground state fraction

[7] Using the Hellmann-Feynman theorem [199, 201–203], it can be shown that this interpretation is still valid in an interacting system, provided the derivative is performed at constant interaction parameter. The knowledge of this quantity is necessary to describe the full thermodynamics of the system [204].

$\eta_0(\mu, T, \omega_\perp)$ as

$$\eta_0(\mu, T, \omega_\perp) = \frac{N_0}{N} = \frac{N_0}{\sum_{s=0}^{+\infty} N_s} = \frac{f_{1/2}(Z)}{\sum_{s=0}^{+\infty}(s+1) f_{1/2}(Z_s)}, \tag{5.75}$$

with $Z = Z_0 = e^{\beta\tilde{\mu}}$. In the 1D limit we have $\eta_0 = 1$, i.e. when $E_F < \hbar\omega_\perp$ and $T = 0$. On the other hand, it is clear that $\eta_0 \to 0$ when $\frac{k_B T}{\hbar\omega_\perp} \to +\infty$, because atoms start filling infinitely many transverse modes in such a way that the relative ground state population becomes vanishingly small. The ground state fraction η_0 is a useful indicator to quantify the dimensionality of a system at any temperature and Fermi energy close to the 1D regime.

5.3 In-situ thermometry

The temperature is a key quantity required to describe the properties of many-body systems. When combined with information on the density, it allows us to distinguish between classical regimes, which are correctly captured by Boltzmann distributions, and quantum regimes where quantum statistics play a crucial role. We have already presented a method to reliably extract the density of our atomic clouds in section 4.1.

There is a remarkable variety of techniques to measure the temperature of atomic samples in ultracold-atoms platforms, which all take advantage of the properties of the system under study, and the various experimental tools available to probe the system. A widely used technique consists performing quantitative analysis of density profiles. One can either measure the density profile *in-situ*, by imaging the atomic cloud in the presence of its external trapping potential, or after switching it off and letting time for the system to evolve. In the second case, several scenarios can happen depending on the nature of the system and interactions therein ranging from ballistic expansion, where the observed distribution reflects the momentum distribution of the gas prior to release, to hydrodynamical expansion or even more exotic dynamics like stabilization to a self bound-state [205] in quantum droplets for instance.

In this experiment, making a time of flight expansion after switching off all the trapping potentials is not desirable as this would lead to mixing the signals of neighbouring atomic wires, and would therefore remove the benefit of having fully-resolved isolated micro traps. One could bypass this issue by leaving the lattice potential on to ensure a purely longitudinal expansion but this is also problematic since the lattice beams produce a potential along the vertical direction too, and thus one would need to compensate it. While this is not technically impossible, it is beyond the scope of this work. As a consequence we will focus on analysing *in-situ* density profiles.

We will briefly introduce the local density approximation and gain insight about the one-

dimensional regime by calculating density profiles in a harmonic trap. Then, we will use it to analyse the density profiles obtained in the experiment and extract the temperature, the degree of quantum degeneracy and dimensionality while reconstructing the missing non harmonic part of the longitudinal potential landscape in the micro traps. Finally, we will present an insightful discussion about the normalized temperature T/T_F in the 1D-3D crossover [206].

5.3.1 Local density approximation

Although some experiments have implemented homogeneous traps in 2D [207, 208] and 3D [209, 210], it is often the case in cold atoms platforms that the atomic sample evolves in an inhomogeneous potential. In that case, the local density approximation, when applicable, allows one to use homogeneous result to analyse profiles provided the external potential is known. It can also be seen from a different angle: if one knows how to model the thermodynamics properties of the system exactly, the trapping potential can be inferred from the information about thermodynamics quantities. The latter point of view allowed to experimentally measure the equation of state of strongly interacting Fermi gases [195, 211–213].

The presence of a non-homogeneous potential in the axial direction is responsible for the non-homogeneous density profiles that we observe in the experiment. On a fundamental level, the presence of an axial external confinement would need to be included explicitly in the Schrödinger equation, like we did for the transverse directions. The correctly anti-symmetrized many-body wavefunction can be calculated, and the density profile can be obtained from it [214]. However, when applicable, the Local Density Approximation (LDA) [56, 145] provides a remarkably simple quantitative description of the density profiles base on the equation of state. In this approximation, the system is thought of as a continuous set of homogeneous systems that are locally in thermal equilibrium thanks to exchanges of particles and energy with their close neighbours. While the whole sub-systems are described by a unique temperature T, the chemical potential of the locally homogeneous systems follows the variations of the external potential. For this approximation to hold at all temperatures[8], the relevant energy scales of the system under study must be much larger than the energy levels of the external potential along the direction(s) of interest. For instance, if the system is confined in a harmonic potential described by frequencies ω_i, $i = x, y, z$, the spacings between the levels in various directions is given by $\hbar\omega_i$. For an ideal Fermi gas, the relevant energy scale is either $k_B T$ or E_F depending on the degeneracy regime. At sufficiently large atom number, the Fermi energy might dominate the trap energy levels, making the LDA applicable at very low temperature[9].

[8] See [215] for a discussion on the validity of LDA.

[9] Whereas for a Bose-Einstein, the absence of Pauli principle cannot prevent the atomic ensemble to reach

For the reasons mentioned above, the use of LDA is not systematic and should be adapted to the system under study. In the case of our tube traps, the external potential is very anisotropic. The energy levels in the transverse direction are associated with the scale $\hbar\omega_\perp$, whereas the axial ones are approximately[10] described by $\hbar\omega_\parallel$. The trap frequency ratio can reach large values $\omega_\perp/\omega_\parallel \sim 200$, which indicates that these directions might need to receive a different treatment. As a consequence, we will use LDA in the axial direction, but not in the transverse ones. As further analysis will show, we will encounter situations where the filling of excited transverse modes is small or very small, which strongly violates the LDA.

Under LDA, the global chemical potential μ_0 is split in two parts,

$$\mu_0 = \mu(z) + V_\parallel(z). \tag{5.76}$$

Here, $\mu(z)$ represents the local chemical potential that describes the gas locally as if it was homogeneous. By combining Eqs (5.69) and (5.76), we see that a quantitative description of a density profiles requires the following inputs: μ_0, T, $V_\parallel(z)$ and $\omega_\perp$. It is given by the equation

$$n_{1D}(z) = \frac{1}{\lambda_{\text{th}}} \sum_{s=0}^{+\infty} (s+1) f_{1/2}(\xi_s(z)), \tag{5.77}$$

where we defined the local fugacity $\xi_s(z) = Z_s e^{-\beta V_\parallel(z)}$ of the transverse mode s. At this stage, $V_\parallel(z)$ is not known beyond 2nd order for our tube traps. However, it is very insightful to have a look the expected density profiles for a purely harmonic axial potential $V_{\parallel,\text{harm}}(z) = \frac{1}{2} m\omega_\parallel^2 z^2$.

First of all, let us focus on the $T = 0$ case. The zero temperature limit can be obtained from Eq (5.77) using the second and third identities from Eqs (5.32). Indeed, we see that

$$\lim_{\beta\to+\infty} f_{1/2}(\xi_s(z)) = \begin{cases} \frac{2}{\sqrt{\pi}}[\beta(\tilde{\mu}_0 - V_\parallel(z) - s\hbar\omega_\perp)]^{1/2} & \text{if } \tilde{\mu} - V_\parallel(z) - s\hbar\omega_\perp > 0 \\ 0 & \text{else} \end{cases}, \tag{5.78}$$

where $\tilde{\mu}_0 = \mu_0 - \hbar\omega$ is central chemical potential from which the zero energy of the two transverse oscillators is subtracted. The density becomes

$$n_{1D}(z) = \frac{\sqrt{2m}}{\pi\hbar^2} \sum_{s=0}^{+\infty} (s+1)(\max(\tilde{\mu}_0 - V_\parallel(z) - s\hbar\omega_\perp, 0))^{1/2}. \tag{5.79}$$

When $V_\parallel(z) = V_{\parallel,\text{harm}}(z)$, we can define a Thomas-Fermi radius $R_s(\tilde{\mu}_0) > 0$ for each band

even lower chemical potentials, unless significant repulsive interactions are present.

[10] The energy $\hbar\omega_\parallel$ is an upper bound of the energy gap between two axial levels since this gap gets smaller and smaller upon approaching the spilling point.

s such that the mode-dependent local chemical potential vanishes provided $\tilde{\mu}_0 > s\hbar\omega_\perp$

$$\tilde{\mu}_0 - \frac{1}{2}m\omega_\parallel^2 R_s^2 - s\hbar\omega_\perp = 0 \Rightarrow R_s = \frac{\sqrt{2}}{\sqrt{m}\omega_\parallel}\sqrt{\tilde{\mu}_0 - s\hbar\omega_\perp}. \tag{5.80}$$

In the opposit case, we set it to zero. We also define $R_{\omega_\perp} = R_{s=0}(\mu_0 = \hbar\omega_\perp)$ which quantifies the highest achievable radius of the ground state transverse mode before excited transverse modes start to be filled.

We can also calculate the total atom number in the trap by integrating the density,

$$N = \int_{z=-\infty}^{+\infty} n_{1D}(z)\,\mathrm{d}z = \frac{\sqrt{2m}}{\pi\hbar}\sum_{s=0}^{+\infty}(s+1)\int_{-R_s}^{R_s}(\tilde{\mu}_0 - \frac{1}{2}m\omega_\parallel^2 z^2 - s\hbar\omega_\perp)^{1/2}\,\mathrm{d}z. \tag{5.81}$$

The integral can be evaluated and we obtain

$$N = \frac{m\omega_\parallel}{2\hbar}\sum_{s=0}^{+\infty}(s+1)R_s^2 = \frac{1}{\hbar\omega_\parallel}\sum_{s=0}^{\left\lfloor\frac{\tilde{\mu}_0}{\hbar\omega_\perp}\right\rfloor}(s+1)(\tilde{\mu}_0 - s\hbar\omega_\perp). \tag{5.82}$$

Let us determine the maximum amount of atoms $N_{\mathrm{max},q}$ that can be put in the trap before filling the q-th transverse mode. Using the above expression, we see that

$$N_{\mathrm{max},q} = N(\tilde{\mu}_0 = q\hbar\omega_\perp) = \frac{\omega_\perp}{\omega_\parallel}\sum_{s=0}^{q}(s+1)(q-s). \tag{5.83}$$

We recover the very expected result $N_{\mathrm{max},q=0} = \omega_\perp/\omega_\parallel$. In other words, As soon at the atom number exceeds the trap frequency ratio, the excess of atoms have to occupy excited transverse modes. The 1D regime is thus associated with the constraint $N < \omega_\perp/\omega_\parallel$. More generally, the filling of a new transverse mode is associated with total atom number beign equal to specific multiples of the trap frequency ratio, for instance $N_{\mathrm{max},q}/(\omega_\perp/\omega_\parallel) = 4, 10, 20, 35, 56$ for $q = 2, 3, 4, 5, 6$. Each time these multiples are reached with increasing N, a new peak appear on the density profile appears at the center of the trap. Indeed, when a new transverse mode starts filling, atoms promptly occupy axial states with a spatial extent in order to minimize the energy. The figure 5.6 a) shows the the evolution of the density profile as μ_0 (or equivalently N) is increased at zero temperature.

At finite temperature, the temperature smooths out the sharp edges occurring in density profiles. When $k_B T \gg \hbar\omega_\perp, T/T_F \gg 1$, the Boltzmann distribution applies and resulting density profiles are correctly fitted by a Gaussian distribution, as shown in figure 5.6 b). An interesting phenomenon happens when a small temperature is introduced: atoms that would otherwise occupy single-particle state corresponding to a highly elongated axial

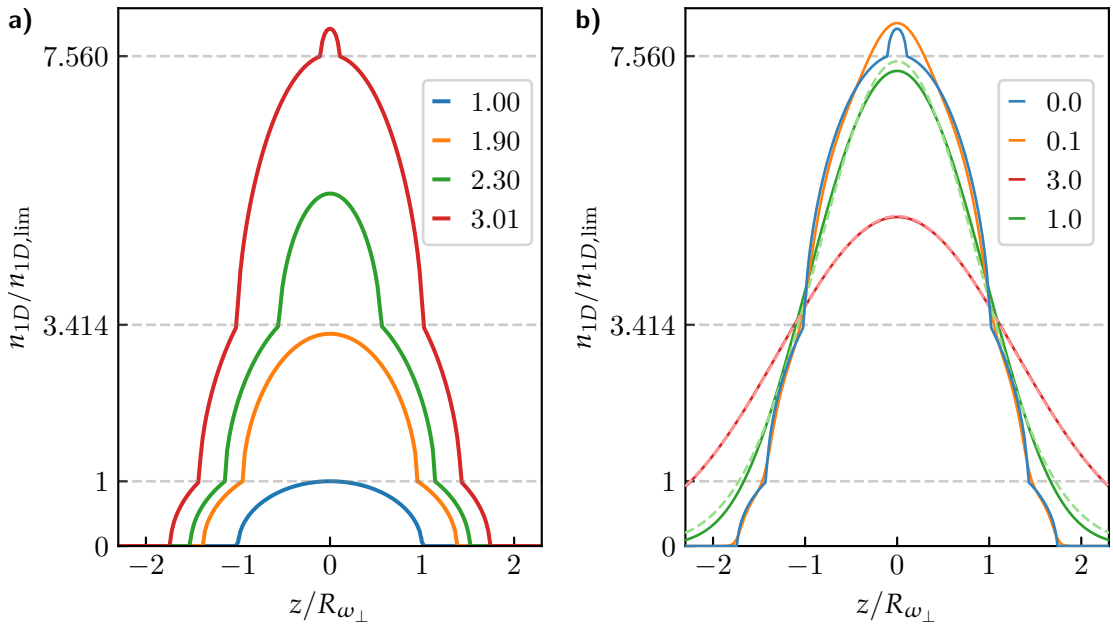

Figure 5.6: Density profile of an elongated ideal gas with transverse modes and LDA. a) Evolution of density profiles at zero temperature for various chemical potentials. The values in the legend represent $\tilde{\mu}_0/\hbar\omega_\perp$. A new peak whenever $\tilde{\mu}_0/\hbar\omega_\perp$ reaches integer values. The ratio $N/(\omega_\perp/\omega_\parallel)$ take the values $1, 3.7, 5.8$ and 10.1 for the blue, orange, green and red lines respectively. b) Evolution of the density profile at fixed atom number $N = 10.1 \times \omega_\perp/\omega_\parallel$. The legend represents the values of $k_B T/\hbar\omega_\perp$. The dashed lines for the two largest temperatures represent a fit with a Gaussian distribution.

modes and transverse mode s might be able to jump to the transverse mode $s+1$, thanks to the finite temperature, but reduce significantly their energy in the axial direction, hence shortening their spatial extent. This leads to a counter-intuitive increase of the central density compared to the ground state configuration, as highlighted by the orange curve in the figure b). For larger temperatures, however, central density decreases according to the classical expectation $n_{1D}(0) \sim 1/\sqrt{T}$.

5.3.2 Potential reconstruction and fitted density profiles

The previous calculations of density profiles focused on the case of an axial harmonic potential. However, we know the longitudinal potential of the microtraps is anharmonic, as detailed in subsection 4.2. This asymmetry is most created by the gravity field and is noticeable on in-situ density profiles, all the more so as the atom number is high and the temperature is large. In this section, we will present a technique to reconstruct the potential beyond 2nd order using a shared fit of many density profiles. A similar technique was used in an interacting one-dimensional Bose gas to reconstruct the potential from a

theoretically calculated equation of state [216]. In this work, the external potential was fully calibrated independently of the density profile measurement, and the agreement between the reconstructed and the calibrated potential was an experimental validation of the equation of state. In our case, the philosophy is different as our goal is not to experimentally validate an interacting equation of state, but rather to use a well established equation of state that we can rely on: the one of an ideal gas. The outcome of the fit is twofold: we obtain a much better characterization of our axial potential that we can use for other experiments (see sec. 7.2.4) where it can be used as an input for the analysis, and we can quantify the degeneracy and the dimensionality of our system.

The shared fit consists in mixing individual parameters describing the thermodynamic properties of the atoms inside each micro trap with shared parameters parametrizing the axial potential of each tube trap beyond 2$^{\text{nd}}$ order. In order to model the high-order terms of the longitudinal potential, we simply use a Taylor expansion,

$$V_{\parallel}(z) = \frac{1}{2} m \omega_{\parallel}^2 z^2 + \sum_{p=3}^{p_{\max}} a_p z^p, \tag{5.84}$$

where the a_p coefficients are assumed to be identical, which as argued in 4.2 results in a small error as long as we consider few micro traps around the global minimum. We restrict the expansion to $p_{\max} = 7$, which is a good empirical compromise between flexibility of the reconstructed potential and stability of the fitting procedure[11]. The coefficient $\omega_{\parallel}$ is an input of the model inferred from the measurement presented in 4.8. It acts as an anchor that prevents the thermodynamic parameter from compensating the lack of knowledge of the potential.

The parametrized axial potential is used to calculate density profiles using LDA. For each density profile, it is also necessary to know the temperature T and the central chemical potential μ_0. Each absorption image contains several tube traps, and we restrict ourselves to analysing the 18 central ones. Because the tube traps are independent and the number of loaded atoms decreases away from the center, the measured density profiles are associated to different sets of (μ, T). On top of that, we varied the amount of evaporation prior to ramping the optical lattice to generate a collection of profiles with significant variations of μ and T, which helps unambiguously reconstructing the potential. In the end, we gathered a total of 270 absorption images obtained from loading procedure described in figure 3.4. After sorting the images in increasing total atom number, we obtained 27 groups of 10 similar images that we averaged together to improve the signal to noise ratio. From these averaged images, we extract 18 density profiles which makes a total of 486 density profiles.

[11] In the sense that it allows the fitting procedure to converge to the optimum parameters in a more robust way that depends less on the initial parameters value. We have checked the successful fit with $p_{\max} > 7$ do not change the reconstructed potential significantly in the region of interest.

These density profiles were fitted using a least-square optimization procedure with the shared coefficients a_p, where $p = 3, 4, .., 7$ and individual coefficients $((\beta\mu)_i, \beta_i)$, where $i = 1, 2, ..., 486$, using Eq. (5.77).
Due to the large amount of fit parameters, the fitting procedure the must be handled with care in order to ensure a reasonable execution time and enough stability for convergence. This is particularly true because the polylog function is costly to numerically evaluate and must be calculated at every pixel of each density profile and for each iteration of the least-square algorithm. The algorithm was made more efficient by using the following standard tricks:

- Evaluating the Jacobian from its analytical expression. By default, most least-squares libraries will evaluate the Jacobian's component of each fit parameter using a finite difference formula. This makes the fitting very slow when the number of parameters is large, and it is often not necessary when the Jacobian can be computed analytically. On top of that, because only the a_p coefficients are shared parameters, the Jacobian matrix is extremely sparse, meaning that we can restrict ourselves to compute only its non-vanishing coefficients. In the end, it is enough to evaluate the polylog $\mathrm{Li}_{1/2}$ for each density profiles points only twice per pixels and per iteration.

- Parallelizing the evaluation of density profiles at each iteration on multiple cores.

- Bin the density profiles along the axial direction to reduce the amount of points per profiles. We used bins of 3 data points, which correspond to a spacing of 1μm per bins. This value is smaller than the resolution of our imaging system, which implies that we are not losing spatial information of the density profile structure by doing so.

With these improvement, it was possible to perform the fit in around an hour in a typical laptop or desktop computer. As a consequence, it was not necessary to use more powerful hardware since we were limited by the experimental acquisition of data rather than the analysis.
A selection of fitted profiles is shown in figure 5.7 a), together with their corresponding atom number and temperature. These sets are associated with a transverse frequency $\omega_\perp = 2\pi \times 17$ kHz. The axial curvature is characterised by the frequency $\omega_\parallel = 2\pi \times 96$ Hz. Our data contain atoms numbers well below than the trap ratio $\omega_\perp/\omega_\parallel = 177$, so that the density 1D condition is satisfied.
In order to *a posteriori* check the applicability of the noninteracting equation of state, we reconstructed the potential after letting the gas thermalize at two different scattering lengths $a = \pm 40 a_0$, corresponding to attractive and repulsive interactions. If the density would be significantly affected by interaction for these values, the would result is noticeable

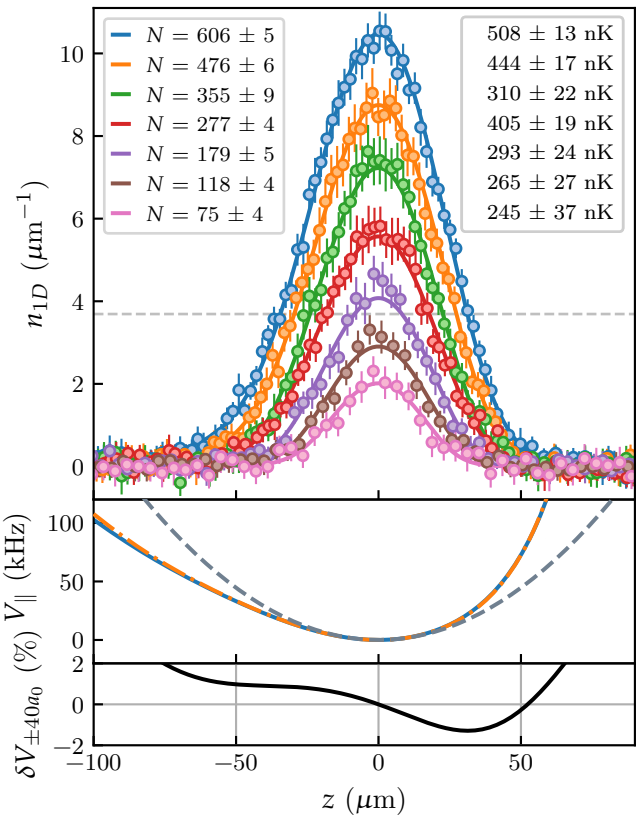

Figure 5.7: Reconstruction of the potential beyond 2nd order. a) Averaged 1D density profiles for individual tubes with a total atom number N per spin state. The solid lines represent fits of the non-interacting equation of state Eq. (5.77). The right box represents the fitted temperature, aligned with their corresponding colour on the left box which shows atom number. The grey line corresponds to $n_{\mathrm{lim}} \approx 3.7\mu\mathrm{m}^{-1}$ defined in (5.62). b) Reconstructed axial potential for $a = -40a_0$ (orange dashed-dotted line) and $a = +40a_0$ (blue solid line). The harmonic part (grey dashed line) of the potential has been independently measured. c) Relative difference $\delta V_{\pm 40a_0}(z)$ between the reconstructed potentials for attractive and repulsive interactions.

differences in the reconstructed density profiles. The reconstructed potentials and their relative difference are shown in figure 5.7 b) and c). The latter are defined as

$$\delta V_{\pm 40a_0} = \frac{V_{\parallel,-40a_0}(z) - V_{\parallel,+40a_0}(z)}{V_{\parallel,-40a_0}(z)}. \tag{5.85}$$

In order to make sure thermal equilibrium was reached, we also performed this measurement at slightly larger scattering length $a = -100a_0$ to increase the collision rate, at longer thermalization time up to 100 ms instead of 40 ms after lattice ramp up. We observed no significant differences in the reconstructed potential.

The information contained in the fitted parameters allow us to fully describe the thermodynamic state of the atomic clouds, and therefore to quantify their degeneracy and dimensionality. It will be the subject of the following section.

It is worth pointing out that both the reconstruction method employed in this section and the longitudinal curvature measurement of section 4.4 ignore the hypothetical details of the potential that could occur below the optical resolution. If such features would exist, they would stay under the radar since they would not imprint visible modulations on the extracted density profiles. One could imagine sub-resolution structures of two natures: disorder, or periodic modulation. Practically speaking, disorder could result from a lattice

beam scattering on an undesired target, such as one or several dust particle(s), resulting in uncontrolled fringes. In order to be unnoticed for us, this hypothetical effect would need to produce disorder with a low-frequency cut-off below the sub-resolution scale. For the latter effect, a sub-resolution periodic modulation could be created if a lattice beam would be partially reflected back through the science cell from below, leading to a lattice spacing $\sim \lambda/(2\cos(\alpha_{\mathrm{latt}/2})) \approx \lambda/2 = 532\mathrm{nm}$. The hypothetical occurrence of these effects is discussed later, in section 7.5.1.

5.3.3 Dimensionality and degeneracy of the quantum wires.

In order to characterize the dimensionality and degeneracy of our system, we use the fitted parameters together with Eqs (5.70) and (5.71) to extract $k_B T/\hbar\omega_\perp$, T/T_F and S/Nk_B for each tube trap. The figure 5.8 a),b) and c) shows the evolution of these quantities for three selected tube traps, represented in e), when the initial evaporation in the crossed dipole traps prior to loading the optical lattice is varied (see fig. 2.5). This way, we control the transverse mode population until we reach the 1D regime. We can reduce the temperature down to $k_B T \leq 0.2\hbar\omega_\perp$ with a typical Fermi energy of $E_F \leq 0.2\hbar\omega_\perp$. The temperature spread across different atomic wires is yet another sign that tunnelling between the tube traps is strongly suppressed (see fig. 3.3), which leads to an early thermal decoupling during the lattice loading procedure.
We observe that S/NkB stays nearly constant in the entire crossover region, whereas T/T_F displays a sudden increase in the low atom number and temperature limit, as shown in figure 5.8 b), c). This is expected to occur in the 1D regime[12], where the equation of state is strongly altered with respect to the 3D case. Note that, compared to the 3D ideal Fermi gas, the role of quantum statistics in 1D remains important at comparatively higher values of T/T_F. For instance, at $T/T_F = 1.6$, Maxwell-Boltzmann statistics overestimate the density of the non-interacting gas by 55% in 1D, versus 12% in 3D.
Interestingly, we observe that the entropy per particle varies between inbetween different micro traps, with an increase towards the center where the density is highest, as shown in 5.8 d). This could be cause by density dependent interaction effect during the loading phase. For example, a realistic scenario in this context could be the occurrence of three body-losses during the early loading phase of the lattice, where the scattering length is still significant (see fig. 2.5). This inhomogeneous redistribution of entropy further highlights the relevance and necessity of our thermometry technique based on resolving individual atomic wires.
To clarify unambiguously the one-dimensional character of our system, we also extracted the ground state fraction defined in Eq. (5.75). In figure 5.9, we observe large local ground state fractions $\eta_0(\mu = \mu(z = 0), T)$ at the center of the of >98% in the 1D limit for

[12] See subsection 5.3.4.

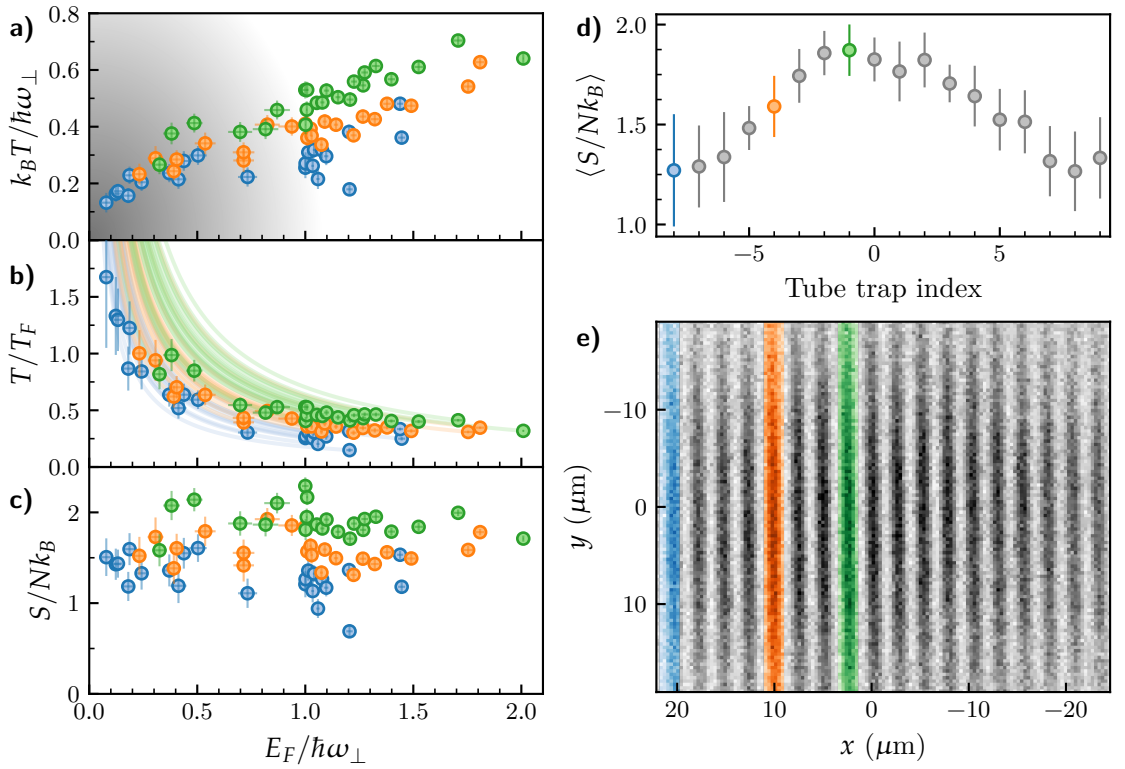

Figure 5.8: Thermodynamics of the 1D-3D crossover. The data points in a), b), c) and d) represent the local quantities at the center of the trap ($z = 0$) where the local Fermi energy is the highest, and the colors indicate the selected tubes, shown in e). a) Temperature normalized by the transverse quantum of energy $\hbar\omega_\perp$. The grey gradient illustrates the 1D region. b) Temperature normalized by the Fermi temperature. The solid lines emanating from the data points represent the continuous change in $E_F/\hbar\omega_\perp$ and T/T_F within each atomic wire according to LDA. c) Normalized entropy per particle. d) Mean value of the entropy per particle obtained by averaging the data of c) for the green, orange, and blue points. The grey points represent the other 15 tubes traps which were omitted in a), b) and c). e) Optical density obtained from a characteristics absorption image. The colour code indicates the selected tubes.

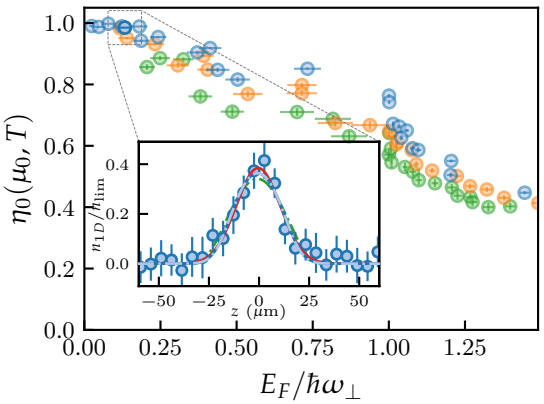

Figure 5.9: Ground state fraction. Relative occupation η_0 of the lowest transverse mode at the center of the tube traps ($z = 0$), where η_0 is the smallest. Different colors represent three characteristic tube traps selected in figure 5.8 e). The inset plot represents the measured density profile associated to the opaque data point. The meaning of the fitted lines is explained in the main text.

$E_F \leq 0.2\hbar\omega_\perp$, indicating that a dominating majority of atoms were populating the same unique lowest energy transverse mode $s = 0$.

The density profiles associated with a very large ground state fraction are not very asymmetric due to their small spatial extent along z. A representative profile is shown in the inset of figure 5.9. As a consequence, these profiles can be used to check both the one-dimensional character and the degenerate character of the cloud without even relying on the reconstructed potential. We re-analysed these profiles under that assumption that the longitudinal potential is purely harmonic and associated with the independently measured axial angular frequency $\omega_\parallel$. We performed several fits, assuming four different equations of states. All of them allow to infer the temperature of the gas, and are represented in the inset of Figure 5.9:

- The red solid line representation a Boltzmann distribution[13]

$$n_{\text{Boltzmann}}(z) = N\sqrt{\frac{\beta m\omega_\parallel^2}{2\pi}}\exp\left(-\frac{\beta}{2}m\omega_\parallel^2 z^2\right), \tag{5.86}$$

  and measures $T_{\text{fit}} = 206 \pm 20$ nK.

- The green dashed line represents 3D Fermi-Dirac distribution integrated radially, where LDA was assumed to hold radially [57]

$$n_{\text{3D,integrated}}(z) = \sqrt{\frac{m}{2\pi}}\frac{1}{\beta^{5/2}\hbar^3\omega_\perp^2} f_{5/2}\left[Z_0\exp\left(-\frac{\beta}{2}m\omega_\parallel^2 z^2\right)\right], \tag{5.87}$$

  and yields $T_{\text{fit}} = 15 \pm 374$ nK. This result is clearly problematic: the model cannot extract the temperature reliably. Despite the lack of accuracy, this model is not self-consistent since it predicts $E_F, k_B T \leq \hbar\omega_\perp$, which contradicts the conditions of applicability of LDA. This observation confirms the relevance of not applying the LDA in the transverse direction *a posteriori*.

- The light blue dashed line represents a 1D Fermi-Dirac distribution with higher tranverse modes from Eq. (5.77), and calculates $T_{\text{fit}} = 143 \pm 20$ nK.

- The dark blue solid line represents 1D Fermi-Dirac without transverse modes, obtained by keeping only the $s = 0$ term from Eq. (5.35), and corresponds to $T_{\text{fit}} = 138 \pm 18$ nK.

[13] The 1D density derived from a Boltzmann distribution in a 1D world is exactly the same as the radially integrated 3D density derived from a Boltzmann distribution in a 3D world, so it is irrelevant to specify the dimension here. More generally, this Boltzmann expression holds no matter how many dimensions are integrated.

All these models are able to fit the density profile with a decent agreement up to the error bars. However, they do not predict the same temperature. The Boltzmann model overestimates the temperature, indicating that degeneracy is playing an important role. The 3D model with radial local density approximation fails too, indicating that dimensionality plays a role as well. The two 1D approaches, with or without additional transverse modes are consistent with each other, indicating that only the ground state transverse mode is populated, as pointed out already by the large value of η_0.

The obtained results highlight that we do not necessarily need to observe the sharp features of the density profiles occurring a very small temperature shown in figure 5.6 in order to probe low-dimensional gases. Not only these low temperatures are very challenging to prepare experimentally, but also the finite optical resolution and signal-to-noise ratio would wash-out these features.

5.3.4 Isentropic 1D-3D transformation

From the measurement of T/T_F figure 5.8 b), it might seem unsatisfactory to observe a rise of T/T_F as one gets closer to the 1D regime. On the one hand, a part of this increase is technical and is due to the lower limit of achievable temperatures, which make this ratio increase when the density, and hence T_F, get close to zero. On the other hand, this increase is also a consequence of the dimensional-dependent definition T_F. We will illustrate the latter effect with a toy model.

Let us imagine an ideal gas of N fermions in thermal equilibrium with temperature T in a 3D homogeneous box with lengths L_x, L_y and L_z such that many levels are occupied in all three directions. In the thermodynamic limit, we can treat the levels in the three directions as continua and calculate various thermodynamic quantities, for instance the ones listed in table 5.1 in the 3D columns.

If we now imagine that the box is smoothly and slowly reshaped in such a way that L_y and L_x become smaller and smaller, while L_z gets larger and larger, the relevant state of the gas at equilibrium will be such that the population of excited states along x and y will become smaller and smaller. At some point, the thermodynamic quantities of the system will be correctly captured by the formulas from Table 5.1 in the 1D columns. Such a transformation is illustrated in figure 5.10, following the straight from left to right.

Provided this reshaping happens infinitesimally slowly and in a presence of a mechanism to guarantee thermalization, the transformation between these two limiting cases has to be reversible. In that case, the entropy S is conserved and the transformation is said to be isentropic. If the box potential is strong enough to prevent atoms from leaving, the system is closed and N is also conserved. Thus, the normalized entropy per particle is conserved, therefore we can write $(S/Nk_B)_{3D} = (S/Nk_B)_{1D}$. Since there is a different one-to-one

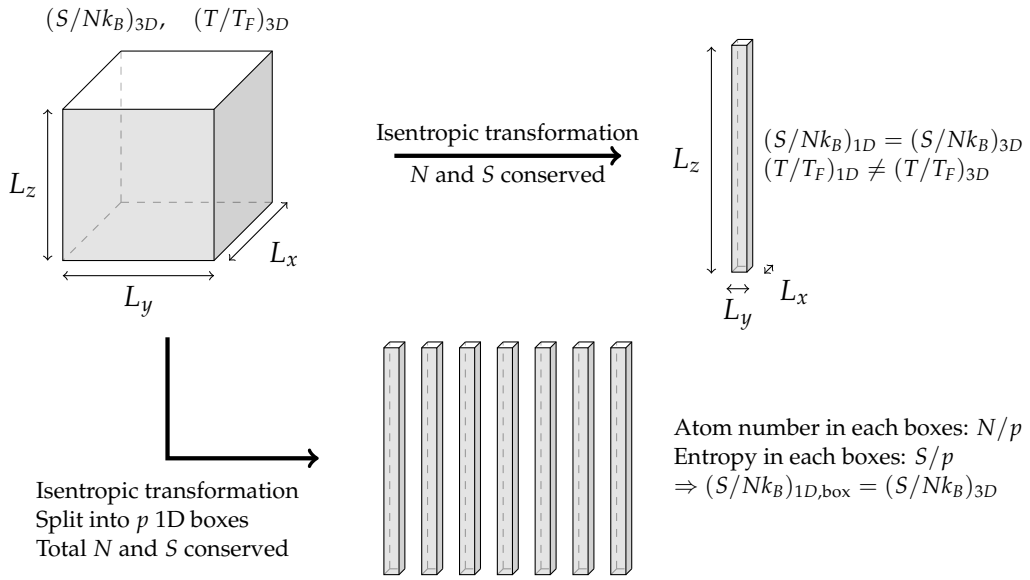

Figure 5.10: Isentropic 3D to 1D transformation. Illustration of the two isentropic transformations described in the main text. In both cases, the starting homogeneous gas is correctly described by 3D thermodynamics. Since both entropy and atom number are extensive quantities, the normalized entropy per particle is conserved even if the initial system is split into several subcomponent, provided the transformation is isentropic. It is necessary that the density of each sub-box remain the same during the transformation before they get completely independent in order to prevent density and entropy flow.

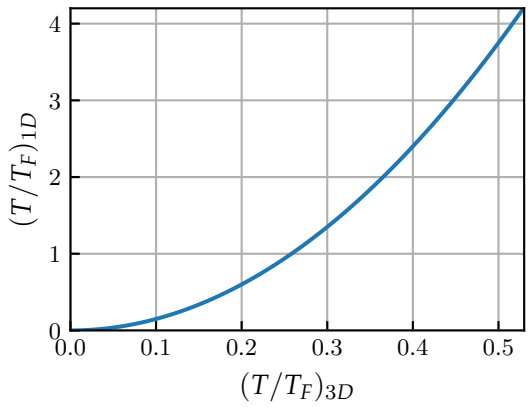

Figure 5.11: Reduced temperature at constant entropy per particle from 1D to 3D. Isentropic relation between the reduced temperatures of a homogeneous non-interacting 3D and 1D Fermi gas. This toy model shows that the normalized temperature is not a conserved quantity during the dimensional crossover and gives a lower bound for its expected increase in the quantum wires when going from 3D to the 1D in the most ideal case.

relation between normalized temperature and normalized entropy per particle[14], we can map the normalized temperatures $(T/T_F)_{3D}$ to $(T/T_F)_{1D}$ in the two limits of the isentropic transformation, as shown in figure 5.11.

This thought experiment clearly reveals that T/T_F is not a conserved quantity during

[14] This can be seen from table 5.1. S/Nk_B depends on the fugacity, and T/T_F too but the link between these two is clearly dimensional dependent.

an isentropic transformation that strongly alters the dimensionality of a system, despite the fact that in a given fixed dimension, it depends only on the normalized entropy per particle. Moreover, it indicates us that in a transformation from 3D to 1D, T/T_F is expected to increase, which certainly contributes to the observation in figure 5.8 b). In the real world, it is extremely challenging to engineer such an isentropic transformation due to either technical or physical reasons. The finite lifetime of the system prevents us from achieving arbitrarily slow transformations. The losses limit the assumption of a closed system. Heating can be induced by the trap instability [189–191]. Thermalizing two-body collisions are expected to be suppressed in the 1D regime [217–219]. If the reversibility of the transformation cannot be guaranteed, the entropy per particle is expected to increase due to the second law of thermodynamics. As a consequence, the normalized temperature T/T_F should increase more than what this toy model predicts. This thought experiment provides lower bound for the increase of normalized temperature that would occur in any real transformation from 3D to 1D in a closed environment.

It is important to note the our experimental realization differs from the transformation described above in at least two aspects. First of all, we are not transforming a single 3D gas into a single 1D gas, but rather into several 1D gases that are independent. As long as we keep on considering homogeneous systems, the conclusion of this experiment are easily generalized if the final state of the transformation is made up of several independent elongated 1D boxes, as illustrated in figure 5.10, following the right angle arrow. Since both S and N are extensive, the normalized entropy per particle S/Nk_B is conserved and equal in each independent 1D boxes, as long as no inhomogeneities are introduced during the splitting process. This brings us to the second reason why this toy model is an incorrect description of our system: we perform the 3D-1D transformation in an inhomogeneous system.

Surprisingly[15], figure 5.8 d) reveals that in our system, the entropy per particle varies between the tubes, with an increase towards the center where the density is highest. Understanding this effect is clearly beyond the reach of this toy model, and could constitute an interesting follow-up for future works.

5.3.5 Outlook: measuring the interacting equation of state

There are many situations where the use of a trapping potential to confine cold gases complicates their theoretical analysis, or wash out signatures of particular phenomena that would be striking in a homogeneous system. However, it was eventually realized that trapped gases which satisfy the local density approximation (see sec. 5.3.1) provide a considerable opportunity to extract thermodynamic quantities [220]. Within this approxi-

[15] If we consider a gas in harmonic trap and apply LDA, S/Nk_B is minimum at the center of trap, where density is the highest.

mation, the spatial variation of the *in-situ* density of the sample can be used to calculate its derivative or integral with respect to the chemical potential, which ultimately reveals a lot of information regarding its equation of state.

This technique[16] was used to measure the equation of state of the 3D Fermi gas at unitarity [222, 223] and for various interaction strengths [224], providing at the same time a remarkable characterization of the superfluid transition.

In 3D, a bound state appears right at the unitary limit when $1/a_{3D} \to 0$ and it exists only on the BEC side $1/a_{3D} > 0$, whereas in 1D and 2D, the bound state is formed as soon as interactions are turned on[17]. This means that the role played by the unitary limit in 3D coincides with the noninteracting limit in 1D and 2D. This profoundly modifies the qualitative features of the equation of state. For instance, in the limit of arbitrarily large $\beta\mu$ the density ratio $n(\beta\mu, \lambda)/n_0(\beta\mu)$ converges to 1 in 1D and 2D [225, 226], where n_0 is the noninteracting density and λ is a dimensionless interaction parameter assumed to be constant. This corresponds to a weak coupling limit. Conversely, in 3D at unitarity, this ratio reaches a non trivial value when $\beta\mu$ becomes large [227, 228].

Measurement of the equation of states of low-dimensional gases have been performed with Bose gases in 1D [229] and 2D [230], and Fermi gases in 2D [231, 232]. However, no measurements have been reported so far in 1D Fermi gases. Theoretically, the ground state and low-temperature regime ($T \ll T_F$) of the interacting 1D Fermi gas can be solved with Bethe Ansatz [233]. For finite temperature, there are no straightforward ansatz that can be used and theoretical studies are sparse [226, 234].

In experiments, the 1D and 2D limits are reached by applying tight confinement along the directions of interest, which are associated with a length scale that can break the universality of the equation of state.

It would be very interesting to investigate the equation of state of balanced strongly interacting Fermi gases in a quasi-1D geometry with our experimental setup, and to study how the presence of transverse mode populations affects it beyond the one-dimensional regime. The influence of imbalanced could also be studied. Since the bias field and the transverse potential are reasonably homogeneous in the tube trap, $\omega_\perp$ and a_{3D} are constants across the measured density profile and using the local density approximation $\mathrm{d}\mu = -\mathrm{d}V_\parallel$ the compressibility and the generalized pressure can be expressed as

$$\kappa = -\frac{1}{n_{1D}^2}\frac{\mathrm{d}n_{1D}}{\mathrm{d}V_\parallel}\bigg|_{T,\omega_\perp,a_{3D}}, \qquad P(V_\parallel) = \int_{V_\parallel}^{+\infty} \mathrm{d}U' n_{1D}(U'). \tag{5.88}$$

They can be extracted experimentally, using the reconstructed axial potential $V_\parallel(z)$ in the

[16] The equations of state of the 3D unitary Fermi gas at finite temperature has also been measured using a different method [221].

[17] For the 1D case, see sec. 7.1.3

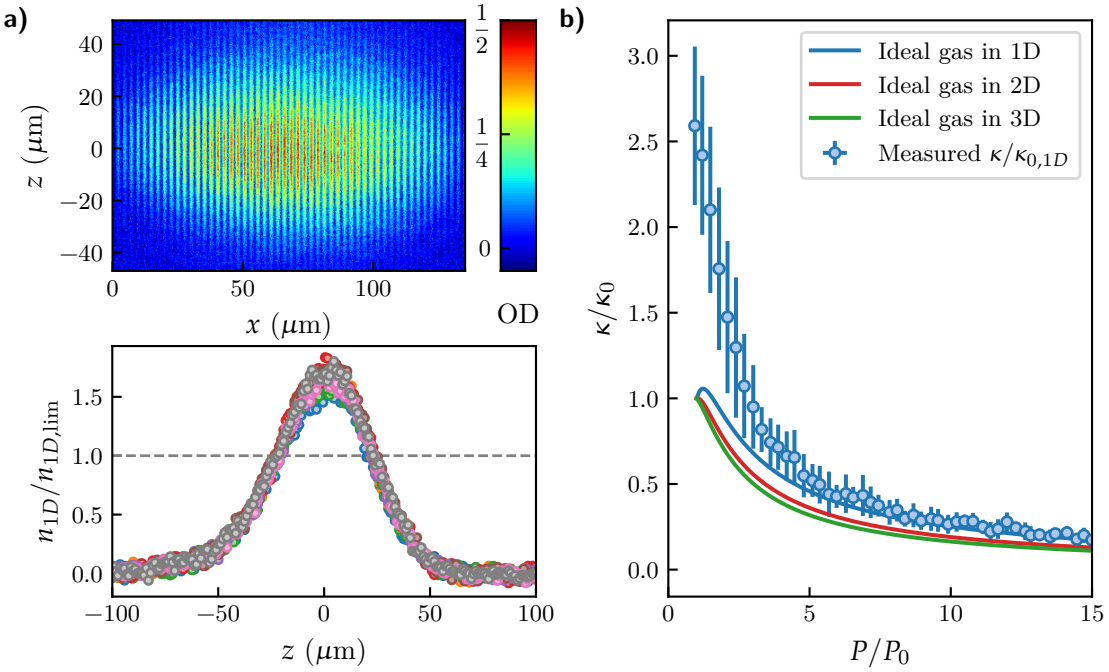

Figure 5.12: Equation of state in the tube traps. a) Top: Absorption images of a single spin state from a balanced Fermi gas averaged over 112 shots. Bottom: Selection of central density profiles to highlight to typical signal-to-noise obtained from this measurement. The density is normalized by the 1D threshold density $n_{1D,\mathrm{lim}}$ defined in Eq. (5.62). b) Extracted κ and P normalized by their value at identical density, $T = 0$ and in the absence of interactions. The continuous lines represent the universal curves in 1D, 2D and 3D for the noninteracting gas, obtained by matching κ/κ_0 and P/P_0 at identical fugacity Z from table 5.1. In the wings where P/P_0 is large and $n_{1D}/n_{1D,\mathrm{lim}}$ is small, the measured data points align with the universal 1D noninteracting curve. In the center of profiles where P/P_0 is the lowest, the 1D conditions are not met for the selected set, and this results in a noticeable increase of κ/κ_0. In this region, the curve is not universal anymore and depends on transverse energy scale, for example through $k_B T/\hbar\omega_\perp$, but also on the interaction strength. In the represented set, fitting the wings yields $k_B T/\hbar\omega_\perp = 0.45 \pm 0.13$.

micro traps. Because of the transverse direction, the knowledge of these two quantities is not enough to fully characterize the equation of state and it is necessary to acquire another thermodynamic quantity, for instance the temperature T. It can be extracted from the wings of the density profile, where the role of interactions is mitigated by the local increase of T/T_F. In figure 5.12, we show a measurement of κ and P for a small scattering length $a_{3D} = -40a_0$. It was beyond the scope of this work to investigate the strongly interacting equation of state. This would constitute a very promising project for future experiments.

Chapter 6

Preparation of large magnetization gradients

The transport properties of strongly interacting fermions constitute an extensive field of research that covers a broad range of systems and technologies, ranging from spintronics [235] to the quark-gluon plasma [236, 237]. Cold atom experiments provide an excellent platform to study these properties in a variety of situations [238–240]. Transport coefficients can directly be extracted from dynamical properties, providing access to the viscosity [241, 242], speed of sound [177, 243–245], spin diffusivity [246–251], and many others.

The spin diffusivity controls the relaxation rate of magnetization gradients [252]. In principle, both longitudinal [246, 247] and transverse diffusion [249–251] can be measured experimentally. Among other diffusion coefficients, the 3D spin diffusivity is predicted to be bounded from below due to fundamental quantum mechanics limits in the degenerate regime [253]. An interesting open question in this regard is whether these quantum bounds hold in lower dimensional systems without a scale-invariant quantum critical point as well [252]. Remarkably, the existing measurements in 2D systems are conflicting [250, 251], and no measurement has yet been performed in 1D. On the theoretical side, only a handful of studies have investigated the transport properties of Fermi gases in one-dimensional bulk systems [254–256]. More recently, the sound diffusivity has been measured through the damping of sound waves in homogeneous quantum gases in both 3D [257] and 2D [258], yielding results that also satisfy the quantum bound $\sim \hbar/m$.

In the present work, we will study spin diffusivity in our low dimensional system. While the next chapter will be dedicated to the quantitative analysis of the demagnetization

dynamics, the current one will detail how to create a longitudinal magnetization gradient on a technical level.

6.1 Transverse and longitudinal magnetization gradient

The spin diffusivity D_s sets the speed at which magnetization gradients are smoothed out over time. When D_s is small, the diffusion process is slow. In a strongly interacting Fermi gas in 3D, D_s decreases as the quantum degenerate regime is reached in the normal state and reaches a minimum around $T \sim T_F$. The effects of superfluidity induce an increase of the spin diffusivity at even lower temperatures. It is expected to always satisfy the lower bound $D_s \gtrsim \hbar/m$ [253].
The system responds differently to longitudinal and transverse magnetization gradients. The former induces a longitudinal spin current given by

$$\vec{J}_{i,s}^{\parallel} = -D_s \partial_i \vec{M}, \tag{6.1}$$

whereas the latter creates a transverse spin current which yields

$$\vec{J}_{i,s}^{\perp} = -D_{s,\text{eff}} \left[\partial_i \vec{M} + \mu \vec{M} \times \partial_i \vec{M} \right]. \tag{6.2}$$

We defined the effective diffusion coefficient $D_{s,\text{eff}} = D_{0,s}/(1+\mu^2 M^2)$, where μ is the Legget-Rice parameter. This parameter quantifies the precession of the spin current about the local magnetization and is responsible for slowing down the demagnetization since $D_{s,\text{eff}} < D_s$ [259–262]. Longitudinal gradients can be achieved by spatially separating two distinct hyperfine eigenstates, [246, 247]. Transverse magnetization gradient can be prepared by letting an initially spin-polarized atomic sample with a finite spin component perpendicular to the quantization axis evolve in the presence of a magnetic field gradient. The locally various spin precession results in a spin spiral due to the differential magnetic moment [249–251] . These two diffusion modes are illustrated in figure 6.1. The table 6.1 presents a summary of the existing experimental studies for both longitudinal and transverse magnetization dynamics, using degenerate Fermi gases in the vicinity of an s-wave resonance.
In the present work, we implemented longitudinal magnetization gradients using a spin separation technique that we will detail now.

6.2 Optimization of the magnetic moment

The spin separation technique consists in applying a magnetic field gradient in order to push the spin states unequally, in proportion to their magnetic moment. In order

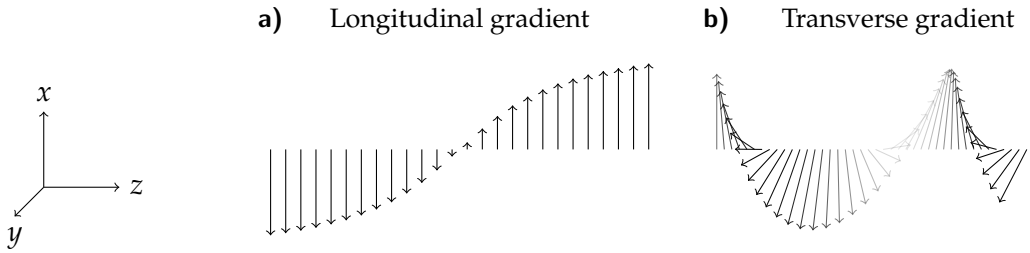

Figure 6.1: Longitudinal and transverse magnetization gradients. Illustration of longitudinal and transverse magnetization gradients. The gradient along a direction associated with a coordinate i is $\partial_i \vec{M} = (\partial_i M)\vec{e} + M(\partial_i \vec{e})$, where $\vec{e}$ is the unit vector locally collinear to $\vec{M}$. The two terms represent the longitudinal and transverse magnetization gradient respectively. a) Purely longitudinal gradient $\vec{M} = M(z)\vec{e}_x$. b) Purely transverse gradient $\vec{M} = M_0(\cos(\kappa z)\vec{e}_x + \sin(\kappa z)\vec{e}_y)$, where M_0 and κ are constants. The arrows represent the magnetization vector.

Dimensionality	Diffusion mode	Spin diffusivity	Reference
3D	longitudinal	$D_{s,\parallel,3D} = 6.3(3)\,\hbar/m$	[247]
3D	longitudinal	not estimated	[246]
3D	transverse	$D_{s,\perp,3D} = 1.08 \pm 0.09^{\pm 0.17}_{-0.13}\,\hbar/m$	[249]
2D	transverse	$D_{s,\perp,2D} = 6.3(3) \times 10^{-3}\,\hbar/m$	[250]
2D	transverse	$D_{s,\perp,2D} = 1.7(6)\,\hbar/m$	[251]

Table 6.1: Spin diffusivity in strongly-interacting Fermi gases. Apart from the noticeable exception of [250], all the experiments observed $D_s \gtrsim \hbar/m$.

to understand the preparation procedure described later in section 6.3, we must first understand evolution of the level structure of ^{40}K in a magnetic field.

We consider the Hamiltonian of a single atom inside a magnetic field with a static component B_z along the z direction. We denote $\hat{\vec{L}}$, $\hat{\vec{S}}$, $\hat{\vec{I}}$ the angular momentum, electronic spin and nuclear spin operator respectively, and introduce $\hat{\vec{J}} = \hat{\vec{L}} + \hat{\vec{S}}$. We denote L, S, I and J the corresponding quantum numbers associated to their norm. The Hamiltonian reads

$$\widehat{H} = \underbrace{\frac{a_{\mathrm{hf}}}{\hbar^2}\hat{\vec{I}}\cdot\hat{\vec{J}}}_{\widehat{H}_{\mathrm{hf}}} + \underbrace{\frac{\mu_B B_z}{\hbar}\left(g_J\hat{J}_z + g_I\hat{I}_z\right)}_{\widehat{H}_z}, \tag{6.3}$$

where $\widehat{H}_{\mathrm{hf}}$ describes the hyperfine structure[1] [130, 133], while $\widehat{H}_z$ describes the Zeeman

[1] In principle, it contains the additional term

$$\frac{b_{\mathrm{hf}}}{\hbar^2}\frac{3(\hat{\vec{I}}\cdot\hat{\vec{J}})^2 + \frac{3}{2}(\hat{\vec{I}}\cdot\hat{\vec{J}}) - \hat{\vec{I}}^2\hat{\vec{J}}^2}{2I(2I-1)J(2J-1)}, \tag{6.4}$$

coupling with the magnetic field B_z. The magnetic dipole constant a_{hf}, as well as the Landé g-factors g_J and g_I can be found in [263]. In the absence of magnetic field, the system is described by the eigenstates $|F, m_F\rangle$ of $\widehat{H}_{\mathrm{hf}}$, where F and m_F are the quantum numbers describing the norm and the projection along z of the total angular momentum operator $\hat{\vec{F}} = \hat{\vec{J}} + \hat{\vec{I}}$. In the presence of a magnetic field however, they no longer constitute a good basis. We focus on the ground state manifold $L = 0$, for which $J = S = 1/2$ and $I = 4$. In that case, it the energy spectrum can be calculated analytically [264] by the so-called Breit-Rabi formula

$$E(B_z) = -\frac{a_{\mathrm{hf}}}{4} + g_I \mu_B m_F B_z \pm \frac{a_{\mathrm{hf}}(I+1/2)}{2}\left(1 + \frac{4m_F\rho}{2I+1} + \rho^2\right)^{1/2}, \tag{6.5}$$

where $\rho = (g_J - g_I)\mu_B B_z/(a_{\mathrm{hf}}(I+1/2))$ is a dimensionless number proportional to the magnetic field, and the sign corresponds to the two manifolds $F = I \pm S$ ($F = 9/2$ and $F = 7/2$, respectively). We will be focusing on the $F = 9/2$ manifold, which has the lowest energies due to the inverted hyperfine structure of ^{40}K . As introduced in section 2.3, we label the states by integers such that they are sorted by increasing energies and correspond to $m_F = -9/2, -7/2, -5/2, \cdots, 9/2$ in Eq. (6.5), see figure 6.2 a). The magnetic moment of each state follows from the definition [265]

$$\mu(B_z) = -\frac{\partial E(B_z)}{\partial B_z}. \tag{6.6}$$

This way, by adding a small linear gradient such that $\vec{B} = [B_z + b(z - z_{\mathrm{CoM}})]\vec{u}_z$, where z_{CoM} the vertical position of the cloud's center of mass, a vertical force $\vec{F} = F_z\vec{u}_z$ is created on center of mass such that

$$F_z \approx \mu(B_z)b. \tag{6.7}$$

Previous experiments on balanced spin-$\frac{1}{2}$ Fermi gases achieved spatial separation through magnetic field gradient using the two lowest energy hyperfine states of ^{6}Li [246, 247]. In that case the nuclear spin is $I = 1$, consequently these states are associated with $m_F = \pm 1/2$, implying that their magnetic moment are opposite and equal in the limit of vanishing field due to Eq. (6.5), which makes them very suitable for separation [246].

In this work, however, we are using ^{40}K also in the two lowest hyperfine states $|1\rangle$ and $|2\rangle$. Due to the large nuclear spin $I = 4$, these states are associated with $m_F = -9/2$ and $m_F = -7/2$ in Eq. (6.5). In that case, the gradient separation is hard to achieve because not only their associated magnetic moment μ_1 and μ_2 point towards the same direction,

but it does not contribute in the ground state manifold considered here.

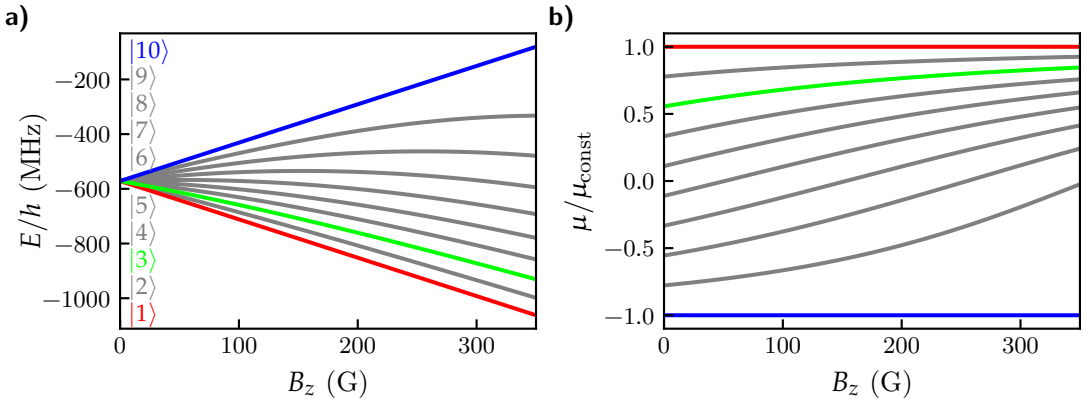

Figure 6.2: Breit-Rabi eigenenergies. a) Energies of the ground state manifold $F = 9/2$, $I = 4$, $J = 1/2$ taking into account the hyperfine structure and the Zeeman shift in a static field B_z, calculated from the Breit-Rabi formula Eq. (6.5). b) The magnetic moments is obtained by differentiation thanks to Eq (6.6). The states $|1\rangle$, $|3\rangle$ and $|10\rangle$ are colored in red, green and blue respectively.

but also their relative difference $\delta_{12}\mu = (\mu_1 - \mu_2)/\mu_2$ is always rather small. Indeed,

$$\delta_{12}\mu(B_z) \leq \delta_{12}\mu(B_z = 0) \approx \frac{9/2 - 7/2}{9/2} \approx 22.22\%. \tag{6.8}$$

This critical limitation makes it necessary to transfer the system in a different pair of states so that an efficient separation can be achieved. The optimal combination is achieved by using states $|1\rangle$ and $|10\rangle$. Eq. (6.5) is linear in $m_F B_z$ when $m_F = \pm 9/2$, leading to constant and opposite magnetic moments $\mu_1(B_z) = -\mu_{10}(B_z) = \mu_{\text{const}}$, $\forall B_z$. Note that $\mu_{\text{const}} = \mu_B(Ig_I + Jg_J) \approx \mu_B > 0$, which means that a positive gradient $b > 0$ generates a force that pushes $|1\rangle$ towards higher z values. The different magnetic moments are shown in figure 6.2 b).

6.3 Separating spins in the tube traps

In short, the experimental procedure to separate and isolate the spin states consists in temporarily populating states $|1\rangle$ and $|10\rangle$ to benefit from the fact that they have opposite magnetic moments in order to separate them using a magnetic field gradient. Then, an optical barrier is applied to keep the two populations separated after removing the gradient. Due to technical reasons, this requires using a large amount of steps that are listed below. They are all depicted in figure 6.3 as well.

1. Initially, the mixture of states $|1\rangle$ and $|2\rangle$ is loaded the crossed optical dipole traps made of the cODT1 and cODT2 beams, as described in section 2.3. However, the recompression value is set to 1.3W instead of 1.07W in order to work with a deeper trap which facilitates the separation process.

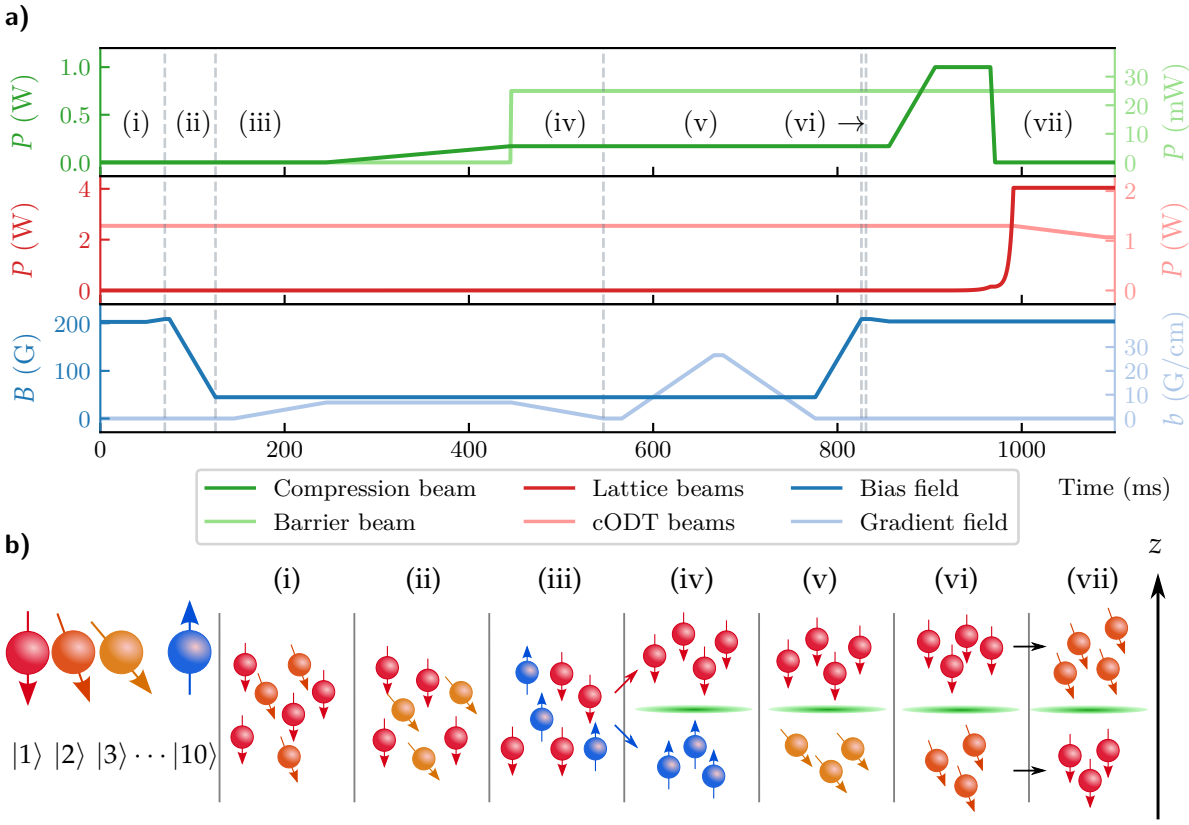

Figure 6.3: Spin separation protocol. a) Representation of the ramps that were implemented in the experimental cycle in order to separate and isolate the spin states. The vertical dashed lines mark of the position of the RF transfers $|2\rangle \rightarrow |3\rangle$, $|3\rangle \rightarrow |10\rangle$, $|10\rangle \rightarrow |3\rangle$, $|3\rangle \rightarrow |2\rangle$, and $|1\rangle \leftrightarrow |2\rangle$ from left to right respectively. b) Illustration of the key intermediate steps in chronological order. The barrier beam is represented in green for steps (iv) to (vii).

2. The bias magnetic field is ramped to 209.7 G, close to the zero crossing of the s-wave Feshbach resonance, see Eq. (2.3).

3. A 5 ms radio-frequency adiabatic linear sweep is performed from 48.45 MHz to 49.15 MHz to achieve to transfer $|2\rangle \rightarrow |3\rangle$.

4. The magnetic field is ramped down to 47.7 G in 50 ms.

5. A 20 ms adiabatic linear sweep is performed from 13.24 MHz to 16.07 MHz to achieve the transfer $|3\rangle \rightarrow |10\rangle$.

6. A magnetic field gradient is ramped up linearly in 100 ms in order to push the spin state $|1\rangle$ and $|10\rangle$ in opposite directions along z.

7. The compression beam is ramped to 170 mW.

8. A barrier beam (see sec. 6.5) is ramped to 25 mW in 1 ms to force the different spin states to stay on their respective sides.

9. The magnetic field gradient is removed with a 100 ms linear ramp.
10. The transfer $|10\rangle \rightarrow |3\rangle$ is performed in 20 ms by inverting the limits of the previous $|3\rangle \rightarrow |10\rangle$ sweep.
11. A magnetic field gradient is ramped up again in 100 ms but to a stronger value until some atoms located in the higher z side start spilling. The gradient is held during 100 ms, and is then ramped down again in 100 ms. This allows to equilibrate the populations on each side of the barrier.
12. The magnetic field is ramped back to 209.7 G is 50 ms. The transfer[2] $|3\rangle \rightarrow |2\rangle$ by performing the same sweep that lead to $|2\rangle \rightarrow |3\rangle$.
13. *Optional*: Depending on whether we want to image the atoms located above or below the barrier beam, the population inversion $|1\rangle \leftrightarrow |2\rangle$ is performed using a linear radio-frequency sweep from 45.32 MHz to 46.72 MHz in 5 ms.
14. The magnetic field is ramped to 203.79 G in 20 ms, which corresponds to the scattering length $a_{3D} = 520 \pm 10 a_0$.
15. The power of the compression beam is increased to 1 W in 50 ms.
16. A single-layer the optical lattice is loaded by ramping the lattice beams exponentially in two steps, in the middle of which the compression beam is ramped off, similarly to figure 3.4 a).
17. The dipole trap is ramped to 1.07 W in 100 ms.

At the end of the process, we obtain two spin-separated clouds in states $|1\rangle$ and $|2\rangle$ loaded in a single layer of the optical lattice. From these initial conditions, spin transport can be studied by removing the barrier beam and letting the system equilibrate. This will be the topic of chapter 7. But before that, we will further detail role of the various steps.

6.4 Spin transfer sequence

In order to transfer spin states, we perform radio-frequency adiabatic sweeps. In that case, we update the Hamiltonian to account for the additional Zeeman coupling with the time-varying magnetic field $B_x(t) = B_{x,0}\cos(\omega_{\mathrm{RF}} t)$ along the x direction originating from the radio-frequency field, such that

$$\widehat{H}_{\mathrm{tot}} = \widehat{H}_{\mathrm{hf}} + \widehat{H}_{\mathrm{z}} + \underbrace{\frac{\mu_B B_{x,0}}{\hbar}\cos(\omega_{\mathrm{RF}} t)\left(g_J \hat{J}_x + g_I \hat{I}_x\right)}_{\widehat{H}_{\mathrm{RF}}}, \tag{6.9}$$

[2] Alternatively, it is possible to omit this transfer and work directly with states $|1\rangle$ and $|3\rangle$, see figure 7.11 for more details.

where the additional term $\widehat{H}_{\mathrm{RF}}$ describes the coupling to the field $B_x(t)$. The Hamiltonian is now time-dependent and hard to solve in its current state. The problem can be simplified by performing a time-dependent unitary transformation using the evolution operator $U = \exp(i\widehat{H}_0 t)$, with $\widehat{H}_0 = \hbar\omega_{\mathrm{RF}}\hat{F}_z$, where $\hat{F}_z$ is the vertical component of $\hat{\vec{F}}$. This transformation leaves $\widehat{H}_{\mathrm{hf}} + \widehat{H}_z$ unchanged as both terms commute with $\hat{F}_z$. The transformed Hamiltonian[3] $\widetilde{H}_{\mathrm{tot}} = U\widehat{H}_{\mathrm{tot}}U^\dagger + i\hbar\dot{U}U^\dagger$ still contains time-dependent terms. Under the rotating wave approximation [266], they are neglected and we are left with

$$\widetilde{H}_{\mathrm{tot}} = \widehat{H}_{\mathrm{hf}} + \widehat{H}_z - \hbar\omega_{\mathrm{RF}}\left(\hat{J}_z + \hat{I}_z\right) + \frac{\hbar\Omega}{4}\left(g_J\hat{J}_x + g_I\hat{I}_x\right). \tag{6.10}$$

We introduced the Rabi angular frequency $\Omega = 2\mu_B B_{x,0}/\hbar$. Contrary to the $\Omega = 0$ case, there are no analytic solutions to this problem. However, this Hamiltonian can be diagonalized numerically as the dimension of the Hilbert space is not large. Calculating the energy spectrum for a given bias field B_z as a function $\nu_{\mathrm{RF}} = \omega_{\mathrm{RF}}/2\pi$ reveals the unavoided and avoided crossings and provides insight regarding to evolution of an initial spin mixture through the sweep.

In the previous section, we argued that working with state combination $|1\rangle$ and $|10\rangle$ is ideal to perform spin separation with a magnetic field gradient. Given an initial is a spin mixture $|1\rangle$ and $|2\rangle$ at $B = 209.7$ G, an ideal operation would consist in directly transferring $|2\rangle \to |10\rangle$ which can be done by adiabatically sweeping over the 8 avoided crossings that separate the initial and the final state while making sure to start sweeping at a frequency larger than the transition between $|1\rangle$ and $|2\rangle$ to ensure that the population in $|1\rangle$ remains unchanged.

While this operation is not fundamentally forbidden, it is technically inconvenient to implement in the experiment. Given that RF sweep limits are usually set empirically and optimized, it is better to be able to resolve the spin state composition when scanning the central frequency of the sweep ramp. At large magnetic field, the absorption imaging technique is spin-selective due to the Zeeman shift. This issue could be bypassed by ramping the magnetic field down before imaging but it introduces another complication. Ramping the bias field through the s-wave resonance between $|1\rangle$ and $|2\rangle$ located 202.1 G leads to the creation of molecules and produces heavy losses [137, 144] if these states are populated. Therefore, this can severely bias the optimization of the ramp.

Consequently, we implemented a technique that uses more steps but allow for a better monitoring. As indicated in section 6.3, we start by transferring $|2\rangle \to |3\rangle$. This way, we end up with a spin composition made of a mixture of $|1\rangle$ and $|3\rangle$. For this pair of states, an s-wave resonance was identified at ~ 224.21 G and a p-wave resonance at ~ 215 G [267–270][4]. However, no additional resonances were referenced for smaller magnetic

[3] The symbols †, $\dot{}$ denote hermitian conjugation and total derivative with respect to time, respectively.

[4] For convenience, all these references were gathered in [88].

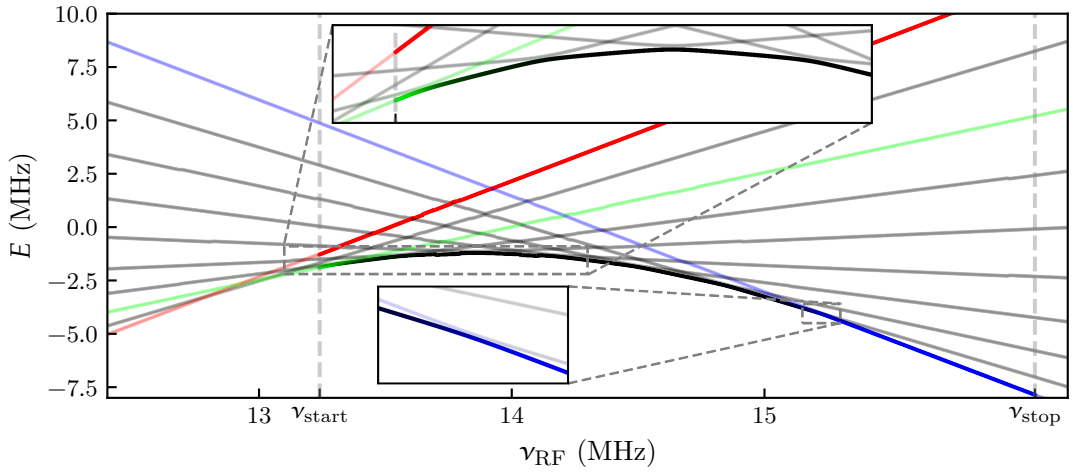

Figure 6.4: Selective adiabatic transfer. Evolution of the energies obtained by numerically diagonalizing Eq. (6.10) as a function of $\nu_{\text{RF}} = \omega_{\text{RF}}/2\pi$, for a static field $B_z = 44.7$ G and Rabi frequency $\Omega = 2\pi \times 30$ kHz. The frequencies $\nu_{\text{start}} = 13.24$ and $\nu_{\text{start}} = 16.07$ represent the sweep range limits, as presented in section 6.3. We set the RGB color values for each ν_{RF} to be $|\langle 1|\phi\rangle|^2$, $|\langle 3|\phi\rangle|^2$ and $|\langle 10|\phi\rangle|^2$ for red, green and blue respectively, where $|\phi(\nu_{\text{RF}})\rangle$ are the normalized eigenstates. For clarity, the relevant states are represented with opaque data points within the sweep range. This way, the initial state $|3\rangle$ at $\nu_{\text{RF}} = \nu_{\text{start}}$ and the lowest energy can be adiabatically transferred to $|10\rangle$ after a succession of 7 avoid crossing (the path it follow turns from green to blue), whereas $|1\rangle$ encounters no avoided crossings in the sweep range (the corresponding path stays red). The two zoomed insets highlight some of the relevant avoided crossings. The energy was defined with an offset such that the average energy over all the states in the absence of RF field is zero.

fields. Thus, we can safely reduce the value of the magnetic field without risking losses and heating.

We chose the value of 44.7 G to perform the sweep[5] $|3\rangle \rightarrow |10\rangle$. The figure 6.4 depicts the evolution of the spin population through the adiabatic sweep, assuming $\Omega = 2\pi \times 30$ kHz[6]. This way we can ramp the field to a small value ~ 1 G so that we can image all the spin states[7], as shown in figure 6.5.

With the optimized sweep, a magnetic field gradient allows us to achieve full separation of the spin states as shown in figure 6.5 c), while d) shows how the separation can be kept by an optical barrier after removing the magnetic gradient. The next section is devoted to give more details about this optical barrier.

[5] During the writing of this manuscript, we realized the existence of a p-wave resonance located at 44.7(2) G which enhances inter-species collisions in $|9\rangle$. Given our observations around another p-wave resonance in figure 7.11, we do not expect this resonance to significantly alter the atomic sample as the atomic density and temperature during this sweep are lower than those of the mentioned measurement.

[6] A Rabi oscillation measurement revealed that our RF antenna can create Rabi frequencies up to $\Omega = 2\pi \times 80$ kHz [89].

[7] However, the various spin states do not couple equally strongly to the probe beam and will have different detectivities.

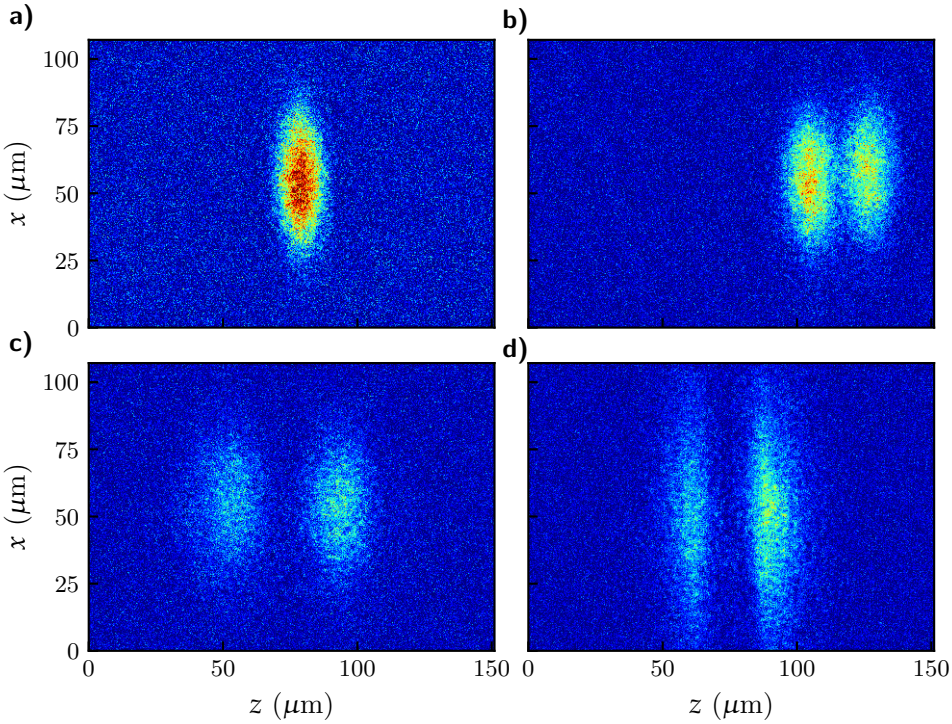

Figure 6.5: Multi-spin imaging at low field. By ramping the magnetic field to ∼1 G, it is possible to image all the spin states simultaneously. a) Image of the gas in the absence of magnetic gradient, giving a reference for the center of the crossed dipole trap along z. b) Magnetic gradient applied to a mixture of states $|1\rangle$ and $|3\rangle$ in the crossed dipole trap. c) Weaker magnetic gradient applied to a mixture of states $|1\rangle$ and $|10\rangle$ in the crossed dipole trap and a weak compression beam potential. d) Same states $|1\rangle$ and $|10\rangle$ without the magnetic gradient. The barrier beam was added to keep spins separated.

6.5 Optical barrier potential

In order to keep the atoms separated after removing the magnetic field gradient, we use a blue-detuned elliptical beam to create a barrier which forces the two spin populations to stay on their respective sides. This standard technique was used in other experiments, for instance [240, 246].

We create the elliptical beam profile with same $\lambda = 532$ nm laser source used for the compression beam 3.2.5. The setup after the mode-cleaning optical fiber is shown in 3.6 b). A cylindrical telescope is used to shape the elliptical Gaussian beam profile, and the beam is later on overlapped with the compression beam and shot along the x direction. The intensity is regulated with a setup similar to the compression beam. The theoretical beam profile is obtained from a slight modification of Eq. 2.2 which, at the focus [271], reads

$$I(\vec{r}) = \frac{2P_{\text{tot}}}{\pi w_y w_z} \exp\left(-\frac{2y^2}{w_y^2} - \frac{2z^2}{w_z^2}\right), \tag{6.11}$$

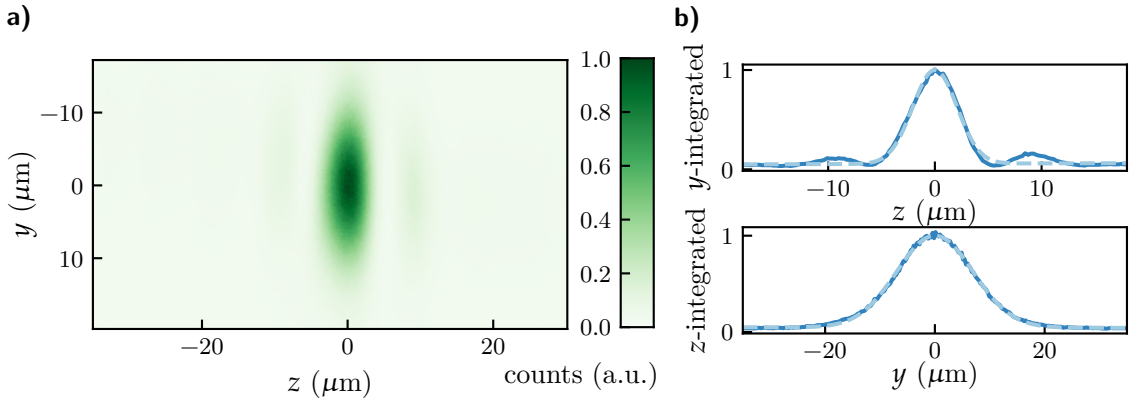

Figure 6.6: Optical barrier profile. a) Elliptical Gaussian profile of the barrier beam. b) Fits of the integrated line profiles with Eq (6.11), yielding $w_z = 4.15 \pm 0.05$ μm and $w_y = 13.95 \pm 0.04$ μm. Along the short direction, side fringes are imprinted due to the finite resolution of the focusing optical system prior to the atoms.

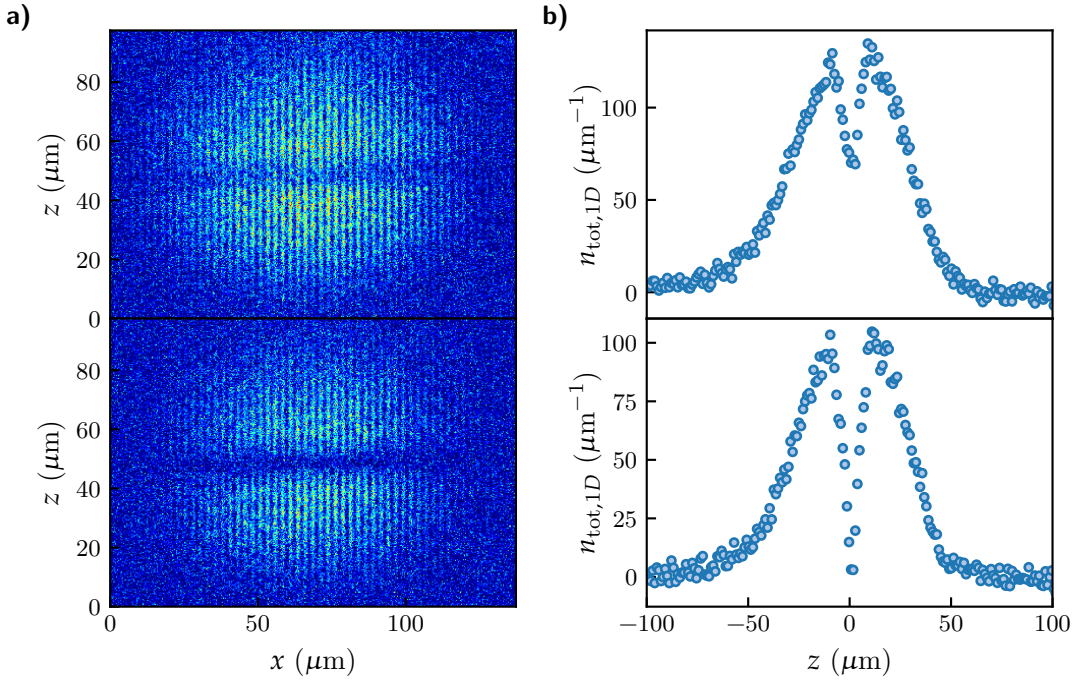

Figure 6.7: Atomic sample with a low optical barrier and no prior spin-separation. a) The optical barrier is ramped up to low power on the initially equilibrated spin-1/2 Fermi gas. As a result, a dent appears on the integrated density profile. Only one spin component is imaged. b) Similar conditions, but the optical barrier is higher. Above a certain optical power, the barrier completely prevents exchanges between the top and bottom sides.

where P is the optical power, w_y and w_z are the waists along the y and z directions respectively, and propagation along x is assumed. The beam was imaged along the x camera and is shown in figure 6.6. The fitted waists are $w_z = 4.15 \pm 0.05$ μm and $w_y = 13.95 \pm 0.04$. The position of the optical barrier can be optimized by applying it to a cloud loaded in the optical lattice with no prior spin-separation, leading to images shown in figure 6.7. Even though it is the largest of the two, the waist along y is rather small and it is necessary to shoot the compression beam to prevent atoms from bypassing the barrier before they are loading in the optical lattice, hence the need for step 7 of section 6.3. The barrier height can be estimated using Eq. (2.1). A power of 25 mW was found to be sufficient to prevent mixing from occurring. Assuming ideal alignment, it corresponds to a barrier height per temperature unit of

$$U(\vec{r}=0)/k_B = \frac{2\alpha_{\text{pol}}P}{\pi k_B w_y w_z} = 16.3 \pm 0.01 \ \mu\text{K}. \tag{6.12}$$

which happens to sufficient to keep spin states isolated, including during the spilling phase (step 11 in section 6.3). It is larger than the typical temperatures obtained in figures 7.8 and 7.9. However, a few amount of atoms can still cross the barrier during and after the optical lattice loading phase.

6.6 Alternate imaging

Once the barrier beam is ramped up, the spin transfers described in section 6.4 are reversed to go back to a mixture of $|1\rangle$ and $|2\rangle$ at high fields $B_z \gtrsim 200$ G, and as mentioned before, the absorption imaging is spin selective. However, as described in section 4.1, it is better to image state $|1\rangle$ and take advantage of its quasi-cycling transition which facilitates quantitative reconstruction of the density profiles.

In order to study transport phenomena, we need to trace the dynamics of each spin population. By default, after the spin separation procedure, the atoms populating state $|1\rangle$ end up above the barrier (higher z) whereas those of state $|2\rangle$ end up below it (lower z). In order to be able to image reliably the population below the barrier, we exchange the spin populations by performing an adiabatic radio-frequency sweep across the splitting between $|1\rangle$ and $|2\rangle$. This process has no influence on the further evolution of the atomic sample has long as no magnetic field gradient exist on the atomic region. This way, the difference in magnetic moments μ_1 and μ_2 do not matter and the external potential in which the two populations evolve is exclusively set by the optical potential through the dipole force, which is spin-independent.

It is important to disentangle the hyperfine states and the population above and below the barrier. From now on, we will refer to the majority population prepared above the barrier as spin up, or $\uparrow$, and the other one spin down, or $\downarrow$. It is clear from the explanations above

that the population of $\uparrow$ can be either in the hyperfine state $|1\rangle$ or $|2\rangle$, as shown in figure 6.8.

6.7 Population balance

If the spilling step is omitted (step 11 in sec. 6.3), we end up with asymmetric populations between $\uparrow$ and $\downarrow$ after loading the lattice. This arises from the fact that the population of $\downarrow$ is reduced upon ramping the optical lattice. This effect originates from the longitudinal expansion of the cloud following the change of trap geometry. It results in spilling happening exclusively on the lower side of the barrier which has a smaller depth.
We mitigate this issue by creating controlled spilling on the other side of the barrier as well, using a magnetic field gradient $b > 0$. During that phase, the system is in a mixture of $|1\rangle$ and $|3\rangle$, where the former is located above the barrier and the latter below. Because μ_1 and μ_3 are both positive (see fig. 6.5 b)), $|3\rangle$ is pushed against the barrier, which happens to be strong enough to prevent tunnelling from happening, whereas $|1\rangle$ is displaced vertically toward higher z as b is increased. The gradient is tuned in such a way that $\uparrow$ population partially spills out of the trap.
Ultimately, we are able to load the separated spin states in a single layer of tube traps while keeping a low amount of imbalance. With the spilling compensation technique, we are able to keep the population imbalance below 20% over long time series. A typical series of absorption images is shown in figure 6.9, featuring the optical density difference between $\uparrow$ and $\downarrow$ which is proportional to the local magnetization.

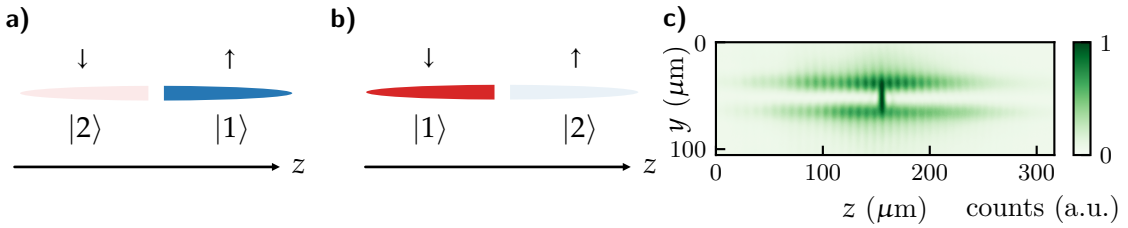

Figure 6.8: Alternated spin-selective absorption imaging. a) By default after the spin separation 6.3, the cycling imaging transition of state $|1\rangle$ reveals the atoms prepared above the green barrier, which we identify as spin up $\uparrow$ population. b) When the exchange $|1\rangle \leftrightarrow |2\rangle$ is made (see step 13 in sec. 6.3), it reveals the atoms prepared below the green barrier, which we identify as spin down $\downarrow$ population. c) Camera image taken along x when both the compression beam (see fig. 3.11) and the barrier beam (see fig. 6.6) are simultaneously present and aligned.

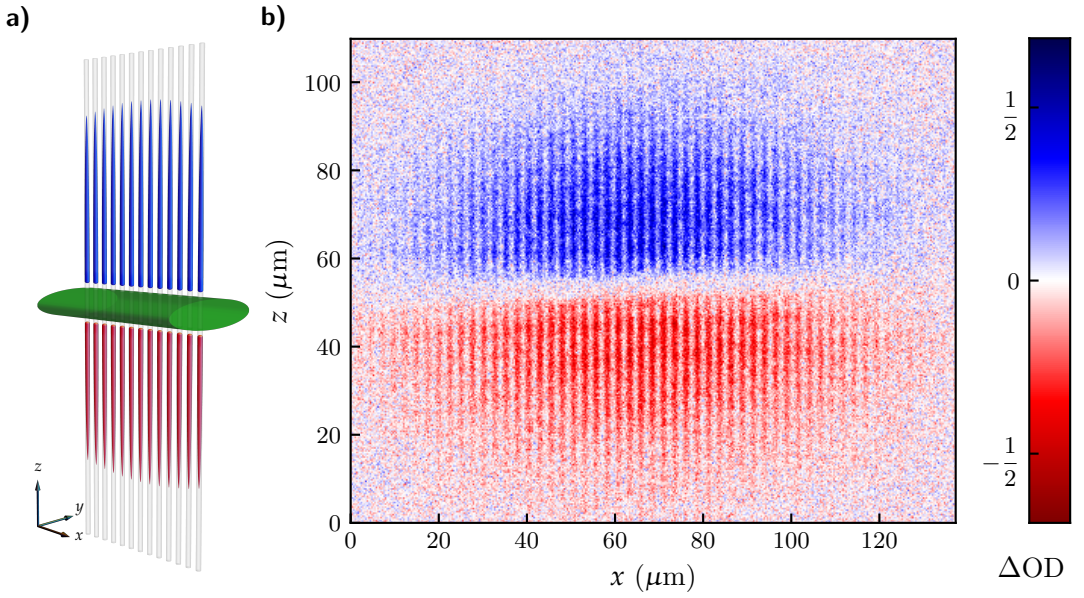

Figure 6.9: Separated spins in the tube traps. a) 3D sketch of the two spin components being separated and loaded in a single layer of the two-dimensional lattice. The compression beam is represented in green, the spin up and down components in blue and red respectively, and the grey tubes materialize a single layer of tube traps. b) Optical density difference $\Delta\mathrm{OD} = \mathrm{OD}_\uparrow - \mathrm{OD}_\downarrow$, where $\mathrm{OD}_\uparrow$ and $\mathrm{OD}_\downarrow$ denote the optical densities of the spin up and spin down components, respectively. The resulting image was obtained from averaging 12 shots of $\uparrow$ population and 12 shots of $\downarrow$ population. The typical atom number ratio in each tube trap for this image is $N_\uparrow/N_\downarrow = 1.2$.

Chapter 7

Spin transport in a tight atomic waveguide

In chapter 6 we have presented an experimental scheme that successfully prepares spin-separated ^{40}K atoms by means of an optical barrier applied to the loaded layer of the two-dimensional lattice. In the present chapter we will analyse the dynamics arising from

the sudden release of the barrier, focusing on the regime of strong interactions leading to spin diffusion.

7.1 Interactions in a tight atomic waveguide

In chapter 5 we studied the thermal equilibrium properties of quantum wires in the non interacting regime. In order to define transport coefficients from a microscopic perspective, the role of interactions on the few-body level must be clarified. In this chapter, we briefly present the formalism that describes two-body scattering in a tight atomic waveguide, and the appearance of a confinement induced resonance (CIR) in the one-dimensional limit.

7.1.1 Two-body scattering

We consider a two-body Hamiltonian describing the kinetic energy of two particles of identical mass m located by $\vec{r}_1$ and $\vec{r}_2$, which are subject to an external transverse harmonic potential of angular frequency $\omega_\perp$ and an interaction potential $V(\vec{r}_1 - \vec{r}_2)$. The CoM motion decouples from the relative motion of the particles. We will exclusively focus on the latter as the former does not couple to interactions. The Hamiltonian of the relative motion reads

$$\widehat{\mathcal{H}}_{\text{rel}} = -\frac{\hbar^2}{2\mu}\widehat{\nabla}_{\vec{r}}^2 + \frac{1}{2}\mu\omega_\perp^2\rho^2 + V(\vec{r}), \tag{7.1}$$

where $\vec{r} = \vec{r}_1 - \vec{r}_2 = (\rho, \phi, z)$ in cylindrical coordinates, and $\mu = m/2$ is the reduced mass. In the absence of interactions, we can write $\widehat{\mathcal{H}}_{\text{rel}} = \widehat{\mathcal{H}}_z + \widehat{\mathcal{H}}_\perp$ where the first term contains only the kinetic term along the z direction and is solved by plane waves $\sim e^{ikz}$, and the second term corresponds to the transverse harmonic oscillator. In contrast to chapter 5, we will use the basis $|n, m_\perp\rangle$ for the transverse states, which simultaneously diagonalizes the transverse Hamiltonian $\widehat{\mathcal{H}}_\perp$ and the angular momentum along the z-axis, denoted $\hat{L}_z$. It satisfies the following properties,

$$\widehat{\mathcal{H}}_\perp|n, m_\perp\rangle = \hbar\omega_\perp(2n + |m_\perp| + 1)|n, m_\perp\rangle, \qquad n = 0, 1, 2, ..., \infty, \tag{7.2}$$

$$\hat{L}_z|n, m_\perp\rangle = \hbar m_\perp|n, m_\perp\rangle, \qquad m_\perp = 0, \pm1, \pm2, ..., \pm\infty. \tag{7.3}$$

In order to understand the role of interactions, we focus on scattering solutions of the form

$$|\psi(\mathcal{E})\rangle = |\psi_{0,n,m_\perp}(\mathcal{E})\rangle + |\psi_s(\mathcal{E})\rangle\,, \tag{7.4}$$

where $|\psi_{0,n,m_\perp}(\mathcal{E})\rangle$ is an incident longitudinal plane wave of wavevector k and transverse state $|n, m_\perp\rangle$. Its normalized energy was defined

$$\mathcal{E} = \frac{E}{2\hbar\omega_\perp} - \frac{1}{2} = \frac{(a_\perp k)^2}{2} + n + \frac{|m_\perp|}{2}, \tag{7.5}$$

where $a_\perp = \sqrt{\hbar/m\omega_\perp}$ is the transverse harmonic oscillator length[1]. The incident wavefunction can be conveniently calculated at the radial origin

$$\langle \rho = 0, z | \psi_{0,n,m_\perp}(\mathcal{E}) \rangle = \frac{\delta_{m_\perp,0}}{\sqrt{2\pi} a_\perp} e^{ikz}, \quad \forall n \tag{7.6}$$

and reveals that only incident waves with zero angular momentum $m_\perp = 0$ can scatter in the $s-$wave approximation. We will exclusively consider this regime in the ensuing sections, and thus the role played by interactions is fully encoded in the scattering length[2] a_{3D}. From now on, we assume $m_\perp = 0$. The scattered wavefunction $|\psi_s(\mathcal{E})\rangle$ was calculated in [272] and yields

$$\langle n', m'_\perp, z \, | \psi_s(\mathcal{E}) \rangle = -\frac{i}{\sqrt{2}} \frac{\delta_{m'_\perp,0}}{\left[\frac{a_\perp}{a_{3D}} + \frac{1}{\sqrt{2}} \zeta(1/2, -\mathcal{E}) \right]} \frac{e^{i \frac{\sqrt{2}}{a_\perp} \sqrt{\mathcal{E}-n'} |z|}}{\sqrt{\mathcal{E}-n'}} \tag{7.7}$$

Consequently, the full wavefunction reads

$$\langle \vec{r} | \psi(\mathcal{E}) \rangle = \sum_{n'=0}^{+\infty} \langle \rho, \phi | n', m_\perp = 0 \rangle \left[\delta_{n,n'} e^{ikz} + f(k_{n'} \leftarrow k_n)_{n' \leftarrow n} e^{i k_{n'} |z|} \right], \tag{7.8}$$

where the $f(k_{n'} \leftarrow k)_{n' \leftarrow n}$ coefficients represent the transversely elastic even-wave scattering amplitudes when $n = n'$, and transversely inelastic otherwise, whose expressions are given by

$$f(k_{n'} \leftarrow k)_{n' \leftarrow n} = -\frac{i}{a_\perp k_{n'}} \frac{1}{\left[\frac{a_\perp}{a_{3D}} + \frac{1}{\sqrt{2}} \zeta\left(1/2, -\frac{(a_\perp k)^2}{2} - n\right) \right]}, \tag{7.9}$$

where $\zeta(\cdots, \cdots)$ is the Hurwitz zeta function [273, 274] and $k_{n'}$ is the outgoing mode-dependent wavevector

$$k_{n'} = \frac{\sqrt{2}}{a_\perp} \sqrt{\frac{(a_\perp k)^2}{2} + n - n'}. \tag{7.10}$$

Obviously, $k_n = k$ is the incident wavevector. The associated transmission and reflection coefficients are given by [272]

$$T(k_{n'} \leftarrow k)_{n' \leftarrow n} = \Theta[\mathcal{E} - n'] \sqrt{\frac{\mathcal{E} - n'}{\mathcal{E} - n}} |\delta_{n,n'} + f(k_{n'} \leftarrow k)_{n' \leftarrow n}|^2, \tag{7.11}$$

$$R(k_{n'} \leftarrow k)_{n' \leftarrow n} = \Theta[\mathcal{E} - n'] \sqrt{\frac{\mathcal{E} - n'}{\mathcal{E} - n}} |f(k_{n'} \leftarrow k)_{n' \leftarrow n}|^2. \tag{7.12}$$

Here, $\Theta[...]$ is the Heavyside step-function. The reflection and transmission coefficients are equal when $n \neq n'$. We can define the total reflection coefficient, starting from the

[1] In the original studies [73, 74, 272], $a_\perp$ is defined with the reduced mass μ through $a_\perp = \sqrt{\hbar/\mu\omega_\perp}$.
[2] We neglect finite-range corrections.

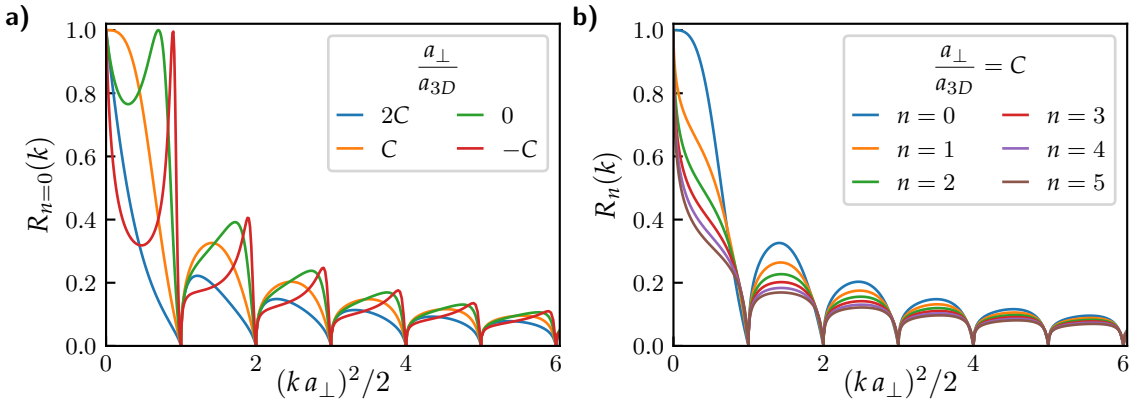

Figure 7.1: Total reflection coefficient in a tight atomic waveguide. We defined the constant $C = -\zeta(1/2)/\sqrt{2} = 1.03263...$ to quantify the shift of the CIR, which occurs when $a_\perp/a_{3D} = C$. a) Reflection coefficient of the transverse ground state mode. At low energies, the reflection coefficient saturates to 1. The reflection coefficient is independent of k to first order in k around 0 at the CIR. b) Reflection coefficient at the CIR for several incident modes n. When n becomes large, there are no longer differences between the modes. Only the $n = 0$ reflection coefficient features an horizontal asymptote when $k^2 \to 0$. Despite the resonant structure that makes the coefficients vanish when $(ka_\perp)2/2$ is a strictly positive integer, we observe that the reflection coefficients globally decays quadratically as $ka_\perp$ increase, which is reminiscent of the 3D free-space cross section result $\sigma(k) = 1/(1/a_{3D}^2 + k^2)$.

incident mode n with wavevector k, by summing all the outgoing modes

$$R_n(k) = \sum_{n'=0}^{+\infty} R(k_{n'} \leftarrow k)_{n' \leftarrow n} \tag{7.13}$$

These coefficients are easily calculated numerically. But before plotting them, it is insightful to consider scattering in 1D limit.

7.1.2 One-dimensional limit

When $\mathcal{E} < 1$, the incident wave has to be in the transverse ground state $n = 0$ and cannot scatter inelastically towards higher transverse modes due to energy conversation. The only relevant scattering amplitude element is

$$f_{1D}(k) = -\frac{1}{1 + ia_{1D}k - i\frac{a_\perp k}{\sqrt{2}}\mathcal{L}\left(\frac{a_\perp^2 k^2}{2}\right)}, \tag{7.14}$$

which corresponds to $f(k \leftarrow k)_{0\leftarrow 0}$ from Eq. (7.9) and was initially calculated in the absence of transverse modes [73]. We introduced the one-dimensional scattering length

a_{1D} and the $\mathcal{L}$ function such that

$$a_{1D} = -a_\perp \left[\frac{a_\perp}{a_{3D}} + \frac{\zeta(1/2)}{\sqrt{2}} \right], \tag{7.15}$$

$$\mathcal{L}(\mathcal{E}) = \sum_{j=1}^{+\infty} \frac{(2j-1)!!\zeta(j+1/2)}{2^j j!} \mathcal{E}^j, \tag{7.16}$$

where $\zeta(\cdots)$ is the zeta function. A confinement-induced resonance (CIR) occurs when $a_\perp/a_{3D} = -\zeta(1/2)/\sqrt{2} \approx 1.03263$, which is detuned to be BEC side compared to the Feshbach resonance. At the CIR, $a_{1D} = 0$ and therefore the scattering amplitude saturates to 1 to second order in k around 0. This peculiar property can be seen on the reflection coefficients shown in figure 7.1. Conceptually, it seems appropriate to describe the system with an effective one-dimensional contact potential in such a way that the scattering amplitude of Eq. (7.14) is recovered. However, due to absence of a transverse length scale in a 1D world, it is impossible to reproduce the higher order terms $\mathcal{O}(a_\perp^3 k^3)$. Remarkably, the leading order can be reproduced using

$$V_{1D}(z) = g_{1D}\delta(z) \qquad g_{1D} = -\frac{2\hbar^2}{m a_{1D}}, \tag{7.17}$$

and provides a correct description of the two-body scattering properties at low energies[3], even though it does not capture the bound state accurately for every value of g_{1D}. The evolution of a_{1D} and g_{1D} are shown in 7.2 a).

7.1.3 Bound state

There exists a single bound state of energy E_b which can be calculated through the implicit equation

$$\frac{\zeta\left(1/2, -\frac{E_b}{2\hbar\omega_\perp}\right)}{\sqrt{2}} = -\frac{a_\perp}{a_{3D}}. \tag{7.18}$$

In the limit $a_{3D}/a_\perp \to 0^-$, it converges to $E_{b,\delta-1D} = -m g_{1D}^2/4\hbar^2$ which happens to coincide with the bound state that is calculated in two-body problem in 1D with the potential given by Eq. (7.17), and exists only when $a_{1D} < 0$. In the limit $a_{3D}/a_\perp \to 0^+$, it converges to the free-space bound state of the contact potential in three dimensions $E_{b,\delta-3D} = -\hbar^2/m a_{3D}^2$, which exists only when $a_{3D} > 0$. At the CIR, it can be calculated explicitly as $E_b = -2\hbar\omega_\perp$. These properties are represented in figure 7.2 b). Note that this formula and all the other results of this section are derived in the context on an

[3] However, on the many-body level, this effective description cannot capture entirely the scattering events involving $q \geq 3$ particles. For instance, the process where a first particle virtually scatters to a higher transverse mode from a second particle, and then virtually scatters off this mode through a third particle is not captured. This leads to higher order corrections at large densities for q-body correlators.

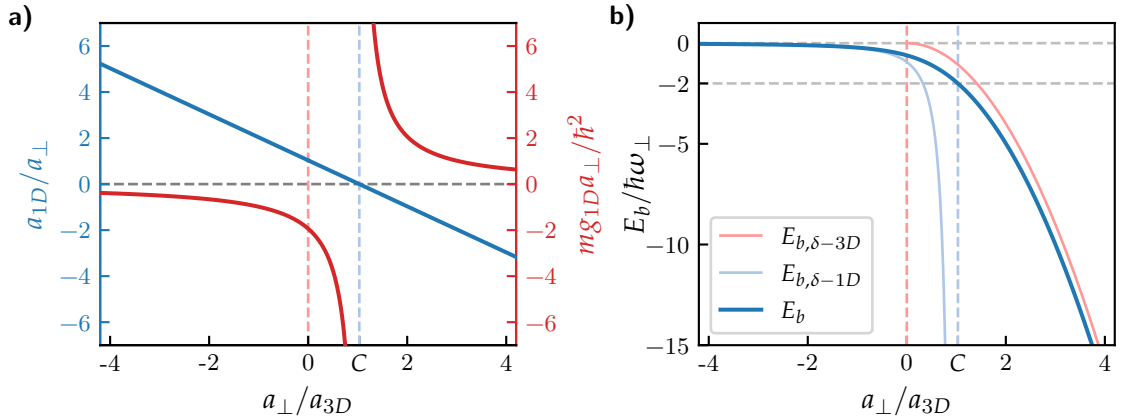

Figure 7.2: Quasi-1D scattering and bound state. a) Evolution of the normalized 1D scattering length (blue) and the normalized 1D coupling strength (red) as a function of the ratio $a_\perp/a_{3D}$. Note that in 1D the coupling strength is maximum when the 1D scattering length vanishes, contrary to 3D. This occurs at the CIR, around which one can tune g_{1D} to $\pm\infty$. b) Evolution of the bound state energy as a function of $a_\perp/a_{3D}$ in blue. The bound states of the delta potential in 1D and 3D and represented in light blue and light red respectively to highlight the asymptotic behaviour of E_B. In contrast to the 3D situation, the bound state exists on the two sides of the resonance.

infinitely deep waveguide. In a waveguide of finite depth, the spacing between the discrete transverse level is no longer constant which leads to new collision channels, and the presence of a continuum of states can significantly change the influence of virtual transverse excitations [272]. In figure 4.3 a), we notice that the ratio between that depth of the waveguide in each direction and the corresponding trap frequency quantum is ~ 23.5 at $\omega_\perp \approx 2\pi \times 17.0$ kHz.

7.1.4 Confinement-induced resonance

Initially derived with a single mode model and a zero-range potential [73], this resonance was shown to be robust for finite potentials at the two-body [74] and many-body levels [275] using numerical simulations. It is characterized by a diverging one-dimensional coupling strength g_{1D}, which correctly describes scattering events a low energy. Experimentally CIRs were observed in many-body system in 1D and 2D by observing the induced enhanced losses and heating [76]. Confinement induced-molecules were observed using radio-frequency spectroscopy to probe the bound-state energy [75].
Using the CIR, a one-dimensional BCS-BEC crossover can be realized. The inverse coupling constant g_{1D} can be varied from $-\infty$ to $+\infty$ and the system evolves from a BCS-like state through a Tonks-Girardeau gas and finally to a weakly interacting Bose gas of dimers [276].
In this section, we focused on $s-$wave scattering in the three-dimensional potential which leads to even-wave in the tight atomic waveguide in Eq. (7.8). In a more general situation,

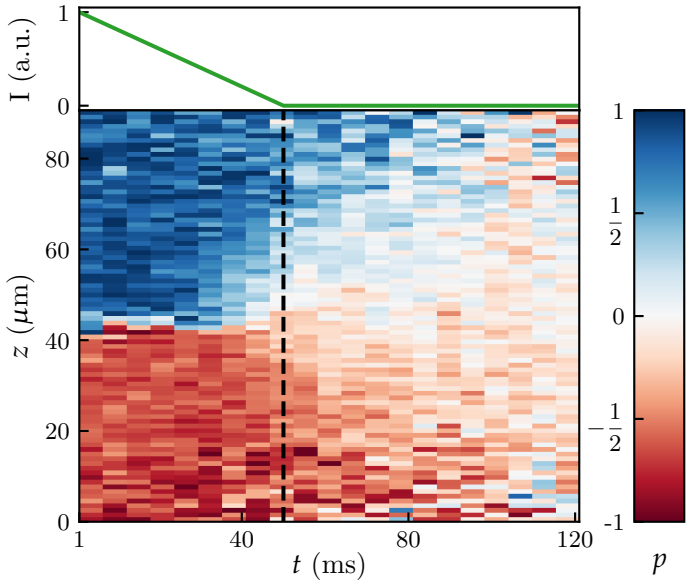

Figure 7.3: Magnetization dynamics. 2D plot representing the evolution of the polarization $p = (n_{1D,\uparrow} - n_{1D,\downarrow})/(n_{1D,\uparrow} + n_{1D,\downarrow})$ in a single tube trap. Each pixel is horizontally associated with time value that varies from 1 ms to 121 ms in steps of 6 ms. Initially, the polarization is close to ± 1 because the green barrier is hermetic. During and after the 50 ms linear ramp down of the barrier, the spin states mix until polarization gradients are smoothed out, thanks to interactions. This set corresponds to $a_{3D} = \infty$ and $\omega_\perp = 2\pi \times 16.5$ kHz.

odd-wave scattering would be described by additional terms proportional to $\mathrm{sign}(z)e^{ik_{n'}|z|}$, but in our case their associated scattering amplitudes were suppressed due to the isotropy of the s-wave potential. CIR have been predicted to also occur around a p-wave resonance [277]. In that case, it was experimentally observed that scattering in $|m| = 1$ states is also allowed and lead to a resonance that is shifted with respect to $m = 0$ scattering [278].

7.2 Magnetization dynamics

It is time to come back to the spin-separated clouds prepared in chapter 6. Since we realize a spin-1/2 system, the total magnetization is defined[4] as $M = n_{1D,\uparrow} - n_{1D,\downarrow}$. From this starting condition, we can initiate magnetization dynamics by simply ramping down the green barrier, as shown in figure 7.3. The goal of the current section is to provide an overview of the key quantities of the dynamics, the parameter regime, and how easily accessible observables evolve over time to understand better the behaviour of the system at the vicinity of an $s-$wave resonance. After the spin separation described in figure 6.3, we ramp the magnetic field to the final target value in 20 ms to set the scattering length to our needs, and hold 20 ms before releasing the barrier.

[4] Defined this way, M should be though of as the integrated magnetization in 3D geometry, or summed over all the transverse modes in a tight waveguide picture.

7.2.1 Releasing the barrier

The evolution of the system strongly depends on the way the green barrier is removed, and the strength of interactions. If the barrier is switched off abruptly, the two spin components acquire a larger relative momentum before attempting to interpenetrate each other. In 3D it was observed that the two spin components can bounce off each other provided interactions are strong and the relative momentum of the two spin clouds is large enough [247]. Conversely, when the relative momentum is small the spin components slowly merge [246, 247]. In addition to the relative center of mass motion, the velocity distribution is also affected. The optical barrier used here is very sharp compared to the tube trap potential. After a sudden switch off, the distributions of each spin component with respect to their center of mass need some time to readjust. We observed that in the presence of strong interactions, the spatial distribution of both spin components rapidly adapts to a Gaussian.

Let us start by looking at the density distribution along z integrated along all the tube traps to have a global picture. We fit the total density of each spin component with

$$n_{\mathrm{tot},1D,s}(z,t) = A_s \exp\left[-\frac{(z-d_{\mathrm{tot},s}(t))^2}{2\sigma^2_{\mathrm{tot},s}(t)}\right], \qquad s = \uparrow,\downarrow . \tag{7.19}$$

In figure 7.4, we present how $d_{\mathrm{tot},s}(t)$ and $\sigma_{\mathrm{tot},s}(t)$ evolve over time from two different initial conditions, and for $a_{3D} = \infty$. In a), we perform the abrupt $\sim$10 ns switch at $t = t_{\mathrm{switch}}$, whereas in b) we linearly ramp down the barrier in 50 ms, and denote $t_{\mathrm{ramp\ end}}$ the instant where the ramp finishes.

In the first case, we observe a rapid expansion of the cloud sizes $\sigma_{\mathrm{tot},s}(t)$ after $t = t_{\mathrm{switch}}$ due to the initial compression imposed by presence of the barrier. Also, we propose to interpret the evolution of $d_{\mathrm{tot},s}(t)$ the following way. The $\uparrow$ population, initially located on the steep side of the potential, acquires more momentum than the $\downarrow$ population before their first contact. As a result from this asymmetric situation, we observe that the $\downarrow$ population is temporarily pushed back at $t \sim 5$ ms, while the $\uparrow$ population is simply slowed down after the impact. Remarkably, the position of the turning point of the $\downarrow$ spin state after this event coincides with $T_{\mathrm{ho}}/2 = 5.2$ ms which corresponds to the half-period a harmonic trap associated with an angular frequency $\omega_{\parallel} = 2\pi \times 96$ Hz, corresponding to the central curvature of the trap. The rest of the dynamics is a slow merging of the two spin components.

In the second case, where the optical barrier a removed slowly, the evolution after $t = t_{\mathrm{ramp\ end}}$ is similar to the late stage of first the case. However, it allows for a more symmetric decay of the center of masses of each component, and also reduce the overall variability of $\sigma_{\mathrm{tot},s}(t)$. The decay of each center of mass agrees very well with an expo-

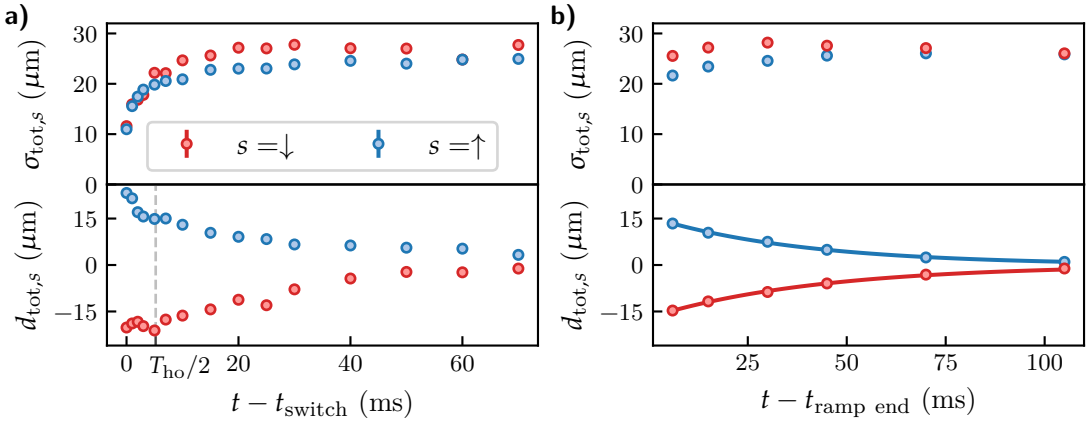

Figure 7.4: Influence of the green barrier ramp. a) Evolution of the fitted Gaussian position $d_{\mathrm{tot},s}$ and width $\sigma_{\mathrm{tot},s}$ after a sudden release of the green barrier occurring at $t = t_{\mathrm{switch}}$. The dashed line represents $T_{\mathrm{ho}}/2 = 5.2$ ms, defined in the main text. b) Similar plot, but instead the optical power of the green barrier is ramped down linearly in 50 ms and vanishes at $t = t_{\mathrm{ramp\ end}}$. The lines correspond to an exponential fit, which feature $\tau_{\mathrm{tot},\uparrow} = 38.8 \pm 0.9$ ms and $\tau_{\mathrm{tot},\downarrow} = 42.8 \pm 1.5$ ms.

nential law $d_{\mathrm{tot},s}(t) = d_{\mathrm{tot},0,s} e^{-t/\tau_{\mathrm{tot},s}}$. This ramp strategy is better suited to studying the diffusive properties of the cloud, and it is the one we will adopt in the rest of this chapter. We will always start measuring at $t = 4$ ms, where profiles are seen to fit very well with a Gaussian ansatz. We notice that despite the improvements, slight asymmetries between $\uparrow$ and $\downarrow$ populations are still noticeable at short time. We discuss their origin in the next section.

7.2.2 Asymmetry of the potential

The asymmetry of potential has a noticeable effect on several level. For later quantitative analysis, it is insightful to estimate the role it plays.

We introduce the local angular frequency of our reconstructed potential as

$$\omega_{\mathrm{loc}}(z) = \sqrt{\frac{\partial_z^2 V_{\parallel}(z)}{m}}, \tag{7.20}$$

where $V_{\parallel}$ is the reconstructed potential obtained from the protocol described in 5.3.2. By definition, $\omega_{\mathrm{loc}}(z = z_0) = \omega_{\parallel}$ if z_0 corresponds to the minimum of the trap, and $\omega_{\parallel}$ the curvature around it, expressed in angular trapping frequency unit (see sec. 4.4). We reconstructed the potential landscape at two lattice powers that correspond to transverse angular frequencies of $\omega_{\perp} = 16.5$ kHz and $\omega_{\perp} = 10.0$ kHz. The former is shown in figure 7.5 b).

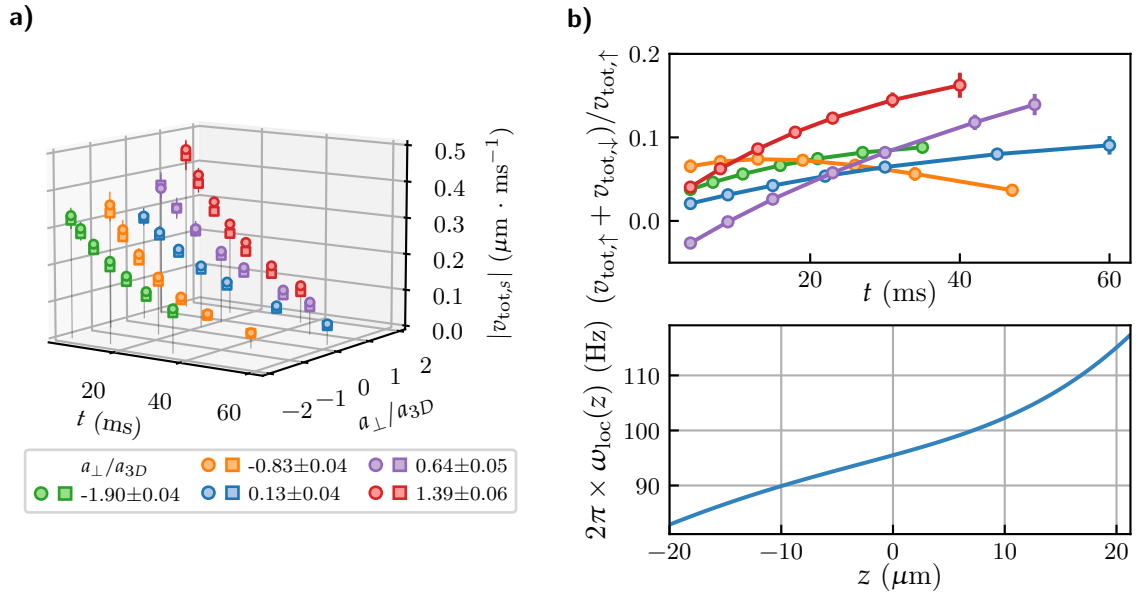

Figure 7.5: Evolution of velocities and plot of the local curvature. When relevant, the ↑ and ↓ populations are represented by circles and squares, respectively. The present figure and the one below represent 5 selected sets at different interaction strength. a) Norm of the velocity for the two spin components. b) Top: relative difference between the velocities as a function of time. Bottom: Evolution of the local curvature along the longitudinal direction. The steeper side correspond to $z > 0$, where ↑ population is initially placed.

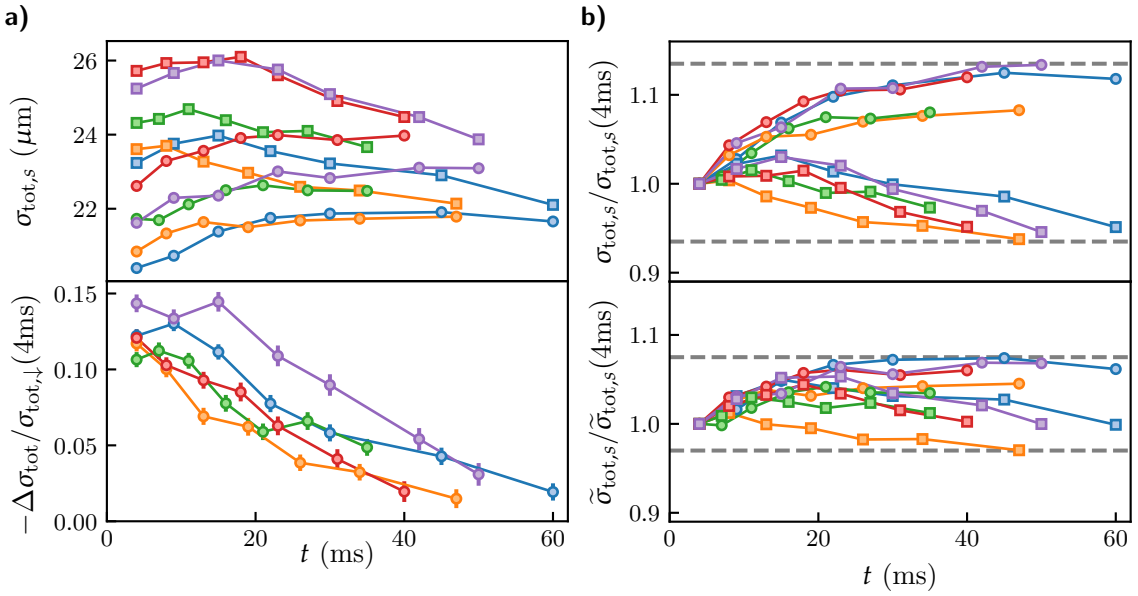

Figure 7.6: Cloud size dynamics. a) Top: Evolution of the two cloud sizes. Initially, the cloud size of ↓ population is smaller, and later on equilibrates with the one of ↑ population. Bottom: Evolution of normalized difference of $\Delta\sigma_{\mathrm{tot}} = \sigma_{\mathrm{tot},\uparrow} - \sigma_{\mathrm{tot},\downarrow}$. b) Variations of the cloud size for each spin state without and with curvature correction (top and bottom, respectively).

Velocity We extract the longitudinal velocity of the centers of mass from the exponential fit as

$$v_{\mathrm{tot},s} = \dot{d}_{\mathrm{tot},s} = -\frac{d_{\mathrm{tot},s}}{\tau_{\mathrm{tot},s}} \tag{7.21}$$

The velocities of the two components are oriented in opposite directions, and vanish when the system reaches an equilibrium state. As shown in figure 7.5 a) and b), we systematically have $|v_{\mathrm{tot},\uparrow}| > |v_{\mathrm{tot},\downarrow}|$. This is because the potential is steeper in the $z > 0$ side, where $\uparrow$ is located. However, the typical relative difference across all the sets we will analyse in the rest of this chapter almost always lies below 10% at all times.

Cloud size The systematic trend related to that quantity, shown in figure 7.5 c), is that $\sigma_{\mathrm{tot},\uparrow} < \sigma_{\mathrm{tot},\downarrow}$ at short times. This stems from the fact that the local curvature is higher on the $z > 0$ side, which implies that the $\uparrow$ population is overcompressed while the $\downarrow$ population is undercompressed with respect to the final static state. At long times, the two sizes become equal.

Local thermal equilibrium Previous studies in 3D have focused in the situation where the two spin distributions are always locally in thermal equilibrium in a harmonic trap, resulting in rigid translating Fermi-Dirac distributions [279, 280]. In the present situation, it would correspond to assuming that the $\sigma_{\mathrm{tot},\uparrow,s}$ $=\uparrow,\downarrow$ are time-independent. If the trap is perfectly harmonic in the longitudinal direction and in the high temperature limit[5], we have $\sigma_{\mathrm{tot},s} \sim 1/\omega_{\parallel}$. Obviously, if the trap is not harmonic, the local curvature is not constant across the trap. But if the latter varies slowly in the spatial extent of the atomic distribution, the local thermal equilibrium assumption implies that the exact value $\sigma_{\mathrm{tot},s}(t)$ will be inversely proportional to the curvature at $z = d_{\mathrm{tot},s}(t)$ at any time t.
In other words for our trap, these assumptions imply that the product

$$\widetilde{\sigma}_{\mathrm{tot},s}(t) = \sigma_{\mathrm{tot},s}(t) \times \omega_{\mathrm{loc}}(z = d_{\mathrm{tot},s}(t)) \tag{7.22}$$

should be constant. In figure 7.5 d), we show the cloud size of both spin state as function of time with and without the local curvature correction. The curvature correction reduces the typical variations of the cloud size to less than 10%, which reduces the variability by a factor larger than two compared to the uncorrected version. This rescaling is a rather crude approximation since the problem is in reality non local: the local variations of the potential curvature are significant in the scale of $\sigma_{\mathrm{tot},s}$. However, the fact the cloud size

[5] In the zero-temperature limit, we do not expect the distribution to be a Gaussian, and the way its characteristic size scales with $\omega_{\parallel}$ will essentially depend on the dimensionality. The exact relation also depends on the interaction parameter, but we approximately expect the characteristic size to also scale like $\omega_{\parallel}^{-1}$ 1D, and $\omega_{\parallel}^{-2/3}$ in 3D.

is nearly constant for the rescaled data reveals that the distributions have a rather well defined temperature T throughout the evolution, despite the non-equilibrium nature of the process.

7.2.3 Losses

The Feshbach resonance that we use between states $|1\rangle$ and $|2\rangle$ is narrow and consequently leads to enhanced losses which have been observed in 3D gases [144] in comparison to broad resonances. These losses are more pronounced on the BEC side $a_{3D} > 0$, and occur due to three-body recombination events. In one dimension, losses induced by the same mechanism are expected to occur [281], and losses in a Fermi gas near a $p-$wave resonance have been studied experimentally with ^{6}Li [87, 282]. In correlated 1D degenerate Bose gases, reduced three-body recombination compared to 3D have been observed [283].
It is beyond the scope of the current work to identify the loss-mechanism and extract the corresponding recombination rates, which would require having data sets which span much longer durations to identify the density dependence of losses unambiguously. The later would be anyway challenging to model due the dynamical nature of the studied process.
As shown in figure 7.7 a), the observed atom number decay is linear versus time in the measured range. We extract the quantity $1/\tau_{\text{loss}} = -\dot{N}_{\text{avg},s}/N_0$, where $N_{\text{avg},s}$ is the atom number in spin state s averaged across all the tube traps and $N_0 = N_{\text{avg},s}(t = 4\text{ms})$, which gives a time scale that we can compare with the one of the transport experiment. Figure 7.7 b) makes it clear that τ_{loss} continuously increases upon going from the BCS to the BEC side in the measured range. In the BCS side, $\tau_{\text{loss}} > 200$ ms is much larger than the time-scale of the spin relaxation. On the BEC side, the smallest measured value is $\tau_{\text{loss}} \approx 85$ ms. The typical measured losses range from 5% to 40% of the initial atom number from the BCS to the BEC side when the system is back to a static configuration.

7.2.4 Temperature evolution

We previously argued that it makes sense to define a temperature during the spin relaxation. In order to further justify this of point of view, we compared the temperature of the atomic samples before the barrier is released and after the spin relaxation is over.

Initial temperature For every spin relaxation data set, we also measured the density distributions of $\uparrow$ and $\downarrow$ prior to removing the barrier. Therefore, we can estimate the initial temperature using our thermometry in the reconstructed potential, assuming the usual noninteracting equation of states in Eq. (5.77). We exclude the region around the green barrier, where the potential is unknown.

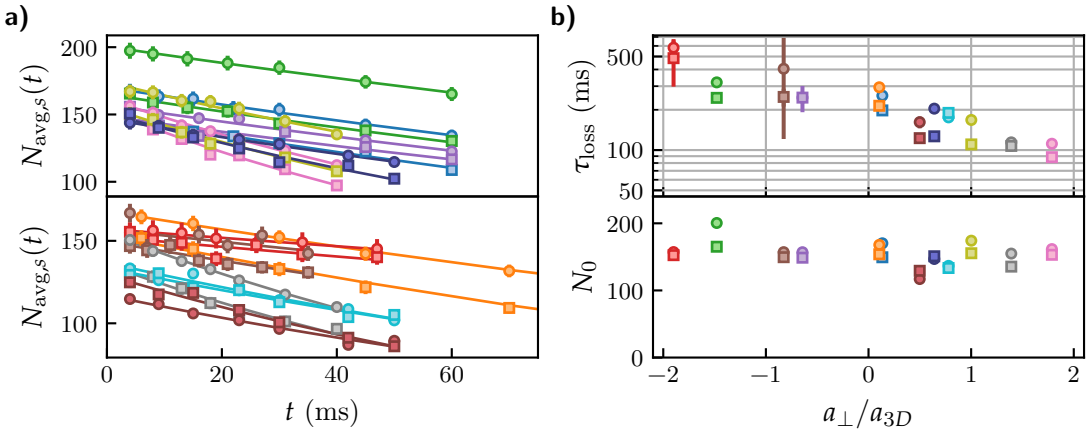

Figure 7.7: Losses during the transport. The ↑ and ↓ populations are represented by circles and squares respectively. a) Evolution of the atom number as a function of time for all the sets that will be analysed in this chapter. b) Extracted loss rate and initial atom number.

The bias field is set to its final value while we take these images. Consequently, the scattering length a_{3D} is large. The usage of a noninteracting equation of state is justified by the large spin imbalance on each side on the barrier. We essentially assume that the minority components[6] allow the system to be in a well-defined thermal equilibrium thanks to collisions with the majority component, but do not contribute to alter the equilibrium distribution of the majority component significantly compared to the ideal noninteracting case.

We empirically observe that the temperature in each side of the barrier is similar. Therefore we include the temperature as a shared parameter when fitting the two distributions of the majority components so that the amount of free parameters is reduced, resulting in smaller statistical errors.

Final temperature Each data set also contains averaged images at large times after the barrier release, where the system is back to being static. In order not to rely on the unknown interacting equation of state, we employ the noninteracting one to exclusively fit the wings of the final distributions, where the local fugacity is lower. Since the cloud are overlapped, we fit both ↑ and ↓ distributions with a shared temperature.

We observe no statistically relevant difference between the initial and the final temperature of the system in each individual tubes. In other words, losses do not contribute to directly increase temperature, however they do influence the degree of degeneracy of the system since they generate a density drop. Representative fits are shown in figure 7.8.

In principle, one could postulate that the ramp of the green barrier could affect the temperature in such a way that it is compensated by an effect of interactions, for example

[6] The fraction of minority atoms is larger on the $z > 0$ side of the green barrier due to the asymmetry of the trap and the loading process.

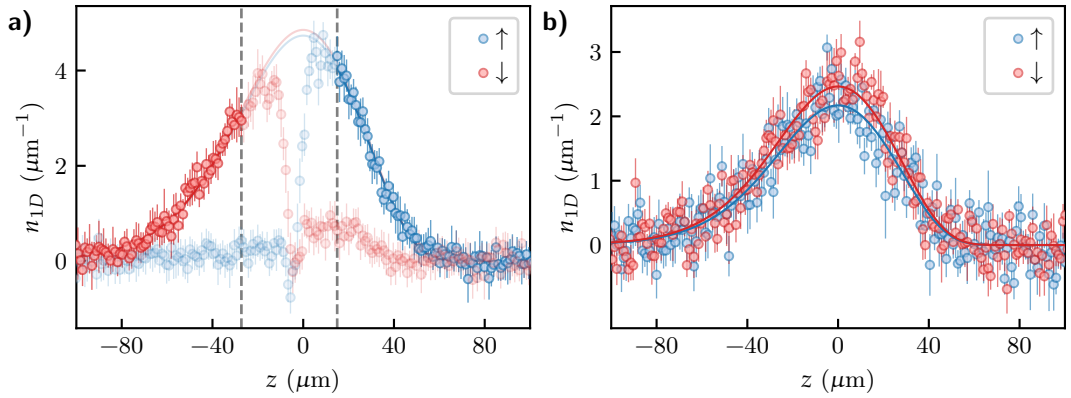

Figure 7.8: Thermometry of the weakly interacting gas before and after separation. Distributions obtained for $a_\perp/a_{3D} = -31.0 \pm 0.2$ and $\omega_\perp = 2\pi \times 16.5$ kHz. a) 16 averaged density profiles prior to the ramp down of the optical barrier. The fitted temperature is $T = 1257 \pm 34$ nK. The central region within the dashed lines is excluded from the non-interacting Fermi gas fits (solid lines). b) 14 averaged profiles after the ramp down of the optical barrier and 100 ms hold time. The fitted temperature is $T = 1212 \pm 49$ nK.

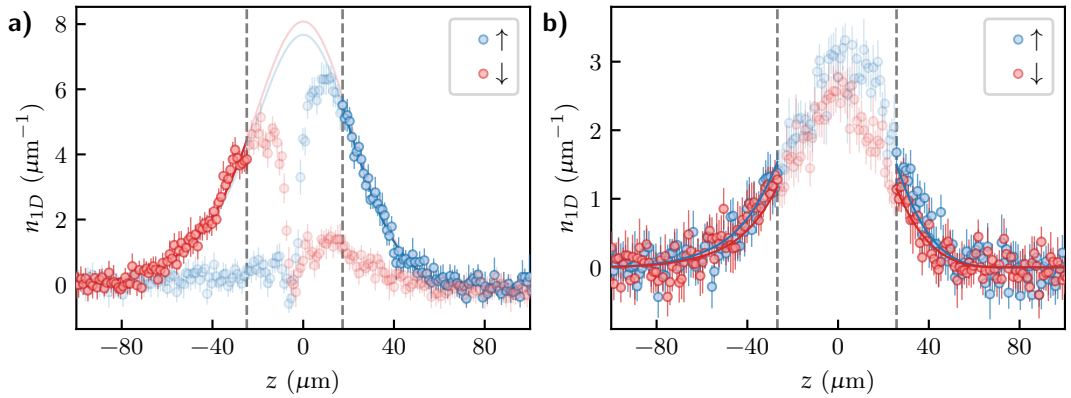

Figure 7.9: Thermometry of the strongly interacting gas before and after separation. Distributions obtained for $a_\perp/a_{3D} = 0.13 \pm 0.04$ and $\omega_\perp = 2\pi \times 10$ kHz. a) 12 averaged density profiles prior to the ramp down of the optical barrier. The fitted temperature is $T = 582 \pm 20$ nK. The central region within the dashed lines is excluded from the non-interacting Fermi gas fits (solid lines). b) 12 averaged profiles after the ramp down of the optical barrier and 60 ms hold time. The fitted temperature is $T = 540 \pm 50$ nK. The central region within the dashed lines with a fugacity $f \gtrsim 0.2$ is excluded from the non-interacting Fermi gas fits (solid lines).

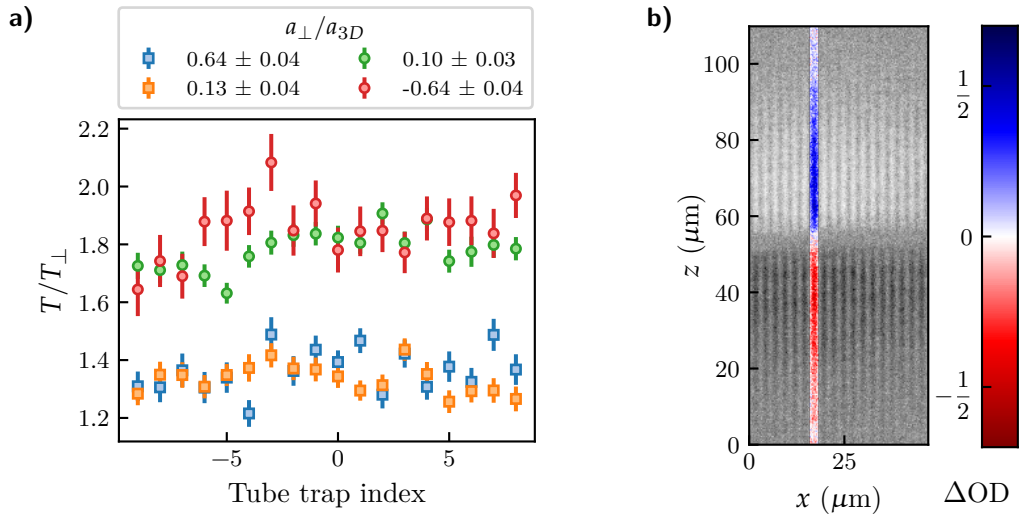

Figure 7.10: Temperature across the tube traps before release. a) Temperature of two selected sets prepared with angular trapping frequencies $\omega_\perp = 2\pi \times 10$ kHz (squares) and $\omega_\perp = 2\pi \times 16.5$ kHz (circles). As expected, the initial temperature varies very little across for the different data sets taken with different parameters a_{3D} and $\omega_\perp$. b) Optical density difference $\Delta\text{OD} = \text{OD}_\uparrow - \text{OD}_\downarrow$. We highlighted a single-tube region by coloring the rest of the image in shades of gray. The temperature of each tube is measured individually.

through losses. We ruled out this option by performing the same check with a small scattering length $a_{3D} = -75\, a_0$ for which we observed no losses. The comparison between initial and final temperature shows no statistically relevant differences, as shown in 7.9. For the final temperature fit in that case, it is not necessary to exclude the central region since the interaction parameter is small.

Ultimately, this process allows us to determine the starting temperature in each tube trap, as shown in figure 7.10. Surprisingly, the measured temperatures normalized by the transverse frequency quantum $k_B T/\hbar\omega_\perp = T/T_\perp$ happen to be lower when we prepare the system with $\omega_\perp = 2\pi \times 10$ kHz compared to $\omega_\perp = 2\pi \times 16.5$ kHz. Overall, the normalized temperatures that we reach are larger than those presented in figure 5.8. This difference likely originates from the spin separation procedure which, on top of requiring many ramps and transfers over relatively large durations, imposes to ramp the optical lattice in a situation where the cloud spin components are nearly fully-separated. This makes adiabaticity conditions difficult to fulfil. Besides, the limitation of interactions due to strong polarization might also explain why we observe a fairly homogeneous temperature across the tubes, in contrast to previous results in figure 5.8. Be that as it may, the preparation of colder spin-separated clouds in the lattice constitutes a challenging experimental puzzle whose solution would undoubtedly lead to interesting observations.

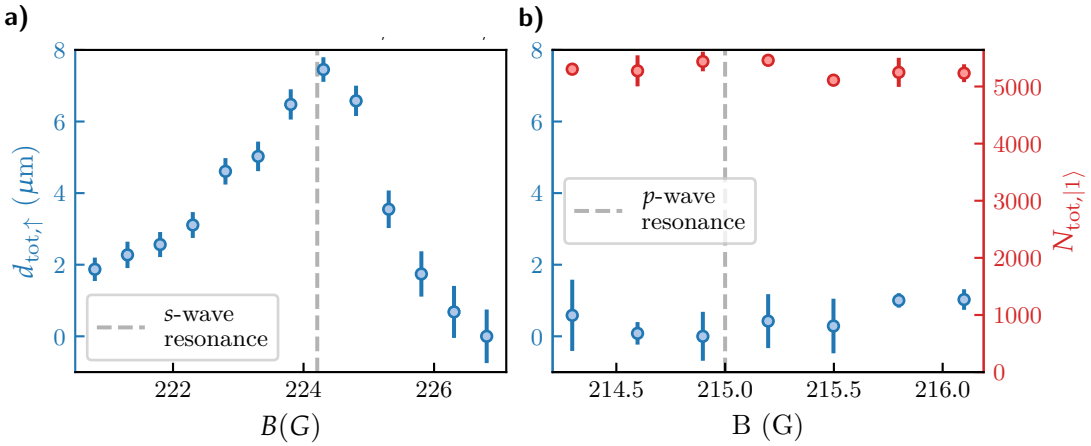

Figure 7.11: Scan around the $s-$ and $p-$wave resonances with $|1\rangle$ and $|3\rangle$. a) Measurement of the center of mass position of $\uparrow$ population around the $s-$wave resonance located at $B \sim 224.21(5)$ G [267] 10 ms after abruptly releasing the optical barrier. b) Similar measurement around the $p-$wave resonance, located at $B \sim 215.0$ G [267]. Also shown is the measured total atom number across all tubes in state $|1\rangle$, in the inset.

7.2.5 Origin of collisions

As discussed in 6.4, we perform the experiment using states $|1\rangle$ and $|2\rangle$, exploiting the $s-$wave interaction located around $B \sim 202.1$ G. However, there is a $p-$wave resonance nearby which influences collisions between two atoms in state $|2\rangle$, around $B \sim 198.8$ G. [284]. It is *a priori* relevant to wonder whether the presence of this additional resonance influences the spin transport, especially on the BEC side[7] where $B < 202.1$ G.

Since these resonances are close and losses stronger on the BEC side, it is challenging to unambiguously distinguish their effect. However, we performed an indirect check of the effect of $p-$wave collisions by using the states $|1\rangle$ and $|3\rangle$ instead. This state composition is obtained by omitting the second $|3\rangle \rightarrow |2\rangle$ transfer in the procedure explained in figure 6.3. In figure 7.11, we show the position of the $\uparrow$ population after releasing abruptly the optical barrier and waiting 10 ms as a function of the magnetic field, both around the $s-$wave and the $p-$wave resonance. We also show the absence of losses around the $p-$wave resonance. From the obtained signal, it is clear that the $p-$wave collisions do not play a significant role. Despite the difference with the previous situation involving $|1\rangle$ and $|2\rangle$, we conclude that it is very likely that the presence of the p-wave resonance at $\sim 198.8G$ does not influence the measurement. This is an important observation because if the p-wave resonance was introducing losses, $|1\rangle$ and $|2\rangle$ would not be interchangeable anymore. Consequently, the alternated imaging method (see sec. 6.6) could introduce a bias.

[7] The smallest field value used in the following sections is $B \sim 201.5$ G.

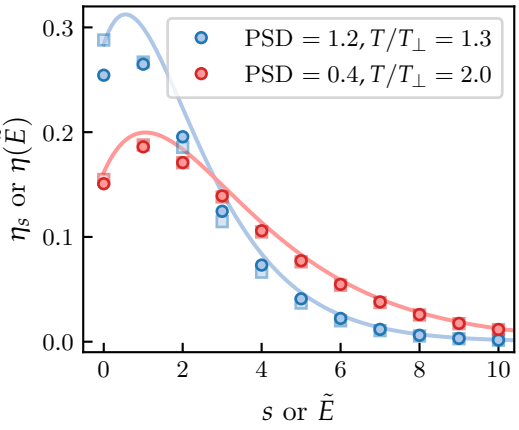

Figure 7.12: Noninteracting transverse mode distribution. Fraction of atoms η_s populating the transverse mode s extracted from the noninteracting EoS using the typical phase-space density (PSD) and $T/T_\perp$ measured in the experiment. Circles represent the Fermi-Dirac distribution whereas squares represent a Boltzmann distribution, for comparison. The solid lines represent the transversely continuous limit defined in the main text.

7.2.6 Population in the transverse modes

In order to have a rough feeling for the population share in the transverse modes, we used the typical densities (extracted at the center of the trap), temperatures and transverse trapping frequencies realized in the experiment to estimate it. Of course, this quantity is not straightforward to evaluate exactly, especially in an out-of-equilibrium situation with strong interactions. However, we can assume use the noninteracting equation of state with LDA in the longitudinal direction as a toy model to do some estimates.

From Eq. (5.69), we can define the fraction of atoms in the mode $s = 0$ as

$$\eta_s = \frac{(s+1) f_{1/2}\left[Z \exp\left(-s\frac{T}{T_\perp}\right)\right]}{\mathrm{PSD}}, \qquad \mathrm{PSD} = \sum_{s=0}^{+\infty} (s+1) f_{1/2}\left[Z \exp\left(-s\frac{T}{T_\perp}\right)\right]. \quad (7.23)$$

This equation takes both degeneracy and dimensionality into account. We define a similar fraction in the limit where transverse quantization does not exist, so that the role of dimensionality can be quantified. It is obtained by letting $\hbar\omega_\perp \to 0$, at constant $T_\perp/T$ and $Z = e^{\beta\mu}$. These three conditions could be implemented by appropriately varying T, n and $\omega_\perp$ for instance. In that case, we make the replacement

$$\sum_{s=0}^{+\infty} \to \frac{1}{\hbar\omega_\perp} \int_0^{+\infty} \mathrm{d}E. \quad (7.24)$$

The index s becomes the continuous variable $\tilde{E} = E/\hbar\omega_\perp$. Then, we express the PSD as a continuous integral in the transverse directions, as well as the transverse distribution $\eta(\tilde{E})$

as

$$\eta(\tilde{E}) = \frac{(\tilde{E}+1) f_{1/2}\left[Z \exp\left(-\tilde{E}\frac{T}{T_\perp}\right)\right]}{\mathrm{PSD}}, \qquad \mathrm{PSD} = \int_0^{+\infty} \mathrm{d}\tilde{E}(\tilde{E}+1) f_{1/2}\left[Z \exp\left(-\tilde{E}\frac{T_\perp}{T}\right)\right]. \tag{7.25}$$

In order to gauge the importance of degeneracy, we can substitute Eq. (7.26) by its classical Boltzmann equivalent defined as

$$\eta_s = \frac{(s+1) Z \exp\left(-s\frac{T}{T_\perp}\right)}{\mathrm{PSD}}, \qquad \mathrm{PSD} = \sum_{s=0}^{+\infty} (s+1) Z \exp\left(-s\frac{T}{T_\perp}\right) \tag{7.26}$$

The comparison of Eqs. (7.26), (7.25) and (7.26) for a given value of PSD and $T/T_\perp$ is shown in figure 7.12, which reveals that both degeneracy and dimensionality are likely to play a role in our coldest atomic samples.

7.3 Spin drag

Now that we introduced the context inside which the dynamics occur, we can perform a more quantitative analysis of the transport properties. In this section we introduce the spin drag and explain how to extract from our measurements. Finally, we briefly discuss how a Boltzmann equation formalism can be adapted from the widely studied 3D case to describe the dynamics in a tight atomic waveguide.

7.3.1 Phenomenological considerations

Two-body collisions between $\uparrow$ and $\downarrow$ populations induce momentum transfers that effectively result in a friction for the relative motion between spin components [285]. For instance, if one of the two spin components is static while the other is set into motion through it, it will drag the former in the same general direction.

In our setup, the relevant direction for the relative motion is the vertical one. If we assume that the resulting friction force depends linearly on the two velocity components $v_{z,\uparrow}$ and $v_{z,\downarrow}$ of the centers of mass, the application of Galilean invariance implies [280]

$$F_{\uparrow\downarrow} = -F_{\downarrow\uparrow} = -\alpha(v_{z,\uparrow} - v_{z,\downarrow}), \tag{7.27}$$

where $F_{\uparrow\downarrow}$ is the force applied on the $\uparrow$ center of mass by the $\downarrow$ population, and vice-versa for $F_{\downarrow\uparrow}$. The first equality results from the Newton's third law. The coefficient $\alpha > 0$ sets the damping rate of the relative motion between the two components. Following the

standard approach from [246, 247, 279, 285], we introduce the spin drag coefficient as

$$\dot{v}_{z,\uparrow} - \dot{v}_{z,\downarrow} = -\Gamma_{\mathrm{SD}}(v_{z,\uparrow} - v_{z,\downarrow}), \tag{7.28}$$

which is related to the damping coefficient through $\Gamma_{\mathrm{SD}} = \alpha/\mu$, with $\mu = m/2$ defined as the usual reduced mass of the two-body problem[8].

7.3.2 Center of mass dynamics

In a harmonic trap, the relative motion of the centers of mass in the presence of the spin drag from Eq. (7.28) is described by [246, 247, 279]

$$\ddot{d} + \Gamma_{\mathrm{SD}}\dot{d} + \omega_{\parallel}^2 d = 0. \tag{7.29}$$

In the overdamped regime $\Gamma_{\mathrm{SD}} \gg \omega_{\parallel}$, the solutions are given by exponential decays

$$d(t) = d_0 e^{-t/\tau}, \tag{7.30}$$

from which the spin drag coefficient can be inferred[9].

$$\Gamma_{\mathrm{SD}} = \omega_{\parallel}^2 \tau + 1/\tau. \tag{7.31}$$

In figure 7.13, we observe an excellent agreement with the exponential decay of the relative CoM evolution in individual tube traps which justifies *a posteriori* the use of Eq. (7.29) to fit the data, despite the longitudinal trap being anharmonic[10]. Furthermore, we have shown the visible effects of the asymmetry in section 7.2 and noticed that they are relatively small. We expect to commit a small systematic error that do not impact significantly the conclusions of this analysis. The overdamped condition can also be written $\omega_{\parallel}\tau \gg 1$. We measured $\omega_{\parallel}\tau \sim 6 - 24$ in the explored range, which justifies the overdamped regime *a posteriori*.

7.3.3 Measurement of the spin drag

We performed a measurement of the spin drag in the vicinity of the Feshbach resonance by taking sets of ~ 200 images for several values of the scattering length a_{3D}, and for two angular transverse trapping frequencies $\omega_{\perp} = 2\pi \times 10.0$ kHz and $\omega_{\perp} = 2\pi \times 16.5$ kHz,

[8] The relation still holds in the mass imbalanced case where $1/\mu = 1/m_1 + 1/m_2$, m_1 and m_2 being the masses of the imbalanced components.

[9] In the overdamped regime, the second term $1/\tau$ is negligible, which is equivalent to say that the inertia term $\ddot{d}$ in Eq. (7.29) is negligible.

[10] The effect of anharmonicity are challenging to model because they do not simply act on the CoM motion but also on the distribution.

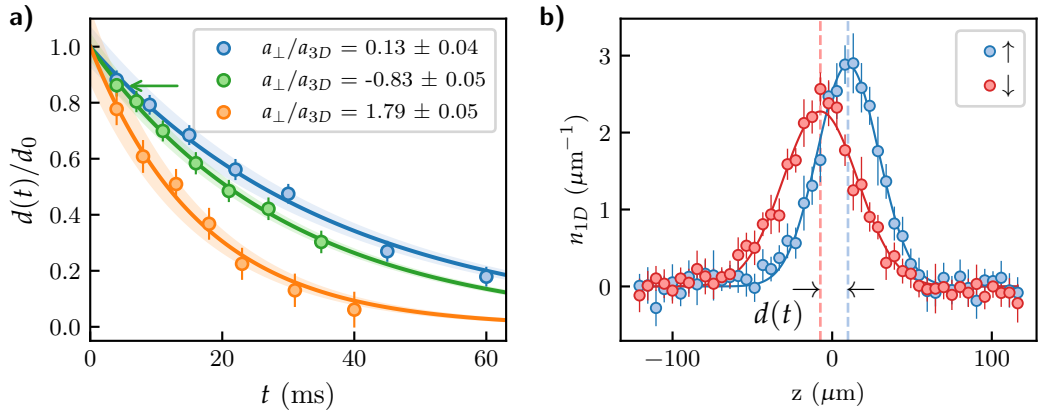

Figure 7.13: Center of mass damping in individual tube traps. a) Evolution of the normalized relative distance between the centers of mass as a function of the interaction strength. The blue, green and orange sets are associated with the lifetimes $\tau = 37.3 \pm 1.7$ ms, 30.0 ± 0.9 ms and 16.9 ± 1.2 ms respectively. a) Selected profiles to highlight the extraction of $d(t)$. In the chosen example, the time duration after the barrier ramp is 4 ms. The profiles are fitted with Gaussian distributions whose centers identify the position of the CoM.

which corresponds to trap ratios of $\omega_\perp/\omega_z \approx 104$ and 172, respectively. As explained in section 6.6, we use alternated imaging to acquire both spin states. The shots are randomized over different hold time values but are always taken by pairs of consecutive $\uparrow$ and $\downarrow$ images. Given that time required to acquire each data set extends over several hours, we often need to interrupt and realign the various beams, mostly crossed dipole traps, compression beam and barrier beam. In order not to depend on the absolute position of the trap which is sensitive to drifts and imperfect realignments, we always use the position along z of $\downarrow$ population to set the origin of positions along z in each pair. With this convention, we can safely average multiple pairs of images with matching hold time so that the signal-to-noise ratio is improved and individual tube analysis can be made.
In figure 7.14, we show the spin drag extracted from fitting the relative center of mass evolution of each individual tube with Eq. (7.30) and then applying Eq. (7.31). For each individual tube, the temperature T, the total one-dimensional density $n_{1D}(z,t) = n_{1D,\uparrow}(z,t) + n_{1D,\downarrow}(z,t)$, is extracted from the images, whereas $a_\perp$ and a_{3D} are common parameters set by the lattice beam's power and magnetic bias field respectively. We label each point with three dimensionless numbers:

- $a_\perp/a_{3D}$ to quantify the interaction strength, which we vary between -2 and 2,
- $\lambda_T n_{1D}/2 \sim 0.3 - 1.3$ to quantify the phase-space density[11], where n_{1D} is measured at the middle position between the two clouds, which coincides with the center of trap.

[11] The factor 2 is introduced because the phase-space density is often defined using the density per spin state.

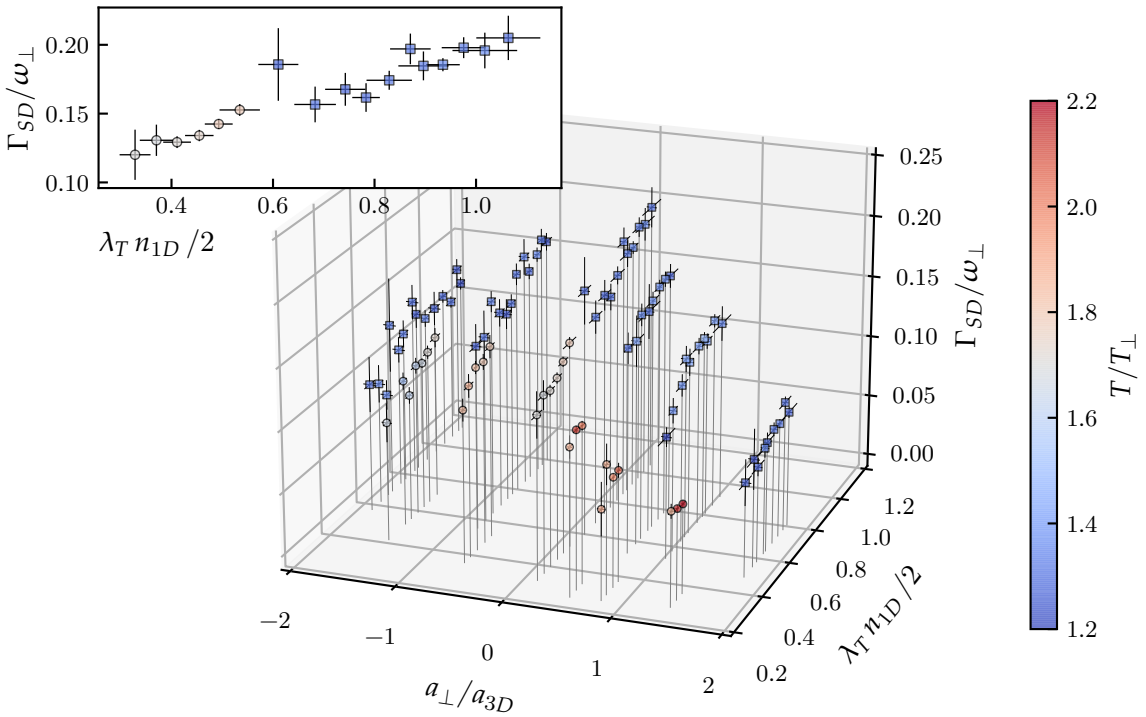

Figure 7.14: Spin drag at the vicinity of the $s-$wave Feshbach resonance. The squares and circles represent data points for $\omega_\perp = 2\pi \times 10.0$ kHz and $\omega_\perp = 2\pi \times 16.5$ kHz, respectively. The inset includes only the data points close to $a_\perp/a_{3D} = 0$. The data points of constant $\omega_\perp$ were binned in the $(a_\perp/a_{3D}, \lambda_T n_{1D}/2)$ plane. The error bars represent the estimated weighted standard errors from the corresponding bins.

- $T/T_\perp \sim 1.3 - 2$ to quantify the dimensionality[12]

where we defined the thermal wavelength $\lambda_T = \sqrt{2\pi\hbar^2/mk_BT}$. We normalized the spin drag by $\omega_\perp$ to have a dimensionless quantity. The measured spin drag is maximal around $a_\perp/a_{3D} \sim 0$, which is expected due to the enhanced collision rate. We also observe an expected increase as a function of density. It is not a straightforward task to compare these results with a simple scaling given that we are in the 1D-3D dimensional crossover. In the next section, we present a formalism that could allow to semi-classically estimate the spin drag in this regime.

7.3.4 Semi-classical approach

In previous works in 3D a semi-classical approach relying on the Boltzmann equation was used to formally derive the Eq. (7.29) [246, 247, 279]. The two spin components were described by the semi-classical distributions $f_s(\vec{r}, \vec{v}, t)$, $s = \uparrow, \downarrow$, which satisfied the

[12] Even though it depends on the density as well, see for instance sec, 5.3.3.

Boltzmann equation

$$\frac{\partial f_s}{\partial t} + \vec{v} \cdot \nabla_{\vec{r}} f_s + \frac{\vec{F}}{m} \cdot \nabla_{\vec{v}} f_s = I_{s,\text{coll}} \left[f_\uparrow, f_\downarrow \right], \tag{7.32}$$

where the collision term was given by the following integral

$$I_{\uparrow,\text{coll}} = -\int \frac{\mathrm{d}^3 p_\downarrow}{(2\pi\hbar)^3} \int \mathrm{d}\Omega \frac{\mathrm{d}\sigma}{\mathrm{d}\Omega} |\vec{v}_\uparrow - \vec{v}_\downarrow| [(1-f_\uparrow)(1-f_\downarrow) f'_\uparrow f'_\downarrow - f_\uparrow f_\downarrow (1-f'_\uparrow)(1-f'_\downarrow)]. \tag{7.33}$$

Using the method of averages developed in [286], the joint distribution $f(\vec{r}_\uparrow, \vec{r}_\downarrow, \vec{v}_\uparrow, \vec{v}_\downarrow) = f_\uparrow(\vec{r}_\uparrow, \vec{v}_\uparrow) f_\downarrow(\vec{r}_\downarrow, \vec{v}_\downarrow)$ was used to define arbitrary averaged quantities

$$\langle \chi \rangle = \frac{1}{N_\uparrow N_\downarrow} \int \mathrm{d}^3 r_\uparrow \mathrm{d}^3 r_\downarrow \mathrm{d}^3 v_\uparrow \mathrm{d}^3 v_\downarrow (\chi f). \tag{7.34}$$

By differentiating this equation with respect to time for $\chi = z_\uparrow - z_\downarrow$ and $\chi = v_\uparrow - v_\downarrow$, then applying Eq. (7.32) and using integration by part it can be shown that

$$\partial_t \langle z_\uparrow - z_\downarrow \rangle = \langle v_{z\uparrow} - v_{z\downarrow} \rangle, \tag{7.35}$$

$$\partial_t \langle v_\uparrow - v_\downarrow \rangle = -\Gamma_{\text{SD}} \langle v_{z\uparrow} - v_{z\downarrow} \rangle - \omega_\parallel^2 \langle z_\uparrow - z_\downarrow \rangle, \tag{7.36}$$

where the spin drag is expressed as

$$\Gamma_{\text{SD}} = \frac{\langle (v_{z\uparrow} - v_{z\downarrow}) I_{\text{coll}}[f] \rangle}{\langle v_{z\uparrow} - v_{z\downarrow} \rangle}. \tag{7.37}$$

Combining Eqs. (7.35) and (7.36) result in (7.29), since $\langle z_\uparrow - z_\downarrow \rangle$ is indeed the relative distance between the centers of mass measured in the experiment. Furthermore, the Eq. (7.37), offers an approach to theoretically estimate the spin drag [246, 247, 279].

In a tight atomic waveguide, we expect this transversely continuous description to break down when only few transverse modes are populated. In that case, we propose to adapt this semi-classical approach in the following way. We introduce mode-dependent one-dimensional distributions $f_{s,n}(z, v_z)$, where $n = 0, 1, ..., +\infty$ label corresponding the transverse mode energies. Each of these distributions satisfy a one-dimensional Boltzmann equations

$$f_{s,n}(z, v_z): \qquad \frac{\partial f_{s,n}}{\partial t} + v_z \cdot \frac{\partial f_{s,}}{\partial z} + \frac{F_z}{m} \cdot \frac{\partial f_{s,n}}{\partial v_z} = I_{s,\text{coll},n} \tag{7.38}$$

The collision integral couples all the distributions $f_{s,n}(z, v_z)$. It has the generic expression

$$I_{\uparrow,\mathrm{coll},n}(z, v_z) = \sum_{n_\downarrow, n'_\uparrow, n'_\downarrow} \int \mathrm{d}v_\downarrow \mathrm{d}v'_\uparrow \mathrm{d}v'_\downarrow \times$$
$$\Big(g(v_z, v_\downarrow, n, n_\uparrow \leftarrow v'_\uparrow, v'_\downarrow, n'_\uparrow, n'_\downarrow)(1 - f_{\uparrow,n}(v_z))(1 - f_{\downarrow,n_\downarrow}(v_\downarrow)) f_{\uparrow,n'_\uparrow}(v'_\uparrow) f_{\downarrow,n'_\downarrow}(v'_\downarrow)$$
$$- g(v'_\uparrow, v'_\downarrow, n'_\uparrow, n'_\downarrow \leftarrow v_z, v_\downarrow, n, n_\uparrow) f_{\uparrow,n}(v_z) f_{\downarrow,n_\downarrow}(1 - f_{\uparrow,n'_\uparrow}(v'_\uparrow))(1 - f_{\downarrow,n'_\downarrow}(v'_\downarrow)) \Big)$$

where all the distributions are evaluated at z. In contrast to the three-dimensional case, the collisional integral is more subtle to express. As presented in section 7.1.1, inelastic collisions occur, coupling the different transverse modes together. The conservations laws for total energy and momentum are encoded in $g(v'_1, v'_2, n'_1, n'_2 \leftarrow v_1, v_2, n_1, n_2)$ which vanishes when they are not satisfied[13]. Otherwise, the functions g can be related to the scattering amplitudes calculated in [272] and reported in Eq. (7.9).

It is beyond the scope of this work to improve the parametrization of this integral and attempt to solve it, however this formalism could allow to study the evolution of the spin drag in the 1D-3D dimensional crossover and benchmark the data presented above. Boltzmann equation in quantum wires have already been introduced in the context of electron transport in condensed matter [287, 288].

By slightly adapting the method of averages from [286], we define the joint distribution average

$$\langle \chi \rangle = \frac{1}{N_\uparrow N_\downarrow} \sum_{n,n'=0}^{+\infty} \int \mathrm{d}z_\uparrow \mathrm{d}z_\downarrow \mathrm{d}v_\uparrow \mathrm{d}v_\downarrow [\chi f_{\uparrow,n}(z_\uparrow, v_\uparrow) f_{\downarrow,n'}(z_\downarrow, v_\downarrow)], \tag{7.39}$$

from which we can rederive Eqs (7.35), (7.36) and (7.37). Therefore, we recover the well-known 3D result, however the spin drag is now defined through a different averaged collisional integral that correctly captures the quantization in the transverse direction, and makes use of the scattering amplitudes calculated in a tight atomic waveguide, rather than a continuous integral with a three-dimensional cross-section like in Eq. (7.33).

Even though this semi-classical approach implements scattering probabilities derived from a quantum treatment and takes into account Pauli blocking through the $(1 - f_{s,n})$ factors the collisional integral, it completely neglects correlations that arise on the many-body level which become relevant at very low temperature. For instance, it cannot include pairing phenomena. In such conditions, a full quantum many-body treatment of the system is required to describe the transport process.

[13] Also, time-reversal symmetry implies $g(v'_1, v'_2, n'_1, n'_2 \leftarrow v_1, v_2, n_1, n_2) = g(v_1, v_2, n_1, n_2 \leftarrow v'_1, v'_2, n'_1, n'_2)$.

7.4 Measurement of the spin diffusivity

In the beginning of section 7.2, we defined the norm of the magnetization for our system. It is natural to consider the associated magnetization vector $\vec{M}$ to be oriented along the vertical direction z, which coincides with the quantization axis. However, since its direction does not vary with time, only its norm matters.The diffusive evolution of the later is captured by the longitudinal spin diffusivity (see sec. 6.1). In this section, we will detail how to define and extract this quantity.

7.4.1 Integrated spin current

In section figure 7.4 b), we have shown that the CoM of each spin distribution decays exponentially, and Eq. (7.21) was used to obtain the center of mass velocity. This observation remains true of the individual tube level, and therefore we calculate the CoM velocity of each spin state inside each individual tube. We will now see how this allows us to calculate the spin current.

Current of a Gaussian distribution Let us calculate the flux J_{1D} of a one-dimensional Gaussian density distribution

$$n_{1D}(z,t) = \frac{N_0}{\sigma(t)\sqrt{2\pi}} e^{-\frac{(d(t)-z)^2}{2\sigma^2(t)}} \tag{7.40}$$

through a fictitious transparent wall located at z_0. The parameter N_0 is the total atom number enclosed by the density distribution. If N_0 is constant, the flux at time t is easily calculated by looking at the atom number evolution on one of the sides wall, say the right side, with atom number $N_R(t)$, between t and $t + \mathrm{d}t$. In the instantaneous limit, the flux at position z_0 and time t is given by the derivative

$$J_{1D}(z_0,t) = \frac{\mathrm{d}N_R(t)}{\mathrm{d}t} = \int_{z_0}^{+\infty} \dot{n}(z,t)\mathrm{d}z. \tag{7.41}$$

The flux is defined such that $J > 0$ when atoms move from the left side of the wall to the right side. The integral can be calculated[14] and yields

$$J_{1D}(z_0,t) = \left(\dot{d}(t) + \frac{\dot{\sigma}(t)}{\sigma(t)}(z_0 - d(t))\right) n(z_0,t). \tag{7.42}$$

[14] Remarkably, this result is robust even when a slight asymmetry is added to the profile. We checked that Eq. (7.42) holds if the distribution is taken to be a translating and expanding skewed Gaussian distribution [289], as long the skewness parameter stays constant.

The first term, independent of z, corresponds to a rigid translation of the profile at velocity $v_z = \dot{d}$, whereas the second term originates from the expansion or contraction. As previously argued, the expansion of the cloud during the diffusion process is fairly small, and consequently we will neglect the associated term. In the following, we will calculate particle currents using Eq. (7.42), taking both translation and expansion or contraction. We observed that the latter contributes to up to 10% of the flux.
Note that if N_0 depends on time, it is not longer possible to write the current as product between the density and the velocity, which originates from the fact that the continuity equation for the current no longer holds and would need to include a source term which describes the details of the loss process. However, provided the loss process is slow, Eq. (7.42) yields a correct estimation of the flux.

Spin current The spin current is obtained from the difference of currents between the two spin components. Since they have opposite velocities, we can write the norm of the flux as

$$|J_{1D,s}(z,t)| = |J_{1D,\uparrow}(z,t) - J_{1D,\downarrow}(z,t)|. \tag{7.43}$$

From individual tube trap data, we can calculate this quantity for each measured time values t and positions z where the two clouds overlap significantly. The velocities from Eq. (7.42) are calculated by differentiating the fitted exponential decay of the center of mass of each spin component. We also fit the evolution of the cloud size with an exponential fit, from which we can estimate the contribution to expansion and contraction. Now, in order to extract the spin diffusivity, we also need to measure the magnetization gradient.

7.4.2 Evolution of the spin diffusivity

Using Eq. 6.1, we estimate the spin diffusivity as

$$D_{s,1D} = \frac{|J_{1D,s}|}{|\partial_z M|}. \tag{7.44}$$

We calculate the spin current and the magnetization gradient at a position $z = z_c$ for every individual tube trap and time t. The position z_c is chosen around the central region so that the total density is large and such that $M(z_c) = 0$, meaning that the system is locally balanced[15]. Consequently, we assign a value of $D_{s,1D}$ for each individual tube and for all times t. At each times, the magnetization gradient is extracted using a linear fit in the region $z_c \pm 15\mu$m, see figure 7.15 a). As shown in figure 7.15 b) for two selected tubes at two interaction strengths, we observe that the extracted diffusivity does not vary significantly as a function of time. We can interpret this as a sign that there are no strong temperature

[15] It can be shown that the spin current can be decomposed into a dissipative part, subject to diffusion, and a non-dissipative part [247]. The latter vanishes locally when the $n_\uparrow = n_\downarrow$.

or density variations during the transport that impacts the diffusivity significantly. Thus, for each individual tube, we assign a final value for $D_{s,1D}$ by calculating the weighted average over the different measured times t.

The result of the measurement across all the sets is presented in figure 7.16. The minimal diffusivity is reached around $a_\perp/a_{3D} = 0$. Remarkably, we observe no density dependence despite n_{1D} varying by a factor 3. We also observe no difference between data point taken at $\omega_\perp = 16.5$ kHz and $\omega_\perp = 10.0$. By averaging the data point shown in the inset, we obtain $D_{s,1D} = 8.9 \pm 0.6\,\hbar/m$. This satisfies the quantum bound $D_{s,1D} \gtrsim \hbar/m$, and surpasses it slightly less than an order of magnitude. It is slightly larger than the 3D value measured using the same technique in deeply degenerate Fermi gases [247].

7.4.3 A relation with the relaxation rate

For a true one-dimensional system, a theoretical study calculated a relation between the relaxation rate Γ_{1D} and the diffusion coefficient in the Boltzmann regime[16] [290] which reads

$$\Gamma_{1D} \approx 2.684 \frac{D_0}{l_z^2}, \tag{7.45}$$

where $l_z^2 = 2k_BT/m\omega_z^2$ and D_0 is the bare diffusion coefficient at the center of the trap. In a 3D anisotropic trap[17] where relation occurs along z, the study predicts that the true relaxation rate $\Gamma = 1/\tau$ is not equal to but proportional to Γ_{1D}, still defined through Eq. (7.45). The proportionality constant integrates the flow distributions occuring in transverse direction. Using our data, we can extract following the dimensionless number[18]

$$K = \frac{l_z^2}{\tau D_{s,1D}}, \tag{7.46}$$

where τ is the exponential time constant from the relative center of mass motion appearing in Eq. (7.30) and measured in each individual tubes. The results are reported in figure 7.17. We observe a systematic difference between the two transverse trapping frequencies. Around $a_\perp/a_{3D} = 0$, we measure $K = 1.6 \pm 0.2$ and $K = 2.8 \pm 0.3$ for $\omega_\perp = 2\pi \times 10.0$ kHz and $\omega_\perp = 2\pi \times 16.5$ kHz respectively. Surprisingly, the former is smaller than 2.684 which should be a lower bound. This could result from the fact that the coefficient $D_{s,1D}$ does not reflect the bare diffusivity at the center of the trap D_0 due the integration on the transverse mode, which leads to $D_{s,1D} > D_0$ and thus contributes to underestimate K.

Also, we notice that $K(\omega_\perp = 2\pi \times 16.5\,\text{kHz}) > K(\omega_\perp = 2\pi \times 10.0\,\text{kHz})$ which may seem

[16] Given the crude estimate of the transverse population share shown in figure 7.12, it is likely that the Boltzmann formalism applies to our measurement.

[17] For an isotropic 3D trap, a relation similar to Eq. (7.45) holds but the proportionality constant in 12.10 [290].

[18] The relaxation rate relates to the relative center of mass exponential decay $\sim e^{-t/\tau}$ by $\Gamma_{1D} = 1/\tau$, and should not be confused with the spin drag defined in the previous section!

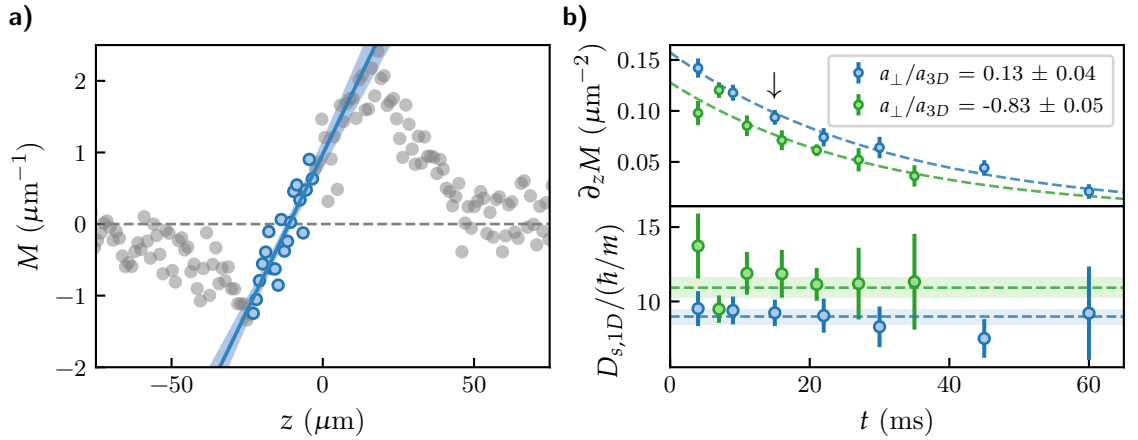

Figure 7.15: Extracting magnetization gradient and diffusion coefficient. a) Spatial evolution of the magnetization from which the gradient is extracted. Only the points in blue contribute to the linear fit (blue line, and shaded area for the error). The value of the extracted slope is used to calculate the spin diffusivity. The fit is performed around $M = 0$, represented by the horizontal dashed line. The represented set lead to the data point marked by an arrow in the right plot. b) Top: evolution of the extracted gradient for two selected tubes at two different scattering lengths as a function of time. Bottom: Corresponding spin diffusivity as a function of time. In Eq. (7.44), both the spin current and the gradient depend on time, however we observe a fairly constant spin diffusivity. Consequently, we extract the weighted average across all the measured time value (dashed lines) and their standard error (shaded areas).

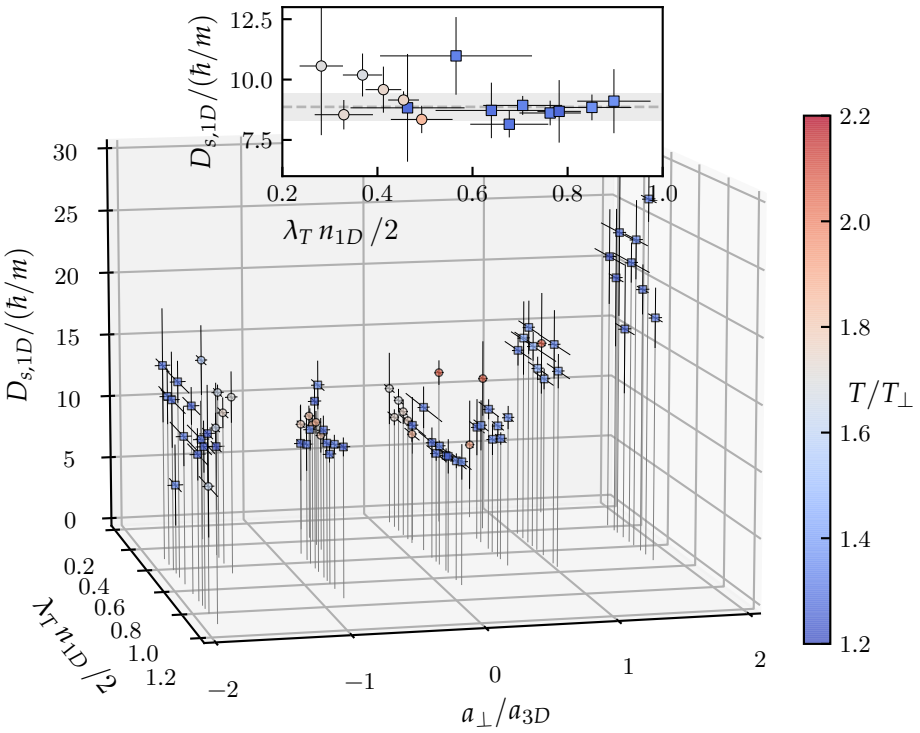

Figure 7.16: Spin diffusivity at the vicinity of the $s-$wave Feshbach resonance. The squares and circles represent data points for $\omega_\perp = 2\pi \times 10.0$ kHz and $\omega_\perp = 2\pi \times 16.5$ kHz, respectively. The inset includes only the data pata points close to $a_\perp/a_{3D} = 0$. The data points of constant $\omega_\perp$ were binned in the $(a_\perp/a_{3D}, \lambda_T n_{1D}/2)$ plane. The error bars represent the estimated weighted standard errors in the corresponding bins.

counter intuitive since the results from [290] seem to suggest that K is expected to become smaller when the dimensionality of the system is reduced. However, this is consistent with the observation discussed in section 7.2.4 that $T/T_\perp(\omega_\perp = 2\pi \times 16.5\,\text{kHz}) > T/T_\perp(\omega_\perp = 2\pi \times 10.0\,\text{kHz})$.

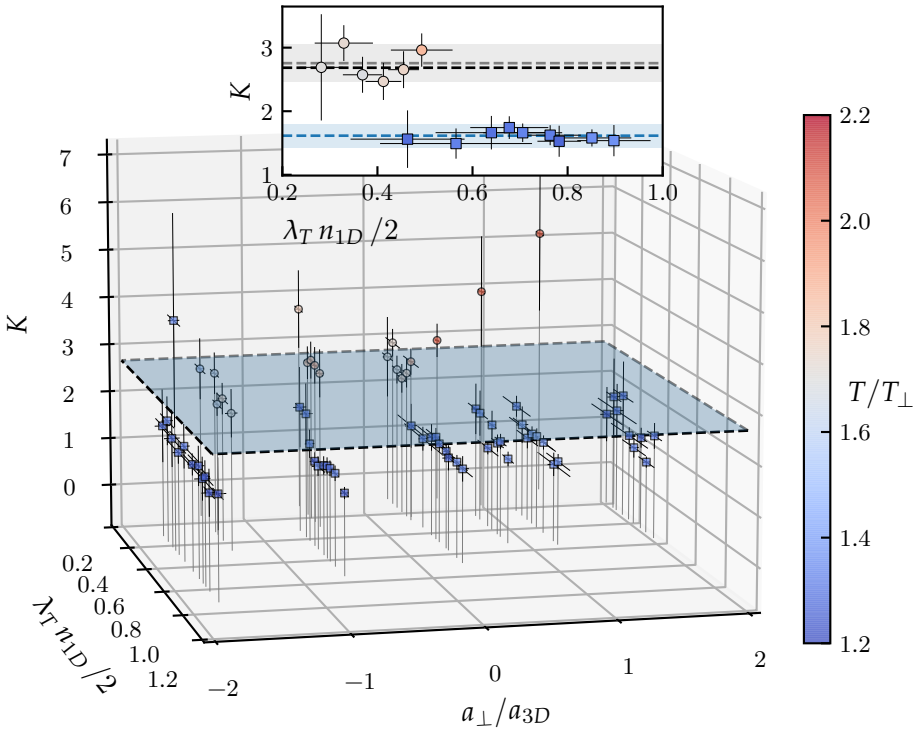

Figure 7.17: Evolution of the K constant. The squares and circles represent data points for $\omega_\perp = 2\pi \times 10.0$ kHz and $\omega_\perp = 2\pi \times 16.5$ kHz respectively. The inset includes only the data points close to $a_\perp/a_{3D} = 0$. The data point of constant $\omega_\perp$ were binned in the $(a_\perp/a_{3D}, \lambda_T n_{1D}/2)$ plane. The error bars represent the estimated weighted standard errors in the corresponding bins. In the 3D plane, the plane corresponds to $K = 2.684$, and in black dashed line in the inset too. The other dashed lines and shaded areas of the inset represent the weighted averages and standard errors of the two transverse frequency sets respectively.

The main results of this chapter are the measurement of the spin drag and the spin diffusivity in figures 7.14 and 7.16, respectively. Despite the presence of discrete transverse modes breaking the scale invariance, we observe a saturation of the spin-diffusivity to $8.9 \pm 0.6\hbar/m$, which satisfies the quantum bound derived for scale-invariant systems. An interesting follow up would be to explore this system at even lower temperatures $T/T_\perp \ll 1$, where the filling of higher transverse modes at equilibrium could be tuned by changing the atom number. The crucial point would be to figure out whether the quantum bound is still satisfied in the 1D regime and for deeply degenerate clouds. Nonetheless, the presented measurement is an important milestone towards studying spin transport in

the deeply degenerated 1D regime.

7.5 Open questions and future experiment

7.5.1 Dynamics in the noninteracting limit

In the absence of interactions, we expect the two spin populations to ignore each other. In a pure harmonic trap, the dynamic consists in undampened oscillations of the separation between the centers of mass of the two components, as other studies observed using a Fermi gas in a 3D geometry [246, 247].
The figure 7.18 depicts the dynamic that occurs after switching off the barrier in ∼10 ns, for various interaction strengths. We represent the evolution of the longitudinal density integrated on all tubes.
At $a_{3D} = 13a_0$, we can calculate the reflectivity coefficients using Eq. (7.13), and it typically yields $\sim 1.0 \times 10^{-4}$ for around $k = 2\pi/\lambda_{\text{th}}$[19]. Considering a spin-up particle going through the spin-down cloud made of ~ 200 atoms results in a typical probability of $\sim$ 2% to be reflected along the way. Consequently, for that regime, we expect to observe clear center of mass oscillations, despite the anharmonic reconstructed potential. However, what we observe is different. Shortly after the release, two broad peaks can be distinguished and take much more time to thermalize into symmetric distributions compared to the sets with stronger interactions. Remarkably, the position of these peaks is stable over time. When interactions are strong, the distributions essentially behave like rigid expanding Gaussian distributions, diffusing into each other.
A hypothetical explanation to the observed evolution at low interaction strength would be the occurrence of sub-resolution structures in the external potential, already mentioned in sec. 5.3.2.
On the one hand, if an additional lattice modulation along the z direction would exist and be deep enough to be significant, then we would expect to observe CoM oscillations centered on the side of the trap where the cloud is initially released, with a reduced frequency due to the increased effective mass [291]. This poorly coincides with the observed dynamics at $a_{3D} = 13a_0$. On the other hand, if a sub-resolution disorder would exist, we could interpret the robustness of the initial distribution peaks as localization, as well the damping of the non-localized fraction. It is not clear which mechanism could produce a disorder with such a sharp frequency cut-off, since the realization of disorder with short correlation length is usually demanding. Finally, thermalization is also expected to be affected in low-dimensional systems, and thus this lead must be investigated as well. Overall, a better understanding of the data shown in 7.18 and complementary checks

[19] This is just a crude estimate. The tight-confinement limit holds only if $|a_{3D}| \gg r_0$ [73], where $r_0 = 65.02\, a_0$ is the effective range of the true interacting potential between ^{40}K atoms [139].

must be performed to identify the mechanism at hand. The hypothetical occurrence of sub-resolution structures would result from a technical issue that could influence the static and dynamic properties of the system and would thus need to be fixed. A straightforward check to disentangle the effect of interactions and the one of the external potential would be to induce density dipole oscillations in the micro trap, like in figure 4.6. If the trap is smooth, the motion of the CoM in the harmonic region should be completely unaffected by interactions as a consequence of Kohn's theorem [193].

7.5.2 Outlook: spin diffusivity in two dimensions

In section 7.4 we reported on a measurement of the diffusivity of a low-dimensional gas in the 1D-3D crossover. However, we would like to stress that a measurement of the longitudinal diffusivity in 2D would also be very interesting and is accessible with no modifications of the experimental setup. Indeed, the spin separation procedure described in section 6.3 could be reused but without ramping the lattice beam pair in the x direction. Consequently, instead of obtaining separated atoms loaded in a single layer of tube traps, one would obtain a single pancake. From there, the spin transport experiment could be performed once again. One caveat is that the external potential would need to be calibrated in the 2D plane in order to characterize the temperature and the dimensionality of the gas.
This measurement would be particularly interesting since it would contribute to clarifying the controversy about spin diffusivity in 2D, which was triggered by contradicting results from transverse spin diffusivity measurements [250, 251], one of them violating the quantum bound, see also table 6.1. However, there are no studies which reported measurement of the longitudinal spin diffusivity extracted from spin dipole mode damping. It would be interesting to perform such a measurement in our setup and compare it to the quantum bound.

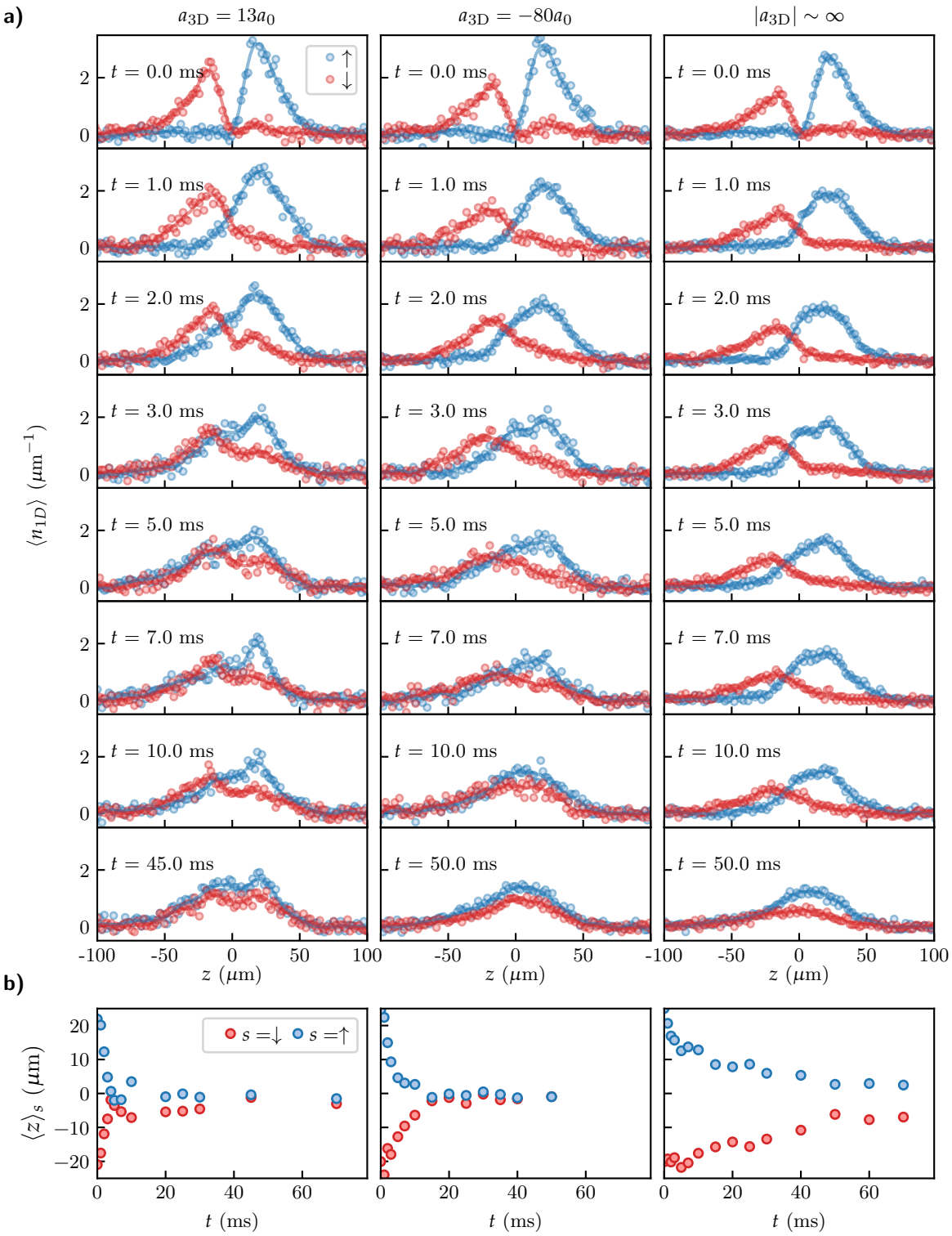

Figure 7.18: Spin dynamics for several interaction strengths. a) Evolution of the density profiles averaged over the 4 central tube traps of both spin components after the optical barrier is abruptly removed. When the interaction strength is too small, the system takes a very long time to recover a Gaussian-looking distribution. The solid lines show a Savitzky-Golay filter applied to smoothen the profiles. Each column corresponds to a different scattering length, the angular transverse trapping frequency is $\omega_\perp = 2\pi \times 16.5$ kHz. b) Center of mass $\langle z \rangle_s = \int z n_{1D,s} \mathrm{d}z$ of the Savitzky-Golay filtered profiles.

Chapter 8

Summary and outlook

After briefly reviewing how we prepared a degenerate gas of ^{40}K atoms in a crossed dipole trap at a temperature $T/T_F \sim 0.15$ in chapter 2, we presented the original techniques which allowed us to convert this ultracold gas into an array of individual quantum wires in chapter 3. The population of only one single row of the underlying optical lattice was achieved by superimposing a TEM_{10}-like repulsive optical potential in order to strongly compress the atomic sample prior to loading. We verified the robustness of this preparation procedure by means of a specialized diagnostic imaging routine applied from below, which unambiguously detected the number of loaded layers. Using a high resolution imaging system, we then fully resolved the flat stack of tube-shaped micro traps, so that their density contributions could be evaluated on an individual basis.
Chapter 4 was dedicated to describing the means to calibrate the external potential's longitudinal and tranverse curvatures as well as the extraction of the density from absorption imaging. In chapter 5, we formulated and characterized the equation of state of an ideal Fermi gas in one dimension as well as in the presence of transverse modes. Its direct application to the data enabled *in-situ* thermometry of the quantum wires, which confirmed that almost all atoms could occupy the transverse ground state. At the same time, this technique has been used to calibrate the longitudinal potential of the tube traps beyond 2$^{\mathrm{nd}}$ order, which was essential for the ensuing experiments studying transport properties.
Making use of all of the methods developed so far, it was possible to accurately study spin transport properties in the presence of interactions. Chapter 6 detailed how to spatially separate, isolate and load the two spin components in the tube traps, resulting in large longitudinal magnetization gradients. We took advantage of the electronic structure of ^{40}K and employed magnetic state-transfers to optimize the difference in magnetic moment between the two spins constituting the system, which thus facilitated their separation by magnetic fields. Finally, a thin optical barrier is used to maintain the separation in lieu of the magnetic gradient. We investigated the dynamics of the system after releasing the optical barrier in chapter 7. Focusing on the strongly interacting regime, we quantitatively studied spin diffusion in the vicinity of a Feshbach resonance, and found no violation of the quantum bounds despite the absence of scale-invariance in the system. At unitarity, we observed a maximal spin drag, and a minimal spin diffusivity $D_s = 8.9 \pm 0.6\hbar/m$.

The latter result did not depend on the atomic density, which varied by a factor 3 in the measured range.

Over the course of this manuscript, we reported on improvements and extensions as well as the first experimental studies with the large-spacing lattice setup. Building on these encouraging results, there are many more interesting studies one can realize on this novel platform. In this final section, we will present a non-exhaustive list of potential future experiments, adding to the previous proposals regarding the measurement of the interacting equation of state and 2D spin diffusivity discussed in 5.3.5 and 7.5.2, respectively.

Thermalization in the vicinity of the 1D regime

In chapter 7 we focused on studying out-of-equilibrium spin transport with strong interactions. In that case, despite a slow merging due to the small diffusivity, the two components approach each other with a locally thermalized distribution. However, when interactions are weak the dynamic is noticeably different. The systems fails to reach a Gaussian-looking distribution even at moderately long times, as shown in figure 7.18.

The typical relaxation time required to reach a thermal distribution as a could be studied function of interaction strength to better understand the mechanisms responsible for thermalization in low dimensional systems. Alternatively, one could apply the optical barrier to the Fermi gas thermalized in the optical lattice without separating the spin components, see figure 6.7. By abruptly removing the optical barrier after some time, one could generate an out-of-equilibrium distribution which features no spin gradients. Consequently, one would probe density thermalization rather than spin thermalization.

The one-dimensional world contains many integrable systems, for which it was proposed that relaxation from an out-of-equilibrium situation is described by a generalized Gibbs ensemble. This description takes into account the kinematic constraints arising from the many conserved quantities instead of the usual thermodynamic ensemble [292]. The former stores in memory the initial conditions in contrast to the latter, and consequently leads to surprising dynamics [217, 219, 293]. It is expected that one-dimensional systems with contact interactions are integrable, even though it was argued that in quasi-1D the existence of virtual excitations give rise to thermalization [218]. It has been observed that the conventional hydrodynamics approach in a weakly interacting integrable one-dimensional Bose gas fails to describe its evolution, and must be replaced by generalized hydrodynamics [294]. It would be interesting to investigate this question using Fermi gases. While the presence of an external potential is expected to compromise integrability [255], the generalized hydrodynamics might still apply to describe these systems.

Itinerant ferromagnetism of ^{40}K in a 1D geometry

Itinerant ferromagnetism in metals is the consequence of repulsive interactions between electrons. The concept was first introduced by Stoner in 1933 in the context of condensed matter systems [295, 296]. Recently, interest grew in realising the Stoner mechanism using ultracold atomic gases. The potential occurrence of itinerant ferromagnetism in two-components Fermi gases has been discussed in great detail [297–302] and Monte Carlo simulations predict a ferromagnetic instability near the strongly interacting regime [303, 304]. An experimental attempt was realised in a 3D geometry, but turned out to be unsuccessful in the end [305, 306]. The complications originated from the fact that, in 3D, the strong repulsive large repulsive interactions are obtained by working in the metastable metastable repulsive branch near an $s-$wave resonance at positive scattering lengths $a_{3D} > 0$. This setting is known to provoke enhanced three-body losses and ultimately prevents equilibrium to occur.

In one dimension, proposals were made to make use of adiabatic magnetic field sweeps around an $s-$wave resonance [307, 308], taking advantage of the reduced loss rate to stabilize the ferromagnetic phase[1] [283]. Remarkably, ^{40}K in particular is a promising candidate to realize itinerant ferromagnetism thanks to its specific resonance structure of the states $|1\rangle$ and $|2\rangle$ [309]. Indeed, this atomic species coincidentally[2] features both an $s-$ and a $p-$wave [284] resonance between these two states at $\sim$202.1 G and $\sim$198.8 G, respectively. In-between these two fields, the $p-$wave resonance is attractive whereas its $s-$wave neighbour is repulsive. This situation can be further enhanced by using an confinement induced-resonance which lowers the position of the ordinary Feshbach resonance in terms of magnetic field. Thanks to the possibility of probing individual tube traps, our setup would allow to directly identify the presence of itinerant ferromagnetism by observing the formation of spin domains *in-situ*. Alternatively, it is possible to artificially engineer spin domain walls by following the spin-separation procedure of chapter 6. This approach was used in a previous study in 3D to investigate the ferromagnetic behaviour of two-components Fermi gases [246]. The authors of [309] argued that the sweet spot to observe itinerant ferromagnetism in ^{40}K corresponds to $T \sim 10 - 20$ nK, $\omega_\perp/2\pi \sim 8 - 24$ kHz, $n_{1D} \sim 1 - 3\ \mu\text{m}^{-1}$, and suggested to work a field strength of $B \sim 199$ G. While the conditions regarding angular trapping frequency and density fall in a range accessible by the experiment, we could not yet satisfy the requirements in terms of temperature due to technical limitations. Despite the encouraging step forward toward studying itinerant ferromagnetism in our setup, this highlights the necessity to further improve the experiment.

[1] Even though this statement is debated in more recent studies about losses around a $p-$wave resonance in 1D fermions [87, 282].

[2] The authors talk about a "present from nature"!

Many-body localisation in interacting systems

The presence of a disorder in the external potential strongly impacts the dynamical behaviour of quantum mechanical systems. It was first shown by Anderson in the 50's that interference effects in a random potential lead to a complete localisation of noninteracting particles [310]. In the presence of interactions, the problem is considerably more difficult to tackle. In this context, Anderson had surmised that the presence of disorder can lead to localised states or non-ergodic behaviour. It took around half a century before a theoretical proof finally justified the existence of many-body localisation (MBL) [311–313]. With the combination of theoretical and experimental efforts, MBL is now a well-established standard property occurring in disordered Hubbard-type systems with interactions [314–319] . However, in the case of continuous bulk systems, the existence of MBL is debated [320–323]. So far, pioneering studies have been focusing on disordered lattice landscapes [324–330]. Therefore, it would be interesting to generate random disordered potentials featuring correlation lengths on the order or below the inter-particle spacing of the atoms, and probe the existence MBL by taking advantage of our tube-resolved low-dimensional system.

Acknowledgements

It is now time to put an end to this manuscript. It resulted from the fruit of many steps which have borne many names: ingenuity, exploration, excitement, passion, challenges, doubt, disillusion, adaptation, persistence, stubbornness, audacity, questioning... Be it directly due to the scientific projects or linked with external events, these stages have all been overcome because there was always at least one person giving me an additional push through its time, energy, creativity, pragmatism and optimism when I was most needing it. I would like to mention and thank all the people whose names could not be omitted if the story of this human adventure had to be told.

First and foremost, I owe a deep sense of gratitude towards Patrizia Vignolo, Isabelle Bouchoule, Rudolf Grimm, Leonardo Fallani and Thierry Giamarchi for reviewing my work and being part of the jury.

Second, I would like to thank Frédéric Chevy, Tarik Yefsah, and Christophe Salomon for the trust they placed in me by accepting me into the Ultracold Fermi Gas Group. As a thesis supervisor, Frédéric's contagious enthusiasm and vast knowledge of physics was helpful and inspiring in many ways. Tarik's energy, determination and frankness allowed to bypass a significant amount of dead ends on the project. His sense of organization and anticipation bought us a lot of time.

Third, I would like to thank all the colleagues with whom I worked on the experiment: Thomas Reimann, Cédric Enesa, Julian Struck, Markus Bohlen and Marin Tharrault.

It would be preposterous not to start by mentioning Thomas and Cédric at the same time. Even though they are different in several very fundamental ways, I met them as a tightly bound pair, being both friends and colleagues. Their positive energy radiated far beyond the range of our small experiment room and created a friendly and comforting environment for everyone around them. Little did I know back then how much of a crucial role they would play in my life even to this day. Through their unlimited patience, pedagogy, and knowledge they allowed me to master the experiment even though I was starting as a layman experimentalist who could barely use a multimeter. As a side effect, I had to comply to their unsettling musical taste on a daily basis... Willingly, I guess. Their mind-blowing sense of humour was an inexhaustible source of joy, which we also took advantage of outside the lab very often. Thank you very much for accompanying on me until the very end of this adventure, and for all the wild memes that came along the way. Special thanks to Thomas for his unbelievable patience in proofreading this manuscript.

Unlike all the other lab mates, Julian and I worked together on the experiment for the

whole duration of my thesis. I can barely remember a third of all the issues we had to face together to progress on the project. Julian was never running out of new ideas and creative solutions. Through his experience, it seemed he always knew what to do, and the facts often proved him right, even when it was painful to admit! I am grateful for all the knowledge I could acquire thanks to him. I had only had little time to work with Markus before he left the lab, but I remember his kindness to help me in my first steps and integrate me in the group. Marin impressed me early on with his outstanding technical knowledge. He was very dedicated and always eager to learn more. I wish him great success in his new project.
I would like to thank all the higher order colleague from Li1 and Li3: Shuwei Jin, Kunlun Dai, Gentle Dash, Joris Verstraten, Bruno Peaudecerf, Tim De Jongh, Maxime Dixmerias, Matthieu Pierce, Ragheed Alhyder, Anwesh Bhattacharya, Joanna Lis, Darby Bates, Clara Bachorz and Yann Kiefer. It was always a pleasure to discuss during lunch or in the corridor, share physics knowledge or trade lab equipments.
I would like to thank Felix Werner for the stimulating discussions we had. Without a doubt, he is a very brilliant, humble physicist and researcher. But I also deeply admire his human qualities through the patience, integrity and empathy that I could witness by interacting with him.
I would like to thank Antoine Heidmann and Jean Dalibard for the flawless professionalism they displayed as director of the institute and "parrain de thèse", respectively. I have deep respect for the availability and understanding they showed towards me for subjects which however moved away very far from physics.
Many thanks go to all the members of the administration and the various workshops: electronics, mechanics, the electricians and the maintenance/infrastructure team. None of this work could exist without their daily efforts. In particular, I would like to thank Thierry Tardieu, Valérie Revelut, Audrey Gohlke, Christelle Rio, Stéphanie Dubois, Didier Courtiade, Catherine Gripe.
A big thanks should go to my friends and my family. It is fair to say that I was not easy to bear on many occasions (unfortunately, it does not seem to improve over time!), and sometimes having quantum physicist problems does not help to get or receive empathy with the outside world. I am grateful for the immense patience my loved ones have shown, they probably have no idea how much this helped me. Special thanks to Vladimir, with whom we discussed so often the meaning of our existence a Ph.D students!
Last but not least, I would like to address a special thanks to Mélissa. We shared almost all the aspects of this adventure together even though she was not explicitly part of it. That means she's carried some of the burden that comes with a Ph.D student's burning passion, while carrying her own. I appreciated the sincere sweetness she was able to bring me, and I respect the suffering she unjustly endured for my well-being.

Publications

***In situ* Thermometry of Fermionic Cold-Atom Quantum Wires.** Clément De Daniloff, Marin Tharrault, Cédric Enesa, Christophe Salomon, Frédéric Chevy, Thomas Reimann and Julian Struck. Physical Review Letters 127, 113602 - Published 9 September 2021.

We study ensembles of fermionic cold-atom quantum wires with tunable transverse mode population and single-wire resolution. From in situ density profiles, we determine the temperature of the atomic wires in the weakly interacting limit and reconstruct the underlying potential landscape. By varying atom number and temperature, we control the occupation of the transverse modes and study the 1D-3D crossover. In the 1D limit, we observe an increase of the reduced temperature T/T_F at nearly constant entropy per particle S/Nk_B. The ability to probe individual atomic wires in situ paves the way to quantitatively study equilibrium and transport properties of strongly interacting 1D Fermi gases.

In Situ Thermometry of Fermionic Cold-Atom Quantum Wires

Clément De Daniloff, Marin Tharrault, Cédric Enesa, Christophe Salomon, Frédéric Chevy, Thomas Reimann, and Julian Struck*

Laboratoire Kastler Brossel, ENS-Université PSL, CNRS, Sorbonne Université, Collège de France, 24 rue Lhomond, 75005 Paris, France

(Received 1 February 2021; accepted 2 August 2021; published 9 September 2021)

We study ensembles of fermionic cold-atom quantum wires with tunable transverse mode population and single-wire resolution. From *in situ* density profiles, we determine the temperature of the atomic wires in the weakly interacting limit and reconstruct the underlying potential landscape. By varying atom number and temperature, we control the occupation of the transverse modes and study the 1D-3D crossover. In the 1D limit, we observe an increase of the reduced temperature T/T_F at nearly constant entropy per particle S/Nk_B. The ability to probe individual atomic wires *in situ* paves the way to quantitatively study equilibrium and transport properties of strongly interacting 1D Fermi gases.

DOI: 10.1103/PhysRevLett.127.113602

The 1D world represents an exotic realm of many-body physics. Quantum and thermal fluctuations are enhanced and the dimensional constraint on the motion of particles strongly increases the impact of interactions [1]. A paradigm for the resulting unconventional behavior is the complete collectivization of elementary excitations in gapless 1D systems, known as Tomonaga-Luttinger liquids (TLLs) [2–4]. Signatures for TLLs and other characteristic 1D states have been observed in a variety of solid-state systems, including organic conductors [5,6], carbon nanotubes [7,8], semiconductor wires [9–11], antiferromagnetic spin chains [12], metallic chains [13], and edge modes of integer and fractional quantum hall states [14]. However, these materials are complex and typically feature uncontrolled interdimensional couplings, rendering quantitative studies difficult.

Ultracold atomic gases provide a complementary approach to low-dimensional many-body systems [15–17]. Their motional degrees of freedom can be tailored precisely via optical or magnetic potentials, and confinement-induced resonances provide a means to tune the sign and strength of interactions [18–21]. This high degree of controllability makes 1D Fermi gases promising candidates for the observation of elusive phenomena such as itinerant ferromagnetism [22–24], Fulde-Ferrell-Larkin-Ovchinnikov (FFLO) pairing [25,26], or Majorana edge states [27,28]. So far, only a handful of experiments investigated the properties of 1D bulk Fermi gases [20,29–33], including pioneering works on the control of interactions [20,33] and the effect of spin imbalance in such systems [29,31]. These experiments, however, suffered from addressing arrays of wires stacked along two spatial directions with varying atom number, yielding ensemble-averaged measurements. Although this drawback did not necessarily bias all previous studies, it certainly prevented progress towards the quantitative understanding of many-body problems in 1D. Indeed, as the thermodynamic state directly depends on the density, these ensemble-averages cover extended regions of the phase diagram, which severely complicates their interpretation and potentially obscures signatures of elusive states. On an even more fundamental level, ensemble averages pose a problem for the observation of critical behavior or states that are characterized by spontaneous pattern formation, e.g., magnetic domains.

In this Letter, we report on the preparation, detection, and thermodynamic characterization of individual fermionic cold-atom quantum wires in the 1D regime and 1D-3D crossover. Our approach relies on the selective loading of a single plane of a 2D optical lattice and high-resolution imaging of the resulting single row of atomic wires. This strategy allows us to circumvent line-of-sight averaging in the absorption images and to directly access the density distribution of each wire. The ability to resolve 1D density profiles *in situ* and perform local thermometry represents the main result of this work. In addition, we precisely characterize the trapping potential, which is a crucial prerequisite for further thermodynamic studies of strongly interacting 1D Fermi gases [34–40].

Experimentally, reaching the 1D regime with an atomic gas requires a tight transverse confinement. The occupation of the energetically lowest transverse mode must be predominant and excitations have to be strongly suppressed. This implies that the transverse quantum of energy has to be large compared to the energy scales of the gas, i.e., the Fermi energy E_F and thermal energy k_BT, where k_B is the Boltzmann constant and T the temperature. We employ a large-spacing 2D optical lattice to create an array of independent tube-shaped traps with the potential $V(\rho, z) = m\omega_\perp{}^2\rho^2/2 + V_\parallel(z)$, where $\rho^2 = x^2 + y^2$, m is

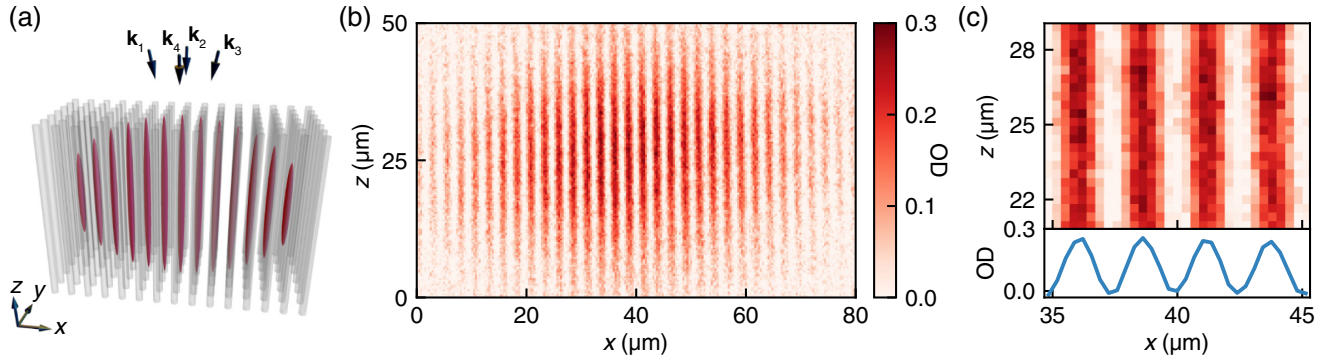

FIG. 1. Individually resolved fermionic quantum wires. (a) Array of tube traps created by superimposing two optical lattices along the x and y directions. The optical lattices are formed by the pairwise interference of the beams under small angles ($\measuredangle(\mathbf{k}_1, \mathbf{k}_3) \approx \measuredangle(\mathbf{k}_2, \mathbf{k}_4) \approx 24°$), resulting in a lattice spacing of $d \approx 2.6$ μm. Here, $\mathbf{k}_i$ denotes the wave vector of the ith beam. Only a single row of tube traps is populated with atoms. (b) 32 averaged *in situ* absorption images of Fermi gases in the 1D regime. Shown is the optical density (OD). (c) Central region of interest of (b) and the corresponding integrated line profile. For a single absorption image see the Supplemental Material [41].

the mass of the atoms, and $V_{\parallel}(z) = m\omega_{\parallel}{}^2 z^2/2 + \mathcal{O}(z^3)$ the axial potential. Given this potential, the 1D limit is expressed as $k_B T \ll \hbar\omega_{\perp}$ and $E_F \ll \hbar\omega_{\perp}$. The transverse and axial trap frequencies are $\omega_{\perp}/2\pi \approx 17$ kHz and $\omega_{\parallel}/2\pi \approx 96$ Hz, which corresponds to a ratio of $\omega_{\perp}/\omega_{\parallel} = 177$ (Supplemental Material [41]). The 2D optical lattice is composed of two orthogonally intersecting standing waves that are each created by interfering a pair of laser beams under a small angle [see Fig. 1(a)]. This results in a lattice constant of $d = 2.6$ μm $= 2.4\lambda$, where $\lambda = 1064$ nm is the wavelength of the laser beams. The large lattice spacing renders tunneling between the tube traps negligible. We measure the *in situ* density distribution of the atomic wires in the tubes through high-resolution absorption imaging [see Fig. 1(b)] (Supplemental Material [41]). Our imaging resolution, as defined by the Rayleigh criterion, is 1.3 μm. This is twice lower than the lattice spacing. Therefore, individual atomic wires are fully resolved [see Figs. 1(c) and 1(d)]. Crucially, to avoid line-of-sight integration along the imaging axis, only a single row of tube traps is populated with atoms [see Fig. 1(a)].

Our experiments are conducted with a balanced mixture of ^{40}K atoms in the two energetically lowest hyperfine states, representing a pseudospin-1/2 system. The interstate contact interactions are controlled via an s-wave Feshbach resonance at 202.10(7) G [44]. Initially, the quantum degenerate gas is strongly compressed in a crossed optical dipole trap by superimposing a repulsive TEM_{10}-like optical potential [see Fig. 2(a)] (Supplemental Material [41]), [45,46]. At full compression beam intensity, the pancake-shaped potential is characterized by trap frequency ratios of $\omega_y/\omega_x = 18$ and $\omega_z/\omega_x = 2.6$. The position of the pancake potential determines which tube traps are selectively loaded when ramping up the optical lattice. Once the lattice depth is sufficient to inhibit tunneling, the compression potential is removed [see Fig. 2(a)].

To verify the loading of a single row of tubes, we image the atomic cloud along the vertical direction (z axis). The large axial spread of the atoms in each tube trap poses a problem for high-resolution imaging given its shallow depth of field. We mitigate this issue by using a tomographic optical pumping scheme that transfers atoms outside the central region into undetected hyperfine states (Supplemental Material [41]), [47,48]. Although it is impossible to resolve individual atomic wires along this imaging direction, we can clearly distinguish between the loading of a single and double row of the lattice [see insets of Fig. 2(b)]. Translating the compression beam orthogonally with respect to the tube traps, we observe a sharp steplike structure when tracking the center of mass of the cloud [see Fig. 2(b)]. The plateaus correspond to the population of different rows. This indicates the robustness of the loading procedure against misalignment of the compression beam and small phase drifts of the optical lattice. In addition, long-term drifts of the lattice are actively compensated by readjusting the phase at the beginning of each sequence (Supplemental Material [41]).

Now, we turn to the thermodynamic analysis of *in situ* density profiles. By splitting the absorption images [see Fig. 1(b)] into sections containing only a single atomic wire and integrating over the x axis, we obtain the individual 1D density distributions $n_{1\mathrm{D}}(z)$ per spin state. To improve the signal to noise ratio, we average profiles with comparable atom numbers prepared under the same experimental conditions [see Fig. 3(a)]. For the thermometry, the 3D scattering length is reduced to $|a| = 40a_0$, which is still sufficient to establish thermal equilibrium. Here, a_0 is the Bohr radius. To determine the temperature T and chemical potential μ, we use the equation of state of the noninteracting Fermi gas

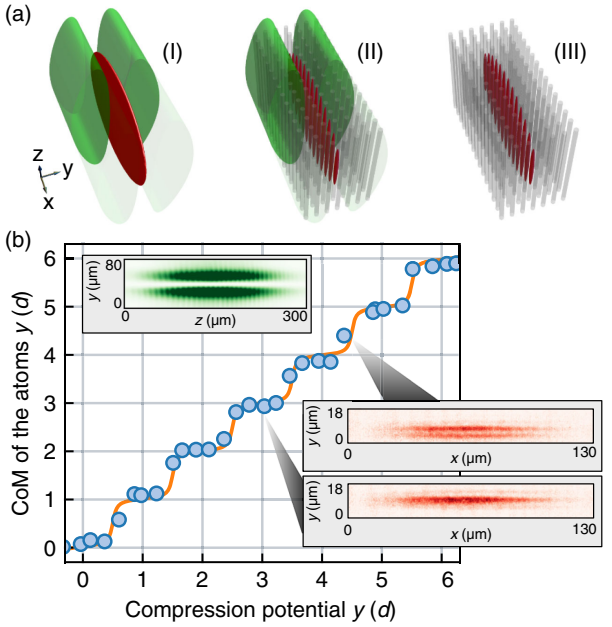

FIG. 2. Lattice loading procedure. (a) (I) First, the gas (red) is strongly compressed along the y direction by a repulsive TEM_{01}-like optical potential (green). (II) Second, the optical lattice is ramped up, populating only a single row of the array of tube traps. (III) Finally, the compression potential is removed. (b) Center of mass (CoM) of the atoms in the lattice as a function of the compression beam center along the y axis in units of the lattice constant d. The solid line is a guide to the eye. The top inset shows the intensity profile of the compression beam. The insets on the right represent characteristic images for single- and double-row loading.

$$n_{1\mathrm{D}}(\mu,T) = -\frac{1}{\lambda_T}\sum_{s=0}^{\infty}(s+1)\mathrm{Li}_{\frac{1}{2}}[-f_s(\mu,T)], \qquad (1)$$

where the sum accounts for the transverse modes with the energy $E_s = \hbar\omega_\perp(s+1)$ and degeneracy $s+1$. Here, $\mathrm{Li}_n(\cdots)$ is the nth order polylogarithm; $\lambda_T = h/\sqrt{2\pi m k_B T}$, the thermal de Broglie wavelength; and $f_s(\mu,T) = \exp(\mu/k_BT)\exp(-s\hbar\omega_\perp/k_BT)$, the fugacity of the sth transverse mode. Our assumption of negligible interaction effects in the thermodynamic analysis is not justified *a priori*. In fact, in the quantum degenerate 1D regime, the ratio of interaction and kinetic energy ($E_{\mathrm{int}}/E_{\mathrm{kin}} \sim 1/n_{1\mathrm{D}}$) diverges in the low-density limit. This leads to a nontrivial competition of kinetic energy and interaction effects in the wings of the atomic wires, where the density and degeneracy drop simultaneously. To estimate the influence of interactions on the density profiles, we perform an *a posteriori* consistency check of our analysis for repulsive and attractive interactions ($a = \pm 40a_0$).

Applying the local density approximation $\mu(z) = \mu_0 - V_\parallel(z)$ to the weakly confined axial direction allows us to fit the equation of state [Eq. (1)] to the measured 1D density distributions. By fitting a set of profiles with varying temperatures and atom numbers [see Fig. 3(a)], we extract μ and T as independent parameters for each profile and the reconstructed axial potential as a shared parameter for the entire set [49]. More precisely, the anharmonic part of the potential is modeled by a higher-order polynomial while the harmonic part is fixed through an independent measurement (Supplemental Material [41]). The asymmetry and anharmonicity of the potential [see Fig. 3(b)] stem from the gravitational force along the z direction as well as the Gaussian profiles of the laser beams forming the optical lattice and crossed optical dipole trap. We observe no significant variation of the axial potential across the 18 central tube traps, which are selected for the data analysis. Comparing reconstructed potentials from sets with attractive and repulsive interactions reveals only minor differences

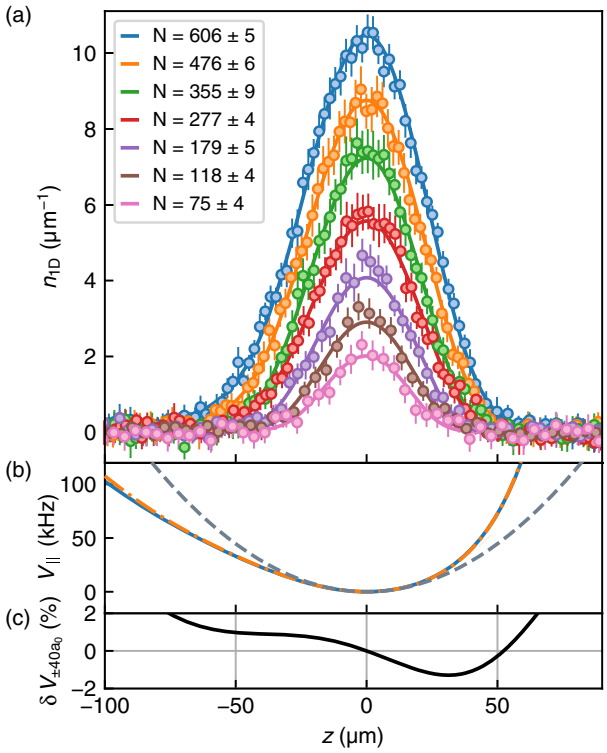

FIG. 3. (a) Averaged 1D density profiles for individual tubes with a total atom number N per spin state. The solid lines represent fits of the noninteracting equation of state, with T (from top to bottom): 0.51(1) μK, 0.44(2) μK, 0.31(2) μK, 0.41(2) μK, 0.29(2) μK, 0.27(2) μK, and 0.25(3) μK. (b) Reconstructed axial potential for $a = -40a_0$ (orange dashed-dotted line) and $a = +40a_0$ (blue solid line). The harmonic part (gray dashed line) of the potential has been independently measured (Supplemental Material [41]). (c) Relative difference $\delta V_{\pm 40a_0}(z) = (V_{\parallel,-40a_0}(z) - V_{\parallel,+40a_0}(z))/V_{\parallel,-40a_0}(z)$ between the reconstructed potentials for attractive and repulsive interactions.

[see Fig. 3(c)] and thus validates the use of the noninteracting equation of state.

With the thermometry at hand, the 1D-3D crossover, driven by the gradual occupation of transverse modes, can be precisely characterized. We obtain local dimensionless quantities by normalizing the relevant energy scales with the Fermi energy, which is determined by the implicit equation

$$n_{1D} = \sqrt{\frac{8mE_F}{h^2}} \sum_{s=0}^{\lfloor \frac{E_F}{\hbar\omega_\perp} \rfloor} (s+1)\sqrt{1 - s\frac{\hbar\omega_\perp}{E_F}}, \qquad (2)$$

where $\lfloor \cdots \rfloor$ denotes the floor function. This equation simplifies to $E_F = h^2 n_{1D}^2/8m$ in the 1D regime. The population of transverse modes can either be caused by thermal excitations or arise as a consequence of Pauli blocking. By changing the initial evaporation parameters in the crossed optical dipole trap ($T/T_F \approx 0.15$–0.25) prior to loading the atoms into the lattice, we vary the final atom number and temperature in the tubes. This way, we control the transverse mode population and can reach the deep 1D regime with $k_B T \lesssim 0.2\hbar\omega_\perp$ and $E_F \lesssim 0.2\hbar\omega_\perp$ [see Fig. 4(a)] (Supplemental Material [41]). The temperature spread across different atomic wires is yet another sign that tunneling between the tube traps is strongly suppressed, which leads to an early thermal decoupling during the lattice loading procedure.

Previous 1D Fermi gas experiments inferred estimates of the degeneracy based on thermometry of the initial 3D cloud before loading the optical lattice. These estimates rely on the assumption of an isentropic loading procedure, which is questionable due to various technical heating processes, e.g., laser intensity noise, and the suppression of thermalizing two-body collisions in the 1D regime [50–52]. More fundamentally, the temperature and reduced temperature T/T_F are not conserved in the isentropic 1D-3D crossover (Supplemental Material [41]). The corresponding isentropic 1D-3D relations depend on interactions and are, in general, not known. With our approach, we do not require any knowledge about the loading process of the tube traps and instead determine *in situ* the temperature, local T/T_F, and local entropy per particle

$$\frac{S}{Nk_B} = \frac{\sum_{s=0}^{\infty}(s+1)(\frac{3}{2}\mathrm{Li}_{\frac{3}{2}}(-f_s) - \ln(f_s)\mathrm{Li}_{\frac{1}{2}}(-f_s))}{\sum_{s=0}^{\infty}(s+1)\mathrm{Li}_{\frac{1}{2}}(-f_s)}. \qquad (3)$$

We observe that S/Nk_B stays nearly constant in the entire crossover region, whereas T/T_F displays a sudden increase in the low atom number and temperature limit [see Figs. 4(b) and 4(c)]. This is a clear signature of the 1D regime, where the equation of state is strongly altered with respect to the 3D case. Note that, compared to the 3D ideal Fermi gas, the role of quantum statistics in 1D remains important at higher values of T/T_F. For instance, at

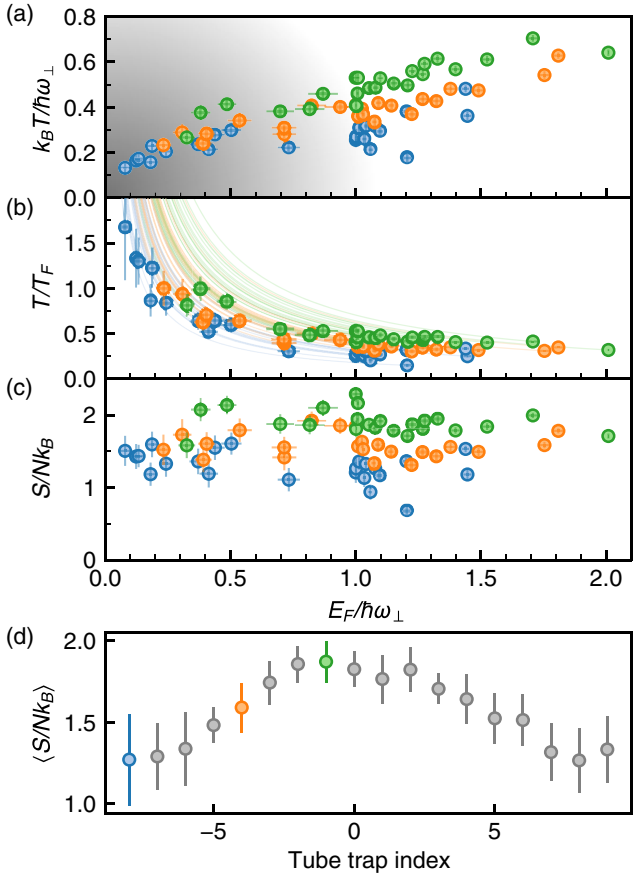

FIG. 4. Thermodynamics of the 1D-3D crossover. The data points in (b), (c), and (d) correspond to the center of each tube trap ($z = 0$), where the Fermi energy is the highest. Green, orange, and blue colors represent a selection of three characteristic tubes whose indices are indicated in (d). Tube trap indices label the 18 selected central tubes from left to right along the x axis. (a) The temperature of individual atomic wires normalized by the transverse frequency $k_B T/\hbar\omega_\perp$ and (b) the reduced temperature T/T_F. The gray gradient in (a) depicts the 1D limit. The solid lines in (b) that emanate from the data points represent the continuous change in T/T_F and $E_F/(\hbar\omega_\perp)$ within each atomic wire according to the local density approximation. (c) The entropy per particle S/Nk_B. (d) Mean value of the entropy per particle obtained by averaging the data of (c) for the green, orange, and blue points. The gray points represent the other 15 tubes traps, which were omitted in (a), (b), and (c).

$T/T_F = 1.6$ [the highest T/T_F in Fig. 4(b)], Maxwell-Boltzmann statistics overestimates the density of the noninteracting gas by 55% in 1D, vs 12% in 3D.

Interestingly, we observe that the entropy per particle varies between the tubes, with an increase toward the center where the density is highest [see Fig. 4(d)]. This may be evidence for a density-dependent interaction effect. For example, a realistic scenario in this context could be the occurrence of three-body losses during the early loading phase of the lattice, where the scattering length is still significant (Supplemental Material [41]).

This inhomogeneous redistribution of entropy further highlights the relevance and necessity of our thermometry technique based on resolving individual atomic wires.

A direct follow-up study to the work presented here is the measurement of the equation of state of strongly interacting fermionic wires. Within the framework of the local density approximation, the precise knowledge of the axial potential will allow us to locally relate the 1D density and chemical potential at any interaction strength. The local pressure and compressibility can then be obtained from the integral and derivative of the density with respect to the chemical potential [38,39,53]. From these observables, further thermodynamic quantities can be determined, such as the reduced temperature T/T_F. Theoretically, the ground state and low-temperature regime ($T \ll T_F$) of the interacting 1D Fermi gas can be solved with the Bethe ansatz [54]. However, for the general finite-temperature case, the situation is significantly more challenging and theoretical studies are sparse [55,56].

The individual probing of 1D Fermi gases promises further insight into elusive states of matter and critical behavior. This includes the observation of the highly sought FFLO phase [25,26,29] and the study of TLLs featuring collectivized excitations and spin-charge separation [32,57–60]. Of particular interest is the interplay of strong interactions and the suppression of thermalizing collisions in 1D [50,52,61], which strongly impacts out-of-equilibrium and transport phenomena.

We thank Tarik Yefsah for stimulating and helpful discussions and critical reading of the manuscript as well as Antoine Heidmann for hosting the project at Laboratoire Kastler Brossel and his active support for the completion of this work. J. S. was supported by LabEX ENS-ICFP: ANR-10-LABX-0010/ANR-10-IDEX-0001-02 PSL*. We acknowledge support from DIM Sirteq (Grant No. EML 19002465 1DFG) and Fondation S. et C. del Duca (Grant No. 61846). C. D. and M. T. conducted the measurements and data analysis. C. D. and J. S. performed the theoretical computations. C. D., M. T., C. E., T. R., and J. S. designed and constructed the relevant parts of the experimental apparatus for the project. J. S. conceptualized, planned, and supervised the project. C. D. and J. S. prepared the manuscript with comments from all authors.

*julian.struck@lkb.ens.fr

[1] T. Giamarchi, *Quantum Physics in One Dimension* (Oxford University Press, New York, 2003).
[2] S.-i. Tomonaga, Remarks on Bloch's method of sound waves applied to many-Fermion problems, Prog. Theor. Phys. **5**, 544 (1950).
[3] J. M. Luttinger, An exactly soluble model of a many-Fermion system, J. Math. Phys. (N.Y.) **4**, 1154 (1963).
[4] F. D. M. Haldane, 'Luttinger liquid theory' of one-dimensional quantum fluids. I. Properties of the Luttinger model and their extension to the general 1D interacting spinless Fermi gas, J. Phys. C **14**, 2585 (1981).
[5] A. Schwartz, M. Dressel, G. Grüner, V. Vescoli, L. Degiorgi, and T. Giamarchi, On-chain electrodynamics of metallic $(TMTSF)_2X$ salts: Observation of Tomonaga-Luttinger liquid response, Phys. Rev. B **58**, 1261 (1998).
[6] T. Giamarchi, From Luttinger to Fermi liquids in organic conductors, in *The Physics of Organic Superconductors and Conductors*, edited by A. Lebed (Springer, New York, 2008), pp. 719–743.
[7] M. Bockrath, D. H. Cobden, J. Lu, A. G. Rinzler, R. E. Smalley, L. Balents, and P. L. McEuen, Luttinger-liquid behaviour in carbon nanotubes, Nature (London) **397**, 598 (1999).
[8] H. Ishii, H. Kataura, H. Shiozawa, H. Yoshioka, H. Otsubo, Y. Takayama, T. Miyahara, S. Suzuki, Y. Achiba, M. Nakatake, T. Narimura, M. Higashiguchi, K. Shimada, H. Namatame, and M. Taniguchi, Direct observation of Tomonaga-Luttinger-liquid state in carbon nanotubes at low temperatures, Nature (London) **426**, 540 (2003).
[9] A. Yacoby, H. L. Stormer, N. S. Wingreen, L. N. Pfeiffer, K. W. Baldwin, and K. W. West, Nonuniversal Conductance Quantization in Quantum Wires, Phys. Rev. Lett. **77**, 4612 (1996).
[10] O. M. Auslaender, H. Steinberg, A. Yacoby, Y. Tserkovnyak, B. I. Halperin, K. W. Baldwin, L. N. Pfeiffer, and K. W. West, Spin-charge separation and localization in one dimension., Science **308**, 88 (2005).
[11] Y. Jompol, C. J. B. Ford, J. P. Griffiths, I. Farrer, G. A. C. Jones, D. Anderson, D. A. Ritchie, T. W. Silk, and A. J. Schofield, Probing spin-charge separation in a Tomonaga-Luttinger liquid, Science **325**, 597 (2009).
[12] B. Lake, D. A. Tennant, C. D. Frost, and S. E. Nagler, Quantum criticality and universal scaling of a quantum antiferromagnet, Nat. Mater. **4**, 329 (2005).
[13] P. Segovia, D. Purdie, M. Hengsberger, and Y. Baer, Observation of spin and charge collective modes in one-dimensional metallic chains, Nature (London) **402**, 504 (1999).
[14] A. M. Chang, Chiral Luttinger liquids at the fractional quantum Hall edge, Rev. Mod. Phys. **75**, 1449 (2003).
[15] I. Bloch, J. Dalibard, and W. Zwerger, Many-body physics with ultracold gases, Rev. Mod. Phys. **80**, 885 (2008).
[16] L. Pitaevskii and S. Stringari, *Bose-Einstein Condensation and Superfluidity*, 1st ed. (Oxford University Press, New York, 2016).
[17] S. Krinner, T. Esslinger, and J.-P. Brantut, Two-terminal transport measurements with cold atoms, J. Phys. Condens. Matter **29**, 343003 (2017).
[18] M. Olshanii, Atomic Scattering in the Presence of an External Confinement and a Gas of Impenetrable Bosons, Phys. Rev. Lett. **81**, 938 (1998).
[19] T. Bergeman, M. G. Moore, and M. Olshanii, Atom-Atom Scattering under Cylindrical Harmonic Confinement: Numerical and Analytic Studies of the Confinement Induced Resonance, Phys. Rev. Lett. **91**, 163201 (2003).
[20] H. Moritz, T. Stöferle, K. Günter, M. Köhl, and T. Esslinger, Confinement Induced Molecules in a 1D Fermi Gas, Phys. Rev. Lett. **94**, 210401 (2005).

[21] E. Haller, M. J. Mark, R. Hart, J. G. Danzl, L. Reichsöllner, V. Melezhik, P. Schmelcher, and H.-C. Nägerl, Confinement-Induced Resonances in Low-Dimensional Quantum Systems, Phys. Rev. Lett. **104**, 153203 (2010).

[22] S. E. Gharashi and D. Blume, Correlations of the Upper Branch of 1D Harmonically Trapped Two-Component Fermi Gases, Phys. Rev. Lett. **111**, 045302 (2013).

[23] X. Cui and T.-L. Ho, Ground-state ferromagnetic transition in strongly repulsive one-dimensional Fermi gases, Phys. Rev. A **89**, 023611 (2014).

[24] Y. Jiang, D. V. Kurlov, X.-W. Guan, F. Schreck, and G. V. Shlyapnikov, Itinerant ferromagnetism in one-dimensional two-component Fermi gases, Phys. Rev. A **94**, 011601(R) (2016).

[25] G. Orso, Attractive Fermi Gases with Unequal Spin Populations in Highly Elongated Traps, Phys. Rev. Lett. **98**, 070402 (2007).

[26] H. Hu, X.-J. Liu, and P. D. Drummond, Phase Diagram of a Strongly Interacting Polarized Fermi Gas in One Dimension, Phys. Rev. Lett. **98**, 070403 (2007).

[27] L. Jiang, T. Kitagawa, J. Alicea, A. R. Akhmerov, D. Pekker, G. Refael, J. I. Cirac, E. Demler, M. D. Lukin, and P. Zoller, Majorana Fermions in Equilibrium and in Driven Cold-Atom Quantum Wires, Phys. Rev. Lett. **106**, 220402 (2011).

[28] X.-J. Liu and H. Hu, Topological superfluid in one-dimensional spin-orbit-coupled atomic Fermi gases, Phys. Rev. A **85**, 033622 (2012).

[29] Y.-A. Liao, A. S. C. Rittner, T. Paprotta, W. Li, G. B. Partridge, R. G. Hulet, S. K. Baur, and E. J. Mueller, Spin-imbalance in a one-dimensional Fermi gas, Nature (London) **467**, 567 (2010).

[30] G. Pagano, M. Mancini, G. Cappellini, P. Lombardi, F. Schäfer, H. Hu, X.-J. Liu, J. Catani, C. Sias, M. Inguscio, and L. Fallani, A one-dimensional liquid of fermions with tunable spin, Nat. Phys. **10**, 198 (2014).

[31] M. C. Revelle, J. A. Fry, B. A. Olsen, and R. G. Hulet, 1D to 3D Crossover of a Spin-Imbalanced Fermi Gas, Phys. Rev. Lett. **117**, 235301 (2016).

[32] T. L. Yang, P. Grišins, Y. T. Chang, Z. H. Zhao, C. Y. Shih, T. Giamarchi, and R. G. Hulet, Measurement of the Dynamical Structure Factor of a 1D Interacting Fermi Gas, Phys. Rev. Lett. **121**, 103001 (2018).

[33] Y.-T. Chang, R. Senaratne, D. Cavazos-Cavazos, and R. G. Hulet, Collisional Loss of One-Dimensional Fermions Near a p-Wave Feshbach Resonance, Phys. Rev. Lett. **125**, 263402 (2020).

[34] T.-L. Ho and Q. Zhou, Obtaining the phase diagram and thermodynamic quantities of bulk systems from the densities of trapped gases, Nat. Phys. **6**, 131 (2010).

[35] S. Nascimbène, N. Navon, K. J. Jiang, F. Chevy, and C. Salomon, Exploring the thermodynamics of a universal Fermi gas, Nature (London) **463**, 1057 (2010).

[36] N. Navon, S. Nascimbene, F. Chevy, C. Salomon, S. Nascimbène, F. Chevy, C. Salomon, S. Nascimbene, F. Chevy, and C. Salomon, The equation of state of a low-temperature Fermi gas with tunable interactions, Science **328**, 729 (2010).

[37] T. Yefsah, R. Desbuquois, L. Chomaz, K. J. Günter, and J. Dalibard, Exploring the Thermodynamics of a Two-Dimensional Bose Gas, Phys. Rev. Lett. **107**, 130401 (2011).

[38] M. J. H. Ku, A. T. Sommer, L. W. Cheuk, and M. W. Zwierlein, Revealing the superfluid lambda transition in the universal thermodynamics of a unitary Fermi gas, Science **335**, 563 (2012).

[39] K. Fenech, P. Dyke, T. Peppler, M. G. Lingham, S. Hoinka, H. Hu, and C. J. Vale, Thermodynamics of an Attractive 2D Fermi Gas, Phys. Rev. Lett. **116**, 045302 (2016).

[40] I. Boettcher, L. Bayha, D. Kedar, P. A. Murthy, M. Neidig, M. G. Ries, A. N. Wenz, G. Zürn, S. Jochim, and T. Enss, Equation of State of Ultracold Fermions in the 2D BEC-BCS Crossover Region, Phys. Rev. Lett. **116**, 045303 (2016).

[41] See Supplemental Material at http://link.aps.org/supplemental/10.1103/PhysRevLett.127.113602 for more information regarding the large-spacing optical lattice, absorption imaging, optical pumping tomography, measurement of the axial frequency, the equation of state fitting procedure, transverse mode occupation, and the isentropic 1D-3D relation of the reduced temperature for the non-interacting Fermi gas, which includes Refs. [42,43].

[42] E. Magnan, J. Maslek, C. Bracamontes, A. Restelli, T. Boulier, and J. V. Porto, A low-steering piezo-driven mirror, Rev. Sci. Instrum. **89**, 073110 (2018).

[43] K. Hueck, N. Luick, L. Sobirey, J. Siegl, T. Lompe, H. Moritz, L. W. Clark, and C. Chin, Calibrating high intensity absorption imaging of ultracold atoms, Opt. Express **25**, 8670 (2017).

[44] C. A. Regal, M. Greiner, and D. S. Jin, Observation of Resonance Condensation of Fermionic Atom Pairs, Phys. Rev. Lett. **92**, 040403 (2004).

[45] N. L. Smith, W. H. Heathcote, G. Hechenblaikner, E. Nugent, and C. J. Foot, Quasi-2D confinement of a BEC in a combined optical and magnetic potential, J. Phys. B **38**, 223 (2005).

[46] S. P. Rath, T. Yefsah, K. J. Günter, M. Cheneau, R. Desbuquois, M. Holzmann, W. Krauth, and J. Dalibard, Equilibrium state of a trapped two-dimensional Bose gas, Phys. Rev. A **82**, 013609 (2010).

[47] M. R. Andrews, C. G. Townsend, H.-J. Miesner, D. S. Durfee, D. M. Kurn, and W. Ketterle, Observation of interference between two Bose condensates, Science **275**, 637 (1997).

[48] M. J. H. Ku, W. Ji, B. Mukherjee, E. Guardado-Sanchez, L. W. Cheuk, T. Yefsah, and M. W. Zwierlein, Motion of a Solitonic Vortex in the BEC-BCS Crossover, Phys. Rev. Lett. **113**, 065301 (2014).

[49] F. Salces-Carcoba, C. J. Billington, A. Putra, Y. Yue, S. Sugawa, and I. B. Spielman, Equations of state from individual one-dimensional Bose gases, New J. Phys. **20**, 113032 (2018).

[50] T. Kinoshita, T. Wenger, and D. S. Weiss, A quantum Newton's cradle, Nature (London) **440**, 900 (2006).

[51] I. E. Mazets, T. Schumm, and J. Schmiedmayer, Breakdown of Integrability in a Quasi-1D Ultracold Bosonic Gas, Phys. Rev. Lett. **100**, 210403 (2008).

[52] M. Gring, M. Kuhnert, T. Langen, T. Kitagawa, B. Rauer, M. Schreitl, I. Mazets, D. A. Smith, E. Demler,

and J. Schmiedmayer, Relaxation and prethermalization in an isolated quantum system, Science **337**, 1318 (2012).

[53] S. Tung, G. Lamporesi, D. Lobser, L. Xia, and E. A. Cornell, Observation of the Presuperfluid Regime in a Two-Dimensional Bose Gas, Phys. Rev. Lett. **105**, 230408 (2010).

[54] X.-W. Guan, M. T. Batchelor, and C. Lee, Fermi gases in one dimension: From Bethe ansatz to experiments, Rev. Mod. Phys. **85**, 1633 (2013).

[55] M. D. Hoffman, P. D. Javernick, A. C. Loheac, W. J. Porter, E. R. Anderson, and J. E. Drut, Universality in one-dimensional fermions at finite temperature: Density, pressure, compressibility, and contact, Phys. Rev. A **91**, 033618 (2015).

[56] H. Tajima, S. Tsutsui, and T. M. Doi, Low-dimensional fluctuations and pseudogap in Gaudin-Yang Fermi gases, Phys. Rev. Research **2**, 033441 (2020).

[57] A. Recati, P. O. Fedichev, W. Zwerger, and P. Zoller, Spin-Charge Separation in Ultracold Quantum Gases, Phys. Rev. Lett. **90**, 020401 (2003).

[58] C. Kollath, U. Schollwöck, and W. Zwerger, Spin-Charge Separation in Cold Fermi Gases: A Real Time Analysis, Phys. Rev. Lett. **95**, 176401 (2005).

[59] B. Yang, Y.-Y. Chen, Y.-G. Zheng, H. Sun, H.-N. Dai, X.-W. Guan, Z.-S. Yuan, and J.-W. Pan, Quantum Criticality and the Tomonaga-Luttinger Liquid in One-Dimensional Bose Gases, Phys. Rev. Lett. **119**, 165701 (2017).

[60] J. Vijayan, P. Sompet, G. Salomon, J. Koepsell, S. Hirthe, A. Bohrdt, F. Grusdt, I. Bloch, and C. Gross, Time-resolved observation of spin-charge deconfinement in fermionic Hubbard chains, Science **367**, 186 (2020).

[61] F. Meinert, M. Knap, E. Kirilov, K. Jag-Lauber, M. B. Zvonarev, E. Demler, and H.-C. Nägerl, Bloch oscillations in the absence of a lattice, Science **356**, 945 (2017).

Supplemental Material: *In Situ* Thermometry of Fermionic Cold-Atom Quantum Wires

Clément De Daniloff,[1] Marin Tharrault,[1] Cédric Enesa,[1] Christophe Salomon,[1] Frédéric Chevy,[1] Thomas Reimann,[1] and Julian Struck[1,*]

[1] *Laboratoire Kastler Brossel, ENS-Université PSL, CNRS, Sorbonne Université, Collège de France, 24 rue Lhomond, 75005 Paris, France*

LARGE-SPACING OPTICAL LATTICE

The 2D optical lattice consists of two superimposed standing waves, which are each created by interfering a pair of laser beams under an angle of $2\theta \approx 24°$. The standing waves along the x- and y-axis are formed by beam pairs with the wavevectors $\mathbf{k}_{1,3} = k\,(\pm\sin(\theta), 0, -\cos(\theta))$ and $\mathbf{k}_{2,4} = k\,(0, \mp\sin(\theta), -\cos(\theta))$, respectively. Here, $k = 2\pi/\lambda$ is the wavenumber and $\lambda = 1064\,\mathrm{nm}$. The waists of the lattice beams are approximately $180\,\mu\mathrm{m}$, which results in a variation of $\omega_\perp$ of less than 2% across the 18 central tube traps that are used for data analysis. We collect all four lattice beams in a microscope objective after they have passed the atomic cloud and image them onto a CCD camera [see Fig. S1]. This gives us an absolute phase reference of the lattice. Through piezo-driven mirrors in the beam paths [42], we control the phase and compensate long-term drifts at the beginning of each experimental sequence.

The intensity ramps of the compression beam and optical lattice for the preparation of a single row of tubes are shown in figure S2. Also depicted is the change of the s-wave scattering length during the loading procedure, starting from $a = -1334\,a_0$ in the crossed optical dipole trap for the initial evaporative cooling of the atomic gas.

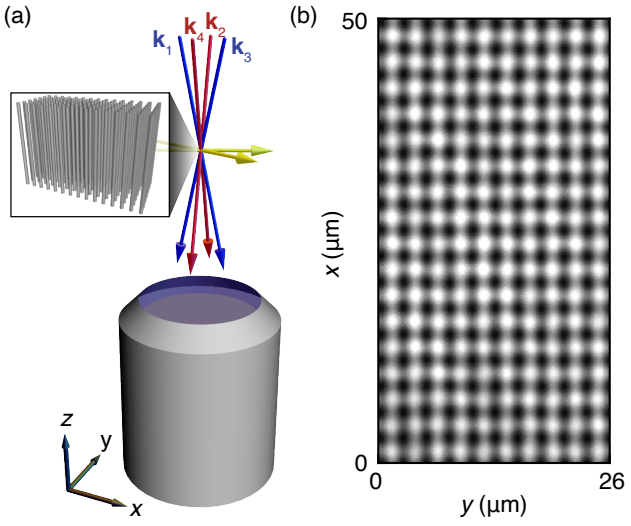

FIG. S1. Direct imaging of the optical lattice. (a) The laser beam pairs (blue and red) forming the lattice are collected by a microscope objective and (b) refocused onto a CCD camera. For the sake of completeness, the crossed optical dipole trap beams (yellow) are also included in (a).

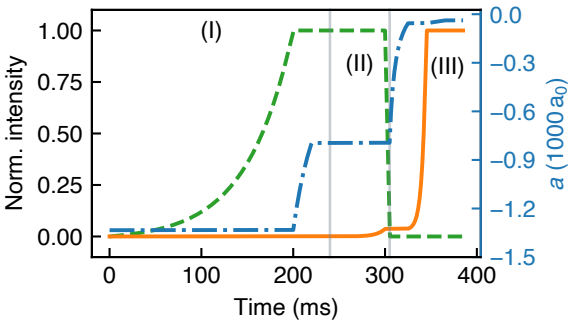

FIG. S2. Lattice loading ramps. (Green dashed line) Normalized intensity of the compression beam. (Orange solid line) Normalized intensity of the lattice laser beams. (Blue dashed-dotted line) s-wave scattering length. The roman numbers correspond to the schematic depiction in figure 2(a).

ABSORPTION IMAGING

We resonantly image the energetically lowest hyperfine state $|F = 9/2,\ m_F = -9/2\rangle$ at a magnetic bias field above 200 G on the D2 cycling transition. Prior to imaging, all optical potentials are switched off in order to avoid spatially dependent AC Stark energy shifts. A short imaging pulse of $t_{\mathrm{img}} = 12\,\mu\mathrm{s}$ ensures that the gas expands only marginally in the transverse direction ($\omega_\perp t_{\mathrm{img}}/2\pi = 0.2$) and that the frequency shift due to the Doppler effect is negligible. We have verified the latter by measuring the velocity of the atomic cloud after imaging pulses of different durations [43]. A linear increase of the velocity with the pulse duration implies a constant force on the atoms during the imaging process and hence no significant frequency shift. The pulse duration of $12\,\mu\mathrm{s}$ lies well within this regime.

To determine the column density $\tilde{n}$ of the atomic gas along the probe beam direction, we use the extended Beer-Lambert law

$$\sigma_0 \tilde{n} = \ln(I_{\mathrm{ref}}/I_{\mathrm{abs}}) + (I_{\mathrm{ref}} - I_{\mathrm{abs}})/I_{\mathrm{sat}}, \qquad \text{(S1)}$$

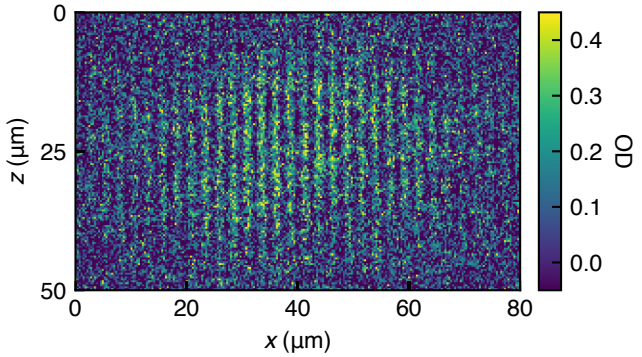

FIG. S3. Individual absorption image of atomic wires in the 1D regime. This image is part of the average of Fig. 1(b).

which accounts for the saturation of the atomic transition. Here, σ_0 is the absorption cross section, I_{sat} the saturation intensity, I_{ref} and I_{abs} the imaging intensities before and after the atoms, respectively. Typically, we operate with a saturation parameter of $s = I_{\mathrm{ref}}/I_{\mathrm{sat}} \approx 3-4$. For its calibration, we prepare clouds of low atom number (OD < 0.5) under the same experimental conditions and vary the probe beam power. Subsequently, we find the saturation parameter that yields a constant column density [see eq. (S1)] for varying probe beam powers. The estimated systematic uncertainty on the saturation parameter is 10%. Figure S3 shows an individual absorption image of atomic wires in the 1D regime.

OPTICAL PUMPING TOMOGRAPHY

The large axial extent of the atomic wires poses a problem for the z-axis imaging system [see Fig. S2(a)], which features a depth of field of $\pm 5\,\mu$m. We mitigate this issue by optically pumping atoms located outside of a central slice into the upper hyperfine ground state manifold ($m_J = 1/2$), rendering them transparent to the probe beam. The pumping beam illuminates an opaque slit on an optical window, which is then projected onto the row of atomic wires [see Fig. S4]. The demagnified size of the slit at the position of the atoms is $6\,\mu$m, while the resolution of the imaging system is $5\,\mu$m. This is consistent with the measured $4\,\mu$m full width at half maximum of the atomic slice after the tomography [see Fig. S4(c)]. In the experiment, the pumping pulse illuminates the atomic cloud for $1\,\mu$s before the absorption image is taken.

MEASUREMENT OF THE AXIAL FREQUENCY

Due to the anharmonicity of the potential and the large axial extent of the atomic wires, a reliable measurement of the axial frequency via induced oscillations is not feasible. Instead, we apply calibrated magnetic

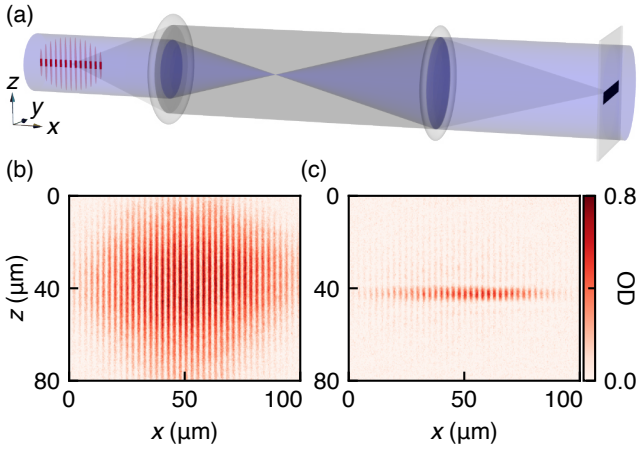

FIG. S4. Optical pumping tomography. (a) Imaging system projecting the shadow of an opaque slit onto the row of atomic wires. (b) and (c) correspond to absorption images of the atomic wires without and with optical pumping, respectively.

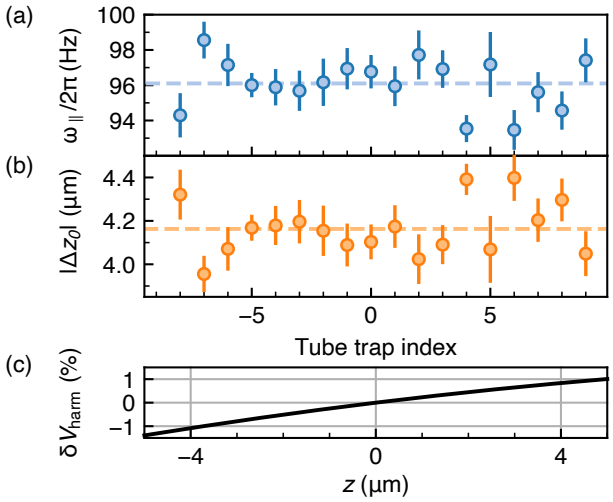

FIG. S5. Gradient measurement of the axial frequency. (a) Axial frequency of each tube trap. (b) Corresponding displacement $|\Delta z_0|$ of the maximum of the 1D density distribution. The dashed lines in (a) and (b) indicate the mean value over all tubes. (c) Relative difference δV_{harm} between the harmonic approximation and the fully reconstructed axial potential.

field gradients $\pm B_z'$ along the axial direction and measure the differential displacement $2\Delta z_0$ of the maximum of the 1D density distribution. In the small displacement limit ($\Delta z_0 \to 0$), the axial trapping frequency is given by $\omega_{\parallel} = \sqrt{\mu B_z'/m\Delta z_0}$, where μ is the magnetic moment.

We observe no statistically significant shift of the measured frequency across the 18 central tube traps [see Fig. S5]. Typically, the displacement from the center of the trap is $\Delta z_0 \approx \pm 4\,\mu$m. A self-consistency check with the fully reconstructed potential demonstrates that the relative deviation from a harmonic potential in this region is

at most 1% [see Fig. S5(c)].

EQUATION OF STATE FITTING PROCEDURE

Using the local density approximation $\mu(z) = \mu_0 - V_\parallel(z)$, with $\mu_0 = \mu(z=0)$, we simultaneously fit a large number of 1D density profiles using the non-interacting equation of state $n(\mu(z), T)$ [Eq. (1)]. In order to account for the anharmonicity of the axial potential, we use a 7th order polynomial model

$$V_\parallel(z) = \frac{1}{2} m\omega_\parallel^2 z^2 + \sum_{p=3}^{7} a_p z^p, \tag{S2}$$

where the axial frequency $\omega_\parallel$ is directly measured as described in the previous section and the higher-order coefficients a_p are left as fit parameters. We have verified that the reconstructed potential in the region with atoms is not changed for polynomial models of higher order than 7.

To prepare the 1D density profiles for the fitting procedure, we first sort all absorption images of a given data set according to their total atom number. Subsequently, this list is grouped in intervals of 10 images, which are then averaged. From the resulting images, the 1D density profiles for each tube are extracted. For example, the entire data set for the s-wave scattering length of $a = +40\,a_0$ consists of 270 absorption images. After averaging and selecting the 18 central tubes, we end up with a set of 486 individual 1D density profiles.

To measure T and μ for a given profile and to determine the polynomial coefficients a_p [Eq. (S2)], we simultaneously fit an entire set of profiles. For each individual 1D profile, $\beta = 1/k_B T$ and $\beta\mu$ constitute independent fit parameters, while the coefficients a_p serve as shared parameters for the whole set. Statistical errors of the thermodynamic quantities are obtained from the covariance matrix of the fit.

TRANSVERSE MODE OCCUPATION

The transverse mode population of the tube traps is a measure of the dimensional character of the atomic wires. The relative occupation of the lowest mode

$$\eta_0(\mu, T) = \frac{\mathrm{Li}_{\frac{1}{2}}(-f_0(\mu,T))}{\sum_{s=0}^{\infty}(s+1)\,\mathrm{Li}_{\frac{1}{2}}(-f_s(\mu,T))}, \tag{S3}$$

is given by the equation of state [Eq. (1)]. In the low atom number and temperature limit, η_0 saturates to one [see Fig. S6], which, by definition, corresponds to the 1D regime.

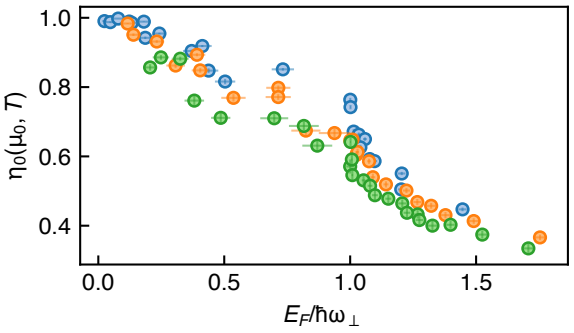

FIG. S6. Relative occupation η_0 of the lowest transverse mode at the center of the tube traps ($z = 0$), where η_0 is the smallest. Different colors represent three characteristic tube traps. The data points correspond to the ones shown in Fig. 4.

ISENTROPIC 1D-3D RELATION OF THE REDUCED TEMPERATURE FOR THE NON-INTERACTING FERMI GAS

In this section we study the isentropic thermodynamic relation between the non-interacting homogeneous 3D and 1D Fermi gas. This elementary (toy) model already demonstrates that the reduced temperature is not conserved in the adiabatic 1D-3D crossover. For the 3D and 1D Fermi gas, the corresponding reduced temperatures are given by

$$\left(\frac{T}{T_F}\right)_{3\mathrm{D}} = 4\pi \left(-6\pi^2\,\mathrm{Li}_{\frac{3}{2}}(-f_{3\mathrm{D}})\right)^{-2/3}, \tag{S4}$$

$$\left(\frac{T}{T_F}\right)_{1\mathrm{D}} = \frac{4}{\pi} \left(\mathrm{Li}_{\frac{1}{2}}(-f_{1\mathrm{D}})\right)^{-2}, \tag{S5}$$

and the entropy per particle reads

$$\left(\frac{S}{Nk_B}\right)_{3\mathrm{D}} = \frac{5\,\mathrm{Li}_{\frac{5}{2}}(-f_{3\mathrm{D}})}{2\,\mathrm{Li}_{\frac{3}{2}}(-f_{3\mathrm{D}})} - \ln(f_{3\mathrm{D}}), \tag{S6}$$

$$\left(\frac{S}{Nk_B}\right)_{1\mathrm{D}} = \frac{3\,\mathrm{Li}_{\frac{3}{2}}(-f_{1\mathrm{D}})}{2\,\mathrm{Li}_{\frac{1}{2}}(-f_{1\mathrm{D}})} - \ln(f_{1\mathrm{D}}), \tag{S7}$$

where $f_{3\mathrm{D}}$ and $f_{1\mathrm{D}}$ are the fugacities of the 3D and 1D gas, respectively. Since the entropy is conserved, i.e. $(S/Nk_B)_{1\mathrm{D}} = (S/Nk_B)_{3\mathrm{D}}$, $f_{3\mathrm{D}}$ and $f_{1\mathrm{D}}$ are directly connected through Eqs. (S6) and (S7). With the isentropic relation between the fugacities we then obtain the isentropic relation of the reduced temperatures in 3D and 1D (see Eqs. (S4), (S5) and Fig. S7).

* Corresponding author: julian.struck@lkb.ens.fr

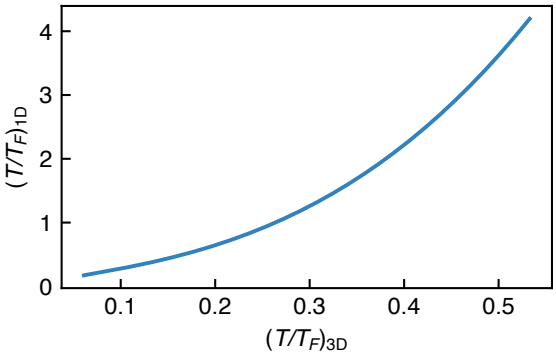

FIG. S7. Isentropic relation between the reduced temperatures of a homogeneous non-interacting 3D and 1D Fermi gas.

[42] E. Magnan, J. Maslek, C. Bracamontes, A. Restelli, T. Boulier, and J. V. Porto, A low-steering piezo-driven mirror, Rev. Sci. Instrum. **89**, 073110 (2018).

[43] K. Hueck, N. Luick, L. Sobirey, J. Siegl, T. Lompe, H. Moritz, L. W. Clark, and C. Chin, Calibrating high intensity absorption imaging of ultracold atoms, Opt. Express **25**, 8670 (2017).

List of Figures

List of Tables

Peer-reviewed publication

1. ***In situ* Thermometry of Fermionic Cold-Atom Quantum Wires.** Clément De Daniloff, Marin Tharrault, Cédric Enesa, Christophe Salomon, Frédéric Chevy, Thomas Reimann and Julian Struck. Physical Review Letters 127, 113602 - Published 9 September 2021.

Bibliography

[1] D. Rickles. *Brief history of string theory*. Springer, 2016 (see p. 11).

[2] T. Giamarchi. *Quantum phase transitions in quasi-one dimensional systems*. In: Understanding Quantum Phase Transitions, CRC Press/Taylor & Francis (2010), p. 291 (see p. 11).

[3] T. Giamarchi. *Quantum physics in one dimension*. Vol. 121. Clarendon press, 2003 (see p. 11).

[4] T. Giamarchi. *One-dimensional physics in the 21st century*. In: Comptes Rendus Physique 17.3-4 (2016), pp. 322–331 (see p. 11).

[5] S.-i. Tomonaga. *Remarks on Bloch's method of sound waves applied to many-fermion problems*. In: Progress of Theoretical Physics 5.4 (1950), pp. 544–569 (see p. 12).

[6] J. Luttinger. *An exactly soluble model of a many-fermion system*. In: Journal of mathematical physics 4.9 (1963), pp. 1154–1162 (see p. 12).

[7] F. Haldane. *'Luttinger liquid theory' of one-dimensional quantum fluids. I. Properties of the Luttinger model and their extension to the general 1D interacting spinless Fermi gas*. In: Journal of Physics C: Solid State Physics 14.19 (1981), p. 2585 (see p. 12).

[8] A. Schwartz, M. Dressel, G. Grüner, V. Vescoli, L. Degiorgi, and T. Giamarchi. *On-chain electrodynamics of metallic $(TMTSF)_2X$ salts: Observation of Tomonaga-Luttinger liquid response*. In: Physical Review B 58.3 (July 1998), pp. 1261–1271 (see p. 12).

[9] T. Giamarchi. *From luttinger to fermi liquids in organic conductors*. In: The Physics of Organic Superconductors and Conductors (2008), pp. 719–743 (see p. 12).

[10] M. Bockrath, D. H. Cobden, J. Lu, A. G. Rinzler, R. E. Smalley, L. Balents, and P. L. McEuen. *Luttinger-liquid behaviour in carbon nanotubes*. In: Nature 397.6720 (1999), pp. 598–601 (see p. 12).

[11] H. Ishii, H. Kataura, H. Shiozawa, H. Yoshioka, H. Otsubo, Y. Takayama, T. Miyahara, S. Suzuki, Y. Achiba, M. Nakatake, et al. *Direct observation of Tomonaga–Luttinger-liquid state in carbon nanotubes at low temperatures*. In: Nature 426.6966 (2003), pp. 540–544 (see p. 12).

[12] A. Yacoby, H. Stormer, N. S. Wingreen, L. Pfeiffer, K. Baldwin, and K. West. *Nonuniversal conductance quantization in quantum wires*. In: Physical review letters 77.22 (1996), p. 4612 (see p. 12).

[13] O. Auslaender, H. Steinberg, 1. A. Yacoby, 1. Y. Tserkovnyak, B. Halperin, K. Baldwin, L. Pfeiffer, and K. West. *Spin-charge separation and localization in one dimension*. In: Science 308.5718 (2005), pp. 88–92 (see p. 12).

[14] Y. Jompol, C. Ford, J. Griffiths, I. Farrer, G. Jones, D. Anderson, D. Ritchie, T. Silk, and A. Schofield. *Probing spin-charge separation in a Tomonaga-Luttinger liquid*. In: Science 325.5940 (2009), pp. 597–601 (see p. 12).

[15] B. Lake, D. A. Tennant, C. D. Frost, and S. E. Nagler. *Quantum criticality and universal scaling of a quantum antiferromagnet*. In: Nature materials 4.4 (2005), pp. 329–334 (see p. 12).

[16] P. Segovia, D. Purdie, M. Hengsberger, and Y. Baer. *Observation of spin and charge collective modes in one-dimensional metallic chains*. In: Nature 402.6761 (1999), pp. 504–507 (see p. 12).

[17] A. Chang. *Chiral Luttinger liquids at the fractional quantum Hall edge*. In: Reviews of Modern Physics 75.4 (2003), p. 1449 (see p. 12).

[18] W. N. Cottingham and D. A. Greenwood. *An introduction to the standard model of particle physics*. Cambridge university press, 2007 (see p. 12).

[19] L. Landau and E. Lifschitz. *Quantum mechanics*. Pergamon Press, 1979 (see p. 12).

[20] P. A. M. Dirac. *The principles of quantum mechanics*. 27. Oxford university press, 1981 (see p. 12).

[21] W. Pauli. *General principles of quantum mechanics*. Springer-Verlag, 1980 (see p. 12).

[22] M. Fierz. *Über die relativistische Theorie kräftefreier Teilchen mit beliebigem Spin*. In: Helvetica Physica Acta 12 (1939), pp. 3–37 (see p. 12).

[23] W. Pauli. *The connection between spin and statistics*. In: Physical Review 58.8 (1940), p. 716 (see p. 12).

[24] M. E. Peskin. *An Introduction to Quantum Field Theory*. Westview Press, 1995 (see p. 12).

[25] A. Einstein. *Quantentheorie des einatomigen idealen gases. zweite abhandlung*. In: Sitzungsberichte der Preußischen Akademie der Wissenschaften (1924), pp. 261–267 (see p. 12).

[26] S. N. Bose. *Plancks gesetz und lichtquantenhypothese*. In: (1924) (see p. 12).

[27] W. Pauli. *Über den Zusammenhang des Abschlusses der Elektronengruppen im Atom mit der Komplexstruktur der Spektren*. In: Zeitschrift für Physik 31.1 (Feb. 1925), pp. 765–783 (see p. 12).

[28] F. J. Dyson and A. Lenard. *Stability of Matter. I*. In: Journal of Mathematical Physics 8.3 (Mar. 1967), pp. 423–434 (see p. 13).

[29] A. Lenard and F. J. Dyson. *Stability of Matter. II*. In: Journal of Mathematical Physics 9.5 (May 1968), pp. 698–711 (see p. 13).

[30] C. Kittel, K. Charles, H. Kroemer, and K. Herbert. *Thermal Physics*. Macmillan, 1980 (see p. 13).

[31] L. Landau, E. Lifshitz, and L. E. Reichl. *Statistical physics, part 1*. In: Physics Today 34.1 (1981), p. 74 (see p. 13).

[32] L. N. Cooper. *Bound electron pairs in a degenerate Fermi gas*. In: Physical Review 104.4 (1956), p. 1189 (see p. 14).

[33] J. Bardeen, L. N. Cooper, and J. R. Schrieffer. *Theory of superconductivity*. In: Physical review 108.5 (1957), p. 1175 (see p. 14).

[34] L. D. Landau. *The theory of a Fermi liquid*. In: Soviet Physics Jetp-Ussr 3.6 (1957), pp. 920–925 (see p. 14).

[35] L. Landau. *Oscillations in a Fermi liquid*. In: Soviet Physics Jetp-Ussr 5.1 (1957), pp. 101–108 (see p. 14).

[36] L. Landau. *On the theory of the Fermi liquid*. In: Sov. Phys. JETP 8.1 (1959), p. 70 (see p. 14).

[37] G. Mahan. *Many-Particle Physics, Plenum, New York 1981.* (See p. 14).

[38] Y. Manin. *Computable and uncomputable*. In: Sovetskoye Radio, Moscow 128 (1980) (see p. 15).

[39] R. P. Feynman. *Simulating physics with computers*. In: *Feynman and computation*. CRC Press, 2018, pp. 133–153 (see p. 15).

[40] I. M. Georgescu, S. Ashhab, and F. Nori. *Quantum simulation*. In: Reviews of Modern Physics 86.1 (2014), p. 153 (see p. 15).

[41] R. Blatt and C. F. Roos. *Quantum simulations with trapped ions*. In: Nature Physics 8.4 (2012), pp. 277–284 (see p. 15).

[42] A. Aspuru-Guzik and P. Walther. *Photonic quantum simulators*. In: Nature physics 8.4 (2012), pp. 285–291 (see p. 15).

[43] C. N. Cohen-Tannoudji. *Nobel Lecture: Manipulating atoms with photons*. In: Reviews of Modern Physics 70.3 (1998), p. 707 (see p. 15).

[44] A. Ashkin. *Acceleration and trapping of particles by radiation pressure*. In: Physical review letters 24.4 (1970), p. 156 (see p. 15).

[45] T. W. Hänsch and A. L. Schawlow. *Cooling of gases by laser radiation*. In: Optics Communications 13.1 (1975), pp. 68–69 (see p. 15).

[46] W. D. Phillips and H. Metcalf. *Laser deceleration of an atomic beam*. In: Physical Review Letters 48.9 (1982), p. 596 (see p. 15).

[47] S. Chu, J. Bjorkholm, A. Ashkin, and A. Cable. *Experimental observation of optically trapped atoms*. In: Physical review letters 57.3 (1986), p. 314 (see p. 15).

[48] E. Raab, M. Prentiss, A. Cable, S. Chu, and D. E. Pritchard. *Trapping of neutral sodium atoms with radiation pressure*. In: Physical review letters 59.23 (1987), p. 2631 (see p. 15).

[49] A. L. Migdall, J. V. Prodan, W. D. Phillips, T. H. Bergeman, and H. J. Metcalf. *First observation of magnetically trapped neutral atoms*. In: Physical Review Letters 54.24 (1985), p. 2596 (see pp. 15, 21).

[50] M. H. Anderson, J. R. Ensher, M. R. Matthews, C. E. Wieman, and E. A. Cornell. *Observation of Bose-Einstein condensation in a dilute atomic vapor*. In: science 269.5221 (1995), pp. 198–201 (see p. 15).

[51] K. B. Davis, M.-O. Mewes, M. R. Andrews, N. J. van Druten, D. S. Durfee, D. Kurn, and W. Ketterle. *Bose-Einstein condensation in a gas of sodium atoms*. In: Physical review letters 75.22 (1995), p. 3969 (see p. 15).

[52] B. DeMarco and D. S. Jin. *Onset of Fermi degeneracy in a trapped atomic gas*. In: science 285.5434 (1999), pp. 1703–1706 (see p. 15).

[53] M. R. Matthews, B. P. Anderson, P. C. Haljan, D. S. Hall, C. E. Wieman, and E. A. Cornell. *Vortices in a Bose-Einstein Condensate*. In: Physical Review Letters 83.13 (Sept. 1999), pp. 2498–2501 (see p. 15).

[54] M. Andrews, C. Townsend, H.-J. Miesner, D. Durfee, D. Kurn, and W. Ketterle. *Observation of interference between two Bose condensates*. In: Science 275.5300 (1997), pp. 637–641 (see pp. 15, 50).

[55] I. Bloch, T. W. Hänsch, and T. Esslinger. *Measurement of the spatial coherence of a trapped Bose gas at the phase transition*. In: Nature 403.6766 (Jan. 2000), pp. 166–170 (see p. 15).

[56] W. Ketterle, D. S. Durfee, and D. M. Stamper-Kurn. *Making, probing and understanding Bose-Einstein condensates*. In: (Apr. 1999). arXiv: `9904034v2 [cond-mat]` (see pp. 15, 92).

[57] W. Ketterle and M. W. Zwierlein. *Making, probing and understanding ultracold Fermi gases*. In: La Rivista del Nuovo Cimento 31.5 (2008), pp. 247–422 (see pp. 15, 26, 28, 101).

[58] I. Bloch, J. Dalibard, and S. Nascimbène. *Quantum simulations with ultracold quantum gases*. In: Nature Physics 8.4 (Apr. 2012), pp. 267–276 (see pp. 15, 29).

[59] W. Hofstetter and T. Qin. *Quantum simulation of strongly correlated condensed matter systems*. In: Journal of Physics B: Atomic, Molecular and Optical Physics 51.8 (2018) (see p. 15).

[60] U. Fano. *Effects of configuration interaction on intensities and phase shifts*. In: Physical Review 124.6 (1961), p. 1866 (see p. 16).

[61] H. Feshbach. *Unified theory of nuclear reactions*. In: Annals of Physics 5.4 (1958), pp. 357–390 (see p. 16).

[62] W. Zwerger. *Strongly interacting Fermi gases*. In: Quantum Matter at Ultralow Temperatures 191 (2016), pp. 63–142 (see pp. 16, 25).

[63] C. Chin, R. Grimm, P. Julienne, and E. Tiesinga. *Feshbach resonances in ultracold gases*. In: Reviews of Modern Physics 82.2 (2010), p. 1225 (see pp. 16, 25).

[64] C. S. De Melo, M. Randeria, and J. R. Engelbrecht. *Crossover from BCS to Bose superconductivity: Transition temperature and time-dependent Ginzburg-Landau theory*. In: Physical review letters 71.19 (1993), p. 3202 (see p. 16).

[65] A. Perali, P. Pieri, L. Pisani, and G. Strinati. *BCS-BEC crossover at finite temperature for superfluid trapped Fermi atoms*. In: Physical review letters 92.22 (2004), p. 220404 (see p. 16).

[66] R. Grimm. *Ultracold Fermi gases in the BEC-BCS crossover: a review from the Innsbruck perspective*. In: arXiv preprint cond-mat/0703091 (2007) (see p. 16).

[67] W. Zwerger. *The BCS-BEC crossover and the unitary Fermi gas*. Vol. 836. Springer Science & Business Media, 2011 (see pp. 16, 25).

[68] T.-L. Ho. *Universal thermodynamics of degenerate quantum gases in the unitarity limit*. In: Physical review letters 92.9 (2004), p. 090402 (see p. 17).

[69] J. Stewart, J. Gaebler, T. Drake, and D. Jin. *Verification of universal relations in a strongly interacting Fermi gas*. In: Physical Review Letters 104.23 (2010), p. 235301 (see p. 17).

[70] I. Bloch, J. Dalibard, and W. Zwerger. *Many-body physics with ultracold gases*. In: Reviews of Modern Physics 80.3 (July 2008), pp. 885–964. arXiv: 0704.3011 (see p. 17).

[71] L. Pitaevskii and S. Stringari. *Bose-Einstein Condensation and Superfluidity*. Oxford University Press, Jan. 2016 (see p. 17).

[72] S. Krinner, T. Esslinger, and J.-P. Brantut. *Two-terminal transport measurements with cold atoms*. In: Journal of Physics: Condensed Matter 29.34 (Aug. 2017), p. 343003 (see p. 17).

[73] M. Olshanii. *Atomic scattering in the presence of an external confinement and a gas of impenetrable bosons*. In: Physical review letters 81.5 (1998), p. 938 (see pp. 17, 123, 124, 126, 149).

[74] T. Bergeman, M. Moore, and M. Olshanii. *Atom-atom scattering under cylindrical harmonic confinement: Numerical and analytic studies of the confinement induced resonance*. In: Physical review letters 91.16 (2003), p. 163201 (see pp. 17, 123, 126).

[75] H. Moritz, T. Stöferle, K. Günter, M. Köhl, and T. Esslinger. *Confinement induced molecules in a 1D Fermi gas*. In: Physical review letters 94.21 (2005), p. 210401 (see pp. 17, 30, 126).

[76] E. Haller, M. J. Mark, R. Hart, J. G. Danzl, L. Reichsöllner, V. Melezhik, P. Schmelcher, and H.-C. Nägerl. *Confinement-Induced Resonances in Low-Dimensional Quantum Systems*. In: Physical Review Letters 104.15 (Apr. 2010), p. 153203. arXiv: 1002.3795 (see pp. 17, 126).

[77] M. Greiner. *Ultracold quantum gases in three-dimensional optical lattice potentials*. PhD thesis. 2003, pp. 1–134 (see pp. 17, 32).

[78] M. Greiner, O. Mandel, T. Esslinger, T. W. Hänsch, and I. Bloch. *Quantum phase transition from a superfluid to a Mott insulator in a gas of ultracold atoms.* In: Nature 415.6867 (Jan. 2002), pp. 39–44 (see pp. 17, 29, 30).

[79] Z. Hadzibabic, P. Krüger, M. Cheneau, B. Battelier, and J. Dalibard. *Berezinskii–Kosterlitz–Thouless crossover in a trapped atomic gas*. In: Nature 441.7097 (2006), pp. 1118–1121 (see p. 17).

[80] A. Recati, P. O. Fedichev, W. Zwerger, and P. Zoller. *Fermi one-dimensional quantum gas: Luttinger liquid approach and spin charge separation*. In: Journal of Optics B: Quantum and Semiclassical Optics 5.2 (Apr. 2003), S55–S64 (see p. 17).

[81] C. Kollath, U. Schollwöck, and W. Zwerger. *Spin-charge separation in cold fermi gases: A real time analysis*. In: Physical Review Letters 95.17 (2005), pp. 1–4 (see p. 17).

[82] B. Yang, Y.-y. Chen, Y.-g. Zheng, H. Sun, H.-n. Dai, X.-W. Guan, Z.-S. Yuan, and J.-W. Pan. *Quantum criticality and the Tomonaga-Luttinger liquid in one-dimensional Bose gases*. In: Physical Review Letters 119.16 (Oct. 2017), p. 165701 (see p. 17).

[83] T. L. Yang, P. Grišins, Y. T. Chang, Z. H. Zhao, C. Y. Shih, T. Giamarchi, and R. G. Hulet. *Measurement of the Dynamical Structure Factor of a 1D Interacting Fermi Gas*. In: Physical Review Letters 121.10 (Sept. 2018), p. 103001. arXiv: 1803.06331 (see pp. 17, 30).

[84] Y.-A. Liao, A. S. C. Rittner, T. Paprotta, W. Li, G. B. Partridge, R. G. Hulet, S. K. Baur, and E. J. Mueller. *Spin-imbalance in a one-dimensional Fermi gas*. In: Nature 467.7315 (Sept. 2010), pp. 567–569 (see pp. 17, 30).

[85] G. Pagano, M. Mancini, G. Cappellini, P. Lombardi, F. Schäfer, H. Hu, X.-J. Liu, J. Catani, C. Sias, M. Inguscio, and L. Fallani. *A one-dimensional liquid of fermions with tunable spin*. In: Nature Physics 10.3 (2014), pp. 198–201. arXiv: 1408.0928 (see pp. 17, 30).

[86] M. C. Revelle, J. A. Fry, B. A. Olsen, and R. G. Hulet. *1D to 3D Crossover of a Spin-Imbalanced Fermi Gas*. In: Physical Review Letters (2016). arXiv: 1605.06986 (see pp. 17, 30).

[87] Y.-T. Chang, R. Senaratne, D. Cavazos-Cavazos, and R. G. Hulet. *Collisional loss of one-dimensional fermions near a p-wave Feshbach resonance*. In: Physical Review Letters 125.26 (2020), p. 263402 (see pp. 17, 30, 132, 155).

[88] T. Reimann. *Resonant spin dynamics and 3D-1D dimensional crossovers in ultracold Fermi gases*. PhD thesis. 2018 (see pp. 19–21, 23, 33, 34, 36, 46, 50, 56, 114).

[89] C. Enesa. *Experimental realization of a strongly interacting 1D fermi gas*. PhD thesis. 2019 (see pp. 19, 23, 33, 34, 36, 50, 56, 115).

[90] A. Ridinger. *Towards quantum degenerate Fermi mixtures : Photoassociation of weakly bound 6Li40K molecules*. PhD thesis. 2011 (see p. 19).

[91] T. Salez. *Towards quantum degenerate atomic Fermi mixtures*. PhD thesis. 2011 (see p. 19).

[92] D. R. Fernandes. *Trapping and cooling of fermionic alkali atoms to quantum degeneracy. Sub-Doppler cooling of Potassium-40 and Lithium-6 in gray molasses.* PhD thesis. 2014, p. 236 (see p. 19).

[93] F. Sievers. *Ultracold Fermi mixtures and simultaneous sub-Doppler laser cooling of fermionic 6Li and 40K*. PhD thesis. 2014 (see p. 19).

[94] N. Kretzschmar. *Experiments with Ultracold Fermi Gases : Quantum Degeneracy of Potassium-40 and All-solid-state Laser Sources for Lithium*. PhD thesis. 2015 (see p. 19).

[95] D. Suchet. *Simulating the dynamics of harmonically trapped Weyl particles with cold atoms*. PhD thesis. 2016 (see p. 19).

[96] M. Rabinovic. *Quasithermalization of fermions in a quadrupole potential and evaporative cooling of 40K to quantum degeneracy*. PhD thesis. 2017 (see p. 19).

[97] M. Berglund and M. E. Wieser. *Isotopic compositions of the elements 2009 (IUPAC Technical Report)**. In: Pure Appl. Chem 83.2 (2011), pp. 397–410 (see p. 19).

[98] B. DeMarco, H. Rohner, and D. S. Jin. *An enriched 40K source for fermionic atom studies*. In: Review of Scientific Instruments 70.4 (1999), pp. 1967–1969 (see p. 19).

[99] E. L. Raab, M. Prentiss, A. Cable, S. Chu, and D. E. Pritchard. *Trapping of Neutral Sodium Atoms with Radiation Pressure*. In: Physical Review Letters 59.23 (Dec. 1987), pp. 2631–2634 (see p. 20).

[100] C. N. Cohen-Tannoudji and D. Guery-Odelin. *Advances In Atomic Physics: An Overview*. World Scientific Publishing, 2011, p. 796 (see pp. 20, 22).

[101] J. Dalibard. *Une brève histoire des atomes froids*. Collège de France, Paris, 2014 (see p. 20).

[102] J. Gordon and A. Ashkin. *Motion of atoms in a radiation trap*. In: Physical Review A 21.5 (1980), p. 1606 (see p. 21).

[103] J. Dalibard and C. Cohen-Tannoudji. *Laser cooling below the Doppler limit by polarization gradients: simple theoretical models*. In: JOSA B 6.11 (1989), pp. 2023–2045 (see p. 21).

[104] D. Rio Fernandes, F. Sievers, N. Kretzschmar, S. Wu, C. Salomon, and F. Chevy. *Sub-Doppler laser cooling of fermionic 40 K atoms in three-dimensional gray optical molasses*. In: EPL (Europhysics Letters) 100.6 (Dec. 2012), p. 63001. arXiv: 1210.1310 (see p. 21).

[105] F. Sievers, N. Kretzschmar, D. R. Fernandes, D. Suchet, M. Rabinovic, S. Wu, C. V. Parker, L. Khaykovich, C. Salomon, and F. Chevy. *Simultaneous sub-Doppler laser cooling of fermionic Li6 and K 40*. In: Physical Review A 91.2 (Feb. 2015), p. 023426 (see p. 21).

[106] M. S. Shahriar, P. R. Hemmer, M. G. Prentiss, P. Marte, J. Mervis, D. P. Katz, N. P. Bigelow, and T. Cai. *Continuous polarization-gradient precooling-assisted velocity-selective coherent population trapping*. In: Physical Review A 48.6 (1993) (see p. 21).

[107] M. Weidemüller, T. Esslinger, M. A. Ol'shanii, A. Hemmerich, and T. W. Hänsch. *A novel scheme for efficient cooling below the photon recoil limit*. In: Epl 27.2 (1994), pp. 109–114 (see p. 21).

[108] C. Valentin, M. C. Gagné, J. Yu, and P. Pillet. *One-dimension sub-doppler molasses in the presence of static magnetic field*. In: Epl 17.2 (1992), pp. 133–138 (see p. 21).

[109] D. Boiron, C. Triché, D. R. Meacher, P. Verkerk, and G. Grynberg. *Three-dimensional cooling of cesium atoms in four-beam gray optical molasses*. In: Physical Review A 52.5 (1995), pp. 3425–3428 (see p. 21).

[110] S. Falke, E. Tiemann, C. Lisdat, H. Schnatz, and G. Grosche. *Transition frequencies of the D lines of K 39, K 40, and K 41 measured with a femtosecond laser frequency comb*. In: Physical Review A 74.3 (2006), p. 032503 (see p. 21).

[111] D. Nath, R. K. Easwaran, G. Rajalakshmi, and C. S. Unnikrishnan. *Quantum-interference-enhanced deep sub-Doppler cooling of 39K atoms in gray molasses*. In: Physical Review A - Atomic, Molecular, and Optical Physics 88.5 (2013), pp. 1–7. arXiv: 1305.5480 (see p. 21).

[112] G. Salomon, L. Fouché, P. Wang, A. Aspect, P. Bouyer, and T. Bourdel. *Gray-molasses cooling of 39 K to a high phase-space density*. In: EPL (Europhysics Letters) 104.6 (Dec. 2013), p. 63002 (see p. 21).

[113] A. T. Grier, I. Ferrier-Barbut, B. S. Rem, M. Delehaye, L. Khaykovich, F. Chevy, and C. Salomon. *Λ-enhanced sub-Doppler cooling of lithium atoms in D1 gray molasses*. In: Physical Review A 87.6 (June 2013), p. 063411 (see p. 21).

[114] A. Burchianti, G. Valtolina, J. A. Seman, E. Pace, M. De Pas, M. Inguscio, M. Zaccanti, and G. Roati. *Efficient all-optical production of large Li6 quantum gases using D1 gray-molasses cooling*. In: Physical Review A 90.4 (Oct. 2014), p. 043408. arXiv: 1406.4788 (see p. 21).

[115] Q. Bouton, R. Chang, A. L. Hoendervanger, F. Nogrette, A. Aspect, C. I. Westbrook, and D. Clément. *Fast production of Bose-Einstein condensates of metastable helium*. In: Physical Review A 91.6 (June 2015), p. 061402 (see p. 21).

[116] G. Colzi, G. Durastante, E. Fava, S. Serafini, G. Lamporesi, and G. Ferrari. *Sub-Doppler cooling of sodium atoms in gray molasses*. In: Physical Review A 93.2 (Feb. 2016), p. 023421 (see p. 21).

[117] H. J. Lewandowski. *Coherences and correlations in an ultracold Bose gas*. University of Colorado at Boulder, 2002 (see p. 21).

[118] S. Händel, A. Marchant, T. Wiles, S. Hopkins, and S. Cornish. *Magnetic transport apparatus for the production of ultracold atomic gases in the vicinity of a dielectric surface*. In: Review of Scientific Instruments 83.1 (2012), p. 013105 (see p. 21).

[119] T. L. Gustavson, A. P. Chikkatur, A. E. Leanhardt, A. Görlitz, S. Gupta, D. E. Pritchard, and W. Ketterle. *Transport of Bose-Einstein Condensates with Optical Tweezers*. In: Physical Review Letters (2002). arXiv: 0108496 [cond-mat] (see p. 21).

[120] J. Léonard, M. Lee, A. Morales, T. M. Karg, T. Esslinger, and T. Donner. *Optical transport and manipulation of an ultracold atomic cloud using focus-tunable lenses*. In: New Journal of Physics 16.9 (2014), p. 093028 (see p. 21).

[121] Y. J. Lin, A. R. Perry, R. L. Compton, I. B. Spielman, and J. V. Porto. *Rapid production of R 87 b Bose-Einstein condensates in a combined magnetic and optical potential*. In: Physical Review A - Atomic, Molecular, and Optical Physics 79.6 (2009), pp. 1–8 (see p. 21).

[122] E. Majorana. *Atomi orientati in campo magnetico variabile*. In: Il Nuovo Cimento (1924-1942) 9.2 (1932), pp. 43–50 (see pp. 22, 25).

[123] W. Petrich, M. H. Anderson, J. R. Ensher, and E. A. Cornell. *Stable, tightly confining magnetic trap for evaporative cooling of neutral atoms*. In: Physical Review Letters 74.17 (1995), p. 3352 (see p. 22).

[124] R. Chicireanu, Q. Beaufils, A. Pouderous, B. Laburthe-Tolra, E. Maréchal, J. Porto, L. Vernac, J. Keller, and O. Gorceix. *Accumulation and thermalization of cold atoms in a finite-depth magnetic trap*. In: Physical Review A 76.2 (2007), p. 023406 (see p. 22).

[125] R. Dubessy, K. Merloti, L. Longchambon, P.-E. Pottie, T. Liennard, A. Perrin, V. Lorent, and H. Perrin. *Rubidium-87 Bose-Einstein condensate in an optically plugged quadrupole trap*. In: Physical Review A 85.1 (2012), p. 013643 (see p. 22).

[126] M.-S. Heo, J.-y. Choi, and Y.-i. Shin. *Fast production of large Na 23 Bose-Einstein condensates in an optically plugged magnetic quadrupole trap*. In: Physical Review A 83.1 (2011), p. 013622 (see p. 22).

[127] R. Grimm, M. Weidemüller, and Y. B. Ovchinnikov. *Optical Dipole Traps for Neutral Atoms*. In: 2000, pp. 95–170 (see p. 22).

[128] S. Chu, J. E. Bjorkholm, A. Ashkin, and A. Cable. *Experimental Observation of Optically Trapped Atoms*. In: Physical Review Letters 57.3 (July 1986), pp. 314–317 (see p. 22).

[129] T. G. Tiecke. *Properties of Potassium*. 2011 (see p. 22).

[130] E. Arimondo, M. Inguscio, and P. Violino. *Experimental determinations of the hyperfine structure in the alkali atoms*. In: Reviews of Modern Physics 49.1 (1977), p. 31 (see pp. 22, 23, 109).

[131] C. Cohen-Tannoudji. *Atomes ultra-froids-piégeage non-dissipatif et refroidissement évaporatif*. In: Cours au College de France 1997 (1996) (see p. 23).

[132] W. Ketterle and N. Van Druten. *Evaporative cooling of trapped atoms*. In: Advances in atomic, molecular, and optical physics 37 (1996), pp. 181–236 (see p. 23).

[133] M. Weissbluth. *Atoms and molecules*. Elsevier, 2012 (see pp. 23, 109).

[134] L. Landau. *On the theory of transfer of energy at collisions II*. In: Phys. Z. Sowjetunion 2.46 (1932), p. 118 (see p. 25).

[135] C. Zener. *Non-Adiabatic Crossing of Energy Levels*. In: Proceedings of the Royal Society A: Mathematical, Physical and Engineering Sciences 137.833 (Sept. 1932), pp. 696–702 (see p. 25).

[136] E. K. G. Stückelberg. *Theorie der unelastischen Stösse zwischen Atomen*. Birkhäuser, 1933 (see p. 25).

[137] C. A. Regal, C. Ticknor, J. L. Bohn, and D. S. Jin. *Creation of ultracold molecules from a Fermi gas of atoms*. In: Nature 424.6944 (July 2003), pp. 47–50 (see pp. 25, 114).

[138] C. Regal, M. Greiner, and D. S. Jin. *Observation of resonance condensation of fermionic atom pairs*. In: Physical review letters 92.4 (2004), p. 040403 (see p. 25).

[139] S. Falke, H. Knöckel, J. Friebe, M. Riedmann, E. Tiemann, and C. Lisdat. *Potassium ground-state scattering parameters and Born-Oppenheimer potentials from molecular spectroscopy*. In: Physical Review A 78.1 (July 2008), p. 012503. arXiv: 0804.2949 (see pp. 25, 149).

[140] J. P. Gaebler. *Photoemission spectroscopy of a strongly interacting Fermi gas*. University of Colorado at Boulder, 2010 (see p. 25).

[141] J. Gaebler, J. Stewart, T. Drake, D. Jin, A. Perali, P. Pieri, and G. Strinati. *Observation of pseudogap behaviour in a strongly interacting Fermi gas*. In: Nature Physics 6.8 (2010), pp. 569–573 (see p. 25).

[142] C. Shkedrov, Y. Florshaim, G. Ness, A. Gandman, and Y. Sagi. *High-Sensitivity rf Spectroscopy of a Strongly Interacting Fermi Gas*. In: Physical Review Letters 121.9 (2018), pp. 1–5. arXiv: 1803.01770 (see p. 25).

[143] T. Hartke, B. Oreg, N. Jia, and M. Zwierlein. *Quantum Register of Fermion Pairs*. In: (2021), pp. 1–10. arXiv: 2103.13992 (see p. 25).

[144] C. A. Regal, M. Greiner, and D. S. Jin. *Lifetime of Molecule-Atom Mixtures near a Feshbach Resonance in K-40*. In: Physical Review Letters 92.8 (Feb. 2004), p. 083201 (see pp. 25, 37, 114, 132).

[145] S. Giorgini, L. P. Pitaevskii, and S. Stringari. *Theory of ultracold Fermi gases*. In: Reviews of Modern Physics 80.4 (2007), p. 63. arXiv: 0706.3360 (see pp. 26, 92).

[146] A. Perali, P. Pieri, L. Pisani, and G. C. Strinati. *BCS-BEC Crossover at Finite Temperature for Superfluid Trapped Fermi Atoms*. In: Physical Review Letters 92.22 (June 2004), p. 220404 (see p. 28).

[147] M. Lewenstein, A. Sanpera, and V. Ahufinger. *Ultracold Atoms in Optical Lattices: Simulating quantum many-body systems*. Oxford University Press, 2012 (see p. 29).

[148] J. Dalibard. *Des cages de lumière pour les atomes: la physique des pièges et des réseaux optiques*. In: Cours du Collège de France (2013) (see pp. 29, 34).

[149] W. Zwerger. *Mott-Hubbard transition of cold atoms in optical lattices*. In: Journal of Optics B: Quantum and Semiclassical Optics 5.2 (2003), S9 (see p. 29).

[150] D. Jaksch and P. Zoller. *The cold atom Hubbard toolbox*. In: Annals of physics 315.1 (2005), pp. 52–79 (see p. 30).

[151] J. Struck, C. Olschlager, R. Le Targat, P. Soltan-Panahi, A. Eckardt, M. Lewenstein, P. Windpassinger, and K. Sengstock. *Quantum Simulation of Frustrated Classical Magnetism in Triangular Optical Lattices*. In: Science 333.6045 (Aug. 2011), pp. 996–999 (see p. 30).

[152] G. Grynberg, B. Lounis, P. Verkerk, J.-Y. Courtois, and C. Salomon. *Quantized motion of cold cesium atoms in two-and three-dimensional optical potentials*. In: Physical review letters 70.15 (1993), p. 2249 (see p. 30).

[153] C. Wu, D. Bergman, L. Balents, and S. D. Sarma. *Flat bands and Wigner crystallization in the honeycomb optical lattice*. In: Physical review letters 99.7 (2007), p. 070401 (see p. 30).

[154] L. Santos, M. Baranov, J. I. Cirac, H.-U. Everts, H. Fehrmann, and M. Lewenstein. *Atomic quantum gases in Kagomé lattices*. In: Physical review letters 93.3 (2004), p. 030601 (see p. 30).

[155] S. Fölling, S. Trotzky, P. Cheinet, M. Feld, R. Saers, A. Widera, T. Müller, and I. Bloch. *Direct observation of second-order atom tunnelling*. In: Nature 448.7157 (2007), pp. 1029–1032 (see p. 30).

[156] R. Landig, L. Hruby, N. Dogra, M. Landini, R. Mottl, T. Donner, and T. Esslinger. *Quantum phases from competing short-and long-range interactions in an optical lattice*. In: Nature 532.7600 (2016), pp. 476–479 (see p. 30).

[157] J. Léonard, A. Morales, P. Zupancic, T. Esslinger, and T. Donner. *Supersolid formation in a quantum gas breaking a continuous translational symmetry*. In: Nature 543.7643 (2017), pp. 87–90 (see p. 30).

[158] S. Kuhr. *Quantum-gas microscopes: a new tool for cold-atom quantum simulators*. In: National Science Review 3.2 (2016), pp. 170–172 (see p. 30).

[159] W. S. Bakr, J. I. Gillen, A. Peng, S. Fölling, and M. Greiner. *A quantum gas microscope for detecting single atoms in a Hubbard-regime optical lattice*. In: Nature 462.7269 (2009), pp. 74–77 (see p. 30).

[160] J. F. Sherson, C. Weitenberg, M. Endres, M. Cheneau, I. Bloch, and S. Kuhr. *Single-atom-resolved fluorescence imaging of an atomic Mott insulator*. In: Nature 467.7311 (Sept. 2010), pp. 68–72 (see p. 30).

[161] A. Eckardt. *Colloquium: Atomic quantum gases in periodically driven optical lattices*. In: Reviews of Modern Physics 89.1 (2017), p. 011004 (see p. 30).

[162] J. Dalibard, F. Gerbier, G. Juzeliūnas, and P. Öhberg. *Colloquium: Artificial gauge potentials for neutral atoms*. In: Reviews of Modern Physics 83.4 (Oct. 2011), pp. 1523–1543 (see p. 30).

[163] M. Aidelsburger, S. Nascimbene, and N. Goldman. *Artificial gauge fields in materials and engineered systems*. In: Comptes Rendus Physique 19.6 (Sept. 2018), pp. 394–432 (see p. 30).

[164] K. Martiyanov, V. Makhalov, and A. Turlapov. *Observation of a two-dimensional Fermi gas of atoms*. In: Physical review letters 105.3 (2010), p. 030404 (see pp. 30, 32).

[165] R. A. Williams. *Vortex nucleation in a rotating optical lattice of ultracold atoms*. PhD thesis. 2009, pp. 1–194 (see pp. 30, 33).

[166] T. Gericke, P. Würtz, D. Reitz, T. Langen, and H. Ott. *High-resolution scanning electron microscopy of an ultracold quantum gas*. In: Nature Physics 4.12 (2008), pp. 949–953 (see p. 32).

[167] N. D. M. Neil W. Ashcroft. *Solid State Physics - Ashcroft, Neil W, Mermin, David N*. Hartcourt College Publishers, 1976, p. 826 (see p. 33).

[168] M. C. Revelle, J. A. Fry, B. A. Olsen, and R. G. Hulet. *1D to 3D crossover of a spin-imbalanced Fermi gas*. In: Physical review letters 117.23 (2016), p. 235301 (see p. 34).

[169] M. C. Revelle. *Quasi-one-dimensional ultracold fermi gases*. PhD thesis. 2016 (see p. 34).

[170] A. Vogler, R. Labouvie, G. Barontini, S. Eggert, V. Guarrera, and H. Ott. *Dimensional phase transition from an array of 1D Luttinger liquids to a 3D Bose-Einstein condensate*. In: Physical review letters 113.21 (2014), p. 215301 (see p. 34).

[171] G. B. Airy. *On the diffraction of an object-glass with circular aperture*. In: Transactions of the Cambridge Philosophical Society 5 (1835), p. 283 (see p. 40).

[172] L. Rayleigh. *Investigations in optics, with special reference to the spectroscope*. In: The London, Edinburgh, and Dublin Philosophical Magazine and Journal of Science 8.49 (1879), pp. 261–274 (see p. 40).

[173] E. Magnan, J. Maslek, C. Bracamontes, A. Restelli, T. Boulier, and J. V. Porto. *A low-steering piezo-driven mirror*. In: Review of Scientific Instruments 89.7 (2018), p. 073110 (see pp. 42, 43).

[174] N. L. Smith, W. H. Heathcote, G. Hechenblaikner, E. Nugent, and C. J. Foot. *Quasi-2D confinement of a BEC in a combined optical and magnetic potential*. In: Journal of Physics B: Atomic, Molecular and Optical Physics 38.3 (Feb. 2005), pp. 223–235. arXiv: 0410101 [cond-mat] (see p. 46).

[175] S. P. Rath, T. Yefsah, K. J. Günter, M. Cheneau, R. Desbuquois, M. Holzmann, W. Krauth, and J. Dalibard. *Equilibrium state of a trapped two-dimensional Bose gas*. In: Phys. Rev. A 82.1 (July 2010), p. 013609. arXiv: 1003.4545 (see p. 46).

[176] M. J. Ku, W. Ji, B. Mukherjee, E. Guardado-Sanchez, L. W. Cheuk, T. Yefsah, and M. W. Zwierlein. *Motion of a solitonic vortex in the BEC-BCS crossover*. In: Physical review letters 113.6 (2014), p. 065301 (see p. 50).

[177] M. R. Andrews, D. M. Kurn, H.-J. Miesner, D. S. Durfee, C. G. Townsend, S. Inouye, and W. Ketterle. *Propagation of sound in a Bose-Einstein condensate*. In: Physical review letters 79.4 (1997), p. 553 (see pp. 55, 107).

[178] B. E. A. Saleh and M. C. Teich. *Fundamentals of Photonics*. Wiley Series in Pure and Applied Optics. New York, USA: John Wiley & Sons, Inc. Aug. 1991 (see pp. 56, 58).

[179] C. J. Foot et al. *Atomic physics*. Vol. 7. Oxford University Press, 2005 (see p. 56).

[180] G. Reinaudi, T. Lahaye, Z. Wang, and D. Guéry-Odelin. *Strong saturation absorption imaging of dense clouds of ultracold atoms*. In: Optics letters 32.21 (2007), pp. 3143–3145 (see p. 56).

[181] K. Hueck, N. Luick, L. Sobirey, J. Siegl, T. Lompe, H. Moritz, L. W. Clark, and C. Chin. *Calibrating high intensity absorption imaging of ultracold atoms*. In: Optics express 25.8 (2017), pp. 8670–8679 (see pp. 56, 57).

[182] K. Bhardwaj, S. Ram, S. Singh, V. Tiwari, and S. Mishra. *Absorption imaging of trapped atoms in presence of AC-Stark shift*. In: Physica Scripta 96.1 (2020), p. 015405 (see p. 57).

[183] J. Ruostekoski and J. Javanainen. *Quantum field theory of cooperative atom response: Low light intensity*. In: Physical Review A - Atomic, Molecular, and Optical Physics 55.1 (1997), pp. 513–526 (see p. 57).

[184] J. Pellegrino, R. Bourgain, S. Jennewein, Y. R. Sortais, A. Browaeys, S. Jenkins, and J. Ruostekoski. *Observation of suppression of light scattering induced by dipole-dipole interactions in a cold-atom ensemble*. In: Physical review letters 113.13 (2014), p. 133602 (see p. 57).

[185] O. Morice. *Atomes refroidis par laser: du refroidissement sub-recul à la recherche d'effets quantiques collectifs*. PhD thesis. Université Pierre et Marie Curie-Paris VI, 1995 (see p. 57).

[186] A. Fuhrmanek, R. Bourgain, Y. R. Sortais, and A. Browaeys. *Light-assisted collisions between a few cold atoms in a microscopic dipole trap*. In: Physical Review A 85.6 (2012), p. 062708 (see p. 58).

[187] A. Litvinov, P. Bataille, E. Maréchal, P. Pedri, O. Gorceix, M. Robert-de-Saint-Vincent, and B. Laburthe-Tolra. *Measuring densities of cold atomic clouds smaller than the resolution limit*. In: arXiv preprint arXiv:2105.10296 (2021) (see p. 58).

[188] F. Pampaloni and J. Enderlein. *Gaussian, Hermite-Gaussian, and Laguerre-Gaussian beams: A primer*. In: (Oct. 2004). arXiv: `0410021 [physics]` (see p. 58).

[189] T. A. Savard, K. M. O'Hara, and J. E. Thomas. *Laser-noise-induced heating in far-off resonance optical traps*. In: Physical Review A 56.2 (Aug. 1997), R1095–R1098 (see pp. 63, 64, 104).

[190] M. E. Gehm, K. M. O'Hara, T. A. Savard, and J. E. Thomas. *Dynamics of noise-induced heating in atom traps*. In: Physical Review A 58.5 (Nov. 1998), pp. 3914–3921 (see pp. 63, 104).

[191] R. Jáuregui. *Nonperturbative and perturbative treatments of parametric heating in atom traps*. In: Physical Review A - Atomic, Molecular, and Optical Physics 64.5 (2001), p. 8 (see pp. 63, 64, 104).

[192] W. Kohn. *Cyclotron resonance and de Haas-van Alphen oscillations of an interacting electron gas*. In: Physical Review 123.4 (1961), p. 1242 (see pp. 65, 67).

[193] J. F. Dobson. *Harmonic-potential theorem: Implications for approximate many-body theories*. In: Physical review letters 73.16 (1994), p. 2244 (see pp. 65, 67, 150).

[194] E. R. Anderson and J. E. Drut. *Pressure, Compressibility, and Contact of the Two-Dimensional Attractive Fermi Gas*. In: Physical Review Letters 115.11 (2015), pp. 1–5 (see p. 74).

[195] K. Fenech, P. Dyke, T. Peppler, M. G. Lingham, S. Hoinka, H. Hu, and C. J. Vale. *Thermodynamics of an Attractive 2D Fermi Gas*. In: Physical Review Letters 116.4 (2016), pp. 1–5. arXiv: 1508.04502 (see pp. 74, 92).

[196] M. Abramowitz, I. A. Stegun, and R. H. Romer. *Handbook of Mathematical Functions with Formulas, Graphs, and Mathematical Tables*. Vol. 56. 10. Oct. 1988, pp. 958–958 (see pp. 79, 85).

[197] K. Iguchi. *Quantum Statistical Mechanics of an Ideal Gas with Fractional Exclusion Statistics in Arbitrary Dimensions*. In: Physical Review Letters 78.17 (Apr. 1997), pp. 3233–3236 (see p. 82).

[198] H. P. Rojas. *On Bose-Einstein condensation in any dimension*. In: Physics Letters A 234.1 (1997), pp. 13–19 (see p. 82).

[199] W. Pauli. *Pauli lectures on physics. V. Wave mechanics*. 1973 (see pp. 82, 90).

[200] B. D. C. Cohen-Tannoudji and F. Laloë. *Quantum Mechanics, Volume 1*. 1973 (see p. 85).

[201] R. P. Feynman. *Forces in molecules*. In: Physical Review 56.4 (1939), pp. 340–343 (see p. 90).

[202] P. Güttinger. *Das Verhalten von Atomen im magnetischen Drehfeld*. In: Zeitschrift für Physik 73.3-4 (Mar. 1932), pp. 169–184 (see p. 90).

[203] H. Hellman. *Einführung in die Quantenchemie*. In: Franz Deuticke, Leipzig 285 (1937) (see p. 90).

[204] V. Romero-Rochín. *Equation of state of an interacting bose gas confined by a harmonic trap: The role of the "harmonic" pressure*. In: Physical Review Letters 94.13 (2005), pp. 8–11 (see p. 90).

[205] M. Schmitt, M. Wenzel, F. Böttcher, I. Ferrier-Barbut, and T. Pfau. *Self-bound droplets of a dilute magnetic quantum liquid*. In: Nature 539.7628 (Nov. 2016), pp. 259–262 (see p. 91).

[206] C. De Daniloff, M. Tharrault, C. Enesa, C. Salomon, F. Chevy, T. Reimann, and J. Struck. *In Situ Thermometry of Fermionic Cold-Atom Quantum Wires*. In: Phys. Rev. Lett. 127 (11 Sept. 2021), p. 113602 (see p. 92).

[207] L. Chomaz, L. Corman, T. Bienaimé, R. Desbuquois, C. Weitenberg, S. Nascimbene, J. Beugnon, and J. Dalibard. *Emergence of coherence via transverse condensation in a uniform quasi-two-dimensional Bose gas*. In: Nature communications 6.1 (2015), pp. 1–10 (see p. 92).

[208] K. Hueck, N. Luick, L. Sobirey, J. Siegl, T. Lompe, and H. Moritz. *Two-Dimensional Homogeneous Fermi Gases*. In: Physical Review Letters 120.6 (Feb. 2018), p. 060402. arXiv: 1704.06315 (see p. 92).

[209] A. L. Gaunt, T. F. Schmidutz, I. Gotlibovych, R. P. Smith, and Z. Hadzibabic. *Bose-Einstein condensation of atoms in a uniform potential*. In: Physical review letters 110.20 (2013), p. 200406 (see p. 92).

[210] B. Mukherjee, Z. Yan, P. B. Patel, Z. Hadzibabic, T. Yefsah, J. Struck, and M. W. Zwierlein. *Homogeneous Atomic Fermi Gases*. In: Physical Review Letters (2017). arXiv: 1610.10100 (see p. 92).

[211] S. Nascimbène, N. Navon, K. J. Jiang, F. Chevy, and C. Salomon. *Exploring the thermodynamics of a universal Fermi gas*. In: Nature 463.7284 (Feb. 2010), pp. 1057–1060 (see p. 92).

[212] N. Navon, S. Nascimbene, F. Chevy, and C. Salomon. *The Equation of State of a Low-Temperature Fermi Gas with Tunable Interactions*. In: Science 328.5979 (May 2010), pp. 729–732. arXiv: 1004.1465 (see p. 92).

[213] M. J. H. Ku, A. T. Sommer, L. W. Cheuk, and M. W. Zwierlein. *Revealing the Superfluid Lambda Transition in the Universal Thermodynamics of a Unitary Fermi Gas*. In: Science 335.6068 (Feb. 2012), pp. 563–567 (see p. 92).

[214] P. Vignolo and A. Minguzzi. *Shell structure in the density profiles for noninteracting fermions in anisotropic harmonic confinement*. In: Physical Review A - Atomic, Molecular, and Optical Physics 67.5 (2003), p. 5 (see p. 92).

[215] A. Bulgac, J. E. Drut, and P. Magierski. *Thermodynamics of a trapped unitary fermi gas*. In: Physical review letters 99.12 (2007), p. 120401 (see p. 92).

[216] F. Salces-Carcoba, C. J. Billington, A. Putra, Y. Yue, S. Sugawa, and I. B. Spielman. *Equations of state from individual one-dimensional Bose gases*. In: New Journal of Physics 20.11 (2018). arXiv: 1808.06933 (see p. 96).

[217] T. Kinoshita, T. Wenger, and D. S. Weiss. *A quantum Newton's cradle*. In: Nature 440.7086 (Apr. 2006), pp. 900–903 (see pp. 104, 154).

[218] I. E. Mazets, T. Schumm, and J. Schmiedmayer. *Breakdown of Integrability in a Quasi-1D Ultracold Bosonic Gas*. In: Phys. Rev. Lett. 100.21 (May 2008), p. 210403 (see pp. 104, 154).

[219] M. Gring, M. Kuhnert, T. Langen, T. Kitagawa, B. Rauer, M. Schreitl, I. Mazets, D. A. Smith, E. Demler, and J. Schmiedmayer. *Relaxation and Prethermalization in an Isolated Quantum System*. In: Science 337.6100 (Sept. 2012), pp. 1318–1322 (see pp. 104, 154).

[220] T.-L. Ho and Q. Zhou. *Obtaining the phase diagram and thermodynamic quantities of bulk systems from the densities of trapped gases*. In: Nature Physics 6.2 (2010), pp. 131–134 (see p. 104).

[221] M. Horikoshi, S. Nakajima, M. Ueda, and T. Mukaiyama. *Measurement of universal thermodynamic functions for a unitary Fermi gas*. In: Science 327.5964 (2010), pp. 442–445 (see p. 105).

[222] S. Nascimbène, N. Navon, K. Jiang, F. Chevy, and C. Salomon. *Exploring the thermodynamics of a universal Fermi gas*. In: Nature 463.7284 (2010), pp. 1057–1060 (see p. 105).

[223] M. J. Ku, A. T. Sommer, L. W. Cheuk, and M. W. Zwierlein. *Revealing the superfluid lambda transition in the universal thermodynamics of a unitary Fermi gas*. In: Science 335.6068 (2012), pp. 563–567 (see p. 105).

[224] N. Navon, S. Nascimbene, F. Chevy, and C. Salomon. *The equation of state of a low-temperature Fermi gas with tunable interactions*. In: Science 328.5979 (2010), pp. 729–732 (see p. 105).

[225] M. Bauer, M. M. Parish, and T. Enss. *Universal equation of state and pseudogap in the two-dimensional Fermi gas*. In: Physical review letters 112.13 (2014), p. 135302 (see p. 105).

[226] M. Hoffman, P. Javernick, A. Loheac, W. Porter, E. Anderson, and J. E. Drut. *Universality in one-dimensional fermions at finite temperature: Density, pressure, compressibility, and contact*. In: Physical Review A 91.3 (2015), p. 033618 (see p. 105).

[227] K. Van Houcke, F. Werner, E. Kozik, N. Prokof'ev, B. Svistunov, M. Ku, A. Sommer, L. Cheuk, A. Schirotzek, and M. Zwierlein. *Feynman diagrams versus Fermi-gas Feynman emulator*. In: Nature Physics 8.5 (2012), pp. 366–370 (see p. 105).

[228] J. E. Drut, T. A. Lähde, G. Wlazłowski, and P. Magierski. *Equation of state of the unitary Fermi gas: An update on lattice calculations*. In: Physical Review A 85.5 (2012), p. 051601 (see p. 105).

[229] F. Salces-Carcoba, C. J. Billington, A. Putra, Y. Yue, S. Sugawa, and I. B. Spielman. *Equations of state from individual one-dimensional Bose gases*. In: New Journal of Physics 20.11 (Nov. 2018), p. 113032 (see p. 105).

[230] T. Yefsah, R. Desbuquois, L. Chomaz, K. J. Günter, and J. Dalibard. *Exploring the thermodynamics of a two-dimensional Bose gas*. In: Physical review letters 107.13 (2011), p. 130401 (see p. 105).

[231] K. Fenech, P. Dyke, T. Peppler, M. Lingham, S. Hoinka, H. Hu, and C. Vale. *Thermodynamics of an attractive 2D Fermi gas*. In: Physical review letters 116.4 (2016), p. 045302 (see p. 105).

[232] I. Boettcher, L. Bayha, D. Kedar, P. Murthy, M. Neidig, M. Ries, A. Wenz, G. Zuern, S. Jochim, and T. Enss. *Equation of state of ultracold fermions in the 2D BEC-BCS crossover region*. In: Physical review letters 116.4 (2016), p. 045303 (see p. 105).

[233] X.-W. Guan, M. T. Batchelor, and C. Lee. *Fermi gases in one dimension: From Bethe ansatz to experiments*. In: Reviews of Modern Physics 85.4 (Nov. 2013), pp. 1633–1691 (see p. 105).

[234] H. Tajima, S. Tsutsui, and T. M. Doi. *Low-dimensional fluctuations and pseudogap in Gaudin-Yang Fermi gases*. In: Physical Review Research 2.3 (2020), p. 033441 (see p. 105).

[235] S. Wolf, D. Awschalom, R. Buhrman, J. Daughton, v. S. von Molnár, M. Roukes, A. Y. Chtchelkanova, and D. Treger. *Spintronics: a spin-based electronics vision for the future*. In: science 294.5546 (2001), pp. 1488–1495 (see p. 107).

[236] H. B. Meyer. *Transport properties of the quark-gluon plasma*. In: The European Physical Journal A 47.7 (2011), pp. 1–52 (see p. 107).

[237] B. Müller. *The physics of the quark-gluon plasma*. Vol. 225. 1985 (see p. 107).

[238] P. T. Brown, D. Mitra, E. Guardado-Sanchez, R. Nourafkan, A. Reymbaut, C.-D. Hébert, S. Bergeron, A.-M. Tremblay, J. Kokalj, D. A. Huse, et al. *Bad metallic transport in a cold atom Fermi-Hubbard system*. In: Science 363.6425 (2019), pp. 379–382 (see p. 107).

[239] M. A. Nichols, L. W. Cheuk, M. Okan, T. R. Hartke, E. Mendez, T. Senthil, E. Khatami, H. Zhang, and M. W. Zwierlein. *Spin transport in a Mott insulator of ultracold fermions*. In: Science 363.6425 (2019), pp. 383–387 (see p. 107).

[240] J.-P. Brantut, C. Grenier, J. Meineke, D. Stadler, S. Krinner, C. Kollath, T. Esslinger, and A. Georges. *A thermoelectric heat engine with ultracold atoms*. In: Science 342.6159 (2013), pp. 713–715 (see pp. 107, 116).

[241] C. Cao, E. Elliott, J. Joseph, H. Wu, J. Petricka, T. Schäfer, and J. E. Thomas. *Universal quantum viscosity in a unitary Fermi gas*. In: Science 331.6013 (2011), pp. 58–61 (see p. 107).

[242] J. Joseph, E. Elliott, and J. Thomas. *Shear viscosity of a unitary Fermi gas near the superfluid phase transition*. In: Physical review letters 115.2 (2015), p. 020401 (see p. 107).

[243] M. R. Andrews, D. M. Stamper-Kurn, H.-J. Miesner, D. S. Durfee, C. G. Townsend, S. Inouye, and W. Ketterle. *Erratum: Propagation of Sound in a Bose-Einstein Condensate [Phys. Rev. Lett. 79, 553 (1997)]*. In: Phys. Rev. Lett. 80 (13 Mar. 1998), pp. 2967–2967 (see p. 107).

[244] J. Joseph, B. Clancy, L. Luo, J. Kinast, A. Turlapov, and J. Thomas. *Measurement of sound velocity in a Fermi gas near a Feshbach resonance*. In: Physical review letters 98.17 (2007), p. 170401 (see p. 107).

[245] L. A. Sidorenkov, M. K. Tey, R. Grimm, Y.-H. Hou, L. Pitaevskii, and S. Stringari. *Second sound and the superfluid fraction in a Fermi gas with resonant interactions*. In: Nature 498.7452 (2013), pp. 78–81 (see p. 107).

[246] G. Valtolina, F. Scazza, A. Amico, A. Burchianti, A. Recati, T. Enss, M. Inguscio, M. Zaccanti, and G. Roati. *Exploring the ferromagnetic behaviour of a repulsive Fermi gas through spin dynamics*. In: Nature Physics 13.7 (2017), pp. 704–709 (see pp. 107–110, 116, 128, 139, 141, 142, 149, 155).

[247] A. Sommer, M. Ku, G. Roati, and M. W. Zwierlein. *Universal spin transport in a strongly interacting Fermi gas*. In: Nature 472.7342 (Apr. 2011), pp. 201–204. arXiv: 1101.0780 (see pp. 107–110, 128, 139, 141, 142, 145, 146, 149).

[248] A. Sommer, M. Ku, and M. W. Zwierlein. *Spin transport in polaronic and superfluid Fermi gases*. In: New Journal of Physics 13.5 (2011), p. 055009 (see p. 107).

[249] A. Bardon, S. Beattie, C. Luciuk, W. Cairncross, D. Fine, N. Cheng, G. Edge, E. Taylor, S. Zhang, S. Trotzky, et al. *Transverse demagnetization dynamics of a unitary Fermi gas*. In: Science 344.6185 (2014), pp. 722–724 (see pp. 107–109).

[250] M. Koschorreck, D. Pertot, E. Vogt, and M. Köhl. *Universal spin dynamics in two-dimensional Fermi gases*. In: Nature Physics 9.7 (2013), pp. 405–409 (see pp. 107–109, 150).

[251] C. Luciuk, S. Smale, F. Böttcher, H. Sharum, B. Olsen, S. Trotzky, T. Enss, and J. Thywissen. *Observation of quantum-limited spin transport in strongly interacting two-dimensional Fermi gases*. In: Physical review letters 118.13 (2017), p. 130405 (see pp. 107–109, 150).

[252] T. Enss and J. H. Thywissen. *Universal spin transport and quantum bounds for unitary fermions*. In: Annual Review of Condensed Matter Physics 10 (2019), pp. 85–106 (see p. 107).

[253] T. Enss and R. Haussmann. *Quantum mechanical limitations to spin diffusion in the unitary Fermi gas*. In: Physical review letters 109.19 (2012), p. 195303 (see pp. 107, 108).

[254] M. Punk and W. Zwerger. *Collective mode damping and viscosity in a 1D unitary Fermi gas*. In: New Journal of Physics 8.8 (2006), p. 168 (see p. 107).

[255] G. Pecci, P. Vignolo, and A. Minguzzi. *Universal scaling of spin mixing dynamics in a strongly interacting one-dimensional Fermi gas*. In: arXiv preprint arXiv:2107.12075 (2021) (see pp. 107, 154).

[256] M. Łebek, A. Syrwid, P. T. Grochowski, and K. Rzążewski. *Repulsive dynamics of strongly attractive one-dimensional quantum gases*. In: arXiv preprint arXiv:2107.05594 (2021) (see p. 107).

[257] P. B. Patel, Z. Yan, B. Mukherjee, R. J. Fletcher, J. Struck, and M. W. Zwierlein. *Universal sound diffusion in a strongly interacting Fermi gas*. In: Science 370.6521 (2020), pp. 1222–1226 (see p. 107).

[258] M. Bohlen, L. Sobirey, N. Luick, H. Biss, T. Enss, T. Lompe, and H. Moritz. *Sound propagation and quantum-limited damping in a two-dimensional Fermi gas*. In: Physical Review Letters 124.24 (2020), p. 240403 (see p. 107).

[259] A. J. Leggett and M. Rice. *Spin echoes in liquid he 3 and mixtures: A predicted new effect*. In: Physical review letters 20.12 (1968), p. 586 (see p. 108).

[260] A. J. Leggett. *Spin diffusion and spin echoes in liquid 3He at low temperature*. In: Journal of Physics C: Solid State Physics 3.2 (1970), p. 448 (see p. 108).

[261] L. Corruccini, D. Osheroff, D. Lee, and R. Richardson. *Spin Diffusion in Liquid He 3: The Effect of Leggett and Rice*. In: Physical Review Letters 27.10 (1971), p. 650 (see p. 108).

[262] S. Trotzky, S. Beattie, C. Luciuk, S. Smale, A. Bardon, T. Enss, E. Taylor, S. Zhang, and J. Thywissen. *Observation of the Leggett-Rice effect in a unitary Fermi gas*. In: Physical review letters 114.1 (2015), p. 015301 (see p. 108).

[263] T. G. Tiecke. *Properties of Potassium*. In: Physics 02.20 (2010), pp. 1–14 (see p. 110).

[264] G. Breit and I. Rabi. *Measurement of nuclear spin*. In: Physical Review 38.11 (1931), p. 2082 (see p. 110).

[265] B. D. Cullity and C. D. Graham. *Introduction to magnetic materials*. John Wiley & Sons, 2011 (see p. 110).

[266] G. Sinuco-León and B. Garraway. *Radio-frequency dressed atoms beyond the linear Zeeman effect*. In: New Journal of Physics 14.12 (2012), p. 123008 (see p. 114).

[267] A. Ludewig. *Feshbach resonances in 40 K*. PhD thesis. University of Amsterdam, 2012 (see pp. 114, 136).

[268] T. G. Tiecke, M. R. Goosen, A. Ludewig, S. D. Gensemer, S. Kraft, S. J. J. M. F. Kokkelmans, and J. T. M. Walraven. *Broad Feshbach Resonance in the Li6-K40 Mixture*. In: Physical Review Letters 104.5 (Feb. 2010), p. 053202. arXiv: 0908.2071 (see p. 114).

[269] T. G. Tiecke. *Feshbach resonances in ultracold mixtures of the fermionic quantum gases 6Li and 40K*. PhD thesis. University of Amsterdam, 2010 (see p. 114).

[270] J. S. Krauser, J. Heinze, S. Götze, M. Langbecker, N. Fläschner, L. Cook, T. M. Hanna, E. Tiesinga, K. Sengstock, and C. Becker. *Investigation of Feshbach resonances in ultracold K40 spin mixtures*. In: Physical Review A 95.4 (Apr. 2017), p. 042701. arXiv: 1701.02085 (see p. 114).

[271] W. H. Carter. *Electromagnetic field of a Gaussian beam with an elliptical cross section*. In: JOSA 62.10 (1972), pp. 1195–1201 (see p. 116).

[272] M. Moore, T. Bergeman, and M. Olshanii. *Scattering in tight atom waveguides*. In: *Journal de Physique IV (Proceedings)*. Vol. 116. EDP sciences. 2004, pp. 69–86 (see pp. 123, 126, 143).

[273] A. Hurwitz. *Einige Eigenschaften der Dirichlet'schen Functionen F (s)= Σ (D n) 1 ns, die bei der Bestimmung der Classenzahlen binärer quadratischer Formen auftreten*. In: Zeitschrift für Math. und Phys 27 (1882), pp. 86–101 (see p. 123).

[274] T. M. Apostol. *Introduction to Analytic Number Theory*. 1976 (see p. 123).

[275] G. Astrakharchik, D. Blume, S. Giorgini, and B. Granger. *Quasi-one-dimensional Bose gases with a large scattering length*. In: Physical review letters 92.3 (2004), p. 030402 (see p. 126).

[276] J. Fuchs, A. Recati, and W. Zwerger. *Exactly solvable model of the BCS-BEC crossover*. In: Physical review letters 93.9 (2004), p. 090408 (see p. 126).

[277] B. E. Granger and D. Blume. *Tuning the interactions of spin-polarized fermions using quasi-one-dimensional confinement*. In: Physical review letters 92.13 (2004), p. 133202 (see p. 127).

[278] K. Günter, T. Stöferle, H. Moritz, M. Köhl, and T. Esslinger. *p-Wave interactions in low-dimensional fermionic gases*. In: Physical review letters 95.23 (2005), p. 230401 (see p. 127).

[279] L. Vichi and S. Stringari. *Collective oscillations of an interacting trapped Fermi gas*. In: Physical Review A 60.6 (1999), p. 4734 (see pp. 131, 139, 141, 142).

[280] A. T. Sommer. *Strongly interacting Fermi gases: non-equilibrium dynamics and dimensional crossover*. PhD thesis. Massachusetts Institute of Technology, 2013 (see pp. 131, 138).

[281] N. P. Mehta, B. Esry, and C. H. Greene. *Three-body recombination in one dimension*. In: Physical Review A 76.2 (2007), p. 022711 (see p. 132).

[282] A. S. Marcum, F. R. Fonta, A. M. Ismail, and K. M. O'Hara. *Suppression of Three-Body Loss Near a p-Wave Resonance Due to Quasi-1D Confinement*. In: arXiv preprint arXiv:2007.15783 (2020) (see pp. 132, 155).

[283] B. L. Tolra, K. O'hara, J. Huckans, W. D. Phillips, S. Rolston, and J. V. Porto. *Observation of reduced three-body recombination in a correlated 1D degenerate Bose gas*. In: Physical review letters 92.19 (2004), p. 190401 (see pp. 132, 155).

[284] C. Regal, C. Ticknor, J. L. Bohn, and D. S. Jin. *Tuning p-wave interactions in an ultracold Fermi gas of atoms*. In: Physical review letters 90.5 (2003), p. 053201 (see pp. 136, 155).

[285] I. D'Amico and G. Vignale. *Theory of spin Coulomb drag in spin-polarized transport*. In: Physical Review B 62.8 (2000), p. 4853 (see pp. 138, 139).

[286] D. Guéry-Odelin, F. Zambelli, J. Dalibard, and S. Stringari. *Collective oscillations of a classical gas confined in harmonic traps*. In: Physical Review A 60.6 (1999), p. 4851 (see pp. 142, 143).

[287] T. Yamada and J. Sone. *High-field electron transport in quantum wires studied by solution of the Boltzmann equation*. In: Physical Review B 40.9 (1989), p. 6265 (see p. 143).

[288] H. Bruus, K. Flensberg, and H. Smith. *Magnetoconductivity of quantum wires with elastic and inelastic scattering*. In: Physical Review B 48.15 (1993), p. 11144 (see p. 143).

[289] A. O'hagan and T. Leonard. *Bayes estimation subject to uncertainty about parameter constraints*. In: Biometrika 63.1 (1976), pp. 201–203 (see p. 144).

[290] G. Bruun and C. Pethick. *Spin diffusion in trapped clouds of cold atoms with resonant interactions*. In: Physical review letters 107.25 (2011), p. 255302 (see pp. 146, 148).

[291] F. Ferlaino. *Atomic Fermi gases in an optical lattice*. PhD thesis. PhD Thesis, University of Florence, 2004 (see p. 149).

[292] M. Rigol, V. Dunjko, V. Yurovsky, and M. Olshanii. *Relaxation in a completely integrable many-body quantum system: an ab initio study of the dynamics of the highly excited states of 1D lattice hard-core bosons*. In: Physical review letters 98.5 (2007), p. 050405 (see p. 154).

[293] F. Meinert, M. Knap, E. Kirilov, K. Jag-Lauber, M. B. Zvonarev, E. Demler, and H.-C. Nägerl. *Bloch oscillations in the absence of a lattice*. In: Science 356.6341 (2017), pp. 945–948 (see p. 154).

[294] M. Schemmer, I. Bouchoule, B. Doyon, and J. Dubail. *Generalized hydrodynamics on an atom chip*. In: Physical review letters 122.9 (2019), p. 090601 (see p. 154).

[295] E. C. Stoner. *LXXX. Atomic moments in ferromagnetic metals and alloys with non-ferromagnetic elements*. In: The London, Edinburgh, and Dublin Philosophical Magazine and Journal of Science 15.101 (1933), pp. 1018–1034 (see p. 155).

[296] D. C. Mattis. *The Theory of magnetism: an introduction to the study of cooperative phenomena*. Vol. 17. Harper & Row, 1965 (see p. 155).

[297] T. Sogo and H. Yabu. *Collective ferromagnetism in two-component Fermi-degenerate gas trapped in a finite potential*. In: Physical Review A 66.4 (2002), p. 043611 (see p. 155).

[298] R. Duine and A. MacDonald. *Itinerant ferromagnetism in an ultracold atom fermi gas*. In: Physical review letters 95.23 (2005), p. 230403 (see p. 155).

[299] H. Zhai. *Correlated versus ferromagnetic state in repulsively interacting two-component Fermi gases*. In: Physical Review A 80.5 (2009), p. 051605 (see p. 155).

[300] G. Conduit and B. Simons. *Repulsive atomic gas in a harmonic trap on the border of itinerant ferromagnetism*. In: Physical review letters 103.20 (2009), p. 200403 (see p. 155).

[301] L. LeBlanc, J. Thywissen, A. Burkov, and A. Paramekanti. *Repulsive Fermi gas in a harmonic trap: Ferromagnetism and spin textures*. In: Physical Review A 80.1 (2009), p. 013607 (see p. 155).

[302] I. Berdnikov, P. Coleman, and S. H. Simon. *Itinerant ferromagnetism in an atom trap*. In: Physical Review B 79.22 (2009), p. 224403 (see p. 155).

[303] S. Pilati, G. Bertaina, S. Giorgini, and M. Troyer. *Itinerant ferromagnetism of a repulsive atomic Fermi gas: A quantum Monte Carlo study*. In: Physical review letters 105.3 (2010), p. 030405 (see p. 155).

[304] S.-Y. Chang, M. Randeria, and N. Trivedi. *Ferromagnetism in the upper branch of the Feshbach resonance and the hard-sphere Fermi gas*. In: Proceedings of the National Academy of Sciences 108.1 (2011), pp. 51–54 (see p. 155).

[305] G.-B. Jo, Y.-R. Lee, J.-H. Choi, C. A. Christensen, T. H. Kim, J. H. Thywissen, D. E. Pritchard, and W. Ketterle. *Itinerant ferromagnetism in a Fermi gas of ultracold atoms*. In: Science 325.5947 (2009), pp. 1521–1524 (see p. 155).

[306] C. Sanner, E. J. Su, W. Huang, A. Keshet, J. Gillen, and W. Ketterle. *Correlations and pair formation in a repulsively interacting Fermi gas*. In: Physical review letters 108.24 (2012), p. 240404 (see p. 155).

[307] S. E. Gharashi and D. Blume. *Correlations of the upper branch of 1D harmonically trapped two-component Fermi gases*. In: Physical review letters 111.4 (2013), p. 045302 (see p. 155).

[308] X. Cui and T.-L. Ho. *Ground-state ferromagnetic transition in strongly repulsive one-dimensional Fermi gases*. In: Physical Review A 89.2 (2014), p. 023611 (see p. 155).

[309] Y. Jiang, D. Kurlov, X.-W. Guan, F. Schreck, and G. Shlyapnikov. *Itinerant ferromagnetism in one-dimensional two-component Fermi gases*. In: Physical Review A 94.1 (2016), p. 011601 (see p. 155).

[310] P. W. Anderson. *Absence of diffusion in certain random lattices*. In: Physical review 109.5 (1958), p. 1492 (see p. 156).

[311] B. L. Altshuler, Y. Gefen, A. Kamenev, and L. S. Levitov. *Quasiparticle lifetime in a finite system: A nonperturbative approach*. In: Physical review letters 78.14 (1997), p. 2803 (see p. 156).

[312] I. V. Gornyi, A. D. Mirlin, and D. G. Polyakov. *Interacting electrons in disordered wires: Anderson localization and low-T transport*. In: Physical review letters 95.20 (2005), p. 206603 (see p. 156).

[313] D. M. Basko, I. L. Aleiner, and B. L. Altshuler. *Metal–insulator transition in a weakly interacting many-electron system with localized single-particle states*. In: Annals of physics 321.5 (2006), pp. 1126–1205 (see p. 156).

[314] E. Altman and R. Vosk. *Universal dynamics and renormalization in many-body-localized systems*. In: Annu. Rev. Condens. Matter Phys. 6.1 (2015), pp. 383–409 (see p. 156).

[315] R. Nandkishore and D. A. Huse. *Many-body localization and thermalization in quantum statistical mechanics*. In: Annu. Rev. Condens. Matter Phys. 6.1 (2015), pp. 15–38 (see p. 156).

[316] D. A. Abanin and Z. Papić. *Recent progress in many-body localization*. In: Annalen der Physik 529.7 (2017), p. 1700169 (see p. 156).

[317] S. Parameswaran and R. Vasseur. *Many-body localization, symmetry and topology*. In: Reports on Progress in Physics 81.8 (2018), p. 082501 (see p. 156).

[318] F. Alet and N. Laflorencie. *Many-body localization: An introduction and selected topics*. In: Comptes Rendus Physique 19.6 (2018), pp. 498–525 (see p. 156).

[319] D. A. Abanin, E. Altman, I. Bloch, and M. Serbyn. *Colloquium: Many-body localization, thermalization, and entanglement*. In: Reviews of Modern Physics 91.2 (2019), p. 021001 (see p. 156).

[320] I. Gornyi, A. Mirlin, M. Müller, and D. Polyakov. *Absence of many-body localization in a continuum*. In: Annalen der Physik 529.7 (2017), p. 1600365 (see p. 156).

[321] X. Li, X. Li, and S. D. Sarma. *Mobility edges in one-dimensional bichromatic incommensurate potentials*. In: Physical Review B 96.8 (2017), p. 085119 (see p. 156).

[322] G. Bertoli, V. Michal, B. Altshuler, and G. Shlyapnikov. *Finite-temperature disordered bosons in two dimensions*. In: Physical review letters 121.3 (2018), p. 030403 (see p. 156).

[323] G. Bertoli, B. Altshuler, and G. Shlyapnikov. *Many-body localization in continuum systems: Two-dimensional bosons*. In: Physical Review A 100.1 (2019), p. 013628 (see p. 156).

[324] S. Kondov, W. McGehee, W. Xu, and B. DeMarco. *Disorder-induced localization in a strongly correlated atomic Hubbard gas*. In: Physical review letters 114.8 (2015), p. 083002 (see p. 156).

[325] M. Schreiber, S. S. Hodgman, P. Bordia, H. P. Lüschen, M. H. Fischer, R. Vosk, E. Altman, U. Schneider, and I. Bloch. *Observation of many-body localization of interacting fermions in a quasirandom optical lattice*. In: Science 349.6250 (2015), pp. 842–845 (see p. 156).

[326] J.-y. Choi, S. Hild, J. Zeiher, P. Schauß, A. Rubio-Abadal, T. Yefsah, V. Khemani, D. A. Huse, I. Bloch, and C. Gross. *Exploring the many-body localization transition in two dimensions*. In: Science 352.6293 (2016), pp. 1547–1552 (see p. 156).

[327] J. Smith, A. Lee, P. Richerme, B. Neyenhuis, P. W. Hess, P. Hauke, M. Heyl, D. A. Huse, and C. Monroe. *Many-body localization in a quantum simulator with programmable random disorder*. In: Nature Physics 12.10 (2016), pp. 907–911 (see p. 156).

[328] H. P. Lüschen, P. Bordia, S. S. Hodgman, M. Schreiber, S. Sarkar, A. J. Daley, M. H. Fischer, E. Altman, I. Bloch, and U. Schneider. *Signatures of many-body localization in a controlled open quantum system*. In: Physical Review X 7.1 (2017), p. 011034 (see p. 156).

[329] K. X. Wei, C. Ramanathan, and P. Cappellaro. *Exploring localization in nuclear spin chains*. In: Physical review letters 120.7 (2018), p. 070501 (see p. 156).

[330] T. Kohlert, S. Scherg, X. Li, H. P. Lüschen, S. D. Sarma, I. Bloch, and M. Aidelsburger. *Observation of many-body localization in a one-dimensional system with a single-particle mobility edge*. In: Physical review letters 122.17 (2019), p. 170403 (see p. 156).

RÉSUMÉ

Le comportement des gaz de Fermi en basse dimension se distingue sensiblement de leurs équivalents tridimensionnels. En trois dimensions et en l'absence d'ordre, la majorité des états fermioniques de la matière sont décrits par la théorie du liquide de Landau-Fermi. Dans son cadre, le système est décrit comme un gaz de quasiparticules fermioniques en interaction faible, voire nulle. En revanche, dans le cas unidimensionnel, le spectre du système à basses énergies est entièrement déterminé par des excitations collectives de nature bosonique.

Cette thèse décrit l'étude expérimentale des gaz de Fermi en basse dimension en utilisant des atomes de ^{40}K. Nous présentons ici trois principaux résultats. Tout d'abord, nous mettons en évidence l'implémentation de techniques nouvelles pour charger et imager individuellement des échantillons d'atomes dans un réseau optique bidimensionnel à espacement large. Ensuite, en utilisant des gaz idéaux, nous conduisons une étude quantitative de profiles de densité in-situ obtenus dans un potentiel externe préalablement calibré pour quantifier le degré de dégénérescence et la dimensionnalité des échantillons préparés. Nous rapportons l'observation de gaz de Fermi dans le régime unidimensionnel. Finalement, nous développons une technique pour séparer et isoler les deux populations de spin d'un gaz de Fermi et l'appliquons pour étudier le transport de spin en présence d'interactions fortes. Nous analysons quantitativement la relaxation du mode dipolaire dans le régime diffusif en fonction de l'intensité des interactions en se plaçant au voisinage d'une résonance de Feshbach en onde s. Nous déterminons la force de traînée ainsi que le coefficient de diffusivité. La valeur minimale mesurée de ce dernier respecte la limite quantique malgré l'absence d'invariance d'échelle dans le système. Ce dernier résultat s'ajoute au corpus de connaissance existante issue de précédentes études expérimentales réalisées avec des gaz de Fermi en deux et trois dimensions.

MOTS CLÉS

Atomes ultrafroids, gaz de Fermi, systèmes quantiques à N corps fortement corrélés, simulation quantique.

ABSTRACT

The behaviour of low-dimensional interacting Fermi gases greatly differs from their three-dimensional counterparts. In absence of order in 3D, the majority of fermionic states of matter can be explained by the Landau-Fermi liquid theory. Within this framework the system is described as a gas of non- or weakly-interacting fermionic quasiparticles. By contrast, in one dimension, the low-energy excitation spectrum of the system is entirely made up of collective excitations obeying bosonic statistics.

This thesis reports on the experimental study of low-dimensional Fermi gases using ultracold ^{40}K atoms. The main results are threefold. First, we describe the conception of novel experimental techniques to load and individually image an array of tube-shaped micro traps in a large-spacing optical lattice. Second, using these atomic ensembles in a noninteracting setting, we perform a quantitative analysis of their in-situ density profiles to extract the degree of quantum degeneracy and effective dimensionality. In this context, we show evidence of the preparation of Fermi gases in the one-dimensional regime. Third, we present a technique to separate the spin components of the gas and apply it to study spin transport in low dimensions in the presence of strong interactions. We quantitatively model the spin dipole relaxation process in the diffusive regime as a function of the interaction strength tuned with an s-wave Feshbach resonance. We determine the spin drag and the diffusivity. This minimal value of the latter is compatible with the quantum bound despite the absence of scale-invariance in the system, and supplements existing experimental studies in two- and three-dimensional Fermi gases.

KEYWORDS

Ultracold atoms, Fermi gases, strongly correlated quantum many-body systems, quantum simulation.